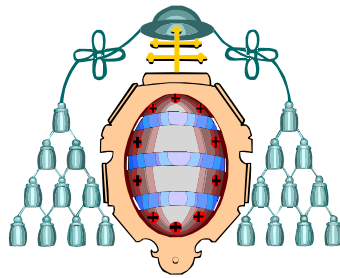
The background of the cover features a complex geometric pattern of teal and yellow shapes, including triangles, squares, and concentric circles, creating a modern and abstract design.

# Modelling of 4-wire low voltage systems for enhanced control strategies of grid-tied power converters

Andrés Suárez González

This dissertation is submitted for the degree  
of Doctor of Philosophy

**University of Oviedo**  
DEPARTMENT OF ELECTRICAL, ELECTRONICS,  
COMPUTERS AND SYSTEMS ENGINEERING



**UNIVERSIDAD DE OVIEDO**

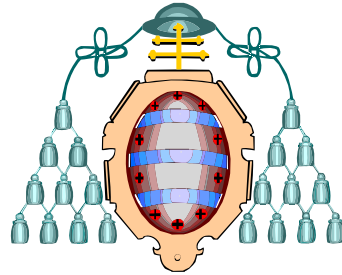
**Ph.D. Thesis**  
**PhD Program in Energy and Process Control**

MODELLING OF 4-WIRE LOW VOLTAGE SYSTEMS  
FOR ENHANCED CONTROL STRATEGIES  
OF GRID-TIED POWER CONVERTERS

Andrés Suárez González

*Gijón, July 2020*

UNIVERSITY OF OVIEDO  
Department of Electrical, Electronics, Computers  
and Systems Engineering



UNIVERSIDAD DE OVIEDO

Ph.D. THESIS DISSERTATION

MODELLING OF 4-WIRE LOW VOLTAGE SYSTEMS  
FOR ENHANCED CONTROL STRATEGIES  
OF GRID-TIED POWER CONVERTERS

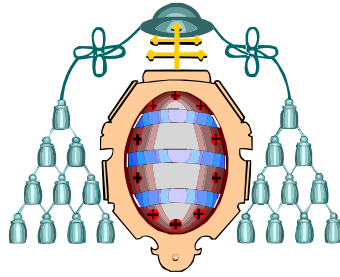
Dissertation submitted in fulfilment of the requirements for the degree of  
Doctor of Philosophy in the Energy and Process Control PhD program of  
the University of Oviedo

**Andrés Suárez González**

Supervisors: Pablo García Fernández.  
José Manuel Cano Rodríguez.  
Department of Electrical, Electronics, Computers  
and Systems Engineering

*Gijón, July 2020*

UNIVERSIDAD DE OVIEDO  
Departamento de Ingeniería Eléctrica, Electrónica,  
de Computadores y Sistemas



UNIVERSIDAD DE OVIEDO

TESIS DOCTORAL

MODELADO DE SISTEMAS DE BAJA TENSIÓN EN 4 HILOS  
PARA ESTRATEGIAS DE CONTROL MEJORADAS DE  
CONVERTIDORES CONECTADOS A RED

Tesis presentada en cumplimiento de los requisitos para la obtención del  
título de Doctor en el programa de doctorado de Energía y Control de  
Procesos de la Universidad de Oviedo

**Andrés Suárez González**

Directores: Pablo García Fernández.  
José Manuel Cano Rodríguez.  
Departamento de Ingeniería Eléctrica, Electrónica,  
de Computadores y Sistemas

*Gijón, Julio 2020*

*A mis padres*

# Agradecimientos

Quiero comenzar agradeciendo a mis dos directores de tesis: Pablo García y José Manuel Cano, toda la ayuda prestada a lo largo de estos años. Su clarividencia, inmensa paciencia, saber hacer y absoluto apoyo, han permitido que este trabajo llegue a su consecución. Su generosidad y empatía han sido un ejemplo tanto a nivel profesional como personal.

A toda la gente del departamento de Ingeniería Eléctrica de la Universidad de Oviedo y en particular a los miembros del grupo LEMUR: Cristina, Jorge, Pablo y Cristian, quienes han logrado formar un equipo competitivo y vanguardista, creando un entorno de trabajo difícil de igualar y del que me he sentido uno más desde el primer momento. También quiero recordar a mis compañeros, en especial a Ramy y a Geber, por toda la ayuda y el apoyo prestado, por las muchas horas invertidas en los diseños de las PCBs de los pedales de guitarra (las fuentes fueron un éxito), por las clases de teoría musical y baile, los conciertos, y un largo etcétera. A Sarah, Irene y María, por las descargas de Cangas, por las cenas con Pipe y las noches por Cimavilla y en definitiva por su calidad humana, siempre dispuestas a echar una mano. A Ángel por toda la ayuda prestada en el laboratorio, que no ha sido poca. A Carlos y Miguel por las charlas de café y a Bassam por su ayuda con los scripts. Hago extensivo este agradecimiento al resto de miembros del grupo: Islam, Rocío, Xavier, Rand, Komal y a todas aquellas personas que mi mala cabeza olvide.

Por supuesto, incluyo también a mis amigos, algunos me han acompañado desde los inocentes años del parvulario de Contrueces: a Manuel, por todos los años y temeridades vividas (yo creo que dan para otra tesis), de las que sin duda la mayor haya sido dejarme ser padrino de Sofía. A Juli, por acompañarme en casi todas mis aventuras musicales y en tantas otras, como tú dijiste: espero que nos queden muchos paseos en bicicleta juntos. A Javi, por los duros tiempos de soltería y cachondeo que ya van quedando atrás. A José, que sin él todo sería más formal y correcto, pero mucho más aburrido. A Adrián, por esa memoria para recordar los buenos momentos (a veces los malos también) con todo lujo de detalle. A Nacho, que a pesar del caos que le rodea, sus consejos tienen un carácter práctico que siempre me abruma. A *Plastic Soul*, por los muchos conciertos y por los muchos más filetes en el Sancho.

No me quiero olvidar tampoco de la gente de Madrid: a Raúl y Marta, por haberme

acogido y por haberme tratado como uno más desde el primer día que llegué a aquella oficina de Iberinco. A Víctor y Ana por quererme como si fuese familia, y por las muchas noches de cañas en San Ildefonso y aquella terraza de Orense. A Diego y David que me animaron a apostar por este camino, cuando ni siquiera yo lo tenía claro.

Por supuesto a Lola. Ella ha sufrido pacientemente mis malos humores, mis silencios y mis negativas, habiendo sabido soportarlo y mostrándose siempre comprensiva conmigo. Ha sido y es una fuente constante de apoyo y amor.

Y por último y en el lugar principal, quiero agradecer a mis padres, Mariangel y Andrés, su apoyo incondicional durante todos mis años de estudiante (que no han sido pocos). Ellos han sido los únicos que han sufrido tanto como yo las frustraciones y los desvelos de este trabajo y los que siempre me han ayudado a levantarme las muchas veces que me he caído. Me resulta imposible encontrar palabras de agradecimiento que estén a la altura de su generosidad. Este trabajo está dedicado a ellos.

# Resumen

La evolución del sistema eléctrico está propiciando la aparición de nuevos condicionantes en el escenario tradicional. Así, la presencia de fuentes renovables, generadores distribuidos, soluciones para el almacenamiento de energía, sistemas inteligentes y la proliferación de cargas no lineales, suponen una serie de nuevos retos para la operación y la seguridad del propio sistema. La incorporación de estos nuevos actores trae de la mano un cambio de paradigma: de un sistema centralizado hacia uno más distribuido. En este nuevo escenario, los generadores se sitúan más cerca de los consumidores, propiciando sistemas con un elevado nivel de autonomía energética que, en el caso límite, pueden llegar a ser independientes de la red pública. Surge así el concepto de microrred, enmarcado en el contexto de lo que hoy conocemos como redes inteligentes. En estas nuevas redes, la incorporación de recursos distribuidos interconectados mediante convertidores de potencia juega un papel decisivo para la correcta operación del sistema.

El presente trabajo se centra en la operación de convertidores de potencia conectados a red en microrredes de corriente alterna. Se ha prestado especial atención al problema de la variabilidad de la impedancia equivalente de la red aguas arriba del punto de conexión en baja tensión de estos convertidores, relacionándolo con el impacto que ocasiona en el comportamiento dinámico del sistema de control de estos dispositivos. Las soluciones propuestas, basadas en técnicas de estimación de impedancia, permiten implementar sistemas de control que reaccionan a cambios en la red y logran la compensación en tiempo real de condiciones de desequilibrio. Para llevar a cabo esta tarea, sólo precisan de la información de variables eléctricas medidas en el punto de conexión, haciendo uso de la flexibilidad de los convertidores para generar señales de excitación superpuestas a la componente fundamental. Además, la estimación de parámetros de red brinda oportunidades relacionadas con la mejora de la eficiencia del sistema, por lo que también se han propuesto soluciones de optimización basadas en la operación de convertidores de potencia a frecuencia variable.

Esta tesis está organizada en seis capítulos principales a los que se añade un capítulo final de conclusiones. Los dos primeros sirven para detallar la motivación, oportunidades de investigación y el estudio del estado actual de la técnica. Esto proporciona una visión general del problema a estudiar y del marco de trabajo, así como la enumeración de los principales retos a los que se enfrentan los convertidores de potencia

conectados a red. Las contribuciones del presente trabajo, desarrolladas a lo largo de los siguientes cuatro capítulos, pueden resumirse en: 1) El desarrollo de una nueva metodología para el modelado de red, la cual permite expresar de forma compacta la impedancia equivalente vista desde el punto de conexión del recurso distribuido. Esta metodología incluye a los sistemas de cuatro hilos y permite ser aplicada tanto en condiciones equilibradas como desequilibradas. El modelo propuesto permite determinar, mediante un sistema de representación en coordenadas estacionarias, la evolución temporal de las tensiones/corrientes ante la conexión y desconexión de diferentes cargas locales; 2) La implementación de una técnica fiable para determinar la impedancia equivalente de un sistema a frecuencia fundamental basada en la inyección de señales de alta frecuencia. Esta técnica utiliza como fuente de excitación los propios convertidores conectados a red; 3) Una estrategia de control, basada en la estimación de la impedancia en el punto de conexión, capaz de compensar las componentes de secuencia negativa y cero sin necesidad de los sensores adicionales que generalmente se emplean para medir estas componentes; 4) La extensión de la metodología de modelado de la impedancia en redes pasivas, entendidas éstas como aquellas que no cuentan con convertidores de potencia adicionales, a redes con distintos convertidores funcionando de forma simultánea en paralelo. Este modelo se ha utilizado para proponer una técnica de estimación alternativa de la impedancia, basada en la inyección de pulsos y en la aplicación de un algoritmo de estimación RLS (del inglés, Recursive Least Squares); 5) Una solución de optimización de la eficiencia del sistema que, basada en la estimación de impedancia de red, hace uso de la operación del convertidor de potencia a frecuencia de conmutación variable.

Todas las contribuciones han sido validadas, tanto en simulación como experimentalmente, en el laboratorio de sistemas de potencia del grupo de investigación LEMUR de la Universidad de Oviedo.

# Abstract

The evolution of the electricity system is leading to the emergence of new determinants in the traditional scenario. Thus, the presence of renewable sources, distributed generators, solutions for energy storage, intelligent systems and the proliferation of non-linear loads, represent a set of new challenges for the operation and safety of the system itself. The incorporation of these new players brings with it a change of paradigm: from a centralized system to a more distributed one. In this new scenario, generators are located closer to consumers, promoting systems with a high level of energy autonomy which, in the extreme case, can become independent from the public grid. This is how the concept of the microgrid arises, framed in the context of what we know today as smart grids. In these new networks, the incorporation of distributed resources interconnected by means of power converters plays a decisive role for the correct operation of the system.

This work focuses on the operation of grid-connected power converters in the context of AC microgrids. Special attention has been paid to the problem of the equivalent impedance variability of the network upstream from the low voltage connection point of these converters, relating this issue to the impact it causes on the dynamic behaviour of the control system of these devices. The proposed solutions, based on impedance estimation techniques, allow the implementation of control systems that react to changes in the network and achieve real-time compensation of unbalanced conditions. To carry out this task, they only need the information of electrical variables measured at the connection point, making use of the flexibility of the converters to generate excitation signals superimposed on the fundamental component. In addition, the estimation of network parameters provides opportunities related to the improvement of system efficiency, so optimization solutions based on the operation of power converters at variable frequency have also been proposed.

This thesis is organized in six main chapters to which a final chapter of conclusions is added. The first two serve to detail motivation, research opportunities and the study of the current state of the art. This provides an overview of the problem to be studied and the context of this work, as well as a description of the main challenges faced by grid-connected power converters. The contributions of this thesis, developed over the next four chapters, can be summarised as follows: 1) The development of a new methodology for network modelling, which allows to express in a compact way the equivalent

impedance seen from the connection point of the distributed resource. This methodology includes four-wire systems and can be applied under both balanced and unbalanced conditions. The proposed model allows to determine, through a system of representation in stationary coordinates, the temporal evolution of the voltages/currents before the connection/disconnection of different local loads; 2) The implementation of a reliable technique to determine the equivalent impedance of a system at the fundamental frequency based on the injection of high frequency signals. This technique uses the converters themselves as a source of excitation; 3) A control strategy, based on the estimation of the impedance at the connection point, capable of compensating the negative and zero sequence components without the need for the additional sensors that are generally used to measure these components; 4) The extension of the methodology of impedance modelling in passive networks, understood as those without additional power converters, to networks with different converters operating simultaneously in parallel. This model has been used to propose an alternative impedance estimation technique, based on pulse injection and the application of a Recursive Least Squares (RLS) estimation algorithm; 5) A system efficiency optimization solution that, based on network impedance estimation, makes use of the operation of power converters at variable switching frequency.

All contributions have been validated, both in simulation and experimentally, in the power systems laboratory of the LEMUR research group at the University of Oviedo.

# Nomenclature

$\mathbf{x}$	Complex Vector.
$\vec{X}$	Phasor.
$x$	Instantaneous value.
$X$	RMS value.
$X_m$	Magnitude of the signal.
$\mathbf{X}$	Matrix of complex elements.
$\mathbf{x}_{\alpha\beta}$	Complex vector in $\alpha\beta$ reference frame.
$\mathbf{x}_{dq}$	Complex vector in $dq$ reference frame.
$\omega_e$	Fundamental positive-sequence pulsation.
$n$	Harmonic order.
$\omega_n$	Pulsation of the $n^{th}$ component.
$\omega_{hf}$	Generic high frequency pulsation.
$u_{\mu g}$	Inverter output filter voltage.
$u_g$	Utility grid voltage.
$U_n$	Magnitude of the $n^{th}$ voltage component.
$i_i$	Inverter-side injected current.
$i_g$	Grid-side injected current.
$x_{\alpha\beta}^{+-}$	Fundamental positive-sequence voltage/current in $\alpha\beta$ reference frame.
$x_{dq}^{+-}$	Fundamental positive-sequence voltage/current in the $dq$ reference frame.
$x_{dq n}$	Voltage/current in the $n^{th}$ $dq$ reference frame.
$x_0$	Zero sequence voltage/current component.
$u_{hf}$	Generic high frequency voltage signal.
$i_{hf}$	Generic high frequency current signal.
$Z_{dqhf}$	High frequency impedance.
$ Z_{dqhf} $	High frequency impedance magnitude.
$\phi_Z$	High frequency impedance phase angle.
$L_i$	Inverter-side filter inductance.
$R_i$	Inverter-side filter inductance.
$L_g$	Grid-side inductance.
$R_g$	Grid-side resistance.
$L_m$	Phase inductive terms matrix.
$R_m$	Phase resistive terms matrix.

$\mathbf{Z}_{\alpha\beta 0}$	Impedance matrix in the stationary reference frame.
$\mathbf{Y}_{\alpha\beta}$	Admittance matrix in the stationary reference frame.
$\Sigma Z_i$	Average impedance term.
$\Delta Z_i$	Differential impedance term.
$\Sigma R_i$	Average resistive term.
$\Delta R_i$	Differential resistive term.
$\Delta R_{\alpha\beta}$	Real and imaginary terms of the differential resistive term.
$\Sigma X_i$	Average reactance term.
$\Delta X_i$	Differential reactance term.
$\Delta X_{\alpha\beta}$	Real and imaginary terms of the differential reactance term.
$\Sigma Y_i$	Average admittance term.
$\Delta Y_i$	Differential admittance term.
$\theta_e^i$	Unbalance angle.
$\phi_i$	Angle of the average impedance term.
$P_0$	Average value of the instantaneous active power.
$Q_0$	Average value of the instantaneous reactive power.
$P_1, P_2$	Instantaneous oscillatory power terms.
$C_i$	Controller transfer function.
$H_i$	Filter transfer function.
$G_i$	Plant transfer function.
$K_p$	Proportional term of the controller.
$K_i$	Integral term of the controller.
$\mathbf{X}$	Variables vector in the RLS implementation.
$\mathbf{W}$	Coefficients vector in the RLS implementation.
$\mathbf{P}$	Covariance matrix in the RLS implementation.
$g$	Adaptation gain in the RLS implementation.
$\lambda$	Forgetting factor in the RLS implementation.

# Abbreviations and acronyms

<b>AC</b>	Alternating Current.
<b>ANF</b>	Adaptive Notch Filter.
<b>APF</b>	Active Power Filter.
<b>BSF</b>	Band Stop Filter.
<b>CSC</b>	Current Source Converter.
<b>DC</b>	Direct Current.
<b>DDSRF</b>	Double Decoupled Synchronous Reference Frame.
<b>DPG</b>	Distributed Power Generation.
<b>DG</b>	Distributed Generation.
<b>DGU</b>	Distributed Generation Unit.
<b>DSOGI</b>	Dual Second Order Generalized Integrator.
<b>DSO</b>	Distribution System Operator.
<b>DSP</b>	Digital Signal Processor.
<b>D – FACTS</b>	Distribution FACTS.
<b>D – STATCOM</b>	Distribution Static Compensator.
<b>EMC</b>	Electromagnetic Compatibility.
<b>EPS</b>	Energy Power System.
<b>EU</b>	European Union.
<b>FACTS</b>	Flexible AC Transmission Systems.
<b>FCC</b>	Flying Capacitor Converter.
<b>FLL</b>	Frequency Locked Loop.
<b>FCC</b>	Flying Capacitor Converter.
<b>HFSI</b>	High Frequency Signal Injection.
<b>HVDC</b>	High-Voltage Direct Current.
<b>IEC</b>	International Electrotechnical Commission.
<b>IEEE</b>	Institute of Electrical and Electronics Engineers.
<b>IIR</b>	Infinite Impulse Response (filter).
<b>IGBT</b>	Insulated-Gate Bipolar Transistor.
<b>LEMUR</b>	Laboratory for Electrical Energy Management Unified Research.
<b>LF</b>	Loop Filter.
<b>LUT</b>	Look-Up Table.
<b>LV</b>	Low Voltage.

<b>MMC</b>	Modular Multilevel Converter.
<b>MPPT</b>	Maximum Power Point Tracking.
<b>NDZ</b>	Non-detection Zone.
<b>NPC</b>	Neutral Point Clamped.
<b>QSG</b>	Quadrature Signal Generator.
<b>PCC</b>	Point of Common Coupling.
<b>PD</b>	Phase Detector.
<b>PI</b>	Proportional Integral (controller).
<b>PQ</b>	Power Quality.
<b>PLC</b>	Power Line Communications.
<b>PLL</b>	Phase Locked Loop.
<b>PSI</b>	Pulsed Signal Injection.
<b>PV</b>	Photovoltaic.
<b>PWM</b>	Pulse-Width Modulation.
<b>RES</b>	Renewable Energy Resources.
<b>RF</b>	Reference Frame.
<b>RLS</b>	Recursive Least Square.
<b>SOGI</b>	Second Order Generalized Integrator.
<b>SF</b>	Switching Frequency.
<b>SAPF</b>	Series Active Power Filter.
<b>ShAPF</b>	Shunt Active Power Filter.
<b>SRF</b>	Synchronous Reference Frame.
<b>STATCOM</b>	Static Compensator.
<b>SVM</b>	Space Vector Modulation.
<b>TDD</b>	Total Demanded Distortion.
<b>THC</b>	Total Harmonic Current.
<b>THD</b>	Total Harmonic Distortion.
<b>UPFC</b>	Unified Power Flow Conditioner.
<b>UPQC</b>	Unified Power Quality Conditioner.
<b>VCO</b>	Voltage Controlled Oscillator.
<b>VOC</b>	Voltage Oriented Control.
<b>VSC</b>	Voltage Source Converter.

# Contents

Agradecimientos . . . . .	V
Nomenclature . . . . .	XI
Abbreviations and acronyms . . . . .	XIII
<b>1 Introduction</b>	<b>1</b>
1.1 Background . . . . .	1
1.2 Motivation . . . . .	3
1.3 Objectives . . . . .	4
1.4 Contributions . . . . .	6
1.5 Publications . . . . .	7
1.5.1 Peer-reviewed Journal Papers . . . . .	7
1.5.2 Peer-reviewed Conference Papers . . . . .	8
1.6 Thesis Structure . . . . .	9
References . . . . .	11
<b>2 Literature Review and State of the Art</b>	<b>13</b>
2.1 Introduction . . . . .	13
2.2 Power Quality Aspects . . . . .	16
2.3 Review of the Instantaneous Power Theory . . . . .	18
2.4 Reactive Power Compensation and Harmonic Filtering Solutions . . . . .	18
2.4.1 Passive Filtering . . . . .	19
2.4.1.1 Series Compensation . . . . .	19
2.4.1.2 Shunt Compensation . . . . .	21
2.4.2 Active Power Filters . . . . .	23
2.4.2.1 Static Var Compensation . . . . .	24

2.4.2.2	Series Power Filters . . . . .	25
2.4.2.3	Shunt Power Filters . . . . .	26
2.4.2.4	Unified Power Quality Conditioner . . . . .	26
2.5	Voltage Source Converters . . . . .	27
2.5.1	Topologies . . . . .	29
2.5.1.1	Single-phase Power Converters . . . . .	29
2.5.1.2	Three-Phase Power Converters . . . . .	30
2.5.1.2.1	Three-Leg-Four-Wire Power Converters . . . . .	30
2.5.1.2.2	Four-Leg-Four-Wire Power Converters . . . . .	31
2.5.1.3	Three-Phase Multilevel Power Converters . . . . .	31
2.5.2	Modulation Techniques . . . . .	33
2.5.2.1	Continuous PWM Techniques on 3-Wire Systems . . . . .	33
2.5.2.2	Discontinuous PWM Techniques on 3-Wire Systems . . . . .	35
2.5.2.3	PWM Techniques on 4-Wire Systems . . . . .	36
2.5.3	Converter Control . . . . .	37
2.5.3.1	Cascade Control . . . . .	37
2.5.4	VSC Efficiency Aspects . . . . .	39
2.5.5	Grid-tied Power Converters . . . . .	41
2.6	Operation of Grid-tied Power Converters . . . . .	43
2.6.1	Grid Synchronization . . . . .	44
2.6.1.1	Phase-Locked Loop . . . . .	44
2.6.1.2	Synchronization of Three-Phase Power Converters under Unbalanced Conditions . . . . .	45
2.6.2	Control Modes . . . . .	45
2.6.2.1	P/Q Control . . . . .	46
2.6.2.2	Droop Control . . . . .	46
2.6.2.3	Enhanced Model-based Control Systems . . . . .	49
2.6.2.4	Unbalance Compensation . . . . .	51
2.7	Grid Impedance Estimation . . . . .	52
2.7.1	Non-invasive Techniques . . . . .	54
2.7.1.1	Power References . . . . .	54
2.7.1.2	Model Based . . . . .	55
2.7.1.3	Kalman Filter . . . . .	56

2.7.2	Invasive Techniques . . . . .	57
2.7.2.1	Frequency Scanning . . . . .	57
2.7.2.2	Pulsed Signal Injection (PSI) . . . . .	58
2.7.2.3	High Frequency Signal Injection (HFSI) . . . . .	59
2.7.2.4	Current Regulator Reaction . . . . .	60
2.7.2.5	Low Frequency Signal Injection . . . . .	61
2.7.2.6	Binary Sequence Signal Injection . . . . .	62
2.8	Conclusion . . . . .	62
	References . . . . .	64
<b>3</b>	<b>System Modelling</b>	<b>75</b>
3.1	Introduction . . . . .	75
3.2	System Definition . . . . .	76
3.2.1	Variables Definition in Time and Frequency Domain . . . . .	76
3.2.2	System Representation in the $\alpha\beta$ Reference Frame . . . . .	77
3.2.3	Impedance Model . . . . .	79
3.2.4	Admittance Model . . . . .	83
3.3	System Definition for Real Time Implementation . . . . .	84
3.4	Equivalence with the Instantaneous Power Theory . . . . .	86
3.5	Model Evaluation . . . . .	88
3.6	Conclusion . . . . .	92
	References . . . . .	94
<b>4</b>	<b>Grid Impedance Estimation Considering Passive Loads</b>	<b>97</b>
4.1	Introduction . . . . .	97
4.2	System Description . . . . .	98
4.2.1	Problem Statement . . . . .	99
4.3	High Frequency Signal Injection . . . . .	102
4.3.1	Frequency Selection . . . . .	102
4.3.2	Method Implementation . . . . .	104
4.3.3	Equivalent Impedance Terms at High Frequency . . . . .	105
4.4	Equivalent Impedance of Passive Loads . . . . .	105
4.4.1	Impedance Estimation at High Frequency . . . . .	106
4.4.2	Impedance Estimation at Fundamental Frequency . . . . .	109

4.5	Negative Sequence Current Estimation . . . . .	111
4.5.1	Filtering System Description . . . . .	112
4.5.2	Current Estimation at Fundamental Frequency . . . . .	114
4.6	Unbalance Compensation . . . . .	115
4.6.1	Stability Analysis . . . . .	116
4.6.2	Negative Sequence Compensation . . . . .	118
4.6.3	Zero Sequence Compensation . . . . .	120
4.7	Conclusion . . . . .	123
	References . . . . .	124
<b>5</b>	<b>Grid Impedance Estimation Considering Grid-tied Power Converters</b>	<b>125</b>
5.1	Introduction . . . . .	125
5.2	System Description . . . . .	126
5.3	Impedance Modelling of Active Loads . . . . .	127
5.4	Equivalent Impedance Estimation Based on a RLS Algorithm . . . . .	132
5.4.1	Pulsed Signal Injection Technique . . . . .	132
5.4.2	RLS Algorithm Implementation . . . . .	133
5.4.3	RLS Accuracy Evaluation . . . . .	134
5.4.4	Experimental Results . . . . .	137
5.5	Conclusion . . . . .	139
	References . . . . .	140
<b>6</b>	<b>Variable Switching Frequency Control of Distributed Resources for Improved System Efficiency</b>	<b>141</b>
6.1	Introduction . . . . .	141
6.2	Efficiency Constrains . . . . .	142
6.2.1	Switching Frequency and Current Harmonics . . . . .	142
6.2.2	Converter Losses and Thermal Limits . . . . .	143
6.2.3	Distortion Losses in the Local Grid . . . . .	144
6.3	On-line Optimization of the Switching Frequency . . . . .	148
6.4	Case Study . . . . .	148
6.5	Experimental Results . . . . .	150
6.5.1	STATCOM Mode . . . . .	151
6.5.2	Inverter Mode . . . . .	152

---

6.6 Conclusion . . . . .	155
References . . . . .	156
<b>7 Conclusion and Future Work</b>	<b>159</b>
7.1 Conclusiones . . . . .	159
7.2 Conclusion . . . . .	162
7.3 Future Work . . . . .	164
<b>A Harmonic Emission Normative</b>	<b>167</b>
A.1 Introduction . . . . .	167
A.2 IEC-61000-2-5 [A.1] . . . . .	167
A.3 IEC-61000-3-2 [A.2] . . . . .	167
A.4 IEC-61000-3-12 [A.3] . . . . .	169
A.5 IEEE-519-2014 [A.4] . . . . .	170
References . . . . .	172
<b>B Review of the Fourier Series</b>	<b>173</b>
B.1 Periodic Signals . . . . .	173
B.2 Trigonometric Functions . . . . .	175
B.3 Circuit Applications . . . . .	176
References . . . . .	178
<b>C Space Vector Transformations of Three-Phase Systems</b>	<b>179</b>
C.1 Introduction . . . . .	179
C.2 Symmetrical Components . . . . .	179
C.3 Stationary Reference Frame Transformation . . . . .	183
C.4 Synchronous Reference Frame Transformation . . . . .	183
References . . . . .	185
<b>D Instantaneous Power Theory</b>	<b>187</b>
D.1 Introduction . . . . .	187
D.2 Instantaneous Power Theory . . . . .	187
References . . . . .	190

---

<b>E</b>	<b>Simulation and Laboratory Setup</b>	<b>193</b>
E.1	Introduction . . . . .	193
E.2	Simulation and Experimental Setup of Chapter 4 . . . . .	193
E.3	Experimental Setup of Chapter 5 . . . . .	195
E.4	Experimental Setup of Chapter 6 . . . . .	196
E.5	Cascade Control Design . . . . .	197
<b>F</b>	<b>Journal Publications</b>	<b>199</b>
F.1	Sensorless Unbalance Modeling and Estimation as an Ancillary Service for LV Four-Wire/Three-Phase Power Converters . . . . .	201
F.2	Variable Switching Frequency Control of Distributed Resources for Im- proved System Efficiency . . . . .	213
<b>G</b>	<b>Conference Publications</b>	<b>225</b>
G.1	Online Impedance Estimation in AC Grids Considering Parallel- Connected Converters . . . . .	227
G.2	Sensorless Unbalance Correction as an Ancillary Service for LV 4- Wire/3-Phase Power Converters . . . . .	237
G.3	Improved Efficiency of Local EPS through Variable Switching Frequency Control of Distributed Resources . . . . .	247

# Chapter 1

## Introduction

### 1.1 Background

Traditionally, electric power systems have been operated in a centralized manner, where generation is grouped in large power plants (Fig. 1.1), based mainly on fossil resources or renewable energies such hydro and large wind or solar power plants. Those power plants, which contribute to the overall system stiffness by their large inertia, are connected to the transmission network and finally delivered to the consumers by the distribution grid. Voltage levels are adapted by transformers, which first step-up the voltage from the generation value to the high-voltage transmission levels. Downstream, at the distribution grid, step-down transformers are used for the conversion to medium and low-voltage levels required by the final consumers

However, the raise on energy demand during last decades and the concern about  $CO_2$  emission and greenhouse effects, added to the growing need of producing more energy with same amount of resources, have fostered the entrance of new solutions in the traditional electric system. In this new environment, energy efficiency, environmental friendliness and operational security are the primary concerns. However, the intermittent and unpredictable nature of the renewable sources may deprecate the generation profile. Future plans for the electrical grid propose a change in the traditional organization, departing from a centralized approach to a distributed operation, in which the generation sources are moved closer to the consumption zones, splitting the grid into smaller autonomous areas in which the gap between generation and consumption is guaranteed or, at least, reduced. This approach has driven the energy sectors to a new scenario, where the smart and microgrid concepts are being successfully deployed.

Based on this situation, European Union (EU) has established very ambitious objectives for 2030: 32% of consumption from renewable energy generation, 40% of  $CO_2$  emissions reduction (from 1990 levels) and an increase of 32.5% in energy efficiency [1.1, 1.2]. A key aspect to achieve these targets is to find effective solutions

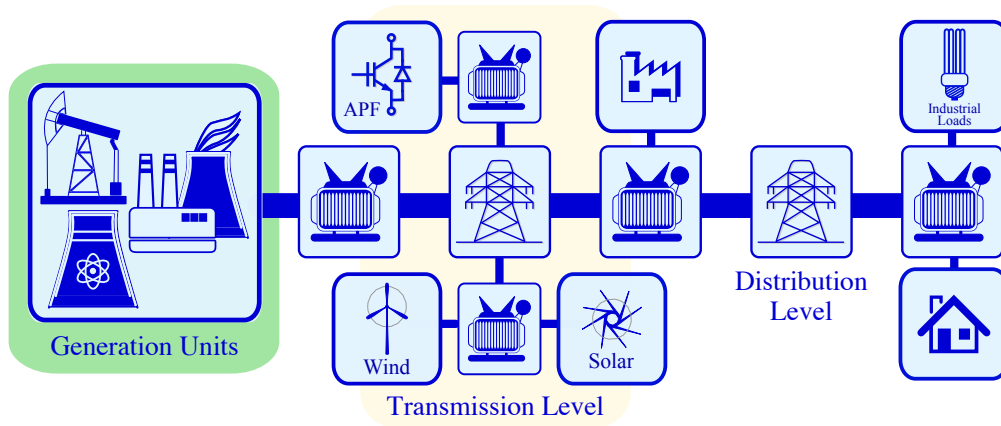


**Figure 1.1:** Traditional electricity grid

for integrating the distributed renewable generation, in particular: solar photovoltaic (PV); wind; biomass and small hydro power into the current and the upcoming distribution systems. This new scenario requires not only new and innovative technical solutions, but also suitable regulatory and economic schemes, as well as new management tools. Moreover, considering that grid codes and power quality standards have to be fulfilled in a more restricted way than in the past, it is crucial to find a right balance between installing large scale renewable energy capacity today and its effective integration in medium and low voltage grids in future.

All these aspects have boosted the introduction of renewable energy sources during the last years. As commented before, the intermittent nature of its generation as well as the need of power electronic converters has jeopardized even more the power quality. However, the solution may be in the root of the problem; Power converters, acting as active filtering systems, are feasible solutions to isolate and lately compensate the harmonic distortion and unbalances from the grid. To do so, the power converter requires a deep knowledge on the power system dynamics. A precise dynamic model often requires the use of additional voltage and current measurements, that are in many occasions difficult to obtain

It is in this context where microgrid, involving generation, load and regulation, emerges as a key solution for the integration of distributed resources into the main grid, coordinating the generation and the local consumption of a group of loads (Fig. 1.2). According the definition provided by [1.3], a microgrid is a system composed by distributed generators, loads, energy storage and control devices, which may operate independently from the main grid, with only one point of connection with it, but that multiple microgrids may be interconnected between each others. These new grid architectures allow to establish a faster response to local demand, reducing power losses and improving system efficiency. However, increasing the number of power converters to the detriment of synchronous generators connected to the grid, becomes an impor-

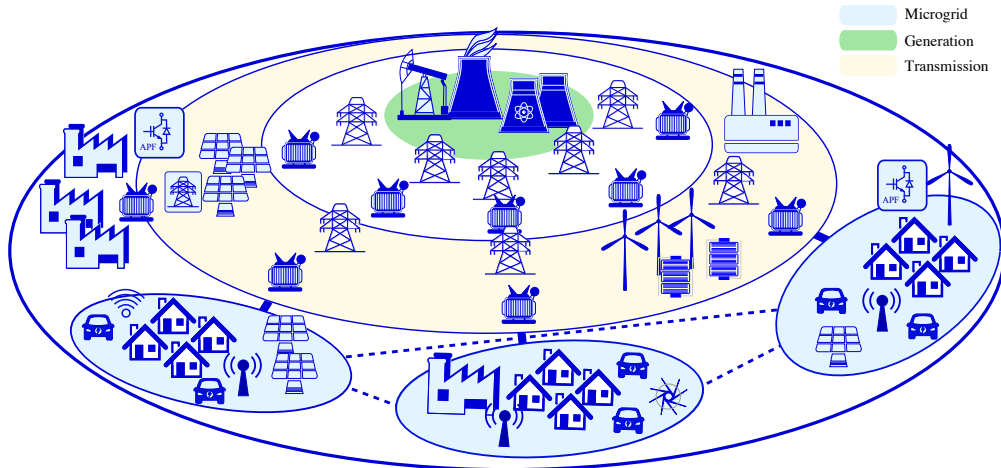


**Figure 1.2:** Disposition of a traditional grid with the inclusion of microgrid systems

tant concern from the point of view of the power quality. It usually results in low short-circuit ratio, high equivalent impedance and low inertia constant, i.e. weak grid characteristics. In particular, weak grids lead to voltage fluctuations, which limit the dynamic performance of power converters. Some of the major challenges concern to grid synchronization, since voltage fluctuations might result in positive feedback mechanism which can provoke instability in the power converter performance, and also to the power transfer capability of the grid, which affects on the stable operating range of the power converter [1.4–1.6].

Grid impedance identification appears to be an effective solution to improve the performance of the power converters within weak grids; By determining the grid voltage at a remote and stronger point in the weak grid it is possible to solve the synchronization issues and determination of the grid impedance allows to improve the dynamic performance of the converter, by adapting its control parameters.

## 1.2 Motivation

The motivation of this work comes from the fact that, traditionally low voltage grids were considered blind spots from the point of view of the grid operator. In the recent years, distribution system operators (DSOs) have started to develop the monitorization infrastructure of the low voltage grids, but a lot of work is still pending, mainly due to the complexity of this type of networks; composed by a large number of small consumers.

This lack of visibility was accepted under a traditional frame of large generators feeding demand, as already explained. However, the growth of Distributed Generation

Units (DGUs); the inclusion of new grid operators and the increase of much sensitive residential equipments, based on power electronic devices, have triggered the evolution to a new operation field with bi-directional power flows, islanding situations and harmonic pollution, requiring efficient solutions based on renewable systems and power electronics technology.

An adequate control of those filtering solutions requires a deep knowledge of the grid dynamics. Nonetheless, due to the nature of low voltage AC-Grids, already mentioned, extra sensors and monitoring devices are required both at load and converter side to provide a good performance. Unfortunately, these devices are not always possible to be installed at the convenient location due to technical or legislative limitations. This aspect has induced the study of *sensorless* solutions to identify the system impedance at the point of connection with the grid, as well as to determine the amount of energy that the power converter should supply to the load without extra sensors acquisition.

Moreover the large growth of sensitive loads at low voltage side and the characteristic of the aforementioned microgrids have induced the study of new grid modelling techniques, to facilitate the accommodation of distributed generation units without compromising the stability limits of the grid.

Additionally, a large number of contributions have appeared in literature in the past years, based on the optimization of the generation units locations and the optimization of the dispatching resources in the search of a coordinated behaviour of the power converters within the microgrid. However, converters are not operated at rated level the majority of the cases. Evaluation of the converter performance based on the actual conditions, based on the grid requirements and load levelling is not studied into deep.

Finally, the lack of a compact modelling tool that links the existent and variable grid impedance at distribution levels with the positive, negative and zero sequence voltage/current components, light enough to allow the identification in real time solely relying on converter-side sensors; triggers an interesting opportunity to explore the possibilities of improving the converter compensation capabilities based on impedance estimation solutions.

### 1.3 Objectives

Based on the aforementioned, the challenges and objectives of the thesis are following enumerated:

- I. A deep state-of-the-art review derived from the motivation and thesis objectives, covering the following aspects:
  - Review of the main power quality issues as well as the regulatory aspects which limits the harmonics emission of electronic devices at the PCC.

- 
- Review of the main harmonic and reactive power compensation solutions present in the industry in order to find a feasible solution for the application required in this work.
  - Review of the traditional converter topologies as well as the technical requirements for the synchronization with the grid, assuring an adequate performance.
  - Review of the main impedance estimation solutions present in the literature.
- II. Develop of alternative impedance estimation solutions that can be implemented using only converter-side sensors, able to work together with the power converter normal operation while inducing the minimum distortion in the system and considering the existence of multiple parallel-connected converters.
  - III. Analysis and development of a modelling tool able to express the grid impedance terms with the corresponding voltage and current sequence magnitudes. This expression, defined both in synchronous and stationary reference frame, has to be dynamically adapted to allow an online implementation. Additionally, the proposed methodology should be able to be compared to the instantaneous power theory as a reference framework.
  - IV. Development of a solution, based on a sensorless technique, for unbalance compensation. The solution will be able to determine the negative and zero sequence currents present under an unbalance situation, without the need of additional measuring equipment from either the load or the grid side, only with the converter measurements, the controller will be able to provide the required energy for the compensation, as well as the active and reactive current of the grid.
  - V. Development, analysis and integration of a grid impedance estimation solution of a system with multiple power converters operating in parallel. The solution will be able to perform under real time operation and provide an estimation in the four quadrant operation for both balanced and unbalanced conditions.
  - VI. Explore the possibility of improving the global efficiency of three-phase converter-based distributed resources (DR) embedded in low-voltage distribution feeders, by the adaptation of their switching frequency (SF) to the operation point of both the converter and local loads. Leaving room for a global optimization of the power losses, i.e., converter losses will be considered together with those losses caused by the current harmonics injected into the local grid.
  - VII. Simulation and experimental validation. One major objective will be the validation of the proposed solutions in the work. Simulations will be carried on under then MATLAB<sup>®</sup> and MATLAB/Simulink<sup>®</sup>. The experimental validation will be performed under a controlled environment within the laboratory of the LEMUR researching group of the University of Oviedo, Spain.

## 1.4 Contributions

The contributions achieved from the work presented in the thesis are briefly summarized as follows:

### A System Modelling Tool [JC2],[JP2]

The main contribution is found in the grid modelling solution, which provides an analytical expression for the positive, negative and zero sequence magnitudes depending on the grid impedance and the unbalance conditions. An analysis of the voltage and current sequences resulting from the fluctuations of the impedance of the system and from the voltage unbalances have also been performed, proving the behaviour of the modelling solution is feasible to be used under different operation conditions.

The adaptation of the model to be implemented under real time operation, based on the measurements from the converter side at the point of common coupling with the grid. An expression for the admittance of a generic system, enabling to obtain the corresponding current draw by the system, which may allow the use of the mentioned algorithm as a tool for sensorless estimation technique. The analysis of the traditional instantaneous power theories in literature has been addressed to provide an expression for the power magnitudes based on the impedance conditions and provide a full range of application of the modelling tool.

### Grid Impedance Estimation Solutions [JC3],[JP2]

The second contribution is found within the application frame of the modelling tool, proving to work under two different approaches:

1. Grid impedance estimation for passive networks, considering only passive loads connected at the point of common coupling and consequently with a constant impedance magnitude at a specific frequency;
2. Grid impedance estimation for active networks, where multiple converters are operating at same time and providing different levels of energy. For this case, the equivalent impedance magnitude is changing according the power references of the converters.

Two different impedance estimation techniques have been also proposed, in the case of the passive elements, the zero and negative sequence terms are determined based on the estimation performed via a high frequency signal injection solution. The study of the control loop stability required for the elimination of the disturbance sequences and the signal isolation to determine the impedance at both frequencies have been also studied, as well as the criteria to determine the frequency of injection and the magnitude of the signal to be injected, to be within the distortion limits.

For the case of the active elements, the modelling tool has been used in an online impedance estimation technique based on pulsed signal injection technique to excite the grid elements and a recursive least square algorithm is used to perform the estimation. The results extracted from the algorithm are compared with the ones derived from the proposed modelling tool, to clarify the validity of the proposal. An expression linking both the converter power references and the impedance terms is also provided, proving to be a reliable estimation solution at four quadrants operation and under both balanced and unbalanced conditions. The validity of both proposals is demonstrated with both simulation and preliminary experimental results.

### **Grid Efficiency Enhancement Proposal [JC1],[JP1]**

The last contribution is related with the power converter efficiency, based on the adaptation of the switching frequency according the grid impedance and the load level. It has been presented an operation strategy for distributed resources based on the use of an adaptive switching frequency framework in the grid-tie converter with the aim of achieving an overall improvement of the efficiency within the local energy power system.

The technical and regulatory constrains which may limit the selection of the switching frequency have been also addressed. An online optimization strategy to adapt SF based on the load conditions and impedance of the system has been proposed. The solution has been supported both with simulations and experiments.

## **1.5 Publications**

The publications derived from the work presented in this thesis are summarized in the following journal and conference publications.

### **1.5.1 Peer-reviewed Journal Papers**

**JP1** J. M. Cano and Á. Navarro-Rodríguez and **A. Suárez** and P. García, "Variable Switching Frequency Control of Distributed Resources for Improved System Efficiency," in *IEEE Transactions on Industry Applications*, vol. 54, no. 5, pp. 4612-4620, Sep. 2018.

**JP2** **A. Suárez-González** and P. García and Á. Navarro-Rodríguez and G. Villa and J. M. Cano, "Sensorless Unbalance Modeling and Estimation as an Ancillary Service for LV Four-Wire/Three-Phase Power Converters," in *IEEE Transactions on Industry Applications*, vol. 55, no. 5, pp. 4876-4885, Sep. 2019.

### 1.5.2 Peer-reviewed Conference Papers

- JC1** J. M. Cano and **A. Suárez** and Á. Navarro-Rodríguez and P. García, "Improved efficiency of local EPS through variable switching frequency control of distributed resources," in *2016 IEEE Energy Conversion Congress and Exposition (ECCE), 2016 IEEE*, Sept. 2016, pp. 1-7.
- JC2** **A. Suárez-González** and P. García and Á. Navarro-Rodríguez and G. Villa and J. M. Cano, "Sensorless unbalance correction as an ancillary service for LV 4-wire/3-phase power converters," in *2017 IEEE Energy Conversion Congress and Exposition (ECCE), 2017 IEEE*, Oct. 2017, pp. 4799-4805.
- JC3** **A. Suárez** and C. Blanco and P. García and Á. Navarro-Rodríguez and J. Manuel and C. Rodríguez, "Online Impedance Estimation in AC Grids Considering Parallel-Connected Converters," in *2018 IEEE Energy Conversion Congress and Exposition (ECCE), 2018 IEEE*, Sep. 2018, pp. 5912-5919.

## 1.6 Thesis Structure

The dissertation is organized in six chapters and seven appendixes as follows:

**Chapter 1** presents a brief background and the motivation that has propitiated this work. Additionally, the fundamental objectives of the thesis and its most essential scientific contributions are highlighted.

**Chapter 2** includes a literature review on the use of power converters in modern grids. A brief introduction to power quality is provided, and the role of power converters in this context is addressed. A description of the most common types of power converters topologies is also provided together with an outline of the most widely used control methods. An especial focus is given to grid-tied power converters, and their inherent capabilities to provide unbalance and harmonic compensation in non-ideal grids. Furthermore, the importance of grid impedance estimation techniques for power converter integration is highlighted in this chapter and a deep review of existing methods is conducted.

**Chapter 3** introduces an impedance modelling technique and the procedure to obtain a suitable and elegant expression which links grid impedance with the positive, negative and zero sequence voltage and current magnitudes, both in the time and the frequency domain. An extension of this modelling technique, capable of being implemented in the context of the instantaneous power theory, is also provided. Eventually, simulation results are presented to support the mathematical apparatus presented in this chapter.

An adaptation of the impedance modeling tool presented in the previous chapter is used in **Chapter 4** in order to develop a new sensorless impedance estimation technique. The limitations faced when trying to perform an accurate estimation of grid impedance are described and a new method, based on the injection of high frequency signals, is presented as a solution to overcome those hurdles. Detailed explanations on the implementation issues related with the proposed sensorless technique and the underlying impedance model are included. Simulation and experimental results are introduced to support the discussion. The estimated impedance is used to obtain the negative sequence current reference which allows the power converter to compensate for the unbalance of the system in the context of a grid with passive loads. Finally, stability control issues and practical considerations on the injection of the high frequency signals are provided within the chapter.

**Chapter 5** might be considered as an extension of **Chapter 4**, with the aim of including the role of active loads. The new impedance modelling technique is used now to determine the equivalent grid impedance of a system with embedded power converters. Here, the modelling tool is used together with a recursive least square algorithm in order to derive grid impedance estimations. In this case, a pulse signal injected by the converter is used as the excitation which triggers the estimation method. Simulation and experimental results are provided to support the validity of the method.

Extensive tests to prove the validity of the impedance model of the converter based on its power references under four quadrant operation are conducted.

A proposal to improve the efficiency of low voltage distribution systems with embedded power converters is presented in **Chapter 6**. The method is based on the operation of power converters at variable switching frequency, in order to achieve a global optimization of the losses in the local system, including both converter and line losses. The proposal takes into account the effect of a variable switching frequency on converter switching losses and its impact on the harmonic distortion causing conduction losses on the local system. The thermal limits of the converter devices are also included into the problem. The method is presented in this chapter with the support of simulation and experimental results.

The conclusions drawn from this dissertation are presented in **Chapter 7**, which also includes proposals to go further on the research lines addressed in this work.

## References

- [1.1] [Online]. Available: <https://www.ec.europa.eu/>
- [1.2] J. Delbeke and P. Vis, *EU Climate Policy Explained*. Routledge, 2015.
- [1.3] R. H. Lasseter and P. Paigi, "Microgrid: a conceptual solution," in *2004 IEEE 35th Annual Power Electronics Specialists Conference (IEEE Cat. No.04CH37551)*, vol. 6, June 2004, pp. 4285–4290 Vol.6.
- [1.4] J. A. Suul, S. D'Arco, P. Rodríguez, and M. Molinas, "Impedance-compensated grid synchronisation for extending the stability range of weak grids with voltage source converters," *IET Generation, Transmission Distribution*, vol. 10, no. 6, pp. 1315–1326, 2016.
- [1.5] A. Adib, B. Mirafzal, X. Wang, and F. Blaabjerg, "On stability of voltage source inverters in weak grids," *IEEE Access*, vol. 6, pp. 4427–4439, 2018.
- [1.6] M. Ashabani and Y. A. I. Mohamed, "Integrating vses to weak grids by nonlinear power damping controller with self-synchronization capability," *IEEE Transactions on Power Systems*, vol. 29, no. 2, pp. 805–814, March 2014.



## Chapter 2

# Literature Review and State of the Art

### 2.1 Introduction

Electric power systems (EPSs) have evolved and changed drastically in last decades. Modern societies are strongly dependent on the quality, reliability and availability of energy. New actors are involved, including smart communications, storage solutions, different renewable energy technologies and definitely new innovative solutions on grid architectures. This new environment may jeopardize the performance of the grid in its main objective: to meet the growing demand. Traditional matters on system security, power quality and cost of supply require a retrofit to cope with modern aspects impacting on environmental protection and energy efficiency. These aspects are included in the definition of smart grid [2.1], consisting on an intelligently integration of all actors connected to the system.

The increased penetration of renewable energy sources and sensitive loads, the growth of the microgrid concept, inducing bi-directional power flows, the presence of harmonic pollution and unbalanced loading or voltage sags at LV side, have made the use of similar power quality solutions, as the ones already present at higher voltage levels, necessary. Contributions in the active filtering field, intelligent monitoring, control or communications have already been proposed at transmission and primary distribution grids; however, few of these proposals have been properly implemented at LV levels.

In summary, distribution system has evolved to an active system; generation units are distributed and a more precise control and knowledge of the grid is required. Different solutions to accomplish quality, stability and reliability levels need to be considered. Power quality issues such unbalances or harmonic distortion must be kept within acceptable ranges. Grid dynamics is a key-issue for operating and controlling grid-connected converters, especially within a microgrid and smart grid environment [2.2]. The smart and microgrid paradigm presents new challenges such new grid topologies, the presence of sensitive loads, harmonic pollution and stability issues as consequence of reduced system inertia. All these challenges

have to be addressed with the enhanced performance of the power converter control as a key-factor of a microgrid environment.

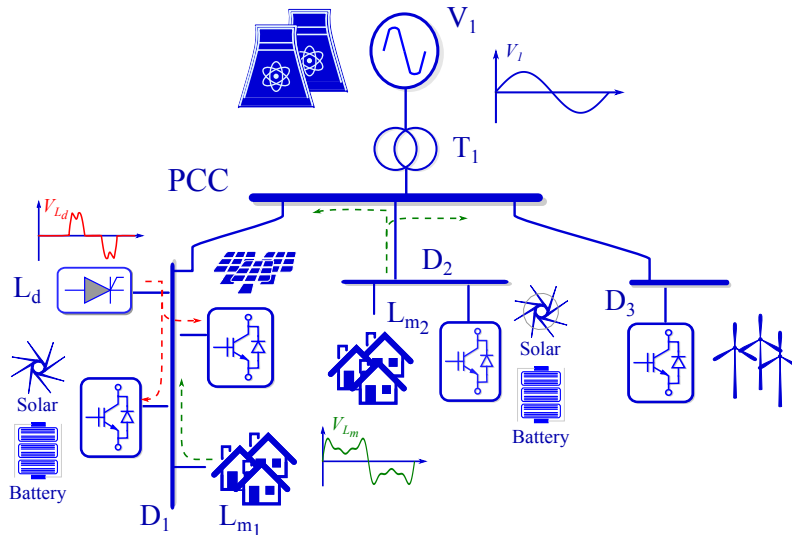


**Figure 2.1:** Schematic of a typical LV grid

A microgrid is conceptually considered as a small scale grid, formed by distributed generators, energy storage systems and loads, which are interconnected among them and hierarchically controlled. However, distributed generation has been gradually integrated in the traditional system, and in the majority of the cases, as supplementary energy source. The lack of a structured plan for the deployment of the distributed energy resources, few specific international standards still in their infancy, [2.3], together with reduced interoperability with the grid operator, leads to a limited operation of the microgrid concept. This configuration is illustrated in Fig. 2.1, where it is shown a simplified example of a LV grid. The main voltage profile is set by a large traditional power plant, which is providing complementary robustness to the system. Nonetheless, the technical improvement along the recent years, have proved that modern Distributed Generation Units (DGUs) present a higher controllability degree than traditional generators, enabling the possibility of contributing to system stability by the use of ancillary services and, particularly, reactive power injection and voltage support, [2.4]. Additionally, the improvements in the storage technologies have contributed to increase the efficiency of renewable resources, opening the door for the inclusion of microgrids within the traditional distribution system. This new paradigm requires intensive research effort to cope with the challenges that such advanced distributed systems require.

The connection of non-linear loads such switch-mode power supplies, lightning systems, data-processing equipment and different power electronic devices result in a deprecation of the power quality service. Grid-tied power converters may be a source of harmonic pollution but also a solution, thus, harmonic limit emission and regulatory constrains need to be addressed to establish the operational limits of converters. This also might open a door for efficiency enhancement, based on the regulatory limits and the operating condition of the converter. In this regard, the study of alternative modulation schemes and strategies that contribute to

reduce converter losses and harmonic emission, within those regulatory constraints, needs to be reviewed.

Wind and photovoltaic power plants are the most suitable renewable energies to be integrated in microgrids. Considering the integration of small-scale distributed resources into the LV grid, the energy path between the generation point and the final user can be largely shortened, thus contributing to a reduction in the overall distribution energy losses. However, it requires the coordinated control of an increased number of generation systems, demanding for an improvement in the hierarchical control system. Depending on the grid conditions, every converter must assume a role, providing different supportive functionalities.

A high penetration level of power converters into the grid results in a system inertia deprecation. The rotating components of traditional synchronous generators contribute to maintain the system robustness, responding to grid transients in a stabilizing way. However, within a system with fewer presence of synchronous generators, stability challenges are known to appear, limiting the reactive power flow and the voltage quality profile. Thus, additional controls algorithms, which provide power converters with the inertia features of synchronous generators, are demanded. Additionally, the same lack of inertia requires power converters to have control synchronization algorithms which allow to keep them permanently synchronized with the grid. These control algorithms have to be able to work under different distorted and unbalance conditions, maintaining converter synchronization at any instant.

LV grids have a predominant resistive profile, as opposed to higher voltage grids, which present a behaviour mainly inductive. This implies that many of the solutions already working in transmission or primary distribution levels need to be re-addressed to satisfactorily work at LV levels, as it might be the case of droop control algorithms. In this regard, impedance estimation is presented as a key factor to enhance the performance of such control algorithms but also for the integration of new distributed generation units. Additionally, impedance estimation techniques offer opportunities in the field of unbalance compensation. By identifying the grid impedance magnitude, it is possible to determine the compensation current magnitude and eliminate the unbalance. Therefore, impedance estimation solutions need to be studied to determine which might be adopted for the requiring purposes.

According to the considerations mentioned above, this chapter covers the state of the art for the most relevant topics related with the integration of distributed resources into the LV grid. Within the vast number of research lines, the focus is kept here on control strategies for grid-tied power converters. The chapter is distributed as follows: firstly, power quality issues are described. Starting with a review of general power quality problems, the focus is shifted towards the impact of switched power converters. A definition of instantaneous variables is provided together with a brief review of the instantaneous power theory. Harmonic regulation as well as mitigation techniques, both passive and active, are discussed. Even if power quality, as a field of study, is not the major topic of the present research, the particular impact of microgrids distribution systems has been included. A review of power converters operating mode is conducted, with an especial focus on the voltage source configuration as the most widely used in practical applications and the one considered throughout this work. The major intention is to provide an overview of this self-commutated converter, starting from the most common topologies present in industry, as well as a review of the most promising modulation techniques available in literature. This analysis also includes the traditional current and voltage control loops required to achieve an adequate performance. Efficiency aspects are also considered in this section as a part of the converter operation, highlighting the major fields of efficiency enhancement and some of the available solutions present in literature. The analysis

of the converter within a microgrid system is then addressed, starting from the hierarchical control algorithms required to establish priorities within a system with large penetration of power converters. The main drawbacks resulting from this aspect are also described, making special emphasis on the control solutions used to provide synchronization features, as well as on the main control algorithms used to provide enhanced inertia to the system and unbalance compensation support. Finally, the chapter is closed with a deep review of the main impedance estimation techniques available in literature, as a key-factor for the control and integration of grid-tied converters within microgrids.

## 2.2 Power Quality Aspects

Power Quality (PQ) definition has been addressed from different perspectives. It can be understood as the resultant combination of the voltage and current quality [2.5], which is the definition proposed by the Institute for Electrical and Electronics Engineers (IEEE) standardization group [2.6]. Based on this, voltage quality may be divided into:

- **Steady-State Voltage Quality Characteristics:** referring to the quality of the normal voltage supplied to a facility.
- **Disturbances:** considering inside this group the voltage quality variations that occur at random intervals and are not associated with the continuous characteristics of the voltage, such as sustained interruptions, momentary interruptions, voltage sags (and swells), and transients.

On the other hand, PQ can also be understood as an Electro-magnetic Compatibility (EMC) issue, [2.7], which corresponds with the definition proposed by the International Electrotechnical Commission (IEC). At this matter, IEC establishes a classification of the main electromagnetic phenomena in IEC 61000-2-5:2017 [2.8] which is shown in Table A.1.

In either case, although definitions differ, the main concern is the susceptibility of electrical power system. According to this, IEEE Std 1159-2009, [2.9], proposes an extensive classification of the PQ disturbances based on the harmonic spectrum, the duration and the amplitude of the induced electromagnetic phenomena. An alternative classification, based on the previous one and considering only the duration of the disturbances is proposed, [2.10]:

- **Transients:** including switching of small magnitude loads and atmospheric events (wind, lightning strokes or rain), which results in short time variations of the voltage and current of the system.
- **Temporary:** related to overloaded transformers, or faults that generally last one minute or less. Considering within this group such voltage deviations like voltage sags or swells
- **Long duration or steady state:** encompasses voltage deviations for periods longer than one minute. This group gathers such PQ disturbances concerning voltage fluctuations (flickering), voltage or current unbalances and waveform distortions such harmonics or notching.

It is in this latter group, where the large presence of non-linear loads and distributed generation in modern power systems offers significant challenges on the PQ field.

Voltage and frequency disturbances are major concerns in microgrid systems. Stability issues are known to appear due to the lack of inertia of this type of systems, leading to frequency fluctuations. On the other hand, voltage deviations are mainly result from load or voltage regulation variations. Frequency is conditioned by the balance of active power, meanwhile, voltage is affected by both the active and reactive power flow, depending on the grid impedance X/R ratio. For satisfactory conditions, frequency should remain nearly constant. Indeed, a frequency drop may result in high magnetizing currents in industrial loads and transformers, ending up in transformer's saturation and increased harmonic pollution [2.11, 2.12]. Norm UNE-EN-50160:2010/A1:2015 [2.13] establishes that frequency variations must be within a range of 50 Hz  $\pm$ 0,1 Hz during 100 % of the time. On the other hand, same norm establishes the voltage deviations must be within a range of  $\pm$ 10% from its RMS value.

Unbalance mitigation has also attracted the attention of the recent studies in PQ issues. It concerns to the presence of negative sequence components in the three-phase voltage supply. This type of disturbance results from the connection of single-phase loads in three-phase systems. On this matter, IEC 61000-2-2:2002 [2.14] specifies a compatibility level of 2% for voltage imbalance, recognizing that systems with large single-phase loads may have voltage imbalance levels as high as 3%. EN 50160:2010/A1:2015 [2.13] requires that utilities maintain voltage imbalance less than 2% for 95% of the 10 min samples in 1 week. For systems with significant single-phase loads, the imbalance can be as high as 3%.

Considering the large impact that harmonic distortion can have on electricity, various organizations have developed norms and lists of guidances for applications of the maximum harmonic emission within the public system. The IEC has established the international norms, IEC 61000-3-2:2018 [2.15], which limits the emission of harmonic currents of those equipment which input current is below 16 A per phase. Equipment with input currents above 16 A and below 75 A are subject to the norm IEC 61000-3-12:2011 [2.16]. Both norms are linked with IEC 61000-2-2, which establishes the EMC limits for electrical equipment connected to the public system.

For the case of IEC 61000-3-2:2018, a set of limits depending on the equipment class are established, and included in Appendix A. The maximum harmonic current distortion accepted is calculated according to (2.1).

$$THC = \sqrt{\sum_{h=2}^{40} I_h^2} \quad (2.1)$$

Similar expression for the Total Harmonic Distortion is calculated based on (2.2)

$$THD = \sqrt{\sum_{h=2}^{40} \left(\frac{I_h}{I_1}\right)^2} \quad (2.2)$$

Based on the class of the equipment and the maximum currents, the values of the emission are depicted in Appendix A. The same appendix gathers all the tables for the case of the IEC 61000-3-12:2011.

IEEE standardization group, has worked on a list of guidances to mitigate the presence of current harmonics, gathered in IEEE Std 519-2014, [2.17]. More than a norm, it consists of a set of practical rules, that establish goals for the designing of the electrical systems, including both linear and non-linear loads. The general structure is similar to the already presented norms, providing limits for the maximum current emitted. The same type of limits is based in

this case on the short-circuit current at the Point of Common Coupling (PCC) with the grid. Additionally, the concept of Total Demanded Distortion (TDD), shown in (2.3), is defined, based on the maximum demand load current at the PCC ( $I_L$ ). The tables and the terms definition are included in Appendix A.

$$TDD[\%] = \frac{\sqrt{\sum_{h=2}^h I_h^2}}{I_L} \quad (2.3)$$

### 2.3 Review of the Instantaneous Power Theory

The presence of non-linear loads and transient grid faults are sources of harmonic distortion and voltage unbalanced. The need of a control tool for power converters under such generic grid conditions, led to *Akagi* to formulate his theory in the 80's [2.18], being since then widely extended for control converter applications. This theory starts from transforming the instantaneous variables into the  $\alpha\beta$ -reference frame. This transformation is widely described in Appendix C. Based on the aforementioned transformation and according to [2.19, 2.20], the theory states that the instantaneous power resulting from the interaction of the voltages and currents vectors may be described as the inner and cross product of the instantaneous voltage and current vectors, which results in the  $p$  and  $q$  terms, respectively.

The physical meaning of every term is understood as the total instantaneous energy flow between two systems in the case of the active power  $p$ . Meanwhile, the imaginary power  $q$  is proportional to the quantity of energy that is being exchanged between the phases of the system but it does not contribute to the energy transfer between the source and the load. Since these terms are resulted from instantaneous variables, the theory is both applicable during transients and steady state conditions.

The initial formulation was proposed for three-phase systems. However, its application over four-wire systems was not a straightforward step and that induced the appearance of multiple formulations of the initial theory [2.21].

### 2.4 Reactive Power Compensation and Harmonic Filtering Solutions

Reactive power compensation addresses mainly two aspects: voltage support, to reduce fluctuations at a given terminal; and load compensation, to increase power factor of the line and compensate voltage drops [2.22]. Traditionally, at high voltage levels, mainly employed at the transmission system, the connection of large banks of capacitors, located at substations, is a satisfactory solution for losses reduction and power factor enhancement, which contributes to provide voltage support across the lines. However, in LV systems with larger presence of non-linear loads, this solution might be inefficient, since it may generate a circuit tank, together with the impedance of the line, inducing a resonance at a certain frequency likely to coincide with one of the harmonics injected by the load [2.10].

On the other hand, the voltage harmonic distortion is mostly present in the system because of the nonlinear customer loads that are served. These loads draw harmonic currents that

interact with the system impedance to create voltage distortion. Thereby, it is usually a local phenomenon, thus cancellation of such harmonic pollution can be achieved by a filtering action within a selected bandwidth, in the vicinity of the harmonic source (passive filtering) or as a result of a real-time monitoring process that leads to the injection of real-time cancelling harmonic currents (active filtering). According to this, solutions can be split into:

- **Passive filtering:** the filter is tuned at certain frequency, drawing the harmonic currents at the specified frequency out of the system. This is a traditional configuration, which is largely extended at high voltage levels.
- **Active filtering:** Power converter based filtering. It is a more versatile solution than the passive alternative due to the enhanced capabilities regarding the dynamic response and the harmonic compensation flexibility.

### 2.4.1 Passive Filtering

Composed by passive elements, its robust performance and economical prize have make them attractive solutions to cope with PQ disturbances. Passive filters are highly extended in industry and can be found in two configurations: shunt and series. The former are mainly oriented to provide voltage support and harmonic cancellation; meanwhile, the latter are used to increase transmission power capabilities [2.11, 2.23–2.25]. Different topologies and structures of both configurations are presented in the following sections.

#### 2.4.1.1 Series Compensation

Series passive filters are quite common in transmission systems, since the actual transmitted power is ultimately controlled by the series line impedance and the voltage angle between every terminal in the line. Series capacitive compensation was introduced to shorten the reactance of the line and increase the transmission power capability [2.25–2.27].

The basic principle of series compensation is illustrated in Fig. 2.2 (a), which represents a generic power line interconnecting two sources,  $V_i$  and  $V_o$ . The phasor diagram of the system is also included. The current demanded by source  $V_o$  proves to have an inductive profile, meaning

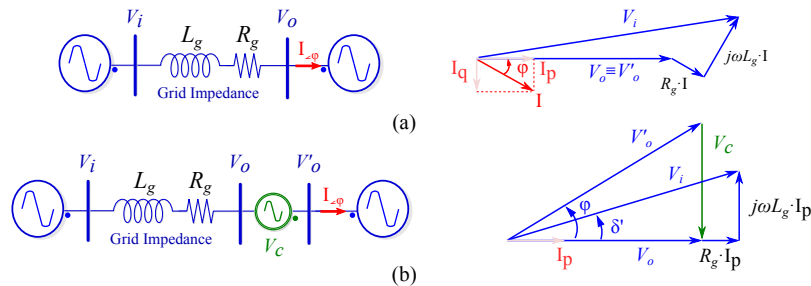


**Figure 2.2:** Basic Principle of Series Compensation. (a) General schematic of the series disposition within a generic system and the phasorial diagram of the system. (b) Schematic including series compensation and the phasorial diagram of the resultant system.

$V_i$  must provide reactive power to assure the proper operation. However, the presence of the reactive current along the line might result in a power line overload or a reduction of the power flow capabilities. Nevertheless, if reactive power is supplied near the source  $V_o$ , the line current can be reduced or minimized, reducing power losses and improving voltage regulation at the output terminals. A possible solution might consist in installing a series compensator, which provides the reactive energy demanded by  $V_o$ . This case is illustrated in Fig. 2.2 (b), where an additional source,  $V_c$  is interconnected between  $V_o$  and  $V'_o$ . This makes  $V_i$  is only responsible to provide the active current demanded by the source  $V_o$ , corresponding to  $I_p$ , being  $V_c$  responsible to provide the reactive component demanded by  $V'_o$ .

Some common series configurations are illustrated in Fig. 2.3.

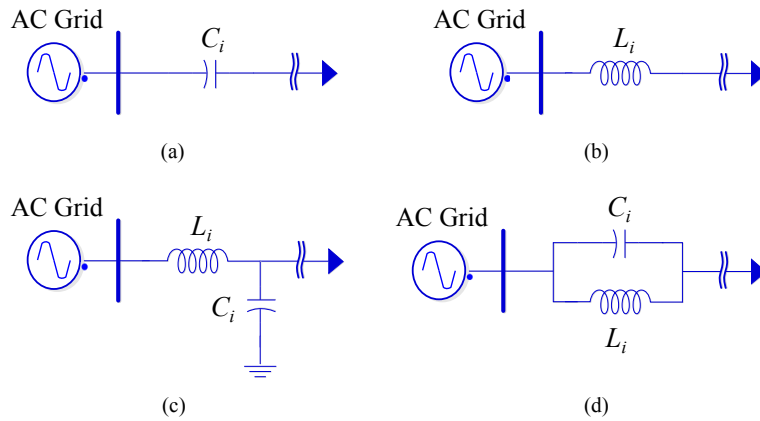


**Figure 2.3:** Passive Series Connection Filters. (a) Series Capacitor; (b) Series Inductor; (c) Low Pass Filter; (d) Series Resonance tank.

- **Series Capacitor:** shown in Fig. 2.3(a), contributes to reduce the inductance effect of the line, in transmission level, increasing the power transfer that can be transmitted. Moreover, they are self-regulated, i.e. the voltage supporting effect increases proportionally to the power flow [2.11, 2.25]. However, this configuration shows important disadvantages that limit their practical applications. Thus, unbalance conditions, and especially fault currents, can rise the voltage across them several times its rated value. Therefore, these devices require a sophisticated and expensive protection system able to by-pass them during certain contingencies. Moreover, the capacitor must be robust enough, to withstand the rated current of the line.
- **Series Reactor:** Fig. 2.3(b) shows the basic configuration of a series reactor. By changing the reactor value it is possible to slightly attenuate some harmonics and improve the power factor. It is a cheap solution and, due to the inductive nature of the power system, cannot be blamed for creating resonance conditions [2.28].
- **Low Pass Filter:** Fig. 2.3(c) This topology is able to eliminate all frequencies above the resonant frequency. The main inconveniences are found on the deep knowledge of the grid harmonics required to obtain a good performance of the system.
- **Series Resonance Tank:** Fig.2.3(d) is a resonant series filter, it traps the currents of the tuned frequency, without inducing any resonance apart.

Series filtering solutions allow for controlling the power flow in the line by adjusting the line equivalent impedance, either by capacitive, Fig. 2.3(a) or inductive, Fig. 2.3(b) compensation. Additionally, they can improve the line harmonic content by offering a high impedance path to prevent undesired harmonic currents to flow through the system (Fig. 2.3(c)-(d)). However, they also must carry full load line currents and require isolation for full line voltages. For all this, shunt filters are a more extended solution.

### 2.4.1.2 Shunt Compensation

This configuration is able to provide both voltage support and harmonic cancellation. In such case, since harmonic pollution is considered a local phenomena, filters need to be installed close to the harmonic sources [2.29, 2.30]. Advantages of this topology can be found on its low price, easy design and robust performance, being for these reasons quite spread in industry.

The basic principle of shunt compensation is shown in Fig. 2.4, which depicts a similar AC-Grid schematic.  $V_0$  is a reactive power consuming source connected through a power line to  $V_i$ . The reactive energy must be provided by  $V_i$ , this might overload the source and increase the losses in the line. To reduce the reactive current supplied by the source, shunt compensation is feasible by connecting a capacitor which attenuates the reactive component of the current. In this case, the compensator is represented by a current source connected in parallel with  $V_0$ . Phasor diagrams for the system with and without compensation are also included.

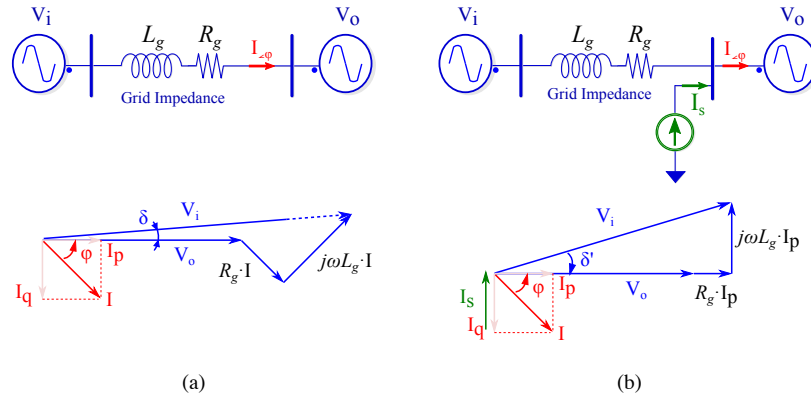


**Figure 2.4:** Simplified schematic of shunt compensation. (a) AC system without compensation; (b) AC system with shunt compensation.

In the system without compensation, Fig. 2.4(a), reactive current is provided by  $V_i$ . The dashed line represents the extra voltage required to achieve  $V_0$  demands, in comparison with the compensated system shown in Fig. 2.4(b). In there, reactive current component is then supplied by the compensator, reducing the  $V_i$  magnitude.

Fig. 2.5(a) and Fig. 2.5(b) shows two types of shunt passive filters, which basically consist in band-pass filters, connected in parallel with the AC-Grid. These are adequate solutions if the load does not present substantial variations; becoming highly unstable, even dangerous, if large changes arise in the system [2.24, 2.29, 2.31]. The size of the capacitor is selected in

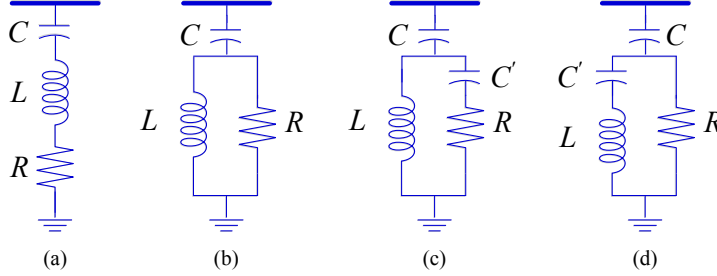


**Figure 2.5:** Passive Shunt Connection Filters. (a) Single Tuned Filter; (b) Second-Order Damped Filter; (c) Third-Order Damped Filter; (d) C-Type Damped Filter.

order to provide an acceptable power factor at grid frequency. The tuning design is based on the resonant frequency of the filter,  $h_i$ , which is the frequency at which inductive and capacitive reactance cancel each other. Resonant frequency can be expressed according to equation (2.4), where  $h_i$  is expressed in hertz,  $L$  is the filter inductance in henry and  $C$  represents the filter capacitance in farad. Regarding the quality factor of the filter,  $Q_f$ , which relates the capability of a filter to dissipate or absorb energy at the tuned frequency, it is expressed according to (2.5a). This magnitude provides information of the sharpness of the tuning and consists of a ratio of the tuning frequency and the bandwidth of two frequencies which are placed opposite at the resonant one ( $\omega_0$ ), and differs each other  $-3$  dB. Quality factor can be also expressed as (2.5b), in terms of the inductive reactance,  $X_L = 2\pi h_i L$ , the capacitive reactance,  $X_C = 1/2\pi h_i C$ , and the  $R$  term. This last term typically consists only in the resistance of the inductor, although additional resistances can be included to limit the maximum current flowing through the filter. Typical values of  $Q_f$  in transmission levels fluctuate between 15 and 80. However, this ratio, in low-voltage systems, ranges between 3 and 7 [2.10].

$$h_i = \frac{1}{2\pi\sqrt{LC}} \quad (2.4)$$

$$Q_f = \frac{\omega_0}{\omega_1 - \omega_2} \quad (2.5a)$$

$$Q_f = \frac{X_L}{R} = \frac{X_C}{R} \quad (2.5b)$$

Alternative topologies are the third-order and C-type damped filters, shown in Fig. 2.5(c) and Fig. 2.5(d), respectively, which include two capacitors, one in series with the resistance and the other one with the inductance. They can be classified as double tuned filters, thus providing the capability to filter two harmonic components simultaneously.

Single-tuned resonant filters only comprises LC components and thus, the cost of the investment and power losses are lower than that of damped filters with same capacity. Moreover, the former imply a simpler design stage. Additionally, single-tuned approaches prove to be efficient in the vicinity of the harmonic source, but it has to be considered, that the interaction of the filter with the source impedance results in an additional resonance peak, which falls slightly below the filter tuning frequency and can be calculated as (2.6), where  $L_S$  represents

the inductance of the system.

$$h'_i = \frac{1}{2\pi\sqrt{(L + L_s)C}} \quad (2.6)$$

According to (2.6), the paralleling resonance-peak can experience a shift every time a change in the installation takes place, like the disconnection or connection of an additional transformer in a substation. This might result in a detuning action of the filter. If the parallel-resonance peak, placed at  $h'_i$ , shifts in such a way that it aligns with the frequency of a characteristic harmonic of the load, it can result in undesired harmonic voltage amplification, producing overvoltage stresses on solid insulation of cables and on machine windings [2.10]. For such reasons, single-tuned filter solutions are mainly suitable for systems with not many harmonics distributed on wide frequency range [2.31, 2.32].

### 2.4.2 Active Power Filters

In general terms, Active Power Filters (APFs) are DC/AC or AC/DC/AC grid-tied power electronics based converters used for grid quality enhancement, which should behave as a linear current/voltage source. However, APFs consist of a power circuit, based on different configurations of switches and passive components, which are not linear. At this point, it has to be accepted that the delivered voltage/current will be built up by a value close to the commanded reference plus a ripple resulting from the commutation states of the converter. This ripple is inversely proportional to the switching frequency, what makes desirable to reach the highest frequencies allowed by the application.

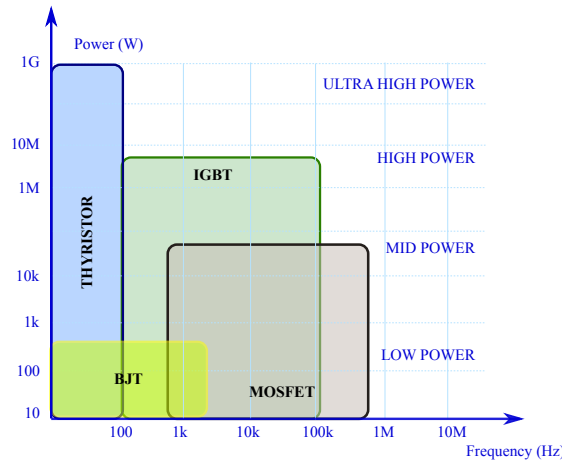


**Figure 2.6:** Operating margins of semiconductor families [2.33]

Historically, thyristors, bipolar junction transistors (BJTs) and power Metal Oxide Semiconductor Field Effect Transistors (MOSFETs) were used as power switches. However, the introduction of Insulated Gate Bipolar Transistors (IGBTs) and its significant evolution in terms of switching frequency, current and voltage range, has boosted the use of APFs as feasible solutions to enhance PQ and specifically, harmonic distortion, at different voltage

levels [2.24, 2.34, 2.35]. Fig. 2.6 presents the current state of semiconductor families based on their power and frequency margins.

The major contribution of APFs is harmonic cancelation, which can be provided by different device configurations and control algorithms [2.23]. In contrast to passive filters, APFs are feasible not only to inject but also to draw reactive power from the system at grid frequency. APFs are present in transmission and distribution networks. However, since the scope of this thesis is focused on the LV level, only those configurations used in the distribution grid will be considered in the following.

The generic solution to cope with the interruptibility and quality of service at end-user level is known as Custom Power [2.36–2.38] and involves technical solutions based on power electronics. These technical solutions are the LV counterpart of the well-known Flexible Alternating Current Transmission System (FACTS), and are mainly oriented to maintain the reliability and good PQ of the system, thus being able to provide voltage balancing and harmonic cancellation. There are multiple APF solutions which can be classified based on the interconnection, the modularity, the nature of the storage device, etc. Some of these technologies are enumerated in the following sections.

#### 2.4.2.1 Static Var Compensation

Static Var Compensators (SVCs) are power electronics devices able to provide a quick response against voltage disturbances derived from fast variations in the reactive power flow of the line [2.24, 2.25, 2.39]. They are split mainly in two categories, shown in Fig. 2.7:

- **Thyristor-controlled reactor (TCR):** it consists of a fixed inductance and a bidirectional switch, consisting of two back-to-back connected thyristors. Neglecting the resistive component, the current through the inductor only depends on the thyristor delay angle and it can be controlled from maximum to zero. The resultant current is full of odd harmonics of order  $h = 3, 5, 7, 9, 11, \dots$  which amplitudes depend on the firing angles [2.24, 2.39, 2.40]. In order to prevent the 3<sup>th</sup> harmonic and its multiples, it is a common practice to use three-phase TCR systems in delta connection, so these harmonics remain trapped within the delta structure and are not transmitted into the

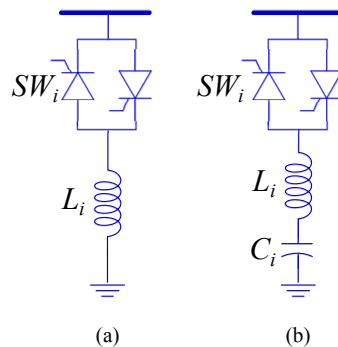


**Figure 2.7:** Static Var Compensation Configurations. (a) TCR; (b) TSC.

AC-Grid. To counteract the effect of other important current harmonics, series-tuned filters are typically connected to mitigate the 5<sup>th</sup> and 7<sup>th</sup>.

- **Thyristor-switched capacitor (TSC):** it uses the same topology of the TCR, except that the inductor is now replaced by a capacitor. To alleviate transient disturbances, the thyristors are switched when grid voltage matches the capacitor voltage. Blocking gate pulses of both switches disconnects the capacitor bank from the grid. A small inductor in series connection can be used to limit the inrush current [2.22–2.24].

### 2.4.2.2 Series Power Filters

In this solution, a VSC is interconnected with the grid through a series transformer. Fig. 2.8 (a) represents the topology of the so-called Dynamic Voltage Restorer (DVR) [2.41]. The phasorial diagram reflects that this topology is perceived from the grid side as controlled voltage source, based on same principle explained in Section 2.4.1.1. In this way, it is capable of compensating the reactive power demand of the loads connected downstream from its PCC. In its role as an APF, this topology emulates the behaviour of a variable impedance, showing a very low value at grid frequency and large values at harmonic frequencies [2.24, 2.25, 2.35]. Series connected active power filters (SAPFs) are focused mainly in voltage distortion issues, compensating for waveform and disturbances in the vicinity of a sensitive load [2.42]. The filter assures that the voltage amplitude at the load is kept constant, and reduces the reactive power flow and current distortion upstream from its point of coupling [2.43]. Additionally, the compensation capabilities of this topology can be boosted by the connection of an auxiliary energy source at the DC-side of the VSC to maintain a constant DC-link voltage. In that case, not only reactive power but also active power can be provided through the filter.

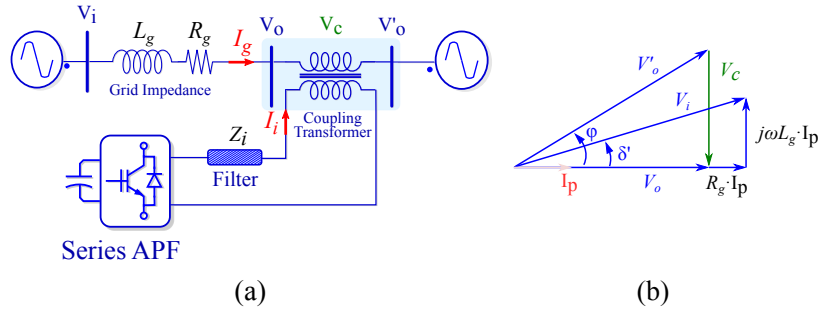


**Figure 2.8:** (a) Series active filter diagram; (b) Phasorial diagram of the compensation

The main drawback of the series topology is that all the current of the grid has to flow directly through the filter, which obliges these devices to be more robust than the ones used in other topologies. The same reason makes it an attractive solution at higher voltage levels. However, stand-alone series active filter is rarely implemented, since the attenuation capability is not fully exploited, thus being less efficient than hybrid topologies such as those shown in Section 2.4.2.4 [2.35, 2.41, 2.44–2.46].

### 2.4.2.3 Shunt Power Filters

Shunt active power filters (ShAPFs) have been widely investigated for current-related issues. Since ShAPFs overcome the technical limitations of the SAPFs, they have become a highly extended topology. A generic schematic of a ShAPF is shown in Fig. 2.9 (a). The phasorial scheme represents the initial variables (light blue) together with the results of the compensation (dark blue). ShAPFs are typically controlled as current sources and are feasible devices to provide reactive power and thus, voltage support. However, with the appropriated control strategy, it is also possible to achieve unbalanced loads compensation and harmonic pollution cancellation [2.47]. This is done by counterphase injection of the load demanded harmonics, thus eliminating them from the grid side. A similar pattern can be used to compensate for load unbalances.

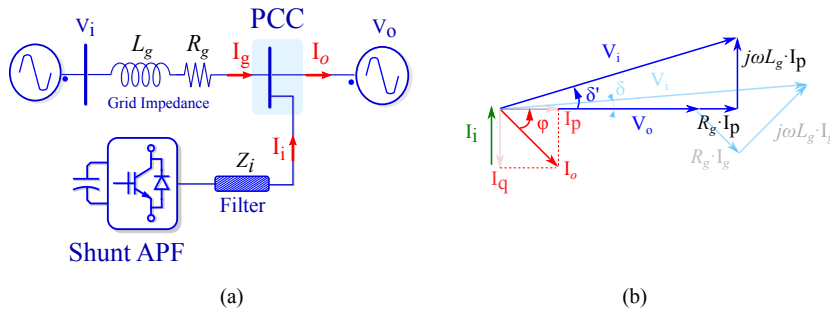


**Figure 2.9:** (a) Shunt active filter diagram; (b) Phasorial diagram of the compensation

At the distribution level this configuration is called Distribution Static Compensator (D-STATCOM) [2.48] and despite of its high switching losses, it is one of most feasible solutions for harmonic cancellation. Switching losses are consequence of the varying switching states derived from the synthesis of current references at the output of the converter. The switching frequency has to be a trade-off between the harmonic distortion induced by the current ripple and the switching losses of the converter [2.42, 2.49]. In general terms, ripple decreases as frequency increases. However, switching losses grow with switching frequency, together with the stress of semiconductors. To cope with this situation, there are different topology configurations, like multilevel converters [2.41, 2.50], cascade control converters [2.51] or resonant structures. Those alternatives are based on cascade connection of the lower DC-voltage terminals of modular bidirectional choppers, in order to increase the number of semiconductors and, consequently, reducing the voltage withstand requirements of these devices. These alternative configurations are mainly oriented to high power applications, however, they are more expensive due to the increase in the number of devices.

### 2.4.2.4 Unified Power Quality Conditioner

This topology is a combination of a SAPF and a ShAPF in a back-to-back configuration, sharing a common DC-link. At the distribution voltage level, this configuration is known as Unified Power Quality Conditioner (UPQC), whereas it is known as Unified Power Flow Conditioner (UPFC) at the transmission voltage level [2.42].

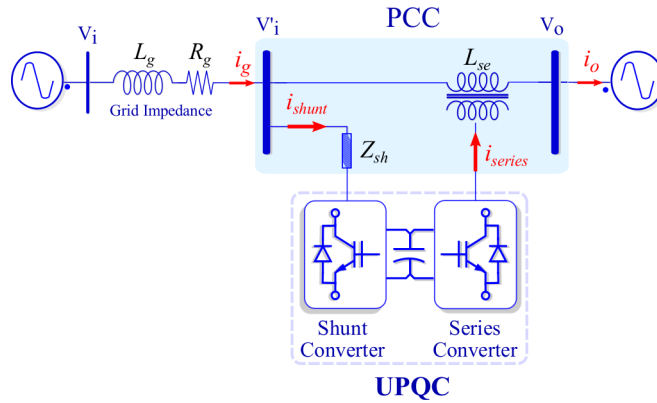


Figure 2.10: UPQC General block diagram

Since this configuration is a combination of series and shunt APFs with a common self-supporting DC-link (Fig. 2.10), UPQC is able to provide support to current and voltage issues as a more cost-effective solution than installing two separate devices. Shunt converter is responsible to maintain constant the voltage level at the DC-link and to provide harmonic compensation. It is operated as a current-controlled converter, in which the current injected to cancel out the harmonics demanded by the load is set based on the difference between the current at the grid side,  $i_g$  and the current demanded by the load,  $i_o$ . On the other hand, the SAPF is operated as a voltage-controlled source, it tracks voltage at PCC, and injects a series voltage of the desired magnitude in case a voltage sag/dip comes up. Therefore, the main purpose of a UPQC is to compensate for supply voltage PQ issues: sags, swells, unbalance, flicker, and harmonics, and for load current PQ problems such as: harmonics, unbalance, reactive currents and neutral currents.

UPQC is a flexible solution to provide PQ support, however, its main drawbacks reside on control aspects: the DC-link has to be constant and free from harmonics, requiring a fast response from the shunt controller against sudden load changes, voltage unbalances or voltage distortion. Moreover, economical aspect play a negative role, considering that all the equipment required for the individual configurations are also necessary in this hybrid topology.

## 2.5 Voltage Source Converters

Voltage Source Converters (VSC) are a kind of self-commutated power converters, i.e. they can change their state at a commanded time, independently of the external voltage/current value. They take their definition from the fact that, inherently, they mimic the role of a controlled voltage source at the AC-side. In the majority of the cases, a DC-link capacitor is used for energy storage in the converter DC-side, while in the AC-side a modulation pattern generates an arbitrary AC voltage waveform. This configuration has become dominant over the Current Source Converter (CSC) topology, due to the advantages of the former respect to the latter: self-commutated versus line-commutated, smaller size and weight, simplicity of control, cheaper and expandable to multilevel and multi-pulse configurations.

To highlight the differences between both solutions, the typical configuration for a three phase CSC is illustrated in Fig. 2.11(b). The system is equivalent to a current source, in which direct current always has one polarity and the power reversal takes place through reversal of DC-voltage polarity [2.25]. CSCs have an inductor as storage device at the DC-side and normally requires a capacitor filter at its output to aim the commutation, which makes them a feasible solution for motor drives due to its robust performance. However, DC-current cannot change instantaneously during transients, which reduces the system dynamics [2.22, 2.23, 2.39, 2.52].

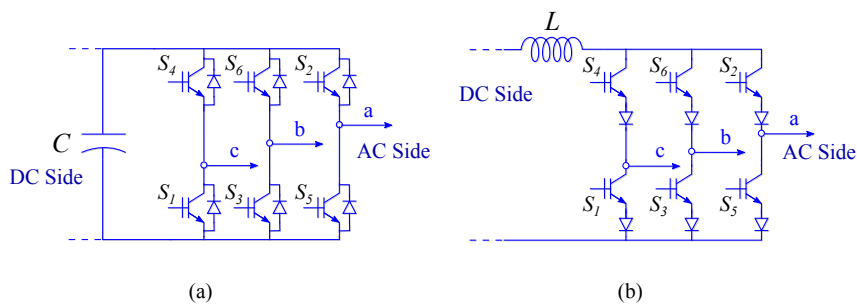


**Figure 2.11:** Power Converters. (a) VSC; (b) CSC.

In similar manner, VSC is equivalent to an AC-voltage source, in which the DC-side voltage always has one polarity and the power reversal takes place through reversal of DC-current polarity. A three phase configuration is shown in Fig. 2.11(a). VSC has a large capacitor at the DC-side and usually requires an  $L$  or  $LC$  filter to be interconnected with the grid.

The interconnection with the grid is generally done through a passive filter; it aims to mitigate the harmonic pollution by reducing the high frequency components induced by the PWM modulation of the VSC [2.53–2.56]. Fig. 2.12 shows three grid interconnection filters highly extended in industry. Fig 2.12 (a) represents the simplest approach, consisting in a  $L$  filter which can achieve a significant reduction in the ripple of the current injected by the VSC. This type of first-order filter provides very good performance and easy control, since resonance is avoided. However, the large voltage drop at the inductor [2.53], and thus, the requirement for larger DC-capacitors, makes this solution unaffordable for high power applications. The other two cases are based on resonance systems, having the capability to block most of the harmonics above the tuning frequency. Moreover, these configurations provide larger attenuation than the single  $L$  filter, which allows to obtain better results with smaller devices. On the other hand, these filters face other inconveniences: filter structure can cause stability problems by undesired resonance effects due to the zero impedance of the filter for some higher order current harmonics. Indeed, resonance in the reactive elements of the filter may lead into instabilities in the current control, making the APFs unstable [2.54, 2.57]. The stability condition of the system is a major issue, being highly dependent on the impedance of the system. If the grid impedance is unknown, resonances may appear and damping methods are necessary. The most simple approach consists in including a damping resistor (passive damping), however, the additional resistor losses are a substantial disadvantage. The alternative consists in including an active damping, what basically consists in the addition of conjugate zeros to isolate the effect of conjugate poles, attracting them to the stable region [2.57]; nevertheless, this approach

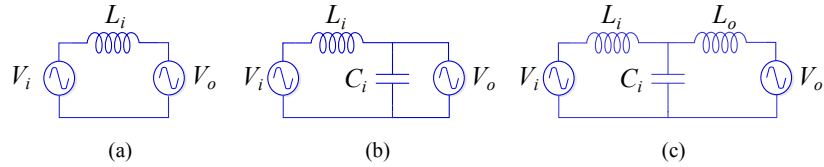


**Figure 2.12:** Passive Filter interconnections with AC-Grid. (a) *L*-filter; (b) *LC*-filter; (c) *LCL*-filter

leads to increase the number of sensors without assuring the robustness of the filter in case of grid impedance changes.

For economic and performance reasons, VSC topologies are often preferred over CSC for filtering applications. As direct current can flow in both directions in VSC configurations, the converter switches have to be bidirectional, and also, since the voltage does not reverse, the turn-off devices do not need to have reverse voltage capability. VSC switching is made up of an asymmetric turn-off device, such as a GTO, with an anti-parallel diode. Other semi-conductors, such as IGBTs and IGCTs, may have a parallel reverse diode built in as part of a complete integrated device. CSC configuration requires a voltage blocking diode connected in series with the IGBT, because direct current is always flowing in the same direction and to perform the power flow reverse, DC voltage reversal is required. For this reason, it has larger power losses and lead to higher costs than the VSC topology and, moreover, it cannot be used in multilevel configuration [2.25].

This thesis is restricted to the use of VSC converters. Consequently, from now on, all discussion will assume a VSC configuration. A review of the topologies, modulation techniques and control systems is performed in the following sections.

## 2.5.1 Topologies

### 2.5.1.1 Single-phase Power Converters

This kind of converters was developed to satisfy the requirements of single phase non-linear loads, such domestic lights, air conditioners, laser printers and such kind of applications that may alter the harmonic content in the LV-grid. Fig. 2.13 shows two possible configurations of single-phase converters, where Fig. 2.13 (a) is a half-bridge VSC and Fig. 2.13 (b) is a two-level, full-bridge VSC for single-phase applications.

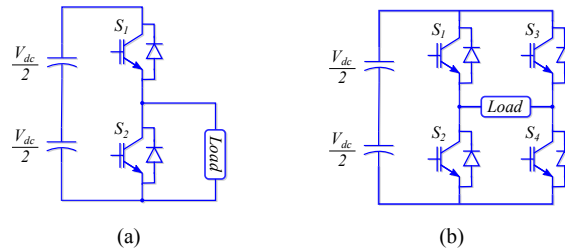


**Figure 2.13:** (a) Half-bridge VSC topology; (b) Full-bridge VSC topology.

The simple control and lower cost of the components of these topologies, together with their good performance under transient conditions, have made them attractive solutions at low and medium power levels. Thus, they have also been adopted as solutions for interconnecting any kind of energy sources to LV grids as well as to feed single-phase motor drives. Additionally, they can also provide load and reactive current compensation [2.38, 2.58].

### 2.5.1.2 Three-Phase Power Converters

Three-phase converters are considered the most extended configuration in industrial power applications. A simplified representation of a three-phase two-level converter has been shown in Fig. 2.11(a).

The interconnection of power converters with the grid is conditioned by the number of phases and wires available at the PCC. At the LV level, the most typical configuration of the distribution transformer is  $\Delta$ -Y, releasing the neutral connection for single-phase devices to be connected. This additional conductor enables two additional configurations for the power converter, as shown in Fig. 2.14. In Fig. 2.14 (a) the three-leg-four-wire (3L-4W) alternative is shown. In there, the neutral is passively connected to the mid-point of the DC-link. Alternatively, if an additional leg is included to actively control the neutral wire, the configuration is known as four-leg-four-wire (4L-4W) and it is represented in Fig. 2.14 (b).

#### 2.5.1.2.1 Three-Leg-Four-Wire Power Converters

With the split-capacitor approach the three-phase converter essentially becomes three single-phase half-bridge converters; thus, it suffers from an insufficient utilization of the DC-link voltage. In addition, large and expensive DC-link capacitors are needed to maintain an acceptable voltage ripple level across the DC-link capacitors in case of a large neutral current due to unbalanced and/or nonlinear loads [2.59].

Another consideration from the point of view of system modelling and control, is the fact that the p-q theory introduced in [2.18], and used for the instantaneous compensation of voltage/current unbalances, is only valid for three phase three-wire systems and for three-phase four-wire systems. However, for three-phase four-wire systems with passive neutral, maximum reactive current compensation cannot guarantee elimination of the neutral current [2.60, 2.61]. This might result in undesired zero-sequence currents flowing through neutral connection, deprecating power quality in the rest of system.

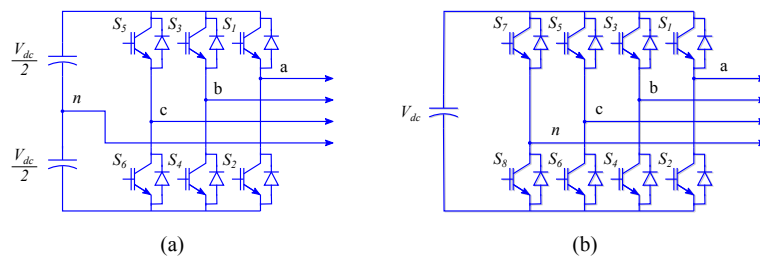


**Figure 2.14:** 3-Phase Converters with Neutral Connection. (a) Three-legs with split capacitor (3L-4W); (b) Four-legs with active neutral control (4L-4W)

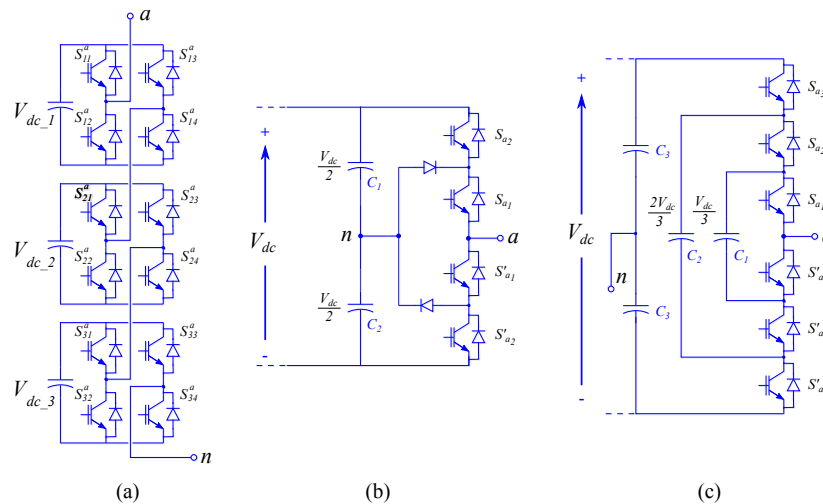
### 2.5.1.2.2 Four-Leg-Four-Wire Power Converters

Figure 2.14 (b) shows a 4-wire configuration, where the neutral connection is provided by a dedicated power converter leg. This approach for creating the neutral connection is usually preferred to the previous one, since the wider range of switching states available in the four-leg topology, enables the performance of the converter to be enhanced in comparison with the three-leg with neutral connection. Thus, it provides more flexibility from the point of view of the homopolar current compensation. Additionally, since the DC-link is fully usable, the power density (power/volume) as well as the specific power density (power/weight) are improved [2.62].

This type of topology is preferred when the supplied three-phase loads are highly unbalanced or in the compensation of grids with large neutral currents. The main drawbacks of this configuration are related with the complexity of the PWM algorithm required for switching the neutral leg of the converter [2.59, 2.63] and with the economic aspects engaged to the addition of an extra leg to the converter.

### 2.5.1.3 Three-Phase Multilevel Power Converters

As it was mentioned in Section 2.4.2.3, this type of converters was developed for high power applications since, among other advantages, its configuration aims to alleviate the stress of semiconductors. These topologies are especially well-suited to reduce the harmonic distortion of the AC-side currents. They were particularly used for utility applications at transmission level, being afterwards spread to lower voltage levels once the technology was mature enough [2.64].



**Figure 2.15:** Three-phase multilevel converters. (a) Branch of an H-bridge three-level converter; (b) Branch of a NPC three-level converter; (c) Branch of a Flying Capacitor four-level converter

Figure 2.15 shows three of the most characteristic configurations of this technology. In this type of topology, an array of switches is used to select the output voltage from a number

of available DC power supplies. A major concern in these architectures is to maintain voltage level constant at every instant, to do so, capacitors with a charge balancing scheme are used.

The first multilevel structure presented in history was the Series H-Bridge multilevel inverter, shown in Fig.2.15(a). As its name says, it is composed by several bridge inverters associated in series in cascaded configuration. The modularity and simplicity are the most attractive points of this topology. However, the large amount of devices as well as the need of several isolated DC-links make them unattractive for applications that require active power exchange.

In Fig.2.15(b), a general schematic of the branch of a Neutral Point Clamped (NPC) converter is shown. This configuration provides and odd number of voltage levels from an even number of capacitors. Leaving access to the neutral connections and distributing the voltage equally among the capacitors, it is possible to modulate the voltage by sharing only a part from the DC-link over every switch, which allow them to withstand lower voltage levels. The increased complexity of the modulation techniques required to obtain a satisfactory performance added to the increased number of devices required to provide the voltage levels are the main drawbacks of the topology.

The last scheme in Fig.2.15(c) shows a phase of a three-phase four-level Flying Capacitor Converter (FCC). In this topology, each phase-leg consists of three complementary switch pairs and two floating capacitors. The voltages across the capacitors  $C_1$  and  $C_2$  are ideally  $2V_{dc}/3$  and  $V_{dc}/3$ , respectively. This topology as well as the NPC one, only requires one DC-voltage source, being the other voltage levels generated internally. Applications and practical deployment of the FCC are limited because of several factors, including (i) the need for bulky per-phase capacitors with their designated precharging circuits and (ii) a complicated capacitor voltage balancing scheme.

Apart from the above mentioned multilevel structures, there is an additional family, which merges the cascaded and modular topologies. It is based on the combination of several identical reduced power submodules, which can be seen as power cells, to achieve a system with higher rated power. This family, which has become extraordinarily popular in high power applications, is known as Modular Multilevel Converter (MMC). There is not a clear uniformity regarding to which group belongs modular converters in literature, being considered both as a group inside the *multicell* or the *cascaded* topologies [2.51]. However, to be considered as a modular structure, besides the series connection of submodels, the scaling to different voltage and power levels should be achieved without including additional central components, [2.65]. Fig. 2.16 shows two possible configurations of MMC. In Fig. 2.16 (a), every cell has each independent DC-link. In Fig. 2.16 (b), every cell contributes to build up a larger common DC-link. In this case, single-coupled or center tapped inductors are used as filter interconnection. The highlighted blue box shows a possible configuration of the individual cells. In this case, a full bridge is represented, but several alternative options are available.

All these topologies are widely spread as distribution FACTS (or D-FACTS) and are today available in the market from different manufacturers. However, the complexity of the control and the large amount of devices required made them unattractive for the purpose of this work; thus, only two-level topologies are considered in the following. A four-leg four-wire configuration has been used in the development of the theoretical framework in Chapter 3 and in the investigations carried out in Chapters 4 and 5. In Chapter 6, focused on the optimization of the switching frequency, a more classical three-leg three-wire topology has been used.

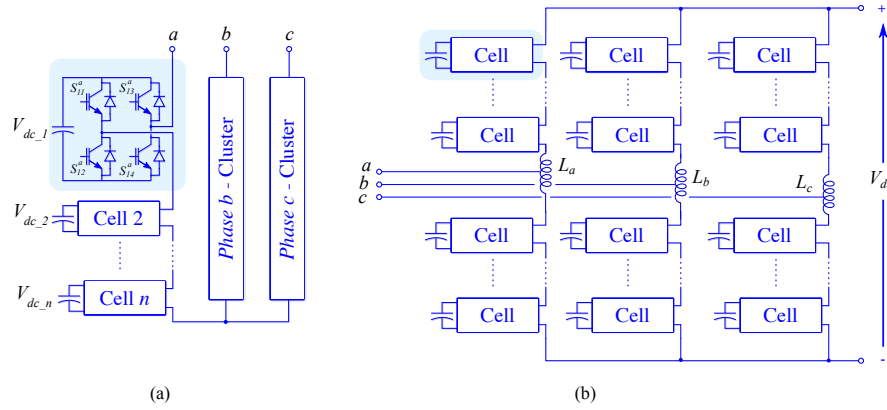


**Figure 2.16:** Multi modular converter topologies [2.51]. (a) MMC without common DC-link; (b) MMC with common DC-link.

## 2.5.2 Modulation Techniques

One of the most typical implementations to determine the duty cycle for each phase leg in switched-mode converters is known as pulse width modulation (PWM). It consists in digitally encode analog signal levels by using square wave signals. Thereby, sinusoidal modulation is the result of the comparison of a sinusoidal modulation signal with a triangular carrier signal. The frequency of the triangular waveform establishes the switching frequency of the semiconductors, while the frequency of the output waveform relies on the frequency of the modulation signal.

In general terms, the ripple of the AC-side current is inversely proportional to the switching frequency, whereas the switching losses in the semiconductors increase proportionally to it. This duality causes a trade-off that will be fully developed in Chapter 6 of the present work.

### 2.5.2.1 Continuous PWM Techniques on 3-Wire Systems

The comparison between the carrier and the control signal can be either naturally sampled, as it is illustrated in Fig. 2.17, or regularly sampled. In the former case, the pulsed width is determined by the intersection of the modulation signal and the carrier triangle signal. Thus, the sampled values are generally not uniformly spaced in time, but a faster reaction to changes in the input signal can be achieved. For the second case, the control signal is considered constant during a complete carrier period (symmetric sampling) or half of it (asymmetric). Alternatively to PWM, Space-Vector-Modulation (SVM) can be used. This method synthesized the output voltage in order to reproduced the desired reference voltage space vector,  $U^*$ , by using two adjacent switching vectors which are sequentially held in on state during a precomputed time. For the actual study, only the regularly sampled PWM is considered.

The amplitude modulation index of the PWM technique is established according to (2.7), where  $V_{mod}$  is the peak-value of the modulating signal and  $V_{carrier}$  is the peak-value of the

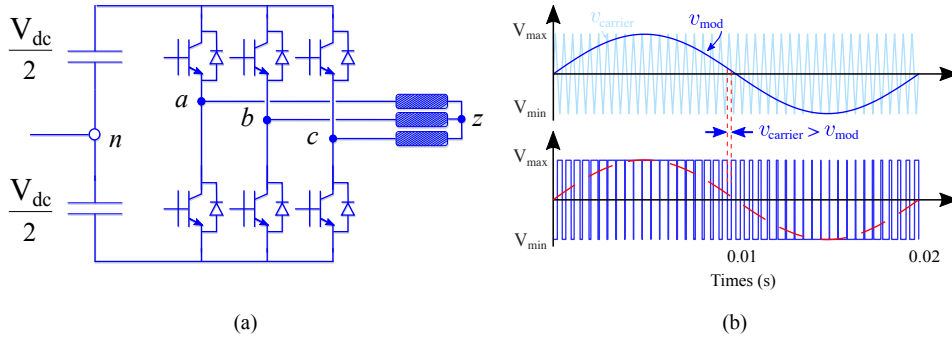


**Figure 2.17:** Pulse-Width Modulation. (a) Phase branch disposition; (b) Train of pulses of the PWM algorithm.

triangular carrier signal.

$$m_a = \frac{V_{mod}}{V_{carrier}} \quad (2.7)$$

$$v_{xz} = m_a \frac{V_{dc}}{2} \sin(\omega_e t + \phi) \quad (2.8)$$

The fundamental component of the synthesized voltage from an arbitrary signal is formulated in (2.8), where  $\omega_e$  corresponds to the fundamental frequency and  $\phi$  is the phase angle of the signal. According to (2.8), the magnitude of the output voltage varies linearly while  $m_a < 1$ . Higher values of  $m_a$ , i.e. above 1, leads to an operating condition known as overmodulation, which is characterized by increased harmonic distortion. In general, this is not a desirable situation, though it allows to reach higher output voltages which can be useful for certain high power applications such as those including induction motor drives.

To facilitate the explanation, the bottom of Fig. 2.17(b) shows the train of pulses that results from the comparison between the triangular and the sinusoidal waveforms shown at the top. When the modulation signal is greater than the carrier, then the output voltage is set to  $V_{max}$ , setting the output signal to  $V_{min}$  in the opposite case. For this case,  $m_a$  is set to 1; in red dashes, it is represented the equivalent resultant sinusoidal waveform with a maximum value of  $\frac{V_{dc}}{2}$ .

In order to cope with the aforementioned voltage limit, the addition of a  $3^{rd}$  harmonic to

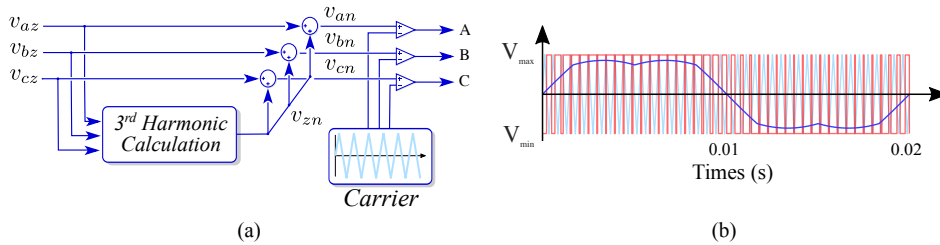


**Figure 2.18:** PWM with  $3^{rd}$  harmonic injection. (a) Modulation structure; (b) Train of pulses of the resulting modulation strategy

the modulating signal is a classical solution, and thus, it has been adopted in the present work. Since all triplen harmonics are cophasal in a three phase system, they are eliminated from the line to line waveforms. Fig. 2.18 shows a schematic of the 3<sup>rd</sup> harmonic injection loop. A solution proposed in [2.66] determines the value of the 3rd harmonic,  $v_{zn}$ , as the instantaneous average of the maximum and minimum of the three reference voltages ( $v_{az}, v_{bz}, v_{cz}$ ), according to (2.9).

$$v_{zn} = -\frac{\max(v_{az}, v_{bz}, v_{cz}) + \min(v_{az}, v_{bz}, v_{cz})}{2} \quad (2.9)$$

The modulation signals are then calculated by adding  $v_{zn}$  to each of the individual reference voltages to obtain the modulation waveforms, i.e. (2.10).

$$\begin{aligned} v_{an} &= v_{az} + v_{zn} \\ v_{bn} &= v_{bz} + v_{zn} \\ v_{cn} &= v_{cz} + v_{zn} \end{aligned} \quad (2.10)$$

In Fig. 2.18, the same conditions stated before for the traditional PWM strategy were used. However, this figure demonstrates that the modulating signal is still not reaching the maximum voltage allowed by the DC-link. This fact opens the door to additional rises of the output voltage.

The addition of the zero sequence is proven to be an effective solution to extend the linear modulation range. The absence of neutral connection between the star point of the load and the midpoint of the DC-Link,  $v_n$ , allows these voltages can take different values. Adding same zero sequence to each of the voltage phases, does not change the inverter output line-to-line voltage per carrier cycle average value, allowing in this way to improve the modulation range [2.66–2.68].

### 2.5.2.2 Discontinuous PWM Techniques on 3-Wire Systems

The previous section introduced the strategy of adding a zero sequence component to each phase voltage used as modulating signals due to its simple implementation and multiple benefits. This modulation strategy considers a continuous zero sequence injection strategy. However, an improved converter performance can be obtained by using a discontinuous injection.

Indeed, by using a switching pattern in two phases of the converter and clamping the other one to provide the DC-bus voltage, it is possible to achieve a high performance modulation technique for obtaining sinusoidal currents. This mode of operation is known as discontinuous pulse-width modulation (DPWM) and reduces the switching losses compared to the conventional continuous pulse-width modulation. It allows to achieve higher switching frequencies without compromising switching losses, thus enhancing converter efficiency. Moreover, for high modulation index values, this technique provides better results in terms of current harmonics reduction in comparison with traditional continuous PWM techniques without zero sequence injection [2.69]. Additionally, since higher switching frequencies are reached, lower filtering efforts are needed to counteract conducted EMI and thus, the power density of the converter is increased [2.68, 2.69].

### 2.5.2.3 PWM Techniques on 4-Wire Systems

As it was stated in Section 2.5.1.2, three-phase converters can provide neutral connection in two different ways: by connecting the neutral wire to the mid-point of a DC-link with split capacitors, Fig. 2.14 (a), or by adding a fourth leg to the converter topology connected to the neutral wire, Fig. 2.19 (a). The addition of a fourth leg allows the use of the neutral connection as an active wire to inject zero currents, thus providing the capability to compensate the effects of single-phase unbalanced loads.

The strategy shown in here is based on the work presented in [2.70]. This PWM technique is an extended version, for neutral connection, of the 3-wire method presented in the previous section. Provided that the measurements of the phase-to-neutral voltages remain within the limits shown in (2.11), the modulating signals can be synthesized according to (2.12).

$$-V_{dc} \leq V_{af}, V_{bf}, V_{cf} \leq V_{dc} \quad (2.11)$$

$$\begin{aligned} v_{an} &= v_{af} + v_{fn}; \\ v_{bn} &= v_{bf} + v_{fn}; \\ v_{cn} &= v_{cf} + v_{fn}; \end{aligned} \quad (2.12)$$

The algorithm is performed based on (2.13), where the maximum and minimum values are selected according to the instantaneous voltage value. The fourth leg is commutated based on the comparison of the resultant  $v_{fn}$  modulating signal with the triangular carrier waveform. Fig. 2.19 (b) shows a block diagram used for the implementation of this strategy.

$$\begin{aligned} v_{max} &= \max \{v_{af}, v_{bf}, v_{cf}\} \\ v_{min} &= \min \{v_{af}, v_{bf}, v_{cf}\} \\ v_{fn} &= \begin{cases} -\frac{v_{max}}{2}, & v_{min} > 0 \\ -\frac{v_{min}}{2}, & v_{max} < 0 \\ -\frac{v_{max} + v_{min}}{2}, & \text{Otherwise} \end{cases} \end{aligned} \quad (2.13)$$

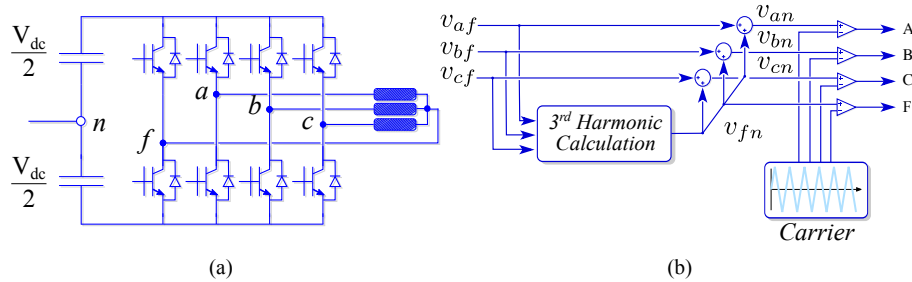


**Figure 2.19:** PWM strategy for 4-wire systems [2.70]. (a) Four-wire converter topology; (b) Modulation structure of the four-wire PWM technique

This technique is also suitable to be applied in SVM, however the simplicity of the method makes it attractive to be implemented within a simple microprocessor due to its low computational burden. This last point has led the choice of this technique as the most adequate solution for this work.

### 2.5.3 Converter Control

VSC-based power converters are suitable to operate in the four quadrants, either as a rectifier or as an inverter. This operation mode is determined by the control references, which are based on the instantaneous active and reactive power components.

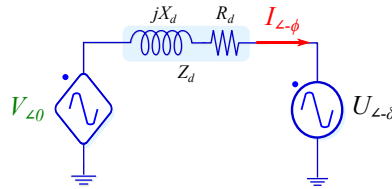


**Figure 2.20:** Equivalent model of a VSC connected to an AC Grid.

The most common approach to VSC control is based on the synthesis of a set of voltage commands by providing the proper semiconductor switching sequence through PWM. These voltage commands are the result of a current control, which satisfy the instantaneous power references.

To achieve a satisfactory behaviour, VSCs usually require to sense ac-side voltages and currents as well as the DC-link voltage. The basic characteristics of the inner control loop strategy are described in the following section. The discussion of this section will be carried out based on the configuration shown in Fig. 2.20, where the VSC is represented by a voltage source,  $V_{L0}$ , the grid by a voltage source,  $U_{L-\delta}$ , and the interconnection filter by an impedance  $Z_d$ .

#### 2.5.3.1 Cascade Control

The main objective of the control structure is to accomplish the power objectives required by the application. This is achieved by a cascade control structure, as the one shown in Fig. 2.21, where the outer loop, devoted to voltage control, is tuned at a frequency around ten times slower than the inner loop, devoted to current control. The reason behind this is to decouple both controllers, allowing this way an independent tuning strategy between each other [2.71]. The current controller is tuned according to the interconnection filter transfer function, whereas the external DC-link voltage control requires the value of the DC-link capacitor. Further details of the controllers implemented both in simulation and experimental validation are included in Appendix E.

The control method described here is known as Voltage Oriented Control (VOC) [2.72]. It is based on the use of a  $dq$ -frame rotating at  $\omega_e$  speed and oriented such that the  $d$ -axis is aligned with the grid voltage vector,  $\mathbf{u} = u_d + ju_q$ . Thus, the space vector of the fundamental harmonic has constant components in the  $dq$ -frame, while the other harmonics space vectors

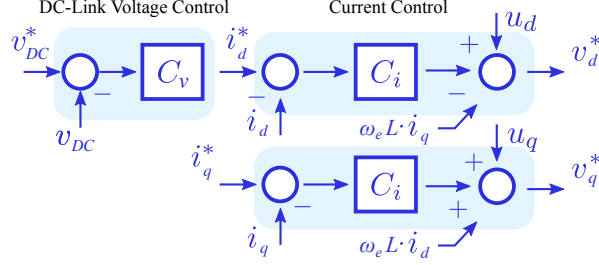


**Figure 2.21:** Cascade Control Structure

have pulsating components. The *Park* transformation, required to establish this relationship, is explained in detail in Appendix C.

The transformation used for this work is power invariant and voltage oriented, so  $u_d = U_n$ , where  $U_n$  stands for the amplitude of grid voltage. Thus, the instantaneous power can be expressed according to (2.14).

$$\mathbf{s} = \mathbf{v} \cdot \mathbf{i}^* = (u_d + ju_q)(i_d - ji_q) = \underbrace{(u_d i_d + u_q i_q)}_p + j \underbrace{(u_q i_d - u_d i_q)}_q \quad (2.14)$$

Considering the case of ideal synchronization:  $u_q = 0$ , the *d-axis* component of the transformation is used for controlling  $p$  and the *q-axis* component is devoted for  $q$ . This allows to establish a decoupled control for the active and reactive power according to (2.15)-(2.16).

$$p = u_d \cdot i_d \quad (2.15)$$

$$q = -u_d \cdot i_q \quad (2.16)$$

As it is illustrated in Fig. 2.21, *d-axis* reference component is used to control the DC-link and so the active power regulation from the grid. Similarly, *q-axis* reference component is controlled to achieve a displacement of the power factor of the system. Both loops are designed with PI controllers (in the case of the current loop, it is established one per axis, since variables are aligned with the rotating  $dq$  reference frame), resulting in zero steady-state error, as it is the case for DC input variables.

The inner current loops are established based on the mathematical model of a three-phase voltage system as the one shown in Fig. 2.20, which can be formulated according to (2.17).

$$\begin{aligned} v_d &= Ri_d + L \frac{di_d}{dt} + \omega_e L i_q + u_d \\ v_q &= Ri_q + L \frac{di_q}{dt} - \omega_e L i_d + u_q \end{aligned} \quad (2.17)$$

This expression results from the application of *Park* transformation to the state equation of the impedance of the interconnection filter, Fig. 2.20. In (2.17),  $v_d$  and  $v_q$  stands for the  $dq$  components of the VSC output voltage space vector and  $u_d$  and  $u_q$  for the  $dq$  components of the grid side voltage space vector. The addends associated to  $\omega_e$ , which stands for grid angular frequency, are the cross-coupling terms, that can be eliminated by feedforward compensation, as shown in Fig. 2.21.

According to (2.15), (2.16), the instantaneous active and reactive power of the VSC is proportional to the  $d$ -axis and  $q$ -axis currents, respectively. Based on this, and considering the power losses in the filter are negligible, the DC-link voltage controller can be designed by establishing a power balance at the DC-link equivalent circuit, shown in Fig. 2.22, according to (2.18).

$$p_i = v_d \cdot i_d \approx p_{C_{dc}} + p_o = u_{dc} \cdot C_{dc} \frac{du_{dc}}{dt} + u_{dc} i_o \quad (2.18)$$

where,  $C_{dc}$  is the capacitor of the DC-link (considering ideal behaviour),  $u_{dc}$  and  $i_{C_{dc}}$  are the voltage and current of the DC-link, respectively and  $i_o$  depends of the operation condition of the VSC: VSC working as rectifier ( $i_o > 0$ ); VSC working as inverter ( $i_o < 0$ ) and  $i_o = \frac{u_{dc}}{R_0}$  with a resistive load connected at converter output.

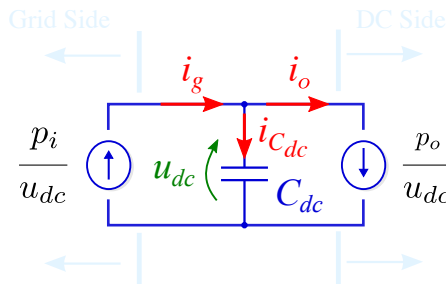


Figure 2.22: Equivalent circuit of the DC-link

As it was mentioned above, voltage control loop generally presents longer settling times than the current loop, often being the voltage control implemented using a cascaded control loop approach. In this manner,  $d$ -axis current reference is established by the DC-link voltage controller, being the  $q$ -axis current reference established based on reactive power control as given by (2.16).

#### 2.5.4 VSC Efficiency Aspects

The soaring use of inverters in distributed generation and energy storage applications has increased the attention paid to the efficiency of these devices in recent years. From the point of view of the VSC operation, efficiency can be improved by reducing losses in the converter components or by achieving a higher performance without increasing the power losses. Based on this, the following points are candidates to enhance VSCs efficiency.

#### Semiconductor Families

Traditionally, silicon has been the most popular material in microsystem technology. Its mechanical properties, and a good cost and energy dissipation ratio, have made it one of the most attractive solutions in the semiconductor manufacturing field. Nevertheless, silicon has low bandgap energy, low critical electric field, low thermal conductivity and limited switching frequency. These aspects have impulse the search for new materials that allow to achieve

devices with faster switching speed and higher voltage blocking capacities. Thus, Silicon Carbide (SiC) or Gallium Nitride (GaN) are offering a new range of possibilities in the energy field by means of new devices with improved characteristics, such as the so-called wide bandgap (WBG) semiconductors.

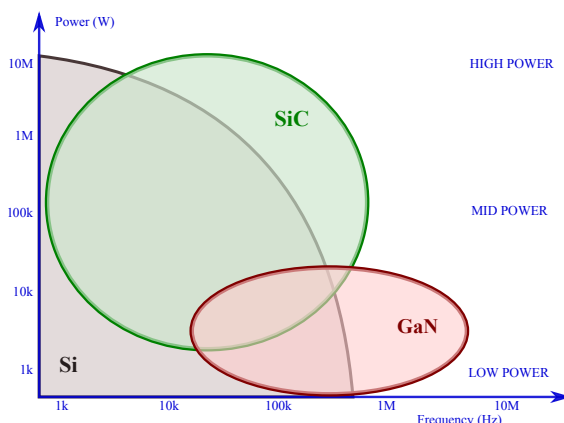


**Figure 2.23:** Operating range of WBG compared with traditional Si technology [2.73]

These semiconductors possess remarkable electronic properties that silicon and other conventional materials lack. WBG semiconductors have a high bandgap, more than 2.0 eV, whereas conventional semiconductors have a small one (around 1.0 eV), [2.74]. As a consequence, WBG devices have much lower leakage currents and higher operating temperatures compared to silicon power devices. Additionally, its higher electron saturation velocity allows to achieve higher switching frequencies and its higher thermal conductivity contributes to a better heat dissipation, thus reaching higher power densities, [2.65]. Fig. 2.23 shows a comparison between traditional silicon technologies and the aforementioned WBG.

The properties of SiC enable the design of minority carrier free unipolar devices instead of the charge modulated IGBT devices. Thus, SiC devices achieve higher efficiency, higher switching frequencies, reduced heat dissipation and space savings; benefits that, in turn, lead to lower costs and an efficiency enhancement of the overall system.

## Power converter topologies

Contributions to VSC efficiency enhancement by means of improved topologies are mainly focused on the reduction of switching losses and harmonic distortion.

As it was stated in Section 2.5.1.3, VSC topologies based on modular structures offer a wider range of possibilities, due to the capability of combining low power submodules in series to achieve a system with a higher power rating. Each of these submodules consists of semiconductor switching devices with low-voltage ratings. When a large number of modules is used, it is possible to obtain a high number of voltage levels, allowing a significant reduction of the switching frequency without compromising the power quality, together with a reduction of switching losses. The reduction of current harmonics, in comparison with a two-level converter, lightens the requirements of the interconnection filter. Eventually, in comparison

with more traditional topologies, modular structures can lead to improvements in terms of cost-weight-volume reduction.

The major field of application of modular converters lies in high power levels, specifically in High-Voltage Direct Current (HVDC) transmission systems. However, some contributions at the LV level can be found, mainly related with the interconnection of DC smart homes with the AC Grid. As an example, [2.75] takes advantage of the low cost and size of the filter resulting from MMC technology, to provide bidirectional exchange of energy between the DC bus and the AC grid.

### Modulation schemes

The efficiency of power converters interconnected to the energy power system (EPS) is influenced by regulations such as [2.3]. This regulation states limits for the harmonic current injection of electronic devices at the PCC, considering as well the interoperability and associated interface aspects. In most cases, increasing the switching frequency reduces the efficiency of the device due to the rise of the converter switching losses, while decreasing this parameter could make the device not conform with regulation. An alternative approach might consist in reducing switching frequency until it is verified that the converter complies with the harmonic emission limits. Then it is possible to mitigate selective harmonics for such conditions, by adopting selective harmonic elimination PWM strategies. This technique is based on the decomposition of the PWM voltage waveform into the Fourier series and calculating the switching angles that eliminate the selected low-order harmonics. In [2.76] a deep review of the technique and the opportunities that brings to the efficiency enhancement field are presented. Likewise, contributions based on a similar strategy and attenuating the fifth, seventh and above order harmonic amplitudes, and complying with regulation in [2.17], are proposed in [2.77, 2.78].

Modulation schemes oriented to extend the linear modulation range of the converter, such as those described in Section 2.5.2.1, contribute to an improved efficiency of the converter. However, there are also advanced modulation schemes which varies the switching frequency according to the operating condition of the VSC, [2.49, 2.79, 2.80], enhancing as well converter efficiency. The study proposed in Chapter 6 deals with efficiency enhancement aspects by accommodating switching frequency depending on the system demand.

Additionally, alternative modulation schemes offer optimization opportunities by reducing switching losses for a certain switching frequency. This is achieved by reducing the number of switches operating at a time. Discontinuous PWM techniques, presented in Section 2.5.2.2, enable to reduce the operating switches by clamping one of the branches at the midpoint of DC-link [2.68, 2.69].

### 2.5.5 Grid-tied Power Converters

The integration of RES and Distributed Generation (DG) into the distribution grid requires an interface, which usually consist of a power converter, to accommodate generation to the AC grid at the expected voltage level. When a power converter is operated for such a function, it is called grid-tied converter. Depending on their operation, grid-tied power converters can be classified into grid-feeding, grid-supporting, and grid-forming power converters [2.81].

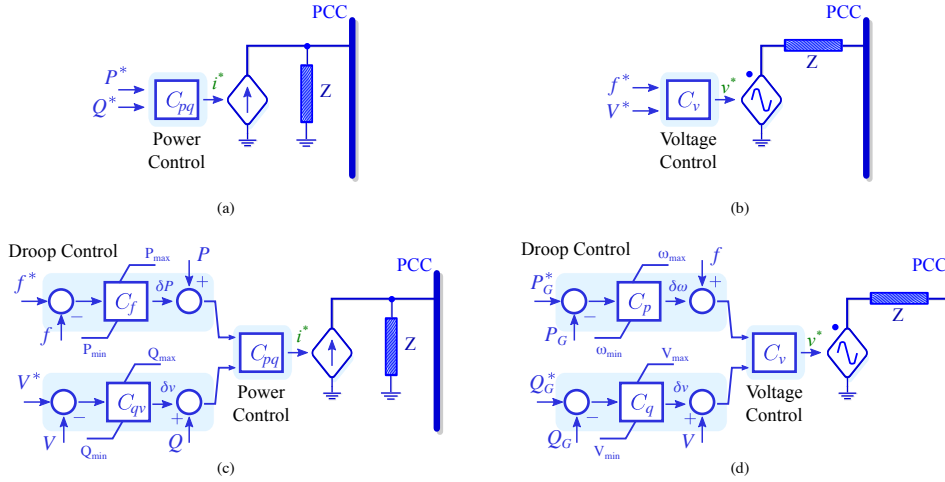


**Figure 2.24:** Converter role [2.81]. (a) Grid-feeding converter; (b) Grid-former converter; (c) Grid-supporting converter controlled as a current source; (d) Grid-supporting converter controlled as a voltage source.

- Grid Feeding:** the converters are controlled to deliver power within an energized grid. This is the most common operation mode for those converters which are operating as DGUs. Their performance emulates a current source with high output impedance, which regulates its output current based on active and reactive power references, Fig. 2.24 (a). This operation mode is feasible to work under an environment with several power converters operating in parallel, but it is not compatible with islanding mode, since another converter or synchronous generator which set the voltage amplitude and the frequency of the grid is required.
- Grid Forming:** Power converters in this mode behave as voltage sources with a low output impedance, Fig. 2.24 (b). Voltage magnitude and frequency are settled in closed-loop mode operation. This type of converters are the responsible to establish the voltage reference for the rest of the converters present in the microgrid during islanding operation. A practical example of this type of converters can be a standby UPS, which stays disconnected from the grid in case the operation is within certain limits.
- Grid Supporting:** The main objective of this group is to participate in the regulation of the AC grid voltage magnitude and frequency, by controlling its power injection. The power converters may be controlled as current or voltage sources, Fig. 2.24 (c),(d). In the former case, voltage amplitude and frequency are regulated based on  $f/P$  and a  $V/Q$  droop control to generate the internal references of the converter. In the second case, the delivered converter power is function of the AC Grid voltage, contributing to regulate voltage amplitude and frequency, based on a  $P/f$  and  $Q/V$  droop control. These converters can work both in islanding and non-islanding configuration, without the need of an additional grid forming converter or synchronous generator. These converters can operate in parallel with the microgrid implementing the aforementioned droop control, which modifies their operating parameters according to the microgrid conditions.

## 2.6 Operation of Grid-tied Power Converters

This section is devoted to the operation of grid-tied VSCs, with a focus on the control structure and requirements. Typically, the control scheme of a grid distribution system operated as a microgrid has been split into three main control layers [2.82].

- A top layer, devoted to distribution network dispatch, responsible for the microgrid coordination, ensuring economic and safe operation at any moment. This energy-management level, namely the tertiary control, is responsible for regulating the power flow between the grid and the microgrid;
- A second layer, devoted to the centralized control for all the elements installed within the microgrid, i.e. DGs, Energy Storage Systems (ESSs), loads. This layer, namely secondary control, can include the loops to compensate for the frequency and amplitude deviations, ensuring a stable and seamless interconnection of the microgrid with the main grid;
- The third layer is composed of local controllers, focusing on the primary regulation of frequency and voltage of each DG unit. This is the primary layer control, and involves the inner and voltage control loops as well as the phase synchronization with the PCC;

The scope of this work is focused on the most-internal layer of the control structure, where the VSCs are responsible to control the power output of the DGs and maintain voltage stability within the microgrid. Since, typically, the power rating of grid-tied converters are much lower than the one managed by the grid, they require synchronization tools and a coordinated performance with the rest of VSCs. These control structures are hierarchically organized [2.83, 2.84] and have been illustrated in Fig. 2.25.

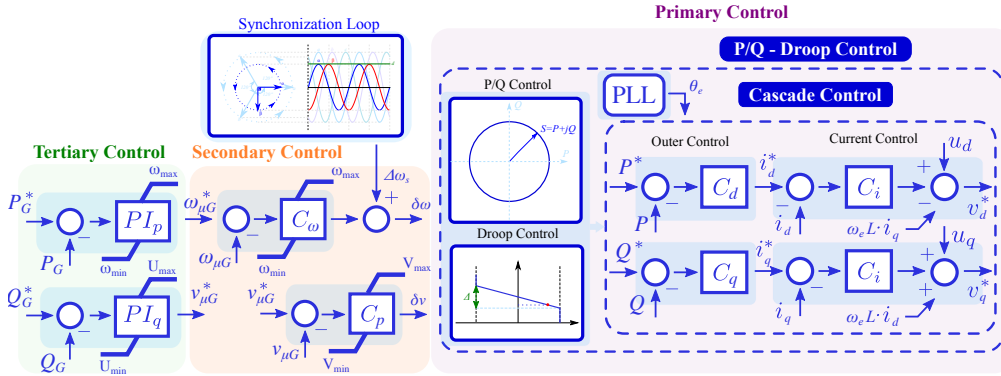


**Figure 2.25:** Hierarchical control of an AC microgrid according to [2.83]

According to the disposition shown in Fig. 2.25, there are three control layers, where the outer layer is responsible to provide the frequency and voltage references for the microgrid control, based on the power flow with the main grid and with some limitations that are established based on the compensation limits of the microgrid. The synchronization control provides an additional reference tracking to continuously stay synchronized with the grid. The next layer implements a droop or P/Q control in order to determine the power injection of the

VSC. This loop works as a coordination tool between the VSCs present in the microgrid. The mode of operation depends on the microgrid status: droop control for islanded mode and P/Q for grid connected mode. The resulting references are feeding the cascade control responsible to establish the PWM signal of the VSC. In the following section a more detailed analysis of the control loops is described.

## 2.6.1 Grid Synchronization

Traditionally, voltage and frequency magnitudes were set by large synchronous generators. The grid frequency was proportional to the angular speed of these electrical machines so, once the generator was synchronized, there was no need of additional considerations, being robust enough to deal with short-time contingencies. However, grid-tied converters do not offer the same inertial characteristic as synchronous generators, being strongly affected by the numerous eventualities that present electrical grids, i.e. load connections, atmospheric events or human errors in the operation of electrical equipment. This situation makes it necessary to deploy additional synchronization methods responsible to estimate, at any instant, the phase and magnitude of the fundamental voltage component at the PCC, to assure a satisfactory performance of the converter.

Voltage positive sequence detection is a crucial aspect of the power converter synchronization and subsequent operation [2.85–2.87]. The most popular synchronization techniques are described in the following subsections.

### 2.6.1.1 Phase-Locked Loop

Time-domain synchronization techniques are based on some kind of oscillatory circuit (Voltage-Controlled Oscillator - VCO) that varies until it matches the oscillating input signal achieving in-phase behavior [2.88–2.90]. The most common approach for this technique is known as Phase-Locked Loop (PLL), which main advantage lies on the fact that does not require any initial frequency acquisition from the input signal.

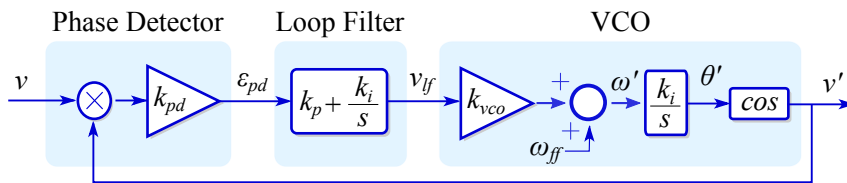


Figure 2.26: PLL structure, [2.85]

Fig. 2.26 presents a generic block diagram for a basic scheme of a PLL. The phase detector provides a DC error output as a result of the phase difference between the input and feedback signal. The loop filter is generally a low-pass filter in charge of eliminating the high frequency components that may affect the correct performance of the VCO. The VCO output provides a signal with a frequency proportional or equal to the input reference [2.85, 2.88]. The feed-forward term,  $\omega_{ff}$ , corresponds to the pre-set grid frequency signal, and can be included to enhance control dynamics. Phase detectors implementation may be done by different

approaches, it exist a huge number of contributions in literature [2.85–2.87, 2.89–2.91]. The one shown in Fig. 2.26 uses a multiplier-based phase detector that feeds a PI controller and an integrator with a cosine function acting as VCO. This configuration is able to track the input signal without error in steady-state.

### 2.6.1.2 Synchronization of Three-Phase Power Converters under Unbalanced Conditions

In the case of a three-phase system, a PLL structure may be connected at each phase. However this approach might require coordinated algorithms resulting in computational burden compared with a single PLL-structure [2.92].

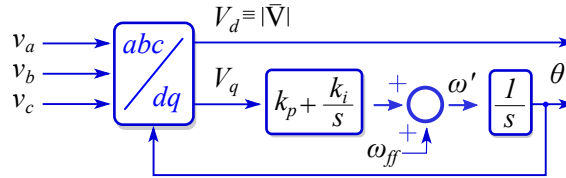


Figure 2.27: Basic  $dq$  PLL structure

A suitable solution to avoid this inconvenience is to take advantage of the *Park* transformation, as explained in Appendix C. This concept is shown in Fig. 2.27, where a three-phase system is transformed into two quadrature signals aligned with the phase angle of the grid space voltage vector. For a three-phase balanced system, the  $v_d$  component equals the grid space voltage vector whereas the  $v_q$  component equals zero. Taking advantage of this fact, a PI controller is fed with the  $v_q$  component, forcing it to zero, and thus, the frequency of the resulting signal replicates grid frequency.

While Fig. 2.27 considers an ideal grid voltage, most LV grids presents different levels of voltage distortion, what hinders angle identification. A combination of the *Park* transformation and two Second Order Generalized Integrator (SOGI), used to isolate the positive sequence voltage component, constitutes a flexible solution to cope with these obstacles. This SOGI structure consists of a second-order active filter, based on a sinusoidal adaptive filter, acting as an amplitude integrator for sinusoidal inputs. The whole system behaves as an adaptive band-pass filter, at a specific frequency. It provides two outputs,  $v$  and  $qv$ , shifted 90 deg. between each other, as shown in Fig. 2.28. This configuration allows the use of the synchronization algorithm as a sequence component identifier under generic grid operation conditions [2.93], which allows an independent isolation of the positive and negative voltage sequences under polluted or distorted grid conditions.

## 2.6.2 Control Modes

The DGs integrated into a microgrid may operate in connecting or islanding mode respect to the grid. In the former case, frequency and voltage are imposed by the grid itself and the VSCs are usually operated under P/Q control. In the second case, the frequency and voltage have to be established by one of the generation units, being the rest of them under some kind of coordinated strategies, which mainly are based on droop control schemes.

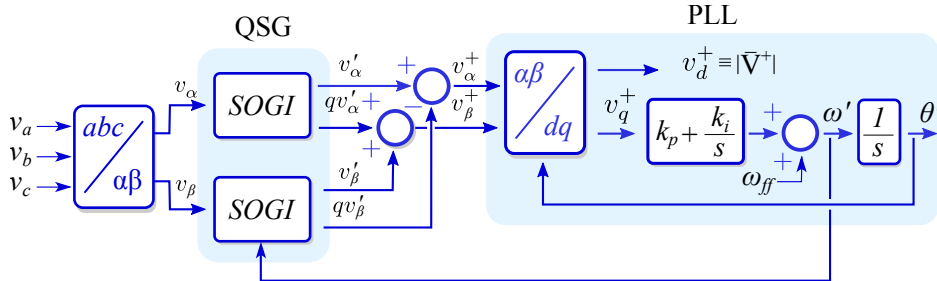


**Figure 2.28:** A dual SOGI is used as a Quadrature Signal Structure (QSS) to serve as an input to the basic  $dq$  PLL [2.94].

### 2.6.2.1 P/Q Control

Under P/Q control strategy, frequency and voltage are treated as given variables imposed by the grid, being the VSC only responsible for power regulation. This strategy implies a higher control layer which commands references to be followed. The control architecture for the P/Q strategy is based on the cascade control shown in Section 2.5.3.1. It is based on the VCO strategy, in which the outer loop is responsible of the control of active and reactive power whereas an inner adopts current control, Fig. 2.29. Current reference calculations are obtained from (2.15) and (2.16).

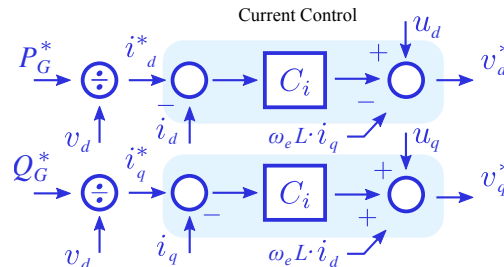


**Figure 2.29:** P/Q control structure

This mode of operation is implemented in grid-feeding converters and cannot be used under islanding conditions if an additional source is not responsible to set the voltage and frequency of the system.

### 2.6.2.2 Droop Control

All the converters in a microgrid must operate under coordinated strategies, achieving parallel operation and load sharing. One of the most popular solutions used to operate in this way, without having to resort to communication links, is based on the droop control, Fig. 2.30. This is a widespread strategy in industry, since it overcomes the physical location limitations, enhancing the microgrid performance. This control technique emulates the behaviour of traditional synchronous generators which reduce their frequencies in response

to increments of the power demand. Similarly, a droop in the voltage amplitude is used to ensure reactive power sharing. To achieve this, the controller makes tight adjustments in the converter output-voltage frequency and amplitude by using local measurements.

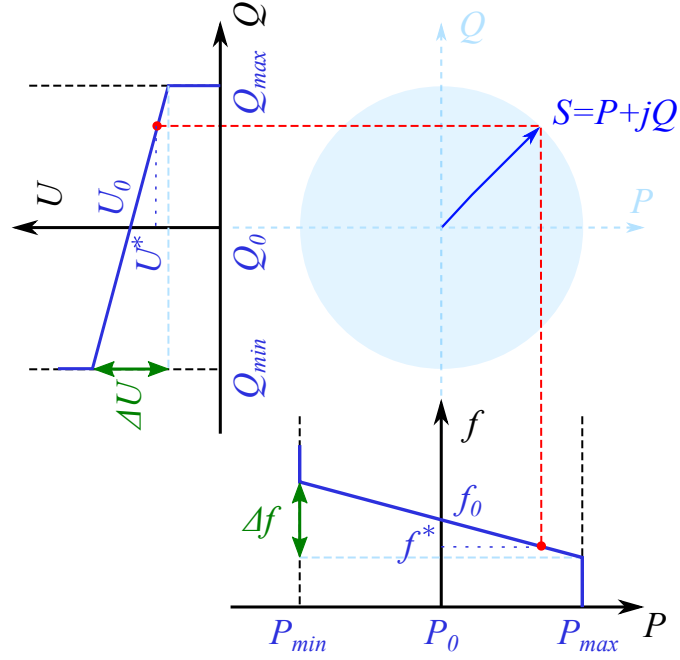


Figure 2.30: Droop control scheme, [2.84]

The conventional droop control is based on the power flow theory in an AC system, which states that the flow of active and reactive power between two sources can be controlled by adjusting the power angle and the voltage magnitude. Consider the system represented in Fig. 2.20, where  $V$  is the voltage from the power converter,  $U$  is the grid voltage,  $Z_d$  is the line impedance and  $\delta$  is the phase angle between both voltage sources. The power delivered into the grid by the voltage source that represents the power converter can be expressed according to (2.19).

$$\begin{aligned} S &= P + jQ = V \cdot I^* \\ &= V \cdot \left[ \frac{V - (U \cos(-\delta) + jU \sin(-\delta))}{jX_d + R_d} \right]^* \end{aligned} \quad (2.19)$$

Gathering real and imaginary terms from (2.19), it is possible to achieve the expressions for the active and reactive power, flowing from the power converter to the grid, according to (2.20) and (2.21).

$$P = \frac{V}{R_d^2 + X_d^2} [R_d \cdot (V - U \cos \delta) + X_d \cdot U \sin \delta] \quad (2.20)$$

$$Q = \frac{V}{R_d^2 + X_d^2} [X_d \cdot (V - U \cos \delta) - R_d \cdot U \sin \delta] \quad (2.21)$$

The droop regulation methods are performed by grid-supporting converters to maintain voltage and frequency within technical margins.

In Fig. 2.20, a grid-tied converter is represented as a controllable voltage source interconnected with the grid by a given line impedance, which depends on the characteristics of the cable. It has been proved that grid impedance can affect the performance of the droop control, [2.81, 2.95]. Based on the grid impedance characteristics, three different scenarios can be analysed:

- *Inductive grid:* In the case of medium and high voltage applications, the grid inductive term is much higher than the resistive one, so it can be assumed as mainly inductive. Additionally, if the phase angle,  $\delta$ , is small, then  $\sin(\delta) \approx \delta$  and  $\cos(\delta) \approx 1$ . Thus, (2.20) and (2.21) can be expressed as  $P \approx \frac{VU}{X_d}\delta$  and  $Q \approx \frac{V^2 - VU}{X_d}$ . Based on this simplification, the delivery of active power depends on  $\delta$  and the reactive power depends on the output voltage magnitude of  $V$ . Therefore, (2.22), (2.23) establishes a droop control expression for inductive lines

$$f^* - f_0 = -k_p(P_0 - P) \quad (2.22)$$

$$U^* - U_0 = -k_q(Q_0 - Q) \quad (2.23)$$

where,  $f^* - f_0$  and  $U^* - U_0$  represent the grid frequency and voltage deviations,  $(P - P_0)$  and  $(Q - Q_0)$  represent the active and reactive power deviations and  $k_p$  and  $k_q$  represent the slope curve characteristic of each control scheme. These parameters can be designed as  $k_p = \frac{\Delta f}{P_{max}}$  and  $k_q = \frac{\Delta U}{2Q_{max}}$ , where  $\Delta f$  and  $\Delta U$  are the maximum frequency and voltage variation allowed and  $P_{max}$  and  $Q_{max}$  are the maximum active and reactive power delivered by the converter [2.84]. These control schemes are illustrated in Fig. 2.30.

- *Resistive grid:* Previous assumptions are not valid in the case of LV systems, where the grid characteristic is predominantly resistive. According to this, and assuming as well, small variations of the power angle,  $\delta$ , the active and reactive power expressions lead to  $P \approx \frac{V}{R_d}(V - U)$  and  $Q \approx -\frac{VU}{R_d}\delta$ . As it appears from the expressions, voltage regulation depends mainly on the active power,  $P$ , and the frequency on the reactive power,  $Q$ . Consequently the droop expressions can be synthesized as follows:

$$U^* - U_0 = -k_p(P - P_0) \quad (2.24)$$

$$f^* - f_0 = -k_q(Q - Q_0) \quad (2.25)$$

- *Generic grid:* In a general case where both  $X_d$  and  $R_d$  are considered, authors in [2.96] proposed the used of an orthogonal linear rotational transformation matrix, to modify the active and reactive powers, according to (2.26).

$$\begin{bmatrix} P' \\ Q' \end{bmatrix} = \begin{bmatrix} \sin \theta & -\cos \theta \\ \cos \theta & \sin \theta \end{bmatrix} \cdot \begin{bmatrix} P \\ Q \end{bmatrix} = \begin{bmatrix} \frac{X_d}{Z_d} & -\frac{R_d}{Z_d} \\ \frac{R_d}{Z_d} & \frac{X_d}{Z_d} \end{bmatrix} \cdot \begin{bmatrix} P \\ Q \end{bmatrix} \quad (2.26)$$

If (2.26) is applied on (2.20) and (2.21), the expression for the power angle leads to  $\delta = \arcsin \frac{ZP'}{VU}$  and the voltage variation into  $V - U \cos \delta = \frac{ZQ'}{V}$ . Considering small  $\delta$

variations, it can be assumed that power angle is affected only by  $P'$  and voltage,  $V$ , is controlled by  $Q'$ . Hence, the droop regulation becomes (2.27) and (2.28).

$$f^* - f_0 = -k_p(P' - P'_0) = -k_p \frac{X_d}{Z_d}(P - P_0) + k_p \frac{R_d}{Z_d}(Q - Q_0) \quad (2.27)$$

$$V^* - V_0 = -k_q(Q' - Q'_0) = -k_q \frac{R_d}{Z_d}(P - P_0) + k_q \frac{X_d}{Z_d}(Q - Q_0) \quad (2.28)$$

A particular case of the droop technique is the reverse droop control. It consists in tracing the predefined droop characteristic by measuring the voltage and frequency of the grid. Power references vary depending on the errors of voltage and frequency. This method is particularly interesting for grid-feeding converters operated in current control mode, since the active and reactive power is directly regulated by the inner current loop [2.97, 2.98].

### 2.6.2.3 Enhanced Model-based Control Systems

Model-based strategies are based on the concept of system emulation by digital control systems. The underpinning idea is to replicate, by using a digital twin, the behaviour of some critical features and elements of power systems: inertia, impedance and synchronous generators.

#### Virtual Inertia

The concept of virtual inertia has been recently developed in the context of distributed generation and microgrid topologies. Traditionally, large conventional synchronous generators aim to maintain system stability through the inertia of their rotating components, turning slower when frequency drops and releasing the kinetic energy stored in the rotor to compensate frequency deviations. However, in the context of microgrids, stability becomes a challenging task, where the predominant presence of power converters makes the systems more sensitive to disturbances [2.99, 2.100].

The virtual inertia is imitated using an advanced control of the converter and energy storage system, enhancing system inertia, damping properties, and frequency stability. At this matter, within renewable energy technology, wind turbines can provide supportive capabilities to enhance the microgrid inertia. Virtual inertia solutions have been proposed based on the maximum power point tracking (MPPT) optimization [2.101, 2.102].

Additional solutions in the matter of enforcing system stability have appeared in the recent years, as the progress along the trajectory of renewable integration continues. Some of them are addressed in the next sections.

#### Virtual Impedance

Some of these solutions are based on the inclusion of a virtual impedance loop, consisting in the addition of an artificial impedance at the output of the converter. This solution mitigates the stability issues resulting from sudden changes in the microgrid. Moreover, it improves the reactive power sharing between parallel converters as well as the performance of the droop control in LV grids with a mainly resistive profile. In this type of networks, a mismatching

in the grid impedance estimation results in an inefficient power sharing among the droop controlled distributed generators [2.81, 2.83, 2.84].

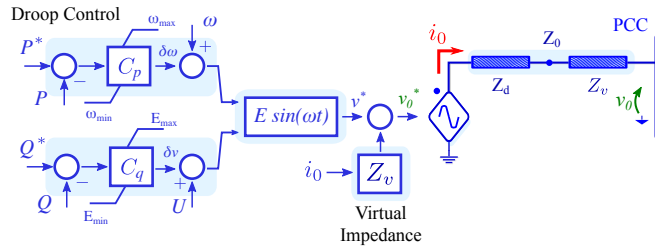


**Figure 2.31:** Equivalent circuit of a power converter with the virtual impedance loop.

The purpose of the virtual impedance is to emulate the series impedance of a synchronous generator. It can be selected arbitrary, but usually, it is chosen so as to turn the mainly resistive characteristic of LV grids into inductive. Fig. 2.31 includes a simplified schematic of a power converter connected to the grid incorporating a virtual impedance loop. The virtual impedance modifies the power converter output voltage reference,  $v_0^*$ , by subtracting the virtual voltage drop across the virtual impedance  $Z_v \cdot i_0$  from the reference value originally provided by the droop equations,  $v^*$ . Since  $Z_v$  is an arbitrary variable, selected according to the converter nominal power, it allows to use the converter impedance output as another control variable, allowing additional feasibilities like harmonic current sharing between converters, [2.83].

## Virtual Synchronous Generator

This approach consists in adding virtual inertia to the system by emulating the behaviour of a synchronous generator against active power changes and, consequently, frequency fluctuations. Multiple contributions and different approaches on this subject can be found in literature, depending on the accuracy of the model. However, the emulation of the oscillatory characteristic and damping of the electromechanical oscillation factors are common features in every implementation. The virtual inertia is modelled within the converter controller. This strategy implies the presence of an additional power source which can feed that inertia, i.e. large DC-link, a battery storage system, a rotating inertia such as the one provided by a wind generator, etc. [2.99, 2.103].

In Fig. 2.32, a simplified schematic of a power converter with a virtual synchronous generator control is shown. The power source connected to the power converter represents the primary source used to feed the virtual inertia. The damping algorithm is fed with the active power reference,  $\omega_n$  represents the nominal frequency of the system and  $\omega_m$  is the equivalent rotor speed. The damping torque block is fed with  $\omega_m$  and  $\omega_x$  which represents the actual grid frequency resulting from an additional synchronization block. Usually, the DC bus is designed not to add significant dynamics to the achieved virtual dynamics. However, in some cases, voltage control can be also included in the control loop, generating the DC-link voltage reference based on the internal frequency of the virtual synchronous generator.

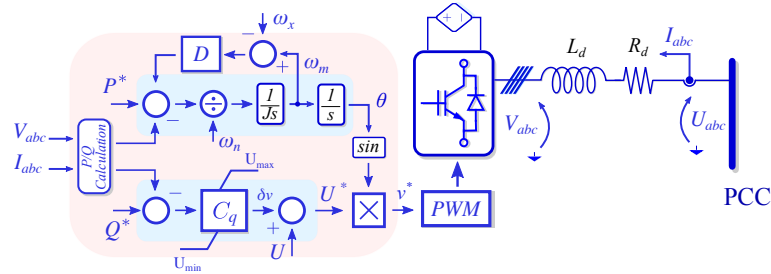


**Figure 2.32:** Simplified representation of a power converter connected to the PCC with a virtual synchronous generator control

### 2.6.2.4 Unbalance Compensation

The large number of unbalanced and non-linear loads connected in microgrid, and the presence of unbalanced voltage, resulted from grid faults, contribute to distort the PQ of the microgrid. Controlling the AC voltages under such conditions becomes a challenging task for grid-tied converters, which must be kept normally operating and connected to the system. Hence, grid-tied converters must be able to provide controllability in both positive and negative sequences. One possible solution might consist in the use of a single current control responsible for compensating both sequences [2.104]. However, this approach implies the presence of a component at double of the main frequency, requiring for the compensation to extend the control bandwidth, which is not always possible. Generally, the most common solution is to establish a dual-current controller structure for each sequence [2.18, 2.105–2.108]. This is done by synchronizing each sequence into the positive and the negative synchronous reference frame, respectively. Thus, allows to the negative-sequence current to be controlled completely as a DC signal. Thus, similar cascade-control structures can be implemented for both loops, without the need of increasing the control bandwidth.

Alternatively to the dual-current controller structure, solutions implemented within the  $\alpha\beta$  stationary-reference frame are also proposed [2.109, 2.110]. For such cases, resonant controllers are used instead of the traditional PI ones, since this type of controllers are able to track non-dc signals. However, the resonant filter has drastic change of phase angle around the resonant frequencies. As a result, even a slight variation of resonant frequencies may introduce substantial phase errors in the extracted signals [2.110].

The negative-sequence compensation can be achieved by using the surplus capacity of the inverters to balance the voltage of the microgrid. However, this extra capacity usually brings together technical issues related either to distorted load currents or power oscillations. Operational limits of the grid-tied converter are studied in [2.108, 2.111], where control strategies, based on the instantaneous power theory, are proposed. These strategies take advantage of the flexibility that alternative configurations, based on the use of an active neutral, can offer.

## 2.7 Grid Impedance Estimation

Power Quality and grid impedance are two terms highly related between each other. The large increase of DGUs along the medium and low voltage grid has triggered the evolution to a new grid scenario, more flexible and efficient. However, the integration of such units might jeopardize stability margins, becoming a major challenge.

Power converters are a proved solution to accommodate DGUs and to maintain stability margins. The stability of inverter-based solutions lies on the Nyquist stability criterion, which is proportional to the grid admittance. This fact is not contingent, since high grid impedance might destabilize converter control loops, leading to harmonic resonance [2.112, 2.113] or degrade converter performance due to an incorrect pre-estimation of the grid impedance. In the same way, interfacing a VSC with the AC-Grid requires a very precise design of the current controller in order to fulfill the requirements of the network. For this reason it is critical to have a deep knowledge of the dynamic model which links the converter output voltage with the resulting grid current. These dynamics are affected by the load connections, the grid topology, the type of interconnection filter, e.g. L, LC, LCL, and the disturbance decoupling capability depending on the number and the position of the voltage and current sensors, which are required in some active damping strategies to maintain stability margins [2.113, 2.114].

Hence, grid impedance identification is a major issue and may be considered as a tool for assessing and improving stability margins and consequently, power quality. Impedance estimation techniques are devoted for two major applications: anti-islanding detection and DGU integration.

- **Anti-islanding:** Islanding is considered as the problem caused by an uninterrupted operation of a grid-connected converter after its disconnection from the grid. Fig. 2.33 illustrates the concept of islanding, where Distributed Energy Resources (DER) are interconnected with the AC-Grid by a power converter. At some point the distributed generator is disconnected from the AC-Grid, but it continues generating energy. This situation may be particularly dangerous if the power injection of the converter matches the power demand of the local loads. Grid standards are restrictive in this field: the system has to be fast enough to detect the islanding situation and avoid inverter operation within a short time.

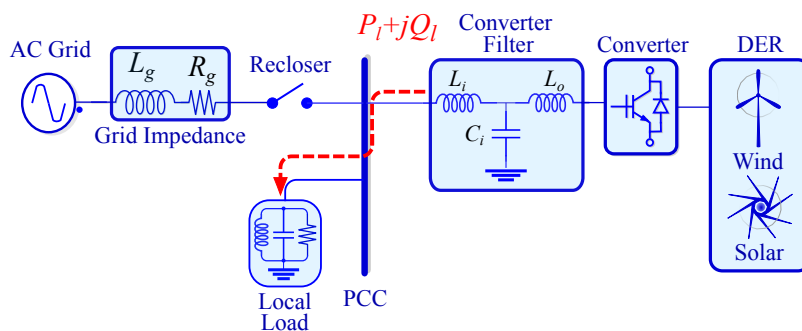
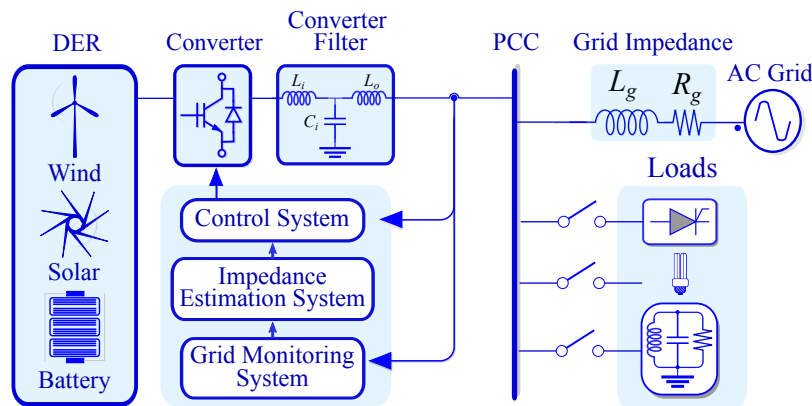


Figure 2.33: Islanding Operation.

- Adaptive Control for Grid Converters:** This type of control takes into account the stability problems that can result from improper assumptions on the value of grid impedance. The adequate performance of the converter is linked with the impedance value of the system. The current controller parameters are tuned based on the converter filter impedance and an assumed value for the impedance of the grid side. Consequently, large variations of the grid impedance may contribute to the instability of the converter. Moreover, the increased penetration of the DER modifies the value of the grid impedance, mainly due to the grid interface filters. Fig. 2.34 illustrates the concept of a varying equivalent impedance at the PCC caused by connection and disconnection of local loads. The use of an online converter-based impedance estimation algorithm, allows to adapt control parameters based on the grid conditions, thus providing a better dynamic response.



**Figure 2.34:** Adaptive control of the grid-connected inverter

Grid impedance may change during normal operating conditions or derived from an abnormal condition, as already illustrated. Estimation techniques have to be fast enough to determine the impedance at every instant. However, grid impedance measurement has to cope with several difficulties: non-stationary power system voltages and currents, time-domain impedance variation, impedance coupling between phases, noise and non-linearity.

The majority of the techniques in literature can be classified under the umbrella of invasive and non-invasive methods. Non-invasive approaches use intrinsic conditions of the grid, such as load variations or grid transients, to perform grid estimation. Generally, these techniques are easy to implement and do not require the injection of additional signals into the grid. Thus, they do not have any negative impact on PQ. However, although these techniques are easy to implement, they present larger Non-Detection Zones (NDZ) than invasive techniques.

On the contrary, invasive methods are based on the inclusion of additional devices or signals into the grid, resulting in small perturbations, which are the key-tool used to obtain information of the system. This type of solutions provide better accuracy and their NDZ is much smaller than that of non-invasive methods; however, their performances might impact negatively on the Power Quality of the system. At any rate, literature has proved that this second group presents a larger field of possibilities, which has become the main reason to select invasive techniques as a key-point in this work.

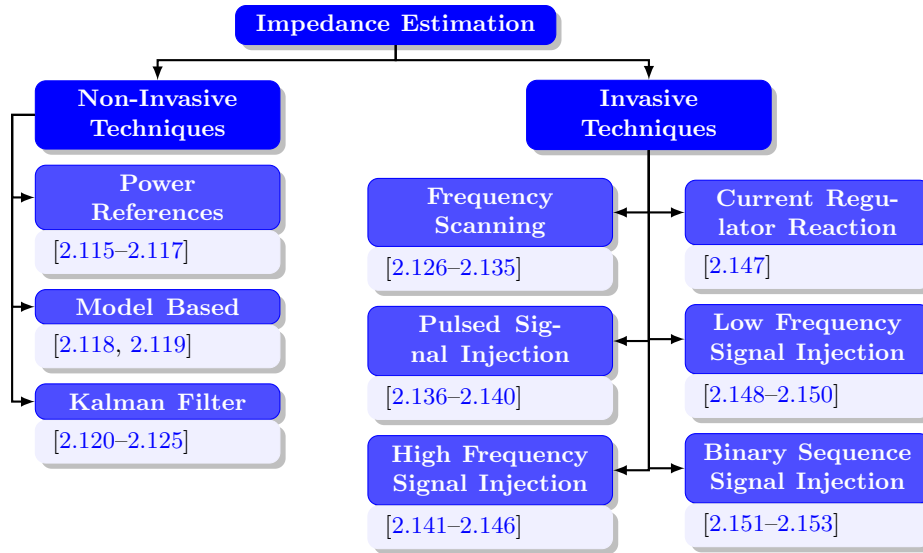


Figure 2.35: Impedance estimation methods.

Additionally, the fast evolution of communications during last decades has triggered the appearance of a considerable number of grid-impedance estimation solutions based on communication systems and data metering. The evolution of smart meters has endowed them with capabilities that goes beyond the simple measurement of power demand, allowing these devices to gather data from low and medium voltage lines, including information about unbalance levels and harmonic distortion. However, this technology requires a deep deployment of communication infrastructure not always present in LV systems.

Figure 2.35 shows a classification based on the grounds of the different approaches used by the estimation techniques.

### 2.7.1 Non-invasive Techniques

As stated above, non-invasive techniques are based on grid monitoring and on the analysis of the characteristic signals already present in the system. These techniques are easy to implement and do not require extra devices nor additional signals that might distort the operation point. As a consequence, there is a vast number of contributions in this field.

#### 2.7.1.1 Power References

This group includes those solutions that base the estimation on the response of the system to power variations. These variations can be either implemented at converter side, as power references steps, or as load system fluctuations.

A method for short-circuit impedance estimation, based on the analysis of the equivalent Thevenin circuit of the power system, is presented in [2.154]. The system proves to work under

real conditions and for different voltage transmission levels but neither transient conditions nor real time measurements are considered, which makes it an invalid solution to cope with short-time disturbances at low and medium voltage levels.

Authors in [2.115] proposed a methodology based on the analysis of the response of the grid to the injection of a varying P and Q reference signal. The operating principle is shown in Fig. 2.36 and consists in the analysis of two consecutive operating points, which are supposed to have the same grid conditions, avoiding in this way to measure the voltage at the grid side. However, the validity of the method has been proved for a specific converter topology and only for single-phase systems. A similar approach is presented in [2.116], where a set of different P and Q references are set to obtain a linear regression line with the impedance value of the system. The method proves to work under real conditions; however, due to the computational burden, it cannot be considered for online estimation. Unfortunately, both methods are affected by the fact that, varying the operating conditions, alters the voltage and grid currents from where the impedance calculation is performed.

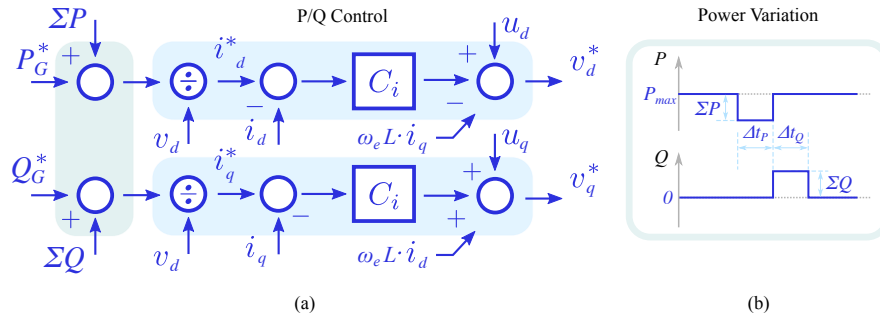


**Figure 2.36:** Principle of variation of active and reactive power according [2.115]. (a) Control schematic implemented within a P/Q control loop; (b) Power variation of active and reactive power.

A similar approach, developed under the synchronous reference frame, is presented in [2.117]. The grid impedance is estimated by the connection and disconnection of resistive and capacitive loads. The resistive load connection implies an active power step, meanwhile the disconnection of a capacitive load is reflected as a reactive power step. Experimental tests are presented in this work; however, the performance of the algorithm is based on the analysis of the response of the system to the change of the conditions previously described. This implies that the system must be kept under steady state conditions in order to compare two operating points before and after the switching event.

### 2.7.1.2 Model Based

The response of a well-known model might be used to understand the current operating conditions or even to estimate the parameters of the system, in case of variations. Solutions based on this idea are included in this group.

Authors in [2.118] present a model based solution based on the excitation of an LCL-filter used to interconnect the power converter with the grid. It is shown that a controlled excitation of the filter may provide information about the grid impedance. However, the size of the grid-side inductor may affect the location of the resonant peaks of the filter, interacting the two

poles between each other and jeopardizing the capability of the impedance estimation. Fig. 2.37 shows the effect of increasing the grid inductance. The positive peaks corresponds to the resonance frequency of the whole system and the negative ones correspond to the double zero of the transfer function. Increasing the magnitude of the grid-side inductance, the resonance-peak can be displaced at higher frequencies and fewer possibilities of interaction between both inductances can be expected. However, the ratio between inductances has to be a trade-off between the power dissipation and the harmonic pollution that might be injected.

In [2.119] an experimentally supported method is proposed for estimating the equivalent inductance and resistance of the grid. It is based on an iterative process which compares the responses of the actual current control loop and the response of a specific plant. The experimental tests did not consider neither unbalance conditions nor sudden impedance variations.

### 2.7.1.3 Kalman Filter

Kalman filter based solutions are under the umbrella of non-invasive techniques.

In [2.120] a grid estimation method is proposed based on the identification of the harmonics in time-domain. Kalman filters are used to track the phase and the amplitude of the harmonics using the state-space form. This study is only supported by simulations and the validation of the method is not proved in case of frequency variations or transients. In [2.121] a Kalman filter working in parallel with an observer is proposed to perform the estimation. The estimation is carried out on a power converter interconnected through an LCL-filter. The model is experimentally supported, but the estimation algorithm requires a fine tuning of the Kalman filter, which implies trial and error tests and makes it not a feasible solution for such kind of systems where connection and disconnection of loads are constantly present.

In [2.122] a similar approach is presented. The estimated coefficients are updated online by using an adaptive linear neuron (ADALINE) algorithm. This method requires measurements of grid side current and voltages, but in any case, it is only demonstrated under balanced conditions. In [2.123] an adaptive current control, based on the uncertainty of grid parameters, is proposed. Grid impedance parameters are obtained based on Lyapunov theory. Simulation and experimental results support the model; however, the system is not evaluated under unbalance conditions. A similar solution based on virtual-flux is presented in [2.124]. Unfortunately, this estimation algorithm is highly dependent on the switching state, which limits

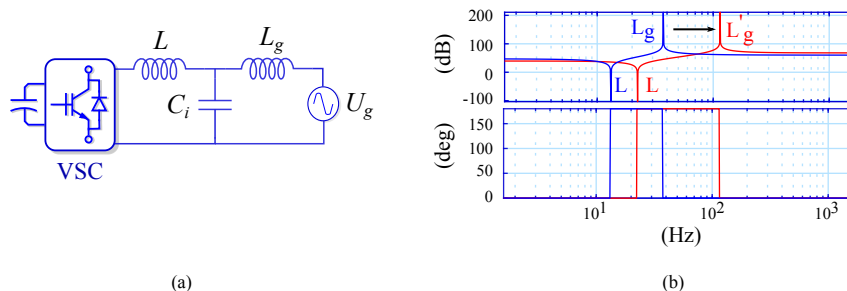


**Figure 2.37:** (a) Grid-tied converter with an LCL-filter interconnecting the grid; (b) Transfer function of the LCL filter for two different cases of inductance and resonant location of the model

its operation at steady state conditions.

In [2.125], grid inductance is estimated using two consecutive samples of the grid current within a switching period. The estimation method is based on the discrete-time model at grid frequency and, as recognized by the authors, the method is only valid for the inductive component. Moreover, the operation is only demonstrated for two different inductance values and unbalanced conditions are not considered.

The major limitation of non-invasive techniques lies in the uncertainty that these methods reveal under stationary conditions when local generation meets load demand. Under such situations, these methods fail to provide the expected accuracy. Invasive techniques may reduce the uncertainty zone, showing some benefits over the technologies described in this section. However, they have to face other stability limitations.

## 2.7.2 Invasive Techniques

This group gathers solutions which base the estimation either on the data resulting from extra devices installed in the system or from the use of additional signals, which are independent from the grid operation requirements. In the majority of cases, these signals are seen as disturbances by the system; however, its response to these interferences is precisely the source of information used to estimate the value of grid impedance. The flexibility and wide range of operation of these solutions have made invasive techniques the most commonly used methods nowadays.

### 2.7.2.1 Frequency Scanning

The estimation method of these family of solutions relies on the analysis of grid frequency. Most of the solutions included in this group require additional devices either to perform the estimation or to gather the data. Solutions as the ones presented in [2.126, 2.127] base the estimation on spectrum analysis performed by an additional device connected at the PCC. With this aim, a signal is injected at a specific frequency and the spectrum of the system response is subjected to an FFT analysis within the range 50 Hz to 10 kHz. A similar solution is presented in [2.128] but, in this case, the signal injection is performed by a dedicated converter which induce a voltage transient and, later on, analyses the FFT of the resultant current. On the other hand, the solution in [2.129] bases the estimation on an iterative process which requires the injection of consecutive signals at different frequencies to build up the impedance matrix of the system and determine an impedance map of the grid. This solution is proved to work under unbalanced conditions and experimental results are presented. However, it operates under the assumption that the impedance of the line is kept constant during the measurement process, which makes the model blind to transient conditions, and thus, disqualifying it for online impedance estimation.

The aforementioned solutions are worthy for systems which require a better understanding of the harmonic content of the grid, such as high power applications with an important content of high frequency harmonics. However, these solutions are not suitable for low power applications due to cost concerns.

In [2.130], a solution based on shunt current injection is proposed. In this case, the authors determine the maximum current to be injected based on the Nyquist stability criterion.

According to the ratio between current and voltage, it is possible to determine the impedance value of the system. However, this approach presents as an additional drawback that the stability region of the system is affected by load changes, which implies a reduction of the maximum current to inject according to the method and, consequently, a deprecation of the estimation.

The technique proposed in [2.131] consists in a steady-state method that injects a non-characteristic harmonic current into the network and records the voltage change response. Fourier analysis is used to process the results at the frequency of the injected harmonic. The interharmonic current is injected from a PV inverter at a frequency close to the grid main one. Assuming impedance terms are quite similar in both frequencies, the further Fourier analysis over the specific harmonic allows to estimate a close value of the grid impedance. Thus, additional injections are required to correct the initial estimation and obtain a more precise term for the grid impedance.

A technique for grid-tied inverters is presented in [2.132]. In this method, a disturbance signal is injected into the grid before the interconnection of the converter, and thus, the grid-side inductance is determined at different operating points. The extracted information is used to tune the deadbeat current controller to ensure stability and optimize the performance. Similar approaches are presented in [2.133–2.135]; however, these methods employ the error as an approximation to adapt system parameter uncertainty, which results in a less efficient performance. In general, these solutions prove to be inefficient when the power network includes capacitive components as may be the case of capacitor banks.

All the solutions in this group present limitations due to the amplitude of field measurements, derived from a conflict between the accuracy of the solution and the acceptable disturbing signal level. Moreover, the accuracy of the solution is limited by non-stationary and time domain issues of the power system. Additionally, the use of extra devices to perform the estimation becomes a drawback, due to the space constraints or legal limitations that may take place at some locations, since it is not always possible to connect external devices at the vicinity of the PCC. These limitations have foster the use of other solutions based on inherited functionalities of the system or the control loop of the filter.

### 2.7.2.2 Pulsed Signal Injection (PSI)

These techniques based the estimation on the response of the system to a small signal injected from the converter side. These small signals, considered in the majority of the cases as small perturbations, are injected at different frequency ranges. Then, voltages and currents are measured and processed through Fourier transformation techniques to obtain the desired impedance or admittance over the frequency range of interest. Most of the methods presented in this section are widely spread in the electric motor industry for parameter estimation.

In most cases, the injection of current signals corresponds to a shunt topology while the injection of voltages follows a series connection. In [2.136], a single-phase current injection system is proposed in order to measure the  $dq$  model impedances of an AC power system. The single-phase current is injected between two of the ac-lines, requiring less power electronics devices and performing the measuring between two different frequencies, which avoids the necessity to align the measurements with the  $d$ - or  $q$ - axis. However, this method requires an additional converter to inject the shunt signal needed to perform the estimation. In [2.137], a similar approach, based on the injection of a signal, is proposed to perform the estimation

of the admittance of the grid. This proposal is based on a DG control in which the grid impedance is estimated from the response to the excitation of two pulses injected in the  $dq0$  reference frame. It bases the estimation on the stability criterion between the ratio of the grid admittance and the source impedance. Unfortunately, this criterion is not valid under weak grid conditions. In both contributions grid impedance changes are considered but not unbalance conditions neither the impact of increasing harmonic contents by the addition of distorted signals.

Authors in [2.138] proposed an online implementation of an impulse response analysis, implemented within a DSP, inside the control routine of a three-phase converter. The grid impedance is characterized by the positive- and negative-sequence components through the Discrete Fourier Transform (DFT), which is applied to each impulse response data set of the phase voltage and phase current. However, Fourier analysis is time consuming, which makes this method not well-suited to be applied in online implementations.

An analysis of the impedance-based stability criterion, as a method to derive the parameters of the adaptive control of a grid-tied converter, is presented in [2.139]. The estimation is used for a grid adaptive control application. The grid-connected converter analyses the impedance of the grid based on the injected pulses and the routine of the control system updates the value of the control parameters based on the variation of the impedance.

Authors in [2.140] have proposed a novel technique combining the pulsed-signal injection technique with observer solutions. A Luenberger observer controls the grid-side current and detect impedance deviations by monitoring current and voltage at the PCC. The estimation is performed based on a recursive least square algorithm fed with the response of the system to the injection of a pulse synchronized with the zero crossing of each three-phase voltages. When compared to other solutions, this method demonstrates a better performance in terms of a minimized impact in voltage distortion. This method has been experimentally tested and the authors claim that it is a valid solution for islanding detection, fault detection and adaptive control.

### 2.7.2.3 High Frequency Signal Injection (HFSI)

Similarly to the previous group, these technologies based the estimation on the analysis of the response of the system to the injection of a signal. However, in contrast to the previous methods, the signal is injected at a distant frequency from the grid one. Thus, interferences are avoided, which reduces the NDZ compared to the methods mentioned before.

Solutions, like the one presented in [2.141], are oriented to islanding detection by the identification of system impedance. The authors proposed the use of a VSC, already present in the microgrid, in order to inject a low-magnitude high frequency voltage signal. The impedance jump that occurs when the islanding operation arises is used to determine the disconnection instant. The method presents the limitation of high-frequency signal attenuation when various converters are exciting the microgrid and could be affected by the distortion. Moreover, the authors introduced a method to determine the impedance of the system based on the high frequency signal; however, the value of the impedance at 50 Hz is not calculated, since the inductive component of the equivalent impedance is frequency dependent.

Similar approaches are presented in [2.142, 2.143], where an interharmonic current signal is injected at the point of connection and the impedance is estimated based on the voltage

response at that frequency. Grid impedance, as function of frequency, is characterized by repeating the injection at different frequencies.

Other solutions present in literature implement the estimation algorithm by embedding the excitation signal within the internal control of a PV inverter. In [2.144], the authors propose a solution based on the analysis of the voltage drop caused by the injection of an interharmonic current through a converter. Similar approaches are presented in [2.145, 2.146], which analyze the system response to the signal injection by means of the Discrete Fourier Transform (DFT). All these solutions have to cope with the increased THD of the system. The same configuration but considering the presence of multiple inverters working in parallel is considered in [2.145]. This technique could also belong to the pulsed-signal excitation group, since the signal is injected repeatedly. However, it has been gathered within this group since the frequency of the excitation signal is 600 Hz. Authors proposed to inject the sinusoidal current harmonic at the voltage zero crossing instant, to mitigate the distortion effect, and then applying the DFT to the voltage and current signals to determine the impedance value. However, the reliability of this method is compromised by the physical limit in the number of inverters connected in parallel, which is established by the number of zero-crossing points during islanding detection as well as by the possible interferences between converters. Authors in [2.146] base the efficiency of the method in the reduction of the spectral leakage. With this aim, they adjust the window of the DFT analysis to a period proportional to the frequency of the injection and perform successive analysis by moving the DFT window. However, the frequency of the estimation signal is significantly below the bandwidth of the current control loop, which puzzles the performance of the method if a voltage signal is injected, since the current control react against it. Current injection is also considered; however, the performance under real conditions is not evaluated. Likewise, the performance of the method within a system with several converters working in parallel is not demonstrated, which might be a common situation in the case of a PV installation.

This strategy presents some intrinsic benefits, since at higher frequencies there is more spectral separation and signal isolation is easier than in other solutions. Moreover, the method can be easily implemented within the control routine of grid-tied converter. For this reason, it has been used in this work as a base to propose a new methodology for impedance estimation which will be described in Chapter 4.

#### 2.7.2.4 Current Regulator Reaction

Current regulator reaction techniques are found to be implemented both as non-invasive and invasive methods [2.145]. Lately, its use in applications including the simultaneous operation of parallel converters has received some attention [2.147, 2.155]. In those applications, the approach can be considered as mixed passive-active, considering one converter (master) performs a signal-injection while slave converters use the current regulation reaction as a passive detection mechanism.

Solutions in this field are oriented to islanding detection on specific systems such as the one described in [2.147], where multiple inverters work in parallel. In this proposal, a master converter injects a high-frequency signal into the grid. If an islanding condition arises, the current regulators of the slave converters react and their output voltage reflects the new operating condition. Thus, slave converters are able to determine the grid impedance at high

frequency based on the voltage output of the current regulator and the current at the output of the LCL filter, Fig. 2.38.

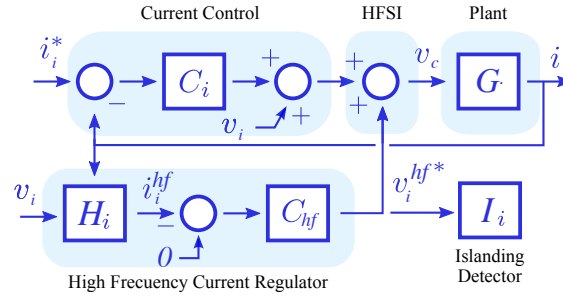


**Figure 2.38:** Control block diagram of the islanded solution proposed in [2.147]

Simulations and experimental results support the aforementioned work; however, although a value of the impedance at high frequency is obtained, the impedance at 50 Hz is not evaluated.

### 2.7.2.5 Low Frequency Signal Injection

These techniques are based on the same operating principles used by high frequency signal injection methods. However, in this case, the signal is injected at a much lower frequency range. In [2.148] a current-based estimation method is proposed. A short-term triangular current pulse is injected into the grid trying to emulate the effect of transient signals caused by capacitor banks at the transmission level. The excitation signal is fully controlled since it is injected by a power converter. The impedance is calculated using the DFT components of the voltage and current signals. The method is experimentally validated; however, to determine a valid impedance estimate, the grid should remain in steady-state during the signal injection and data acquisition processes.

A similar approach, based on an energized system and considering PV generation, is presented in [2.149]. The estimation method is based on the linearity between impedance terms at close frequencies and thus, deviation errors in the estimation of the impedance can be expected. This work offers a comparison between the magnitude of the injected current and the THD associated to that injection.

In [2.150], the authors proposed a method not based on the injection but on the perturbation of the current injected by a power converter. A train of pulses is modulated at the zero-crossing of the current injected by the converter. Beyond the simplicity of the injection pattern, this solution allows to obtain the impedance of the system directly and is not affected by the transients of the fundamental current, as it happens in the case of HFSI techniques. Although signal processing is more complicated, it does not require any additional filtering stage, since the estimation may be performed by a recursive least squares (RLS) algorithm. All these considerations allow to acknowledge this solution as an especially well-suited method for impedance estimation, and thus, it is taken as a basis for advanced proposals which are presented in the next chapters of this work.

### 2.7.2.6 Binary Sequence Signal Injection

These solutions are based on the injection of an excitation signal consisting of a train of pulses. It allows to obtain the system response which is further evaluated through Fourier Transform analysis.

The authors in [2.151] present a solution based on the injection of a multiperiod pseudo random binary signal (PRBS) to the control input of a power converter. The frequency response of the system can be derived by cross-correlation of the input signal and the sensed output signal. Simulation and experimental results prove that this solution might work satisfactorily at low frequency ranges and under balanced conditions. However, a larger processing time and a heavier computation burden is required in this case, in comparison with other family of impedance estimation methods.

A similar approach, based on a discrete-interval binary sequence, where the response of the train of pulses is evaluated by means of FFT analysis to obtain the frequency response of the system, is proposed in [2.152]. Contrary to previous solution, this method operates only on a specific frequency band, concentrating as much power as possible into the desired harmonic frequencies without increasing the signal time-domain amplitude. However, the solution has not been addressed within a weak grid environment and has not been tested under unbalanced conditions.

An update of the previous method has been presented by some of the same authors in [2.153]. The new method is based on a ternary-sequence injection, which improves the performance of the previous version against the effect on non-linear distortion and unbalance conditions, since the ternary-sequence injection does not present energy in the even-harmonics. However, this method still presents limitations at high frequency ranges, which limits the estimation for high frequency harmonics; furthermore, it retains the heavy computation burden of the previous version.

## 2.8 Conclusion

In this chapter, a wide and deep review of the main challenges faced by grid-tied converters within LV systems, as well as of the solutions available in literature to afford them, has been carried out. The main aspects addressed are summarized as follows:

- The chapter is opened with the definition of the microgrid paradigm and the new challenges brought up by the smart grid era. The increased presence of distributed resources and a massive connection of non-linear loads highlight the importance of grid-tied converters as a key-element in microgrid systems.
- The problems associated with the large presence of renewable sources and distributed generation at LV grids, such as bi-directional power flows, harmonic content and voltage fluctuations, lead to introduce the regulatory framework to set the operational constraints of grid-tied converters. A review of the power quality concept as well as the main regulatory key-aspects have been presented, highlighting the need of active compensation to cope with harmonic pollution and unbalance conditions.
- A review of the instantaneous power theories and its contributions to VSC control strategies have been reviewed to establish a reference frame for the discussion of the alternative modelling technique proposed in Chapter 3.

- 
- A deep review of the more extended passive and active filtering solutions have been addressed, with an especial emphasis on power converter topologies and, particularly, on the study of the voltage source converter.
  - This new environment requires that, some functionalities traditionally offered by large power plants and their synchronous generators, which are mainly related with stability issues, must be assumed now by distributed resources. A review of the main strategies to reduce the impact of lack of inertia in weak grids has been included. The need for control algorithms that emulate not only the static but also the dynamic behaviour of the synchronous generators, which can be addressed together with the inclusion of virtual inertia loops has been explained.
  - A review of the main hierarchical structures found in literature has been used to introduce the need of a coordinated behaviour between grid-tied converters, establishing roles within the microgrid and sharing tasks to deal with the aforementioned problems.
  - Modulation schemes and the regulatory framework have opened the door for an efficiency enhancement analysis by determining the operating range of converters used in distributed resources.
  - System identification has been presented as a key-factor to assess the system dynamic responses and stability margins and, consequently, for an active compensating and accommodation of power electronics-based loads. A deep review of impedance estimation techniques has been conducted. This study enables a starting point for the discussion on system identification that will be conducted in next chapters, where an impedance identification algorithm and estimation techniques based on a high frequency and pulsed signal injection are proposed.

## References

- [2.1] E. S. G. T. Platform, “Vision and strategy for europe’s electricity networks of the future,” European Commission, Tech. Rep., 2006.
- [2.2] H. Gu, X. Guo, D. Wang, and W. Wu, “Real-time grid impedance estimation technique for grid-connected power converters,” in *2012 IEEE International Symposium on Industrial Electronics*, May 2012, pp. 1621–1626.
- [2.3] “IEEE standard for interconnecting distributed resources with electric power systems,” *IEEE Std 1547-2003*, pp. 1–28, July 2003.
- [2.4] G. Pepermans, J. Driesen, D. Haeseldonckx, R. Belmans, and W. D’haeseleer, “Distributed generation: definition, benefits and issues,” *Energy Policy*, vol. 33, no. 6, pp. 787 – 798, 2005. [Online]. Available: <http://www.sciencedirect.com/science/article/pii/S0301421503003069>
- [2.5] M. H. Bollen, *Appendix C: Power Quality Definitions and Terminology*. IEEE, 2000. [Online]. Available: <https://ieeexplore.ieee.org/document/5271135>
- [2.6] I. Std. Ieee standards coordinating committee 22. [Online]. Available: <http://sites.ieee.org/scc-22/>
- [2.7] IEC-61000-1-1:1992, “Electromagnetic compatibility (emc), part 1: General, section 1: Application and interpretation of fundamental definitions and terms, iec-61000-1-1, 1992.” IEC, Tech. Rep., 1992.
- [2.8] IEC-61000-2-5:2017, “Electromagnetic compatibility (emc) - part 2-5: Environment - description and classification of electromagnetic environments,” IEC, Tech. Rep., 2017.
- [2.9] “Ieee recommended practice for monitoring electric power quality,” *IEEE Std 1159-2019 (Revision of IEEE Std 1159-2009)*, pp. 1–98, 2019.
- [2.10] F. C. D. L. Rosa, *Harmonic, Power Systems, and Smart Grids*, 2nd ed., L. Taylor & Francis Group, Ed. CRC Press, April 2015.
- [2.11] P. Kundur, N. J. Balu, and M. G. Lauby, *Power system stability and control*. McGraw-Hill, 1994.
- [2.12] P. Schavemaker and L. van der Sluis, *Electrical Power System Essentials*. Wiley, August 2017.
- [2.13] UNE-EN-50160:2010/A1:2015, “Voltage characteristics of electricity supplied by public distribution systems,” *UNE-EN-50160:2010/A1:2015*, 2015.
- [2.14] IEC-61000-2-2:2002, “Electromagnetic compatibility (emc)—part 2-2: Environment— compatibility levels for low-frequency conducted disturbances and signalling in public low-voltage power supply systems.” 2002.
- [2.15] IEC-61000-3-2:2018, “Electromagnetic compatibility (emc) - part 3-2: Limits - limits for harmonic current emissions (equipment input current below 16 a per phase),” IEC, Tech. Rep., 2018.
- [2.16] IEC-61000-3-12:2011, “Electromagnetic compatibility (emc) - part 3-12: Limits - limits for harmonic currents produced by equipment connected to public low-voltage systems with input current over 16 a and below 75 a per phase,” IEC, Tech. Rep., 2011.
- [2.17] “Ieee recommended practice and requirements for harmonic control in electric power systems,” *IEEE Std 519-2014 (Revision of IEEE Std 519-1992)*, pp. 1–29, 2014.
- [2.18] H. Akagi, Y. Kanazawa, and A. Nabae, “Instantaneous reactive power compensators comprising switching devices without energy storage components,” *IEEE Transac-*

- tions on Industry Applications*, vol. IA-20, no. 3, pp. 625–630, 1984.
- [2.19] M. A. Hirofumi Akagi, Edson Hirokazu Watanabe, *Instantaneous Power Theory and Applications to Power Conditioning*. Wiley-IEEE Press, March 2007.
- [2.20] Fang Zheng Peng, G. W. Ott, and D. J. Adams, “Harmonic and reactive power compensation based on the generalized instantaneous reactive power theory for three-phase four-wire systems,” *IEEE Transactions on Power Electronics*, vol. 13, no. 6, pp. 1174–1181, Nov 1998.
- [2.21] R. S. Herrera and P. Salmeron, “Instantaneous reactive power theory: A comparative evaluation of different formulations,” *IEEE Transactions on Power Delivery*, vol. 22, no. 1, pp. 595–604, 2007.
- [2.22] J. Dixon, L. Moran, J. Rodriguez, and R. Domke, “Reactive power compensation technologies: State-of-the-art review,” *Proceedings of the IEEE*, vol. 93, no. 12, pp. 2144–2164, Dec 2005.
- [2.23] N. M. Tabatabaei, A. J. Aghbolaghi, N. Bizon, and F. Blaabjerg, *Reactive Power Control in AC Power Systems: Fundamentals and Current Issues*. Springer, 2017.
- [2.24] N. Mohan, T. M. Undeland, and W. P. Robbins, *Power Electronics: Converters, Applications, and Design*, 3rd Edition, Ed. Wiley, October 2002, no. ISBN: 978-0-471-22693-2.
- [2.25] N. G. Hingorani and L. Gyugyi, *Understanding FACTS: Concepts and Technology of Flexible AC Transmission Systems*. IEEE, 2000.
- [2.26] S. Mikkili and A. K. Panda, *Power Quality Issues: Current Harmonics*, 1st ed., ser. ISBN 9781498729628. CRC Press, August 2015.
- [2.27] J. Das, *Power System Analysis: Short-Circuit Load Flow and Harmonics*, 2nd ed. CRC Press, 2017.
- [2.28] T. L. Skvarenina, *The Power Electronics Handbook*, 1st ed. CRC Press, 2001.
- [2.29] H. Akagi and H. Fujita, “A new power line conditioner for harmonic compensation in power systems,” *IEEE Transactions on Power Delivery*, vol. 10, no. 3, pp. 1570–1575, July 1995.
- [2.30] Y. Baghzouz, “Effects of nonlinear loads on optimal capacitor placement in radial feeders,” *IEEE Transactions on Power Delivery*, vol. 6, no. 1, pp. 245–251, Jan 1991.
- [2.31] S. N. A. L. Yousif, M. Z. C. Wanik, and A. Mohamed, “Implementation of different passive filter designs for harmonic mitigation,” in *PECon 2004. Proceedings. National Power and Energy Conference, 2004.*, Nov 2004, pp. 229–234.
- [2.32] C.-J. Chou, C.-W. Liu, J.-Y. Lee, and K.-D. Lee, “Optimal planning of large passive-harmonic-filters set at high voltage level,” *IEEE Transactions on Power Systems*, vol. 15, no. 1, pp. 433–441, Feb 2000.
- [2.33] P. Friedrichs and M. Buschkühle, “Rugged, high-performance sic transistors are the future of power semiconductors,” *Energetica: Power Generation Magazine*, vol. 57, May-June 2016.
- [2.34] R. I. Amirnaser Yazdani, *Voltage-Sourced Converters in Power Systems: Modeling, Control, and Applications*. Wiley-IEEE Press, February 2010.
- [2.35] B. Singh, K. Al-Haddad, and A. Chandra, “A review of active filters for power quality improvement,” *IEEE Transactions on Industrial Electronics*, vol. 46, no. 5, pp. 960–971, Oct 1999.
- [2.36] N. G. Hingorani, “Introducing custom power,” *IEEE Spectrum*, vol. 32, no. 6, pp. 41–48, June 1995.
- [2.37] S. Nilsson, “Special application considerations for custom power systems,” in *IEEE Power Engineering Society. 1999 Winter Meeting (Cat. No.99CH36233)*, vol. 2, Jan

- 1999, pp. 1127–1131 vol.2.
- [2.38] Y. Y. Kolhatkar and S. P. Das, “Experimental investigation of a single-phase upqc with minimum va loading,” *IEEE Transactions on Power Delivery*, vol. 22, no. 1, pp. 373–380, Jan 2007.
- [2.39] B. Wu, *High-Power Converters and AC Drives*. IEEE, 2006.
- [2.40] A. Luo, Z. Shuai, W. Zhu, and Z. J. Shen, “Combined system for harmonic suppression and reactive power compensation,” *IEEE Transactions on Industrial Electronics*, vol. 56, no. 2, pp. 418–428, Feb 2009.
- [2.41] R. Gupta, A. Ghosh, and A. Joshi, “Performance comparison of vsc-based shunt and series compensators used for load voltage control in distribution systems,” *IEEE Transactions on Power Delivery*, vol. 26, no. 1, pp. 268–278, Jan 2011.
- [2.42] V. Khadkikar, “Enhancing electric power quality using upqc: A comprehensive overview,” *IEEE Transactions on Power Electronics*, vol. 27, no. 5, pp. 2284–2297, May 2012.
- [2.43] E. Acha, V. Agelidis, O. Anaya-Lara, and T. Miller, “Electrical power systems — an overview,” in *Power Electronic Control in Electrical Systems*, ser. Newnes Power Engineering Series, E. Acha, V. Agelidis, O. Anaya-Lara, and T. Miller, Eds. Oxford: Newnes, 2002, pp. 1 – 30.
- [2.44] Z. Wang, Q. Wang, W. Yao, and J. Liu, “A series active power filter adopting hybrid control approach,” *IEEE Transactions on Power Electronics*, vol. 16, no. 3, pp. 301–310, May 2001.
- [2.45] J. W. Dixon, G. Venegas, and L. A. Moran, “A series active power filter based on a sinusoidal current-controlled voltage-source inverter,” *IEEE Transactions on Industrial Electronics*, vol. 44, no. 5, pp. 612–620, Oct 1997.
- [2.46] D. Figueroa, L. Moran, P. Ruminot, and J. Dixon, “A series active power filter scheme for current harmonic compensation,” in *2008 IEEE Power Electronics Specialists Conference*, June 2008, pp. 3587–3591.
- [2.47] J. Sun, “Impedance-based stability criterion for grid-connected inverters,” *IEEE Transactions on Power Electronics*, vol. 26, no. 11, pp. 3075–3078, Nov 2011.
- [2.48] A. K. Sahoo and T. Thyagarajan, “Modeling of facts and custom power devices in distribution network to improve power quality,” in *2009 International Conference on Power Systems*, Dec 2009, pp. 1–7.
- [2.49] J. M. Cano, Á. Navarro-Rodríguez, A. Suárez, and P. García, “Variable switching frequency control of distributed resources for improved system efficiency,” *IEEE Transactions on Industry Applications*, vol. 54, no. 5, pp. 4612–4620, Sep. 2018.
- [2.50] J. Rodriguez, J.-S. Lai, and F. Z. Peng, “Multilevel inverters: a survey of topologies, controls, and applications,” *IEEE Transactions on Industrial Electronics*, vol. 49, no. 4, pp. 724–738, Aug 2002.
- [2.51] H. Akagi, “Classification, terminology, and application of the modular multilevel cascade converter (mmcc),” *IEEE Transactions on Power Electronics*, vol. 26, no. 11, pp. 3119–3130, Nov 2011.
- [2.52] T. Miller, *Reactive Power Control in Electric Systems*. New York: Wiley, 1982.
- [2.53] R. N. Beres, X. Wang, M. Liserre, F. Blaabjerg, and C. L. Bak, “A review of passive power filters for three-phase grid-connected voltage-source converters,” *IEEE Journal of Emerging and Selected Topics in Power Electronics*, vol. 4, no. 1, pp. 54–69, March 2016.
- [2.54] R. N. Beres, X. Wang, F. Blaabjerg, M. Liserre, and C. L. Bak, “Optimal design of high-order passive-damped filters for grid-connected applications,” *IEEE Transac-*

- tions on Power Electronics*, vol. 31, no. 3, pp. 2083–2098, March 2016.
- [2.55] S. Cobreces, E. Bueno, F. J. Rodriguez, F. Huertal, and P. Rodriguez, “Influence analysis of the effects of an inductive-resistive weak grid over l and lcl filter current hysteresis controllers,” in *2007 European Conference on Power Electronics and Applications*, Sep. 2007, pp. 1–10.
- [2.56] Y. W. Li, “Control and resonance damping of voltage-source and current-source converters with lcl filters,” *IEEE Transactions on Industrial Electronics*, vol. 56, no. 5, pp. 1511–1521, May 2009.
- [2.57] M. Malinowski and S. Bernet, “A simple voltage sensorless active damping scheme for three-phase pwm converters with an lcl filter,” *IEEE Transactions on Industrial Electronics*, vol. 55, no. 4, pp. 1876–1880, April 2008.
- [2.58] B. Singh, S. S. Murthy, and R. S. R. Chilipi, “Statcom-based controller for a three-phase seig feeding single-phase loads,” *IEEE Transactions on Energy Conversion*, vol. 29, no. 2, pp. 320–331, June 2014.
- [2.59] R. Zhang, V. H. Prasad, D. Boroyevich, and F. C. Lee, “Three-dimensional space vector modulation for four-leg voltage-source converters,” *IEEE Transactions on Power Electronics*, vol. 17, no. 3, pp. 314–326, May 2002.
- [2.60] J. C. Montano and P. S. Revuelta, “Strategies of instantaneous compensation for three-phase four-wire circuits,” *IEEE Power Engineering Review*, vol. 22, no. 6, pp. 63–63, June 2002.
- [2.61] P. Salmeron and J. C. Montano, “Instantaneous power components in polyphase systems under nonsinusoidal conditions,” *IEE Proceedings - Science, Measurement and Technology*, vol. 143, no. 2, pp. 151–155, March 1996.
- [2.62] C. Burgos-Mellado, J. Llanos, R. Cárdenas, D. Sáez, D. E. Olivares, M. Sumner, and A. Costabeber, “Distributed control strategy based on a consensus algorithm and on the conservative power theory for imbalance and harmonic sharing in 4-wire microgrids,” *IEEE Transactions on Smart Grid*, pp. 1–1, 2019.
- [2.63] J. P. R. A. Mélo, C. B. Jacobina, and M. B. d. Rossiter Corrêa, “Three-phase four-wire inverters based on cascaded three-phase converters with four and three legs,” *IEEE Transactions on Industry Applications*, vol. 53, no. 6, pp. 5539–5552, Nov 2017.
- [2.64] M. Eremia, C. Liu, and A. Edris, *Advanced Solutions in Power Systems: HVDC, FACTS, and Artificial Intelligence*. IEEE, 2016. [Online]. Available: <https://ieeexplore.ieee.org/document/7656871>
- [2.65] A. M. Trzynadlowski, Ed., *Power Electronic Converters and Systems: Frontiers and Applications*. IET, 2015.
- [2.66] L. M. Tolbert and T. G. Habetler, “Novel multilevel inverter carrier-based pwm method,” *IEEE Transactions on Industry Applications*, vol. 35, no. 5, pp. 1098–1107, Sep. 1999.
- [2.67] D. G. Holmes, “The significance of zero space vector placement for carrier-based pwm schemes,” *IEEE Transactions on Industry Applications*, vol. 32, no. 5, pp. 1122–1129, Sep. 1996.
- [2.68] O. Ojo, “The generalized discontinuous pwm scheme for three-phase voltage source inverters,” *IEEE Transactions on Industrial Electronics*, vol. 51, no. 6, pp. 1280–1289, 2004.
- [2.69] L. Dalessandro, S. D. Round, U. Drogenik, and J. W. Kolar, “Discontinuous space-vector modulation for three-level pwm rectifiers,” *IEEE Transactions on Power Electronics*, vol. 23, no. 2, pp. 530–542, 2008.
- [2.70] J.-H. Kim and S.-K. Sul, “A carrier-based pwm method for three-phase four-leg volt-

- age source converters," *IEEE Transactions on Power Electronics*, vol. 19, no. 1, pp. 66–75, Jan 2004.
- [2.71] V. Blasko, V. Kaura, and W. Niewiadomski, "Sampling of discontinuous voltage and current signals in electrical drives: a system approach," *IEEE Transactions on Industry Applications*, vol. 34, no. 5, pp. 1123–1130, Sep. 1998.
- [2.72] M. Malinowski, M. P. Kazmierkowski, and A. M. Trzynadlowski, "A comparative study of control techniques for pwm rectifiers in ac adjustable speed drives," *IEEE Transactions on Power Electronics*, vol. 18, no. 6, pp. 1390–1396, Nov 2003.
- [2.73] I. T. A. AG. [Online]. Available: <https://www.infineon.com/dgdl/>
- [2.74] M. Fraga, M. Bosi, and M. Negri, *Silicon Carbide in Microsystem Technology — Thin Film Versus Bulk Material*, 09 2015.
- [2.75] A. Ghazanfari and Y. A. I. Mohamed, "Decentralized cooperative control for smart dc home with dc fault handling capability," *IEEE Transactions on Smart Grid*, vol. 9, no. 5, pp. 5249–5259, 2018.
- [2.76] M. S. A. Dahidah, G. Konstantinou, and V. G. Agelidis, "A review of multilevel selective harmonic elimination pwm: Formulations, solving algorithms, implementation and applications," *IEEE Transactions on Power Electronics*, vol. 30, no. 8, pp. 4091–4106, 2015.
- [2.77] J. Pontt, J. Rodriguez, and R. Huerta, "Mitigation of noneliminated harmonics of shepwm three-level multipulse three-phase active front end converters with low switching frequency for meeting standard ieee-519-92," *IEEE Transactions on Power Electronics*, vol. 19, no. 6, pp. 1594–1600, 2004.
- [2.78] M. Sharifzadeh, H. Vahedi, R. Portillo, L. G. Franquelo, and K. Al-Haddad, "Selective harmonic mitigation based self-elimination of triplen harmonics for single-phase five-level inverters," *IEEE Transactions on Power Electronics*, vol. 34, no. 1, pp. 86–96, 2019.
- [2.79] D. Jiang and F. Wang, "Variable switching frequency PWM for three-phase converters based on current ripple prediction," *IEEE Transactions on Power Electronics*, vol. 28, no. 11, pp. 4951–4961, Nov 2013.
- [2.80] T. Xu, F. Gao, K. Zhou, and F. Blaabjerg, "Optimized design for ac filter and switching frequency of parallel-connected inverters with global synchronous pulse width modulation," *IEEE Transactions on Power Electronics*, pp. 1–1, 2020.
- [2.81] J. Rocabert, A. Luna, F. Blaabjerg, and P. Rodríguez, "Control of power converters in ac microgrids," *IEEE Transactions on Power Electronics*, vol. 27, no. 11, pp. 4734–4749, Nov 2012.
- [2.82] R. P. Aguilera, P. Acuna, G. Konstantinou, S. Vazquez, and J. I. Leon, "Chapter 2 - basic control principles in power electronics: Analog and digital control design," in *Control of Power Electronic Converters and Systems*, F. Blaabjerg, Ed. Academic Press, 2018, pp. 31 – 68.
- [2.83] J. M. Guerrero, J. C. Vasquez, J. Matas, L. G. de Vicuna, and M. Castilla, "Hierarchical control of droop-controlled ac and dc microgrids—a general approach toward standardization," *IEEE Transactions on Industrial Electronics*, vol. 58, no. 1, pp. 158–172, Jan 2011.
- [2.84] J. M. Guerrero, M. Chandorkar, T. Lee, and P. C. Loh, "Advanced control architectures for intelligent microgrids—part i: Decentralized and hierarchical control," *IEEE Transactions on Industrial Electronics*, vol. 60, no. 4, pp. 1254–1262, April 2013.
- [2.85] R. Teodorescu, M. Liserre, and P. Rodríguez, *Grid Synchronization in Single-Phase Power Converters*. John Wiley & Sons, Ltd, 2010, ch. 4, pp. 43–91.

- [2.86] Z. Xin, R. Zhao, P. Mattavelli, P. C. Loh, and F. Blaabjerg, "Re-investigation of generalized integrator based filters from a first-order-system perspective," *IEEE Access*, vol. 4, pp. 7131–7144, 2016.
- [2.87] S. Golestan, J. M. Guerrero, and J. C. Vasquez, "Three-phase plls: A review of recent advances," *IEEE Transactions on Power Electronics*, vol. 32, no. 3, pp. 1894–1907, March 2017.
- [2.88] D. B. Talbot, *Frequency Acquisition Techniques for Phase Locked Loops*. Wiley-IEEE Press, 2012.
- [2.89] F. M. Gardner, *Phase-lock Techniques*, 3rd ed. Wiley, 2005.
- [2.90] M. Karimi-Ghartemani, H. Karimi, and M. R. Iravani, "A magnitude/phase-locked loop system based on estimation of frequency and in-phase/quadrature-phase amplitudes," *IEEE Transactions on Industrial Electronics*, vol. 51, no. 2, pp. 511–517, April 2004.
- [2.91] M. Karimi-Ghartemani and M. R. Iravani, "A method for synchronization of power electronic converters in polluted and variable-frequency environments," *IEEE Transactions on Power Systems*, vol. 19, no. 3, pp. 1263–1270, Aug 2004.
- [2.92] A. Luna, J. Rocabert, J. I. Candela, J. R. Hermoso, R. Teodorescu, F. Blaabjerg, and P. Rodríguez, "Grid voltage synchronization for distributed generation systems under grid fault conditions," *IEEE Transactions on Industry Applications*, vol. 51, no. 4, pp. 3414–3425, July 2015.
- [2.93] P. Rodríguez, A. Luna, M. Ciobotaru, R. Teodorescu, and F. Blaabjerg, "Advanced grid synchronization system for power converters under unbalanced and distorted operating conditions," in *IECON 2006 - 32nd Annual Conference on IEEE Industrial Electronics*, Nov 2006, pp. 5173–5178.
- [2.94] P. Rodríguez, R. Teodorescu, I. Candela, A. V. Timbus, M. Liserre, and F. Blaabjerg, "New positive-sequence voltage detector for grid synchronization of power converters under faulty grid conditions," in *2006 37th IEEE Power Electronics Specialists Conference*, 2006, pp. 1–7.
- [2.95] H. Laaksonen, P. Saari, and R. Komulainen, "Voltage and frequency control of inverter based weak lv network microgrid," in *2005 International Conference on Future Power Systems*, Nov 2005, pp. 6 pp.–6.
- [2.96] K. De Brabandere, B. Bolsens, J. Van den Keybus, A. Woyte, J. Driesen, and R. Belmans, "A voltage and frequency droop control method for parallel inverters," *IEEE Transactions on Power Electronics*, vol. 22, no. 4, pp. 1107–1115, July 2007.
- [2.97] Dan Wu, Fen Tang, J. C. Vasquez, and J. M. Guerrero, "Control and analysis of droop and reverse droop controllers for distributed generations," in *2014 IEEE 11th International Multi-Conference on Systems, Signals Devices (SSD14)*, Feb 2014, pp. 1–5.
- [2.98] A. Villa, F. Belloni, R. Chiumeo, and C. Gandolfi, "Conventional and reverse droop control in islanded microgrid: Simulation and experimental test," in *2016 International Symposium on Power Electronics, Electrical Drives, Automation and Motion (SPEEDAM)*, June 2016, pp. 288–294.
- [2.99] S. D'Arco and J. A. Suul, "Virtual synchronous machines — classification of implementations and analysis of equivalence to droop controllers for microgrids," in *2013 IEEE Grenoble Conference*, June 2013, pp. 1–7.
- [2.100] J. Alipoor, Y. Miura, and T. Ise, "Power system stabilization using virtual synchronous generator with alternating moment of inertia," *IEEE Journal of Emerging and Selected Topics in Power Electronics*, vol. 3, no. 2, pp. 451–458, June 2015.

- [2.101] K. Shi, H. Ye, W. Song, and G. Zhou, "Virtual inertia control strategy in microgrid based on virtual synchronous generator technology," *IEEE Access*, vol. 6, pp. 27 949–27 957, 2018.
- [2.102] J. Fang, H. Li, Y. Tang, and F. Blaabjerg, "On the inertia of future more-electronics power systems," *IEEE Journal of Emerging and Selected Topics in Power Electronics*, vol. 7, no. 4, pp. 2130–2146, 2019.
- [2.103] S. A. Khajehoddin, M. Karimi-Ghartemani, and M. Ebrahimi, "Grid-supporting inverters with improved dynamics," *IEEE Transactions on Industrial Electronics*, vol. 66, no. 5, pp. 3655–3667, 2019.
- [2.104] P. Rioual, H. Pouliquen, and J. . Louis, "Regulation of a pwm rectifier in the unbalanced network state using a generalized model," *IEEE Transactions on Power Electronics*, vol. 11, no. 3, pp. 495–502, May 1996.
- [2.105] R. Teodorescu, M. Liserre, and P. Rodriguez, *Control of Grid Converters under Grid Faults*. IEEE, 2007, pp. 237–287. [Online]. Available: <https://ieeexplore.ieee.org/document/5732935>
- [2.106] A. Khoshooei, J. S. Moghani, I. Candela, and P. Rodriguez, "Control of d-statcom during unbalanced grid faults based on dc voltage oscillations and peak current limitations," *IEEE Transactions on Industry Applications*, vol. 54, no. 2, pp. 1680–1690, March 2018.
- [2.107] Hong-Seok Song and Kwanghee Nam, "Dual current control scheme for pwm converter under unbalanced input voltage conditions," *IEEE Transactions on Industrial Electronics*, vol. 46, no. 5, pp. 953–959, 1999.
- [2.108] A. Milicua, G. Abad, and M. Á. Rodríguez Vidal, "Online reference limitation method of shunt-connected converters to the grid to avoid exceeding voltage and current limits under unbalanced operation—part i: Theory," *IEEE Transactions on Energy Conversion*, vol. 30, no. 3, pp. 852–863, 2015.
- [2.109] M. Savaghebi, A. Jalilian, J. C. Vasquez, and J. M. Guerrero, "Autonomous voltage unbalance compensation in an islanded droop-controlled microgrid," *IEEE Transactions on Industrial Electronics*, vol. 60, no. 4, pp. 1390–1402, 2013.
- [2.110] J. He, Y. W. Li, and M. S. Munir, "A flexible harmonic control approach through voltage-controlled dg-grid interfacing converters," *IEEE Transactions on Industrial Electronics*, vol. 59, no. 1, pp. 444–455, 2012.
- [2.111] K. Ma, W. Chen, M. Liserre, and F. Blaabjerg, "Power controllability of a three-phase converter with an unbalanced ac source," *IEEE Transactions on Power Electronics*, vol. 30, no. 3, pp. 1591–1604, 2015.
- [2.112] M. Liserre, R. Teodorescu, and F. Blaabjerg, "Stability of photovoltaic and wind turbine grid-connected inverters for a large set of grid impedance values," *IEEE Transactions on Power Electronics*, vol. 21, no. 1, pp. 263–272, Jan 2006.
- [2.113] J. Xu, S. Xie, and T. Tang, "Active Damping-Based Control for Grid-Connected-Filtered Inverter With Injected Grid Current Feedback Only," *IEEE Transactions on Industrial Electronics*, vol. 61, no. 9, pp. 4746–4758, Sep. 2014.
- [2.114] H. Xiao, X. Qu, S. Xie, and J. Xu, "Synthesis of active damping for grid-connected inverters with an LCL filter," in *2012 IEEE Energy Conversion Congress and Exposition (ECCE)*, Sep. 2012, pp. 550–556.
- [2.115] M. Ciobotaru, R. Teodorescu, P. Rodriguez, A. Timbus, and F. Blaabjerg, "Online grid impedance estimation for single-phase grid-connected systems using pq variations," in *2007 IEEE Power Electronics Specialists Conference*, June 2007, pp. 2306–2312.

- [2.116] S. Cobreces, E. J. Bueno, D. Pizarro, F. J. Rodriguez, and F. Huerta, "Grid impedance monitoring system for distributed power generation electronic interfaces," *IEEE Transactions on Instrumentation and Measurement*, vol. 58, no. 9, pp. 3112–3121, Sep. 2009.
- [2.117] V. Valdivia, A. Lazaro, A. Barrado, P. Zumel, C. Fernandez, and M. Sanz, "Black-box modeling of three-phase voltage source inverters for system-level analysis," *IEEE Transactions on Industrial Electronics*, vol. 59, no. 9, pp. 3648–3662, Sep. 2012.
- [2.118] M. Liserre, F. Blaabjerg, and R. Teodorescu, "Grid impedance estimation via excitation of *lcl*-filter resonance," *IEEE Transactions on Industry Applications*, vol. 43, no. 5, pp. 1401–1407, Sep. 2007.
- [2.119] A. Vidal, A. G. Yepes, F. D. Freijedo, O. López, J. Malvar, F. Baneira, and J. Doval-Gandoy, "A method for identification of the equivalent inductance and resistance in the plant model of current-controlled grid-tied converters," *IEEE Transactions on Power Electronics*, vol. 30, no. 12, pp. 7245–7261, Dec 2015.
- [2.120] A. K. Broen, M. Amin, E. Skjong, and M. Molinas, "Instantaneous frequency tracking of harmonic distortions for grid impedance identification based on kalman filtering," in *2016 IEEE 17th Workshop on Control and Modeling for Power Electronics (COMPEL)*, June 2016, pp. 1–7.
- [2.121] N. Hoffmann and F. W. Fuchs, "Minimal invasive equivalent grid impedance estimation in inductive-resistive power networks using extended kalman filter," *IEEE Transactions on Power Electronics*, vol. 29, no. 2, pp. 631–641, Feb 2014.
- [2.122] A. Bechouche, D. O. Abdeslam, H. Seddiki, and A. Rahoui, "Estimation of equivalent inductance and resistance for adaptive control of three-phase pwm rectifiers," in *IECON 2016 - 42nd Annual Conference of the IEEE Industrial Electronics Society*, Oct 2016, pp. 1336–1341.
- [2.123] R. M. Milasi, A. F. Lynch, and Y. Li, "Adaptive vector control for voltage source converters," *IET Control Theory Applications*, vol. 7, no. 8, pp. 1110–1119, May 2013.
- [2.124] P. Antoniewicz and M. P. Kazmierkowski, "Virtual-flux-based predictive direct power control of ac/dc converters with online inductance estimation," *IEEE Transactions on Industrial Electronics*, vol. 55, no. 12, pp. 4381–4390, Dec 2008.
- [2.125] A. Ghanem, M. Rashed, M. Sumner, M. A. Elsayes, and I. I. I. Mansy, "Grid impedance estimation for islanding detection and adaptive control of converters," *IET Power Electronics*, vol. 10, no. 11, pp. 1279–1288, 2017.
- [2.126] J. P. Rhode, A. W. Kelley, and M. E. Baran, "Complete characterization of utilization-voltage power system impedance using wideband measurement," *IEEE Transactions on Industry Applications*, vol. 33, no. 6, pp. 1472–1479, Nov 1997.
- [2.127] Z. Staroszczyk, "A method for real-time, wide-band identification of the source impedance in power systems," *IEEE Transactions on Instrumentation and Measurement*, vol. 54, no. 1, pp. 377–385, Feb 2005.
- [2.128] M. Sumner, B. Palethorpe, D. W. P. Thomas, P. Zanchetta, and M. C. D. Piazza, "A technique for power supply harmonic impedance estimation using a controlled voltage disturbance," *IEEE Transactions on Power Electronics*, vol. 17, no. 2, pp. 207–215, Mar 2002.
- [2.129] M. Nagpal, W. Xu, and J. Sawada, "Harmonic impedance measurement using three-phase transients," *IEEE Transactions on Power Delivery*, vol. 13, no. 1, pp. 272–277, Jan 1998.
- [2.130] Y. A. Familiant, J. Huang, K. A. Corzine, and M. Belkhat, "New techniques for

- measuring impedance characteristics of three-phase ac power systems,” *IEEE Transactions on Power Electronics*, vol. 24, no. 7, pp. 1802–1810, July 2009.
- [2.131] L. Asiminoaei, R. Teodorescu, F. Blaabjerg, and U. Borup, “A new method of on-line grid impedance estimation for pv inverter,” in *Nineteenth Annual IEEE Applied Power Electronics Conference and Exposition, 2004. APEC '04.*, vol. 3, Feb 2004, pp. 1527–1533 Vol.3.
- [2.132] D. Martin and E. Santi, “Autotuning of digital deadbeat current controllers for grid-tie inverters using wide bandwidth impedance identification,” *IEEE Transactions on Industry Applications*, vol. 50, no. 1, pp. 441–451, Jan 2014.
- [2.133] J. M. Espi, J. Castello, R. García-Gil, G. Garcera, and E. Figueres, “An adaptive robust predictive current control for three-phase grid-connected inverters,” *IEEE Transactions on Industrial Electronics*, vol. 58, no. 8, pp. 3537–3546, Aug 2011.
- [2.134] J. R. Massing, M. Stefanello, H. A. Grundling, and H. Pinheiro, “Adaptive current control for grid-connected converters with lcl filter,” *IEEE Transactions on Industrial Electronics*, vol. 59, no. 12, pp. 4681–4693, Dec 2012.
- [2.135] Y. Abdel-Rady Ibrahim Mohamed and E. F. El-Saadany, “An improved deadbeat current control scheme with a novel adaptive self-tuning load model for a three-phase pwm voltage-source inverter,” *IEEE Transactions on Industrial Electronics*, vol. 54, no. 2, pp. 747–759, April 2007.
- [2.136] J. Huang, K. A. Corzine, and M. Belkhatay, “Small-signal impedance measurement of power-electronics-based ac power systems using line-to-line current injection,” *IEEE Transactions on Power Electronics*, vol. 24, no. 2, pp. 445–455, Feb 2009.
- [2.137] M. A. Azzouz and E. F. El-Saadany, “Multivariable grid admittance identification for impedance stabilization of active distribution networks,” *IEEE Transactions on Smart Grid*, vol. 8, no. 3, pp. 1116–1128, May 2017.
- [2.138] M. Céspedes and J. Sun, “Online grid impedance identification for adaptive control of grid-connected inverters,” in *2012 IEEE Energy Conversion Congress and Exposition (ECCE)*, Sep. 2012, pp. 914–921.
- [2.139] M. Céspedes and J. Sun, “Adaptive control of grid-connected inverters based on online grid impedance measurements,” *IEEE Transactions on Sustainable Energy*, vol. 5, no. 2, pp. 516–523, April 2014.
- [2.140] P. García, M. Sumner, Á. Navarro-Rodríguez, J. M. Guerrero, and J. García, “Observer-based pulsed signal injection for grid impedance estimation in three-phase systems,” *IEEE Transactions on Industrial Electronics*, vol. 65, no. 10, pp. 7888–7899, Oct 2018.
- [2.141] D. Reigosa, F. Briz, C. B. Charro, P. Garcia, and J. M. Guerrero, “Active islanding detection using high-frequency signal injection,” *IEEE Transactions on Industry Applications*, vol. 48, no. 5, pp. 1588–1597, Sep. 2012.
- [2.142] M. Tsukamoto, S. Ogawa, Y. Natsuda, Y. Minowa, and S. Nishimura, “Advanced technology to identify harmonics characteristics and results of measuring,” in *Ninth International Conference on Harmonics and Quality of Power. Proceedings (Cat. No.00EX441)*, vol. 1, Oct 2000, pp. 341–346 vol.1.
- [2.143] M. B. Harris, A. W. Kelley, J. P. Rhode, and M. E. Baran, “Instrumentation for measurement of line impedance,” in *Proceedings of 1994 IEEE Applied Power Electronics Conference and Exposition - ASPEC'94*, Feb 1994, pp. 887–893 vol.2.
- [2.144] L. Asiminoaei, R. Teodorescu, F. Blaabjerg, and U. Borup, “A digital controlled pv-inverter with grid impedance estimation for ens detection,” *IEEE Transactions on Power Electronics*, vol. 20, no. 6, pp. 1480–1490, Nov 2005.

- [2.145] M. Ciobotaru, R. Teodorescu, and F. Blaabjerg, "On-line grid impedance estimation based on harmonic injection for grid-connected pv inverter," in *2007 IEEE International Symposium on Industrial Electronics*, June 2007, pp. 2437–2442.
- [2.146] R. Petrella, A. Revelant, and P. Stocco, "Advances on inter-harmonic variable-frequency injection-based grid-impedance estimation methods suitable for pv inverters," in *2009 IEEE Energy Conversion Congress and Exposition*, Sep. 2009, pp. 1173–1179.
- [2.147] D. Reigosa, F. Briz, C. Blanco, P. García, and J. Manuel Guerrero, "Active islanding detection for multiple parallel-connected inverter-based distributed generators using high-frequency signal injection," *IEEE Transactions on Power Electronics*, vol. 29, no. 3, pp. 1192–1199, March 2014.
- [2.148] M. Sumner, B. Palethorpe, and D. W. P. Thomas, "Impedance measurement for improved power quality-part 1: the measurement technique," *IEEE Transactions on Power Delivery*, vol. 19, no. 3, pp. 1442–1448, July 2004.
- [2.149] L. Asiminoaei, R. Teodorescu, F. Blaabjerg, and U. Borup, "Implementation and test of an online embedded grid impedance estimation technique for pv inverters," *IEEE Transactions on Industrial Electronics*, vol. 52, no. 4, pp. 1136–1144, Aug 2005.
- [2.150] P. García, J. M. Guerrero, J. García, Á. Navarro-Rodríguez, and M. Sumner, "Low frequency signal injection for grid impedance estimation in three phase systems," in *2014 IEEE Energy Conversion Congress and Exposition (ECCE)*, Sep. 2014, pp. 1542–1549.
- [2.151] B. Miao, R. Zane, and D. Maksimovic, "System identification of power converters with digital control through cross-correlation methods," *IEEE Transactions on Power Electronics*, vol. 20, no. 5, pp. 1093–1099, Sep. 2005.
- [2.152] T. Roinila, M. Vilkkö, and J. Sun, "Online grid impedance measurement using discrete-interval binary sequence injection," *IEEE Journal of Emerging and Selected Topics in Power Electronics*, vol. 2, no. 4, pp. 985–993, Dec 2014.
- [2.153] T. Roinila and T. Messo, "Online grid-impedance measurement using ternary-sequence injection," *IEEE Transactions on Industry Applications*, vol. 54, no. 5, pp. 5097–5103, Sep. 2018.
- [2.154] K. O. H. Pedersen, A. H. Nielsen, and N. K. Poulsen, "Short-circuit impedance measurement," *IEE Proceedings - Generation, Transmission and Distribution*, vol. 150, no. 2, pp. 169–174, March 2003.
- [2.155] A. V. Timbus, R. Teodorescu, F. Blaabjerg, and U. Borup, "Online grid impedance measurement suitable for multiple pv inverters running in parallel," in *Twenty-First Annual IEEE Applied Power Electronics Conference and Exposition, 2006. APEC '06.*, 2006, pp. 5 pp.–.



# Chapter 3

## System Modelling

### 3.1 Introduction

The change of philosophy, concerning distributed generation, has induced the emerging of a large number of power converter units devoted to both energy generation and voltage level adaptation. The feasibility of these units have enable them to be used as APFs, coping among the problems related to distributed generation paradigm [3.1, 3.2], current and/or voltage unbalances or sags, which have recently received much attention [3.3–3.7]. Unbalance compensation can be achieved by any of the previous topologies shown in Chapter 2. However, measurement of the unbalanced components, i.e. negative and zero sequence voltages and currents, is a challenging task.

In this chapter, a modelling technique which analytically highlights the coupling between the positive, negative and zero current sequences with non-balanced loads and voltage unbalances is presented. The proposed analysis allows obtaining the expressions of the complex current vectors at the  $\alpha\beta 0$  reference frame from the values of the voltages and loads at the  $abc$  reference frame using a compact representation. The method is not only valid for the analysis at the fundamental frequency, but also when a high frequency signal is injected by the converter. This fact will be of paramount importance in the following chapters, for the estimation technique further presented.

This chapter begins with the presentation of the system and an analytical expression of the impedance and the admittance. The expression used to link the unbalance terms with the impedance of the grid are also presented, both in the frequency and the time domain. A verification of the feasibility of the model is also proven under a set of simulations. A comparison between the traditional modelling approaches and the one presented here is also provided as well as an adaptation of the technique to the traditional instantaneous power theory. The chapter is closed with a simulation, where different impedance steps are induced with the resultant voltage and current sequences derived from those impedance variations and also the ones derived from the voltage unbalances.

## 3.2 System Definition

The importance of a generic model, relies on the flexibility to make it adaptable to every system condition. In order to conduct the discussion within the chapter, let's consider the generic system from Fig. 3.1, where an undetermined number of loads are connected to a three-phase four-wire AC-Grid in parallel to an APF at the PCC of the system.

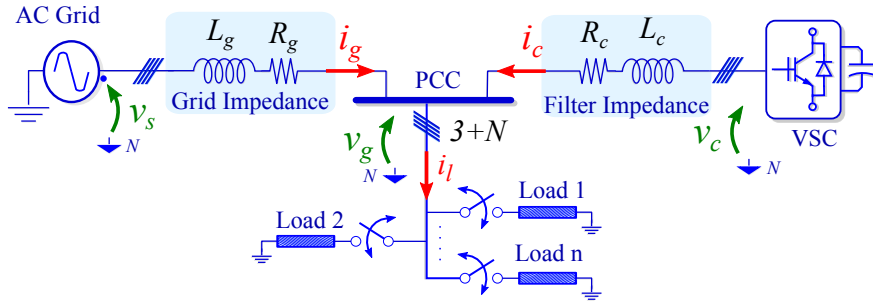


**Figure 3.1:** Schematic for power converter and load connection to the point of common coupling. Loads can be both  $3\phi$  or  $1\phi$ .

From the point of view of the reference generation for the APF, it would be extremely useful to provide an expression able to link both the impedance of the system and the current and voltages demanded by the load and the grid. In the following sections, a modelling solution to identify the impedance terms of a generic grid according to the voltage and currents demanded by the system is proposed.

### 3.2.1 Variables Definition in Time and Frequency Domain

Assuming that most of the loads connected to LV systems have an inductive profile, the analysis is initially conducted considering  $RL$  elements for describing the impedance of every load connected at the PCC in Fig. 3.1. Later in the discussion, this analysis is also extended to capacitive elements. If  $RL$  loads are considered, the voltage equation in time domain is given by (3.1), where  $i$  stands for the individual current demanded by every load.

$$v = Ri + L \frac{di}{dt} \quad (3.1)$$

The expression of each current harmonic in the time domain may be defined according to (3.2).

$$i = \sqrt{2}I_n \cos(n\omega_e t + \phi_n) \quad (3.2)$$

where  $I$  is the RMS value of the current,  $n$  is the order of the harmonic,  $\omega_e$  is the grid frequency in radians per second and  $\phi$  is the initial phase angle in radians.

Expressions (3.1) and (3.2) are valid for every element of the circuit, however, time domain operations involve more complex and puzzling calculations. On the contrary, working in the frequency domain enlighten the computational effort required, expressing the voltage and current value in vectorial notation and assuming impedance constant values. Consequently,

expression (3.2) may be expressed in the frequency domain as (3.3), based on the reasoning presented in Appendix B.

$$\mathbf{i} = I\angle\phi = Ie^{j\phi} \quad (3.3)$$

Similarly, time domain expression in (3.1) may be reformulated as (3.4), in vector notation.

$$\mathbf{v} = RIe^{j\phi} + \omega_e LIe^{j(\phi+\frac{\pi}{2})} = \left(R + \omega_e L e^{j\frac{\pi}{2}}\right) Ie^{j\phi} = (R + j\omega_e L) \mathbf{i} \quad (3.4)$$

Notice that, from (3.4), the remaining expression strictly corresponds to the voltage vector, which is time independent and valid for steady state analysis. Similarly, frequency is not explicitly shown in the vector notation because  $\omega_e$  is constant; however, the response depends on it.

Combination of (3.3) and (3.4) allows to define the impedance value as the ratio between voltage vector and current vector, and consequently, it is a frequency-dependent term,

$$\mathbf{z} = \frac{\mathbf{v}}{\mathbf{i}} = (R + j\omega_e L) \quad (3.5)$$

where it is assumed  $\mathbf{z}$  is a complex element. This vector  $\mathbf{z}$  represents the impedance of the system, with a magnitude and a direction. This consideration allows to introduce the change of reference frame in the next section. Additionally, as it has been highlighted, this analysis is also valid in case of capacitive terms, replacing the imaginary term of  $\mathbf{z}$  by  $-j\frac{1}{\omega_e C}$ .

### 3.2.2 System Representation in the $\alpha\beta$ Reference Frame

The voltage vector for a three phase system is expressed as (3.6), where  $\mathbf{Z}_{abc}$  are complex elements and the problem is stated algebraically in vector notation.

$$\mathbf{v}_{abc} = (\mathbf{R}_{abc} + j\omega_e \mathbf{L}_{abc}) \mathbf{i}_{abc} = \mathbf{Z}_{abc} \cdot \mathbf{i}_{abc} \quad (3.6)$$

Expression (3.6) may be defined within the  $\alpha\beta$  stationary reference frame which, based on *Clark* Transformation, is widely explained in Appendix C.

The transformation for both currents and voltages is common and is based on (3.7a), where  $\mathbf{A}$  is defined according to (C.19). For the case of the impedance, the transformation leads to (3.7b), which results from applying the same transformation to the phase impedances.

$$\mathbf{x}_{abc} = \mathbf{A} \cdot \mathbf{x}_{\alpha\beta 0} \quad (3.7a)$$

$$\mathbf{Z}_{\alpha\beta 0} = \mathbf{A}^{-1} \cdot \mathbf{Z}_{abc} \cdot \mathbf{A} \quad (3.7b)$$

Moving from the  $abc$  to the  $\alpha\beta 0$  reference frame has the advantage of using a more compact notation for the modelling, including the case of the symmetrical component analysis, also provided in Appendix C. Under this transformation, the impedance matrix, expressed according to (3.7b), leads to (3.8).

$$\mathbf{Z}_{abc} = \begin{pmatrix} Z_a & 0 & 0 \\ 0 & Z_b & 0 \\ 0 & 0 & Z_c \end{pmatrix} \Rightarrow \mathbf{Z}_{\alpha\beta 0} = \begin{pmatrix} Z_{\alpha\alpha} & Z_{\alpha\beta} & Z_{\alpha 0} \\ Z_{\beta\alpha} & Z_{\beta\beta} & Z_{\beta 0} \\ Z_{0\alpha} & Z_{0\beta} & Z_{00} \end{pmatrix} \quad (3.8)$$

At this point, the expressions for the voltages and currents may be simplified to a more easy and elegant notation, however, same transformation leads to a much more complex model for the impedance matrix, with terms outside of the main diagonal. This fact would greatly complicate the calculations, unless a transformation is yielded to achieve a diagonal matrix, i.e. one without non-zero elements out of the main diagonal.

A solution proposed to simplify these terms is based on the use of multiple stationary reference frames. Multiple reference frame is a solution highly adopted in such grids where the presence of unbalance and harmonic distortion deprecated the proper performance of the current control of the power converter [3.8, 3.9].

This strategy is based on the isolation of each harmonic component of the current and use a specific controller for each of them. Current and voltage components may be expressed using different transformations by choosing an arbitrary angular frequency,  $\omega_e$ , for the reference frame [3.10], where  $\omega_e = d\theta_e/dt$ .

The approach proposed in this work follows the same principle of the *Clarke* transformation [3.11], based on the projection of the three phase vectors over orthogonal axes, which is explained into more detail in Appendix C. However, in the present proposal, the angle of the reference frame will depend on the impedance of the system, instead of being zero. Fig 3.2 shows a graphical representation of the concept.

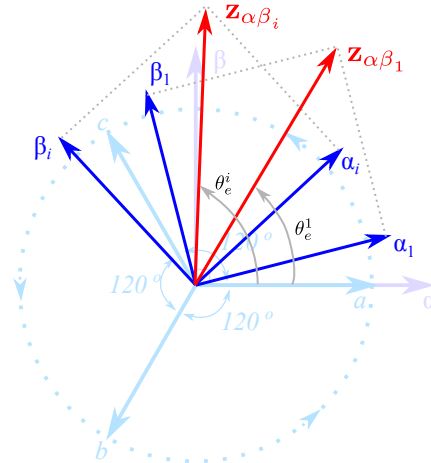


**Figure 3.2:** Axis orientation for system loads ( $\alpha_i \beta_i$ ) and general stationary reference frame axis ( $\alpha \beta$ ).

Every term named by the subscripts  $i$  represents one of the impedances involved into the system under analysis. Each of these impedances is represented in a reference frame aligned with the unbalance direction ( $\theta_e^i$  in Fig. 3.2). Using that approach, and assuming that there is no cross-coupling between the phases, the impedance can be represented by (3.9).

$$\mathbf{Z}_{\alpha\beta\mathbf{0}_i} = \begin{pmatrix} Z_{\alpha\alpha i} & 0 & 0 \\ 0 & Z_{\beta\beta i} & 0 \\ 0 & 0 & Z_{00i} \end{pmatrix} \quad (3.9)$$

In the case cross-coupling is to be considered, it will be represented by non-diagonal terms

[3.12]. However, it should be noted that cross-coupling impedances in low-voltage distribution networks have, generally, a negligible value compared to the phase impedances [3.13].

The resultant diagonal matrix reduces noticeable the needed algebra for the modelling of the expression, easing future calculations to obtain the impedance model of the system.

### 3.2.3 Impedance Model

According to the algebraic transformation presented in (3.7a), a possible set of independent elements for each element,  $i$ , within the system in Fig. 3.1 can be defined as (3.10).

$$\mathbf{Z}_{\alpha\beta 0} = \left[ \Sigma Z_i \begin{pmatrix} 1 & 0 & 0 \\ 0 & 1 & 0 \\ 0 & 0 & 1 \end{pmatrix} + \Delta Z_i \begin{pmatrix} \cos \theta_e^i & -\sin \theta_e^i & \sqrt{2} \cos \theta_e^i \\ -\sin \theta_e^i & -\cos \theta_e^i & \sqrt{2} \sin \theta_e^i \\ \sqrt{2} \cos \theta_e^i & \sqrt{2} \sin \theta_e^i & 0 \end{pmatrix} \right] \quad (3.10)$$

In (3.10),  $\Sigma Z_i$  represents the averaged impedance values and  $\Delta Z_i$  is the term associated with the unbalanced impedance. Both terms can be defined as (3.11) and (3.12) respectively.

$$\Sigma Z_i = \frac{Z_{\alpha\alpha i} + Z_{\beta\beta i}}{2} = \frac{Z_a + Z_b + Z_c}{3} \quad (3.11)$$

$$\Delta Z_i = \frac{Z_{\alpha\alpha i} - Z_{\beta\beta i}}{2} = \frac{Z_a + a \cdot Z_b + a^2 \cdot Z_c}{3} \quad (3.12)$$

$$\theta_e^i = \tan^{-1}(\Delta Z_i) \quad (3.13)$$

$\theta_e^i$  is the angle of the term linked with the unbalance magnitude and consequently is considered the impedance unbalance angle and  $a = e^{j2\pi/3}$ . Note that, for the case of a balanced load, i.e.  $Z_{\alpha\alpha i} = Z_{\beta\beta i} = Z_{00i}$ , the incremental impedance term,  $\Delta Z_i$ , becomes zero.

For the case of single phase loads at phases  $a$ ,  $b$ ,  $c$ ,  $\theta_e^i$  equals  $0$ ,  $2\pi/3$  and  $4\pi/3$  respectively. It is worth noting that for the case of single phase loads, in which the impedance at the two remaining phases are infinity, the expressions (3.11) and (3.12) will be also evaluated as infinity.

The terms under unbalanced conditions in (3.10) may be rewritten as (3.14).

$$\mathbf{Z}_{\alpha\beta 0} = \left[ \begin{pmatrix} \Sigma Z_{\alpha\alpha i} & 0 & 0 \\ 0 & \Sigma Z_{\beta\beta i} & 0 \\ 0 & 0 & \Sigma Z_{00i} \end{pmatrix} + \begin{pmatrix} \Delta Z_{\alpha\alpha i} & \Delta Z_{\alpha\beta i} & \Delta Z_{\alpha 0i} \\ \Delta Z_{\beta\alpha i} & \Delta Z_{\beta\beta i} & \Delta Z_{\beta 0i} \\ \Delta Z_{0\alpha i} & \Delta Z_{0\beta i} & 0 \end{pmatrix} \right] \quad (3.14)$$

Similarly, expression (3.14) may be expanded into a complex magnitude as (3.15), maintaining the consistency between the  $\alpha\beta$  terms and every element of the impedance term, and considering both inductive or capacitive profile based on the positive or negative characteristic of the imaginary term.

$$Z_{\alpha\beta} = (\Sigma R_i + \Delta R_i) \pm j (\Sigma X_i + \Delta X_i) \quad (3.15)$$

In the same way, the summation and incremental terms are defined according to:

$$\Sigma R_i = \frac{R_{\alpha\alpha} + R_{\beta\beta}}{3} = \frac{R_a + R_b + R_c}{3} \quad (3.16)$$

$$\Delta R_i = \frac{R_{\alpha\alpha} - R_{\beta\beta}}{3} = \frac{R_a + a \cdot R_b + a^2 \cdot R_c}{3} \quad (3.17)$$

$$\theta_r^i = \angle \Delta R_i \quad (3.18)$$

$$\Sigma X_i = \frac{X_{\alpha\alpha} + X_{\beta\beta}}{3} = \frac{X_a + X_b + X_c}{3} \quad (3.19)$$

$$\Delta X_i = \frac{X_{\alpha\alpha} - X_{\beta\beta}}{3} = \frac{X_a + a \cdot X_b + a^2 \cdot X_c}{3} \quad (3.20)$$

$$\theta_x^i = \angle \Delta X_i \quad (3.21)$$

Similarly, for the case of balanced load, i.e.  $R_{\alpha\alpha i} = R_{\beta\beta i} = R_{00i}$ ,  $X_{\alpha\alpha i} = X_{\beta\beta i} = X_{00i}$ , being the incremental terms equal to zero. However, expression (3.15) is expressed in terms of complex variables and thus the zero sequence terms are calculated according to  $\Delta R_{\alpha 0 i} = \sqrt{2} \Delta R_i \cos \theta_r^i$  and  $\Delta R_{\beta 0 i} = \sqrt{2} \Delta R_i \sin \theta_r^i$ , replicating the expressions for the reactance terms.

Additionally, in the set of expressions (3.19)-(3.20), the reactance may be considered inductive or capacitive; depending on the nature of the circuit. This term is also affected by the excitation frequency of the system, being the generic expression involving both terms as  $X_L = \omega_e L$  or  $X_C = \frac{1}{\omega_e C}$ .

To prove the consistence of the algorithm, a simulation test is presented, where different changes have been induced in the impedance of the system, both in the resistive and the inductance term of every phase. The initial values and the steps induced at each phase are included in Table 3.1.

**Table 3.1:** Resistive and inductive values

Time [s]	0	0.2	0.4	0.6	0.8
$R_a$ [ $\Omega$ ]	17.78	5.93	8.89	53.33	8.89
$L_a$ [mH]	9.0	18.0	27.0	9.0	9.0
$R_b$ [ $\Omega$ ]	17.78	17.78	53.33	17.78	5.93
$L_b$ [mH]	9.0	4.50	1.29	22.5	4.5
$R_c$ [ $\Omega$ ]	17.78	53.33	17.78	5.93	35.56
$L_c$ [mH]	9.0	3.0	9.0	4.5	13.5

In Fig. 3.3 it is presented, in blue trace the values of the terms of the resultant matrix from expression (3.7b) and in red trace the values obtained according to the proposed method in (3.14). As it can be concluded from the graphs in Fig 3.3, both expressions, (3.7b) and (3.14), are equivalent, what makes possible to obtain an elegant model based on the magnitude of the unbalance and the resultant impedance of the system. Similarly, it might be strongly beneficial to express every phase impedance according to the  $\alpha\beta$  expression. Based on (3.15), expressions (3.22) and (3.23) link the  $\alpha\beta$  terms with the  $abc$  reference frame.

$$R_m = \begin{bmatrix} R_a \\ R_b \\ R_c \end{bmatrix} = [M_R]^{-1} \cdot \begin{bmatrix} \Sigma R_i \\ \Delta R_{\alpha i} \\ \Delta R_{\beta i} \end{bmatrix}; \quad M_R = \frac{1}{3} \begin{bmatrix} 1 & 1 & 1 \\ 1 & -1/2 & -1/2 \\ 0 & \sqrt{3}/2 & -\sqrt{3}/2 \end{bmatrix} \quad (3.22)$$

where  $\Delta R_{\alpha i} = |\Delta R_i| \cos(\theta_e^i)$  and  $\Delta R_{\beta i} = |\Delta R_i| \sin(\theta_e^i)$ .

$$L_m = \begin{bmatrix} L_a \\ L_b \\ L_c \end{bmatrix} = [M_X]^{-1} \cdot \begin{bmatrix} \Sigma X_i \\ \Delta X_{\alpha i} \\ \Delta X_{\beta i} \end{bmatrix}; \quad M_X = \frac{1}{3j\omega_e} \begin{bmatrix} 1 & 1 & 1 \\ 1 & -1/2 & -1/2 \\ 0 & \sqrt{3}/2 & -\sqrt{3}/2 \end{bmatrix} \quad (3.23)$$

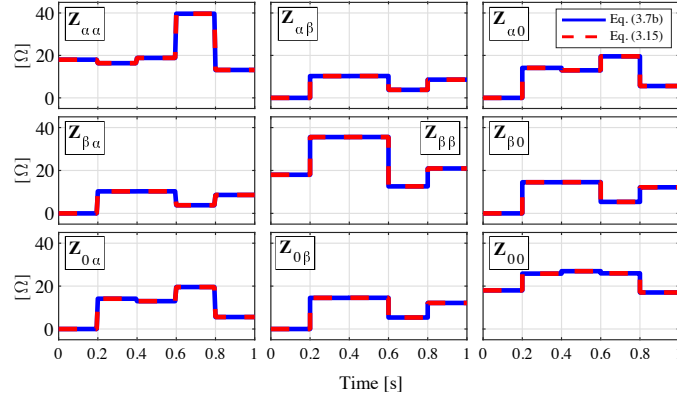


**Figure 3.3:** Simulation results. Analytical representation of every element of the impedance matrix according to (3.7b) and the equivalent values resulting from the proposed expression in (3.15).

where  $\Delta X_{\alpha_i} = |\Delta X_i| \cos(\theta_e^i)$  and  $\Delta X_{\beta_i} = |\Delta X_i| \sin(\theta_x^i)$ .

Figure 3.4 proves the equivalence of both expressions, comparing the initial values of the system impedance with the ones derived from (3.15) and (3.22). The interesting aspect of this approach is the reversible capability of the algorithm, which allows to move from different reference frames maintaining the consistency at every element.

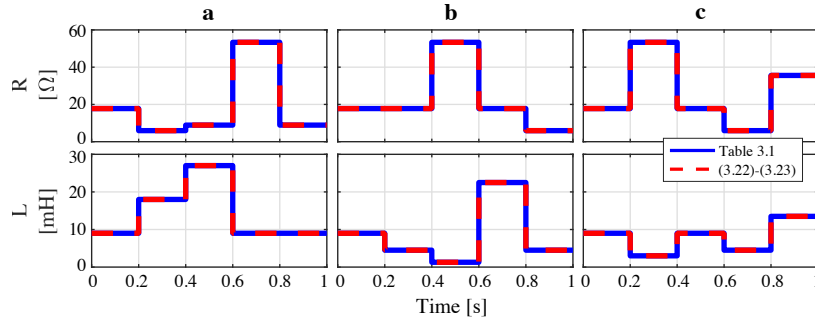


**Figure 3.4:** Simulation results. Comparison between the original resistive and inductive values according to the terms shown in Table 3.1 and the ones obtained according to expressions (3.22) and (3.23).

The evaluations performed until here were considering the resistive term as the real part of the impedance and the imaginary one as the reactive. However, in the case of parallel connections, the real and imaginary terms are no longer the resistive and the reactance values, but the equivalent impedance of the system might be defined according to (3.24) or (3.25), depending if inductive or capacitive terms are considered.

$$Z_i = \frac{R_i}{1 + R_i / (j\omega_i L_i)} \quad (3.24)$$

$$Z_i = \frac{R_i}{1 + j\omega_i R_i C_i} \quad (3.25)$$

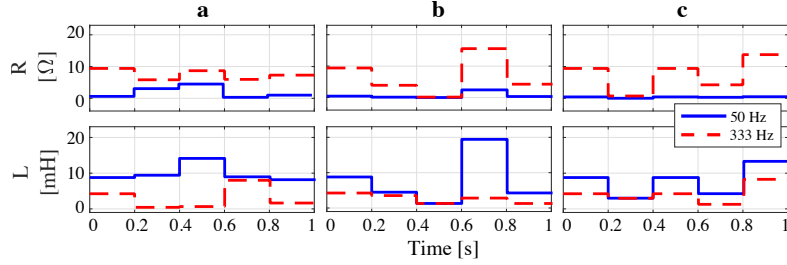


**Figure 3.5:** Simulation results: Equivalent values for the resistance and inductance based on the evaluation of expression (3.26) according to the values in Table (3.1).

Under such consideration, expressions (3.24) and (3.25) can be expressed in a generic form as (3.26), where the positive or negative term stands for the inductive or capacitive characteristic of the component.

$$Z_i = \Re\{Z_i\} \pm j\Im\{Z_i\} \quad (3.26)$$

This expression can be modelled under the same algorithm; considering the resistive part of the impedance as the real part of the system and the imaginary, as the reactive for positive values and capacitive for the negative ones. However, as a consequence of the algebra, every impedance term is distorted from the original value and the identification of the resistive and the reactive components is not a straightforward, resulting in different expressions for capacitive or reactive terms, according to (3.24) and (3.25).

An approach to engage with the original terms might consist on the addition of a second high frequency signal, evaluating same terms but at different frequencies, that allows to establish a correlation between both magnitudes and frequencies. These expressions are modelled according to (3.27) and (3.28), where  $Z_i^{hf}$  is the resultant impedance at the frequency,  $\omega_{hf}$ . As said, the inductive case has been selected due to the characteristics of most of the LV loads. From hereinafter, the analysis will be performed under such consideration. However, all the reasoning can be easily extended to capacitive terms.

$$R_m = \frac{Z_i \cdot Z_i^{hf} \cdot (\omega_e - \omega_{hf})}{\omega_e \cdot Z_i^{hf} - \omega_{hf} \cdot Z_i} \quad (3.27)$$

$$L_m = j \frac{Z_i \cdot Z_i^{hf} \cdot (\omega_{hf} - \omega_e)}{(Z_i - Z_i^{hf}) \cdot \omega_e \cdot \omega_{hf}} \quad (3.28)$$

To prove the dissonance at the two frequencies, an evaluation of the expression (3.26) with the same values as those shown in Table (3.1) has been performed. In this test,  $\omega_e = 2\pi 50$  and  $\omega_{hf} = 2\pi 333$  rad/s. Fig. (3.5) reflects the difference between terms.

Similarly and to prove the correlation of the model, a similar simulation was performed over the expressions (3.27) and (3.28). Evaluating these expressions according to the resulting terms from (3.26) at both frequencies, makes it possible to obtain the original  $R_{abc}$  and  $L_{abc}$  terms, as it is reflected on Fig. 3.6, which has similar results as the ones shows in Fig. 3.4.

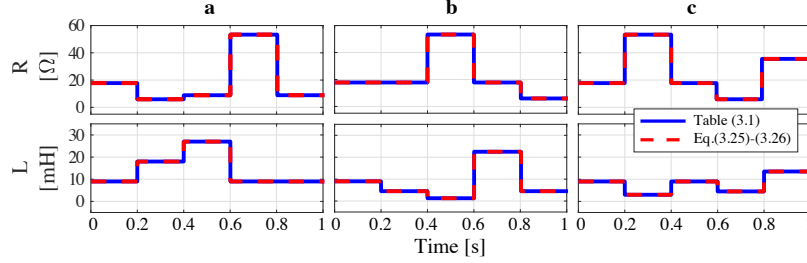


**Figure 3.6:** Simulation Results: Comparison between the original resistive and inductive values and the ones obtained from the expressions (3.27) and (3.28).

### 3.2.4 Admittance Model

Considering the admittance as the inverse of the impedance, it might be interesting to propose another expression based on (3.10), which allows to express the flowing current of the system based on the admittance and the voltage across the system. Based on this, the admittance model may be defined as (3.29), where  $n$ , correspond to every load considered in the system.

$$\mathbf{Y}_{\alpha\beta} = \sum_{i=1}^n \left( \underbrace{\frac{\Sigma Z_i}{\Sigma Z_i^2 - \Delta Z_i^2}}_{\Sigma Y_i} \begin{bmatrix} 1 & 0 \\ 0 & 1 \end{bmatrix} - \underbrace{\frac{\Delta Z_i}{\Sigma Z_i^2 - \Delta Z_i^2}}_{\Delta Y_i} \begin{bmatrix} -\cos \theta_i & \sin \theta_i \\ \sin \theta_i & \cos \theta_i \end{bmatrix} \right) \quad (3.29)$$

Moreover, considering that the voltage at the PCC is a variable easily measured, it would be greatly convenient to have an expression for the current in terms of the symmetrical components and the aforementioned voltage. Since current results from the product of the admittance and the voltage, it may be expressed as depicted in (3.30).

$$\mathbf{i}_{\alpha\beta} = \mathbf{Y}_{\alpha\beta} \cdot \mathbf{v}_{\alpha\beta} \quad (3.30)$$

Additionally, in order to provide a physical reasoning to every term presented in (3.10), it is interesting to appeal to the symmetrical components theorem, described in Appendix C. According this, any unbalanced system of  $n$  elements may be decomposed in a sum of the same number of balanced elements. Consequently, voltage and currents may be defined as (3.31).

$$\begin{aligned} \mathbf{x}_{\alpha\beta}^+ &= \mathbf{A}^{-1} \cdot \mathbf{x}_{abc}^+ \\ \mathbf{x}_{\alpha\beta}^- &= \mathbf{A}^{-1} \cdot \mathbf{x}_{abc}^- \\ x_0 &= \frac{1}{3}(x_a + x_b + x_c) \end{aligned} \quad (3.31)$$

The combination of the three set of equations (3.29), (3.30) and (3.31) yields to decomposition of the currents into (3.32).

$$\begin{aligned} \mathbf{i}_{\alpha\beta} = & V_{\alpha\beta}^+ \sum_{i=1}^n \left[ \Sigma Y_i e^{j\omega_e t} - \Delta Y_i e^{-j(\omega_e t + \theta_e^i)} \right] \\ & + V_{\alpha\beta}^- \sum_{i=1}^n \left[ \Sigma Y_i e^{-j\omega_e t} - \Delta Y_i e^{j(\omega_e t - \theta_e^i)} \right] \end{aligned} \quad (3.32)$$

$$\begin{aligned} \mathbf{i}_0 = & V_0 \sum_{i=1}^n \left[ \frac{1}{\Sigma Z_i} \right] \\ & + V_{\alpha\beta}^+ \sum_{i=1}^n \left[ \frac{\Delta Y_i^2}{\Sigma Y_i} k_0 \left( e^{j\omega_e t} - \frac{\Sigma Y_i}{\Delta Y_i} e^{j(\omega_e t + \theta_e^i)} \right) \right] \\ & + V_{\alpha\beta}^- \sum_{i=1}^n \left[ \frac{\Delta Y_i^2}{\Sigma Y_i} k_0 \left( e^{-j\omega_e t} - \frac{\Sigma Y_i}{\Delta Y_i} e^{-j(\omega_e t - \theta_e^i)} \right) \right] \end{aligned} \quad (3.33)$$

where

$$\Sigma Y_i = \frac{\Sigma Z_i}{\Sigma Z_i^2 - \Delta Z_i^2}; \quad \Delta Y_i = \frac{\Delta Z_i}{\Sigma Z_i^2 - \Delta Z_i^2} \quad (3.34)$$

Equations (3.32) and (3.33) show the relation between every term of the unbalance and the impedance, where  $\omega_e$  is the grid frequency,  $k_0$  is a constant that may be  $\sqrt{2}$  in case the *Clarks transformation* is power invariant or 2 in case the transformation is magnitude invariant.  $V_{\alpha\beta}^+$ ,  $V_{\alpha\beta}^-$  and  $V_0$  are the positive, negative and zero sequence magnitudes of the voltage vector.

The proposed model allows obtaining a compact expression, at constant frequency, based on the  $\alpha\beta 0$  terms of the current vector and depending on the equivalent impedance as seen from a voltage source. This can be used for isolating the different parameters in real time, having applications ranging from impedance estimation to unbalance compensation.

### 3.3 System Definition for Real Time Implementation

Once the impedance model has been presented, it is necessary to find a suitable implementation that allows the use under real time applications. In order to compare the proposed model with the traditional symmetrical components approach, (3.35) provides the expression for the positive, negative and zero components derived from equation (3.32).

$$\begin{aligned} \begin{pmatrix} \mathbf{i}_{\alpha\beta}^+ \\ \mathbf{i}_{\alpha\beta}^- \\ \mathbf{i}_0 \end{pmatrix} = & \sum_{i=1}^n \left\{ \Sigma Y_i \begin{pmatrix} 1 & 0 & 0 \\ 0 & 1 & 0 \\ 0 & 0 & 1 \end{pmatrix} - \right. \\ & \left. \Delta Y_i \begin{pmatrix} 0 & e^{j\theta_e^i} & 0 \\ e^{j\theta_e^i} & 0 & 0 \\ \sqrt{2} \left( e^{j\theta_e^i} - \frac{\Delta Y_i}{\Sigma Y_i} \right) & \sqrt{2} \left( e^{j\theta_e^i} - \frac{\Delta Y_i}{\Sigma Y_i} \right) & \frac{\Delta Y_i}{\Sigma Y_i} \end{pmatrix} \right\} \begin{pmatrix} V_{\alpha\beta}^+ \\ V_{\alpha\beta}^- \\ V_0 \end{pmatrix} \end{aligned} \quad (3.35)$$

The expression presented in (3.35) is in vectorial notation, where  $\alpha$  is associated with the real term and  $\beta$  with the complex one. Symmetrical components are linked with the positive and negative terms based on the interpretation of the  $\Sigma Y_i$  and  $\Delta Y_i$  elements. According to (3.35),  $\Delta Y_i$  represents the cross-term and links opposite sequences between each other. Considering the symmetrical components theory, the current terms are related with the voltage ones according to (3.36).

$$\begin{bmatrix} i_{\alpha}^{+} \\ i_{\beta}^{+} \\ i_{\alpha}^{-} \\ i_{\beta}^{-} \end{bmatrix} = \begin{bmatrix} \Sigma Y_{\alpha i} & -\Sigma Y_{\beta i} & -\Delta Y_{\alpha i} & \Delta Y_{\beta i} \\ \Sigma Y_{\beta i} & \Sigma Y_{\alpha i} & \Delta Y_{\beta i} & \Delta Y_{\alpha i} \\ \Delta Y_{\alpha i} & -\Delta Y_{\beta i} & \Sigma Y_{\alpha i} & -\Sigma Y_{\beta i} \\ -\Delta Y_{\beta i} & -\Delta Y_{\alpha i} & \Sigma Y_{\beta i} & \Sigma Y_{\alpha i} \end{bmatrix} \begin{bmatrix} v_{\alpha}^{+} \\ v_{\beta}^{+} \\ v_{\alpha}^{-} \\ v_{\beta}^{-} \end{bmatrix} \quad (3.36)$$

Where,  $\Delta Y_{\alpha i} = |\Delta Y_i| \cos \theta_e^i$  and  $\Delta Y_{\beta i} = |\Delta Y_i| \sin \theta_e^i$  and  $\Sigma Y_{\alpha i}$  corresponds to real elements of  $\Sigma Y_i$  and the  $\Sigma Y_{\beta i}$  with the imaginary ones. This relation is very useful for on-line impedance estimation techniques, since it is possible to determine a relation of the unbalance magnitude, based on the measured variables at the PCC. Equations (3.32) to (3.35) build the proposed model, in Fig. 3.1, by adding together all the admittances at the PCC using the superposition theorem. The equivalent admittance at the PCC can be defined as (3.37).

$$\mathbf{Y}_{\alpha\beta} = \frac{1}{\Sigma Z_{eq}^2 - \Delta Z_{eq}^2} \left( \Sigma Z_{eq} \begin{bmatrix} 1 & 0 \\ 0 & 1 \end{bmatrix} + \Delta Z_{eq} \begin{bmatrix} -\cos(\theta_{eq}) & \sin(\theta_{eq}) \\ \sin(\theta_{eq}) & \cos(\theta_{eq}) \end{bmatrix} \right) \quad (3.37)$$

The equivalent mean and differential admittance terms can be obtained based on (3.38) and (3.39). Clearly, the two equations can be solved in real time with low computational burden, thus allowing for a simple identification method.

$$\Sigma Y_{eq}^{\alpha\beta} = \frac{i_{\alpha\beta}^{+} \cdot v_{\alpha\beta}^{+} - i_{\alpha\beta}^{-} \cdot v_{\alpha\beta}^{-}}{(v_{\alpha\beta}^{+})^2 - (v_{\alpha\beta}^{-})^2} \quad (3.38)$$

$$\Delta Y_{eq}^{\alpha\beta} = \frac{i_{\alpha\beta}^{-} \cdot v_{\alpha\beta}^{+} - i_{\alpha\beta}^{+} \cdot v_{\alpha\beta}^{-}}{(v_{\alpha\beta}^{+})^2 - (v_{\alpha\beta}^{-})^2} \quad (3.39)$$

Equivalent expressions for the impedance terms are also obtained by the combination of (3.34) with (3.38) and (3.39) terms, resulting in (3.40) and (3.41), respectively.

$$\Sigma Z_{eq}^{\alpha\beta} = \frac{v_{\alpha\beta}^{+} \cdot i_{\alpha\beta}^{+} - v_{\alpha\beta}^{-} \cdot i_{\alpha\beta}^{-}}{(i_{\alpha\beta}^{+})^2 - (i_{\alpha\beta}^{-})^2} \quad (3.40)$$

$$\Delta Z_{eq}^{\alpha\beta} = \frac{v_{\alpha\beta}^{-} \cdot i_{\alpha\beta}^{+} - v_{\alpha\beta}^{+} \cdot i_{\alpha\beta}^{-}}{(i_{\alpha\beta}^{+})^2 - (i_{\alpha\beta}^{-})^2} \quad (3.41)$$

However, it has to be considered that  $\Sigma Z_i$  and  $\Delta Z_i$  are complex magnitudes based on its definition in (3.11) and (3.12), which implies the need for an additional correlation between them and the real physical magnitudes obtained from (3.40) and (3.41). According to (3.15), real terms are linked with the resistive components and the imaginary terms with the reactive ones. But, due to the algebra of the transformation, the initial imaginary terms are rotated and they are not aligned with the imaginary axis any more. Additionally the frequency of the system affects the magnitude of the terms in (3.40) and (3.41). Consequently the use of the model within a real time identification technique requires an additional expression able to engage every term with the initial definition from (3.15). Expansion of the expressions (3.17)

and (3.20) leads to (3.42) and (3.43), which are the resulting terms based on the phase component of the system. These expressions are particularly relevant since they engage the inductive phase terms according to their frequency and the incremental terms associated to  $\Delta Z$ , which is required for the identification of the impedance magnitude at different frequencies.

$$\Delta R_i = \underbrace{\frac{1}{3} \left( R_a - \frac{R_b}{2} - \frac{R_c}{2} \right)}_{\Delta R_\alpha} + j \underbrace{\frac{1}{3} \left( \frac{\sqrt{3}}{2} (R_b - R_c) \right)}_{\Delta R_\beta} \quad (3.42)$$

$$\Delta X_i = \underbrace{\frac{1}{3} \omega_i \left( L_a - \frac{L_b}{2} - \frac{L_c}{2} \right)}_{\Delta X_\alpha} + j \underbrace{\frac{1}{3} \omega_i \left( \frac{\sqrt{3}}{2} (L_b - L_c) \right)}_{\Delta X_\beta} \quad (3.43)$$

Expressions (3.44)-(3.47) link every term obtained according to (3.40) and (3.41) with the expressions in (3.42) and (3.43).

$$\Re\{\Sigma Z_{eq}^{\alpha\beta}\} = \Sigma R_i; \quad (3.44)$$

$$\Im\{\Sigma Z_{eq}^{\alpha\beta}\} = \Sigma X_i; \quad (3.45)$$

$$\Re\{\Delta Z_{eq}^{\alpha\beta}\} = \Delta R_\alpha - \Delta X_\beta; \quad (3.46)$$

$$\Im\{\Delta Z_{eq}^{\alpha\beta}\} = \Delta X_\alpha + \Delta R_\beta; \quad (3.47)$$

These expressions are used on the analytical simulation presented in Fig. 3.7, which proves the equivalence between terms in the expressions (3.44)-(3.47).

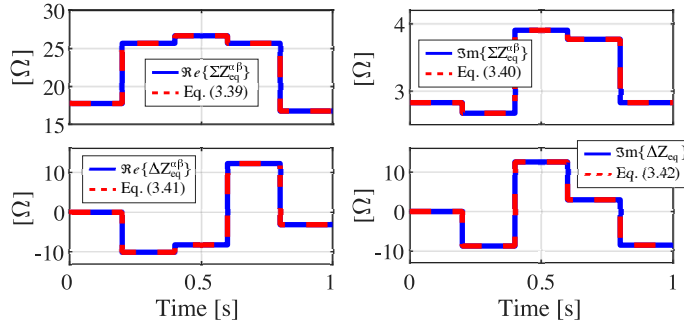


**Figure 3.7:** Simulation results: Comparison between the expressions (3.40)-(3.41) and (3.44)-(3.47).

### 3.4 Equivalence with the Instantaneous Power Theory

According to the review provided in Appendix D, in a generic three phase system, instantaneous active and reactive power are defined in the traditional  $abc$  components as (3.48) and

(3.49).

$$p = v_a i_a + v_b i_b + v_c i_c \quad (3.48)$$

$$q = \frac{1}{\sqrt{3}} (v_{ab} i_c + v_{bc} i_a + v_{ca} i_b) \quad (3.49)$$

These power equations can be expressed in terms of the  $\alpha\beta$  components according to the conventional imaginary complex power expression,  $\mathbf{s}$ , as (3.50).

$$\mathbf{s} = \mathbf{v} \cdot \mathbf{i}^* = (v_\alpha + jv_\beta)(i_\alpha - ji_\beta) = \underbrace{(v_\alpha i_\alpha + v_\beta i_\beta)}_p + j \underbrace{(v_\beta i_\alpha - v_\alpha i_\beta)}_q \quad (3.50)$$

Expression (3.50) is the result of the product of the voltage space vector and the conjugated current space vector. Generally,  $\mathbf{s}$  is expressed in terms of phasors, however using space vector components yields the same results as applying equation (D.3) in  $\alpha\beta$  components, resulting in (3.51) and (3.52).

$$p = \mathbf{v}_{\alpha\beta} \cdot \mathbf{i}_{\alpha\beta} = v_\alpha i_\alpha + v_\beta i_\beta \quad (3.51)$$

$$q = \mathbf{v}_{\alpha\beta} \times \mathbf{i}_{\alpha\beta} = v_\beta i_\alpha - v_\alpha i_\beta \quad (3.52)$$

Particularizing the system for the unbalance conditions induced by an impedance change, together with a distorted input voltage, equations (D.4) and (D.5) lead to (3.53).

$$\begin{bmatrix} p \\ q \end{bmatrix} = \begin{bmatrix} (v_\alpha^+ + v_\alpha^-) \cdot (i_\alpha^+ + i_\alpha^-) + (v_\beta^+ + v_\beta^-) \cdot (i_\beta^+ + i_\beta^-) \\ (v_\beta^+ + v_\beta^-) \cdot (i_\alpha^+ + i_\alpha^-) - (v_\alpha^+ + v_\alpha^-) \cdot (i_\beta^+ + i_\beta^-) \end{bmatrix} = \begin{bmatrix} \bar{P} + \tilde{P} \\ \bar{Q} + \tilde{Q} \end{bmatrix} \quad (3.53)$$

where  $\bar{P}$  and  $\bar{Q}$  represent the average power term resulting from the interaction of voltage and current components with the same frequency and sequence. On the other hand,  $\tilde{P}$  and  $\tilde{Q}$  represent the oscillating energy flow from the interaction of the negative sequence and harmonic terms. A more detailed explanation of obtaining these variables is provided in Appendix D. Based on (3.35), the current space vectors can be defined in terms of the grid admittance as it is reflected in (3.54).

$$\begin{aligned} \mathbf{i}_{\alpha\beta}^{(+)} &= \Sigma Y \cdot V_{\alpha\beta}^+ - \Delta Y \cdot V_{\alpha\beta}^- \cdot e^{-j\theta} \\ \mathbf{i}_{\alpha\beta}^{(-)} &= \Sigma Y \cdot V_{\alpha\beta}^- - \Delta Y \cdot V_{\alpha\beta}^+ \cdot e^{-j\theta} \end{aligned} \quad (3.54)$$

The combination of (3.53) with (3.54) enables to establish a link between the proposed expression and the instantaneous power theory.

$$p = \Sigma Y [v_\alpha^2 + v_\beta^2] + \Delta Y_\alpha [v_\alpha^2 - v_\beta^2] + 2\Delta Y_\beta [v_\alpha v_\beta] \quad (3.55)$$

$$q = \Sigma Y [v_\alpha^2 + v_\beta^2] + \Delta Y_\beta [v_\alpha^2 - v_\beta^2] + 2\Delta Y_\alpha [v_\alpha v_\beta] \quad (3.56)$$

where  $\Delta Y_\alpha = |\Delta Y| \cdot \cos(\theta)$ ;  $\Delta Y_\beta = |\Delta Y| \cdot \sin(\theta)$  and  $v_\alpha^2 = (v_\alpha^+ + v_\alpha^-)^2$ ;  $v_\beta^2 = (v_\beta^+ + v_\beta^-)^2$ . Multiple studies on the control of active filters under unbalanced grid voltage conditions [3.14–3.18] have collected the terms in (D.13) and (D.14) according to (3.57).

$$\begin{bmatrix} P_0 \\ Q_0 \\ P_1 \\ P_2 \end{bmatrix} = \frac{3}{2} \begin{bmatrix} v_\alpha^+ & v_\beta^+ & v_\alpha^- & v_\beta^- \\ v_\beta^+ & -v_\alpha^+ & v_\beta^- & -v_\alpha^- \\ v_\alpha^- & v_\beta^- & v_\alpha^+ & v_\beta^+ \\ v_\beta^- & -v_\alpha^- & -v_\beta^+ & v_\alpha^+ \end{bmatrix} \begin{bmatrix} i_\alpha^+ \\ i_\beta^+ \\ i_\alpha^- \\ i_\beta^- \end{bmatrix} \quad (3.57)$$

where  $P_0$  and  $Q_0$  represent the average value of the instantaneous active and reactive power, whereas  $P_1$  and  $P_2$ , are related to the oscillatory terms which does not contribute to the power transfer. Expression (3.57) results from the following criterion:

- i. Under regular operation, the active power exchanged in an ideal network is based on  $P_{ref} = P_{average} = P_0$  and the reactive power is based on the requirements of the system  $Q_{ref} = Q_{average} = Q_0$
- ii. Under unbalance, the amplitude of the voltage harmonic has to be reduced to the lowest feasible level, ideally zero, resulting in  $P_{c2} = P_{s2} = 0$ .

Thus, it is possible to establish four levels of freedom, according to  $[i_{\alpha}^+, i_{\alpha}^-, i_{\beta}^+, i_{\beta}^-]$  to calculate four out the six power magnitudes already defined. Expanding and combining equations (3.55), (3.56) and (3.57), the resulting power equations yields to (3.58).

$$\begin{bmatrix} P_0 \\ Q_0 \\ P_1 \\ P_2 \end{bmatrix} = \frac{3}{2} \left[ \Sigma Y_{\alpha i} \begin{pmatrix} v_{\alpha}^+ & v_{\beta}^+ & v_{\alpha}^- & v_{\beta}^- \\ 0 & 0 & 0 & 0 \\ v_{\alpha}^- & v_{\beta}^- & v_{\alpha}^+ & v_{\beta}^+ \\ v_{\beta}^- & -v_{\alpha}^- & -v_{\beta}^+ & v_{\alpha}^+ \end{pmatrix} \right. \quad (3.58) \\ \left. + \Sigma Y_{\beta i} \begin{pmatrix} 0 & 0 & 0 & 0 \\ v_{\beta}^+ & -v_{\alpha}^+ & v_{\beta}^- & -v_{\alpha}^- \\ 0 & 0 & 0 & 0 \\ 0 & 0 & 0 & 0 \end{pmatrix} + \Delta Y_{\alpha i} \begin{pmatrix} 0 & 0 & 0 & 0 \\ 0 & 0 & 0 & 0 \\ v_{\alpha}^+ & -v_{\beta}^+ & -v_{\alpha}^- & v_{\beta}^- \\ -v_{\beta}^+ & -v_{\alpha}^+ & -v_{\beta}^- & -v_{\alpha}^- \end{pmatrix} \right. \\ \left. + \Delta Y_{\beta i} \begin{pmatrix} 0 & 0 & 0 & 0 \\ 0 & 0 & 0 & 0 \\ -v_{\beta}^+ & -v_{\alpha}^+ & v_{\beta}^- & v_{\alpha}^- \\ -v_{\alpha}^+ & v_{\beta}^+ & -v_{\alpha}^- & v_{\beta}^- \end{pmatrix} \right] \begin{bmatrix} v_{\alpha}^+ \\ v_{\beta}^+ \\ v_{\alpha}^- \\ v_{\beta}^- \end{bmatrix}$$

As can be noticed in (3.58), the pulsating terms,  $P_1, P_2$ , are only present under unbalanced conditions, since they are result of the interaction between sequences and the combination with  $\Delta Y$ . Keep in mind that  $\Delta Y$  is the term associated with the unbalance of the impedance, being zero in case of balanced condition. On the contrary, the average terms,  $P, Q$ , are always present independently of the conditions.

Algebraic manipulation of (3.58) allows to provide an expression, (3.59), which relates the admittances with the power commands. This is meaningful from the point of view of the converter operation, since it is possible to define the impedance of the system based on the commanded power references.

$$\begin{bmatrix} \Sigma Y_{\alpha i} \\ \Sigma Y_{\beta i} \\ \Delta Y_{\alpha i} \\ \Delta Y_{\beta i} \end{bmatrix} = \frac{1}{(v_{\alpha}^+)^2 + (v_{\beta}^+)^2 + (v_{\alpha}^-)^2 + (v_{\beta}^-)^2} \begin{bmatrix} P_0 \\ Q_0 \\ P_1 \\ P_2 \end{bmatrix} \quad (3.59)$$

### 3.5 Model Evaluation

In previous sections, the consistency of the algorithm based on the equivalence between the impedance phases and the terms in the  $\alpha\beta$  reference frame has been proved. In the present

section, the developed model accuracy is evaluated by comparing its results from the ones given by a time-domain circuitual simulation under Matlab/Simulink<sup>®</sup>. The resulting currents and voltages are calculated based on the equivalent impedance, according to the proposed method. To maintain the consistency in the explanation, the same step changes as those presented in Table 3.1 are considered in this section. To prove the validity of the model under voltage variations, changes at the voltage source are also considered.

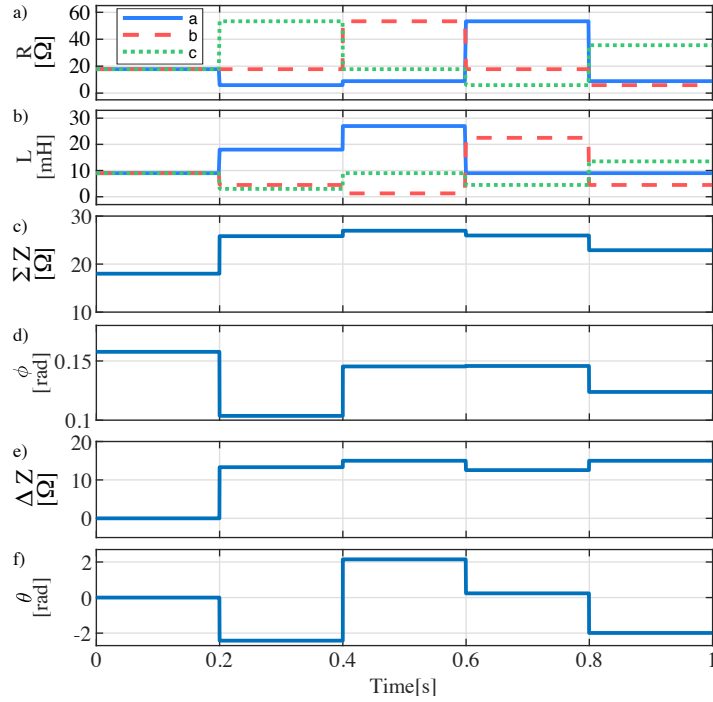
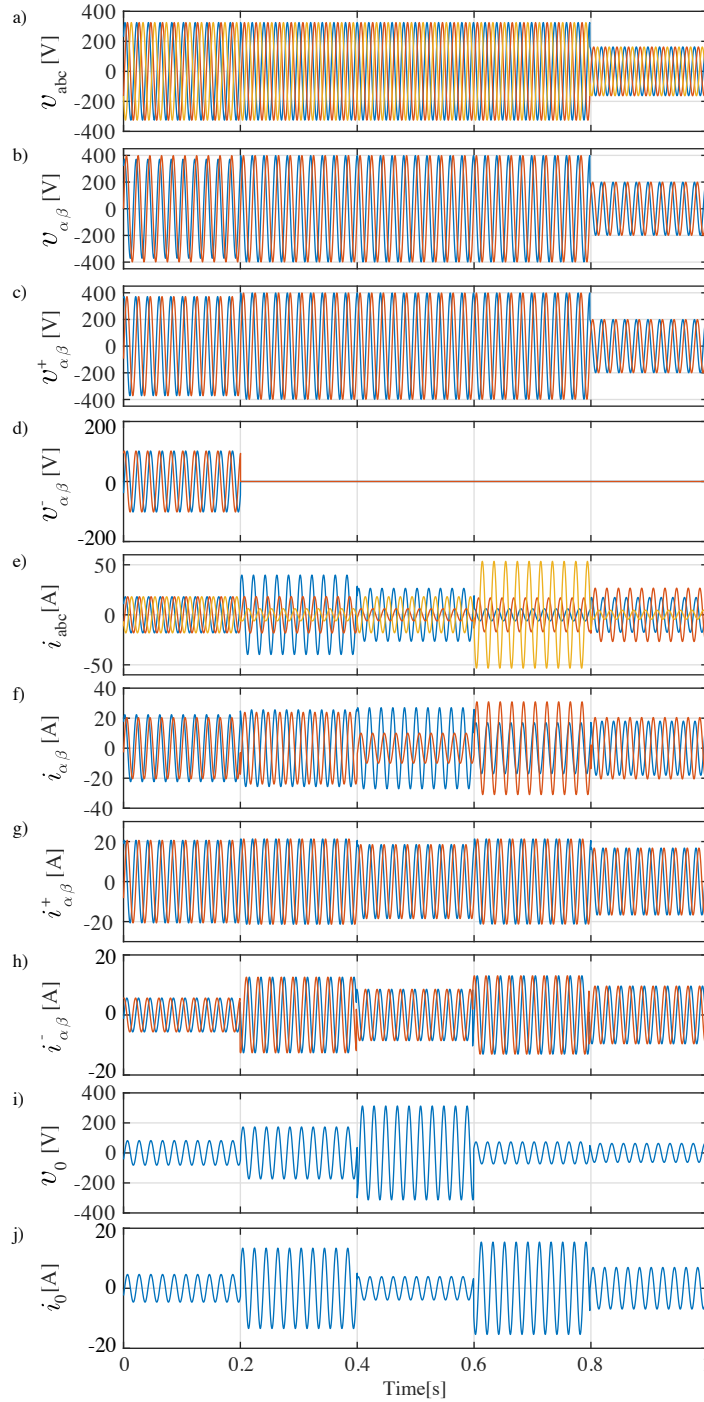


**Figure 3.8:** Simulation test. a) Resistive component of phase impedances; b) Inductance component of phase impedances; c)  $\Sigma Z$  value according to the equivalent impedance; d)  $\Sigma Z$  angle; e)  $\Delta Z$  value according to the equivalent impedance; f)  $\Delta Z$  angle, corresponding with the unbalance angle.

The simulation is carried out for a three phase system in a wye-connection with neutral configuration, as the one depicted in Fig. 3.1. All the currents and voltages represented in this section are those obtained at the PCC of the system. Figure 3.8 a) and b) show the impedance steps induced in every phase, according to the resistive and the inductive terms. In the graphs below the corresponding values for the impedance terms  $\Sigma Z$  c), its angle  $\phi$  d) and  $\Delta Z$  e) and its angle  $\theta$  f) are included.

Figure 3.9 a) and b) shows the three phase voltages at the PCC and its  $\alpha\beta$  component. Fig. 3.9 c), d) and e) shows the positive, negative and zero sequence voltage, respectively. The same correspondence is replicated for the current components in the graphs from f) to j).

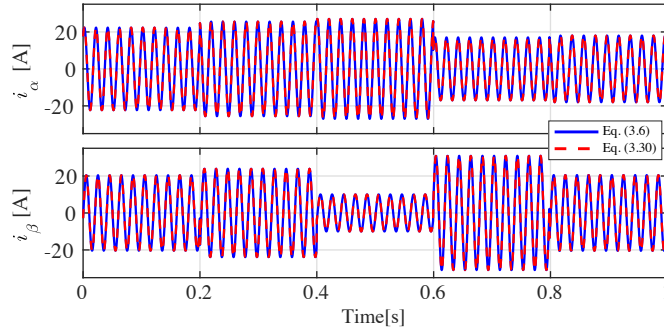
The different test conditions are enumerated in the following: Initially, the system is under balanced condition. As expected,  $\Delta Z = 0$  and the angle of the asymmetry is also held at zero.



**Figure 3.9:** Simulation results based on the voltage and impedance variations at the PCC. a) Phase voltages; b)  $\alpha\beta$  Voltage components; c) Positive sequence voltage; d) Negative sequence voltage; e) Phase currents; f)  $\alpha\beta$  Current components; g) Positive sequence currents; h) Negative sequence currents; i) Zero voltage component; j) Zero sequence current.

**Table 3.2:** Impedance values

	$t_1$	$t_2$	$t_3$	$t_4$	$t_5$
$\Sigma Z$ [ $\Omega$ ]	17.78	25.82	26.95	25.95	17.03
$\phi$ [rad]	0.1577	0.1036	14.54	0.1458	0.1668
$\Delta Z$ [ $\Omega$ ]	0.0	13.31	14.99	12.55	9.11
$\Theta$ [rad]	0.0	-2.42	2.15	0.23	-1.92

**Figure 3.10:** Simulations Results. Current comparison; a)  $\alpha$  current component; b)  $\beta$  current component.

However, grid voltage at *phase a* lags 45 deg., demonstrating that the algorithm takes into consideration the voltage distortion to estimate the current components. A negative sequence voltage is induced into the system with a magnitude of 100 V and, similarly, the zero sequence voltage component, shown in Fig. 3.9 i), reaches a magnitude of 82 V, as result of the distorted voltage.

At  $t = 0.2$  s, the impedance from the three phases is changed according to the values in Table 3.1. Consequently, both  $\Sigma Z$  and  $\Delta Z$  vary from 18  $\Omega$  to 25.82  $\Omega$  and from 0  $\Omega$  to 13.31  $\Omega$  respectively.

Similarly, angle  $\phi$  varies from 0.157 rad to 0.1036 rad and  $\theta$  from 0 rad to  $-2.42$  rad. It is also important to note that the value of  $\theta$  is equal to the unbalance orientation, resulting in an angle of  $-139$  deg. In summary, the unbalance level is codified by the  $\Delta Z$  level and the  $\theta$  angle provides its direction. The effect of the unbalance is coupled to the current vector components, as shown in Fig. 3.9 f),g), h) and j). When the impedance unbalance is applied, the negative sequence component of the current vector ( $i_{\alpha\beta}^-$ ), shown in Fig. 3.9 h), is modulated according to the developed expressions, resulting in 12.57 A. Considering the neutral connection, a zero sequence current ( $i_0$ ) of 13.4 A, flows into the system, as it is reflected in Fig. 3.9 j). In the same manner a zero sequence voltage is also present in the system, with a magnitude of 173.3 V. The rest of the values for every component of the impedance are shown in Table 3.2.

At instant  $t = 0.4$  s, the impedance of *phase a*, *phase b* and *phase c* is changed, according to the values in Table 3.1. These changes induced a negative sequence current, with a magnitude of 8.56 A. This also causes an increase in the resulting zero sequence voltage from 173.3 V to 313 V. At  $t = 0.6$  s, another system impedance change is induced, although the unbalance between phases as  $|Z_a| = 0.8$  p.u.;  $|Z_b| = 1$  p.u. and  $|Z_c| = 0.7$  p.u. remains constant. This results in a variation of the negative sequence current and in the homopolar voltage as well,

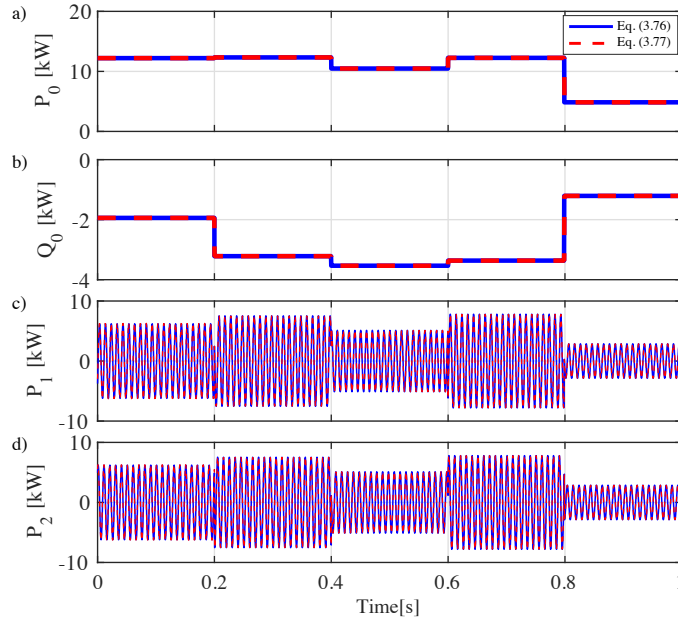


**Figure 3.11:** Simulations Results. Comparison between the results obtained based on expression (3.57) and (3.58); a) Active power component,  $P_0$ ; b) Reactive power component,  $Q_0$ ; c) First pulsating term associated with the active component,  $P_1$ ; d) Second pulsating term associated with the active component,  $P_2$ .

with a magnitude of 15.15 A and 74 V, respectively. Finally, at  $t = 0.8$  s the voltage grid is stepped down into 163 V in the three phases, as reflected in Fig. 3.9 a). Moreover, the impedance is not kept balanced, as becomes apparent from the zero sequence current and voltage, which are reduced to 6.8 A and 63 V, respectively.

Additionally, in Fig. 3.10 there is a comparison between the  $\alpha\beta$  currents resulting from (3.6) and the ones obtained from expression (3.32). The close agreement proves the equivalence of the proposed expression.

Figure 3.11 shows the results of an additional simulation by depicting the signals derived from the application of (3.58) to the instantaneous voltage and currents from the simulation presented in Fig. 3.9 and under the same conditions as depicted above.

As it can be seen in Fig. 3.11 a) and b), the  $P_0$  and  $Q_0$  terms are kept independently of the simulated conditions. Thus, only the terms linked with the harmonics show an oscillatory behaviour. The negative value of the  $Q_0$  component is associated with the inductive characteristic of the load used to prove the consistency of the algorithm.

### 3.6 Conclusion

A novel modelling technique has been presented in this chapter in order to express the impedance of a generic system, independently from the number of loads connected at the PCC.

This technique highlights the coupling between the positive, the negative and the zero sequence components of both currents and voltages, providing a coherent and intuitive expression linked with the voltage distortion and the load unbalanced.

The main contributions of this chapter are summarized in:

- An elegant expression for the impedance linked with the positive, negative and zero sequences arising under unbalance conditions.
- An expression for the admittance at the PCC, enabling to obtain the corresponding current drawn by the system. This expression allows the use of the mentioned algorithm as a tool for sensorless estimation, which will be the starting point for the discussions of the next chapters.
- An analysis of the traditional power theories in literature and the derivation of an equivalent expression for the power, based on the impedance of the system, linked with the impedance variations presented under unbalance conditions.
- An analysis of the voltage and current sequences resulting from the fluctuations of the impedance of the system and from the voltage unbalances.

## References

- [3.1] F. Bastiao, P. Cruz, and R. Fiteiro, "Impact of distributed generation on distribution networks," in *Electricity Market, 2008. EEM 2008. 5th International Conference on European*, may 2008, pp. 1–6.
- [3.2] R. Walling, R. Saint, R. Dugan, J. Burke, and L. Kojovic, "Summary of distributed resources impact on power delivery systems," *Power Delivery, IEEE Transactions on*, vol. 23, no. 3, pp. 1636–1644, july 2008.
- [3.3] V. Khadkikar, "Enhancing electric power quality using upqc: A comprehensive overview," *IEEE Transactions on Power Electronics*, vol. 27, no. 5, pp. 2284–2297, 2012.
- [3.4] M. Savaghebi, A. Jalilian, J. Vasquez, and J. Guerrero, "Autonomous voltage unbalance compensation in an islanded droop-controlled microgrid," *IEEE Transactions on Industrial Electronics*, vol. PP, no. 99, p. 1, 2012.
- [3.5] C. Po-Tai, C. Chien-An, L. Tzung-Lin, and K. Shen-Yuan, "A cooperative imbalance compensation method for distributed-generation interface converters," *IEEE Transactions on Industry Applications*, vol. 45, no. 2, pp. 805–815, 2009.
- [3.6] C. J. Melhorn, T. D. Davis, and G. E. Beam, "Voltage sags: their impact on the utility and industrial customers," *IEEE Transactions on Industry Applications*, vol. 34, no. 3, pp. 549–558, May 1998.
- [3.7] A. Tuladhar, , T. Unger, and K. Mauch, "Control of parallel inverters in distributed ac power systems with consideration of line impedance effect," *IEEE Transactions on Industry Applications*, vol. 36, no. 1, pp. 131–138, Jan 2000.
- [3.8] P. L. Chapman and S. D. Sudhoff, "A multiple reference frame synchronous estimator/regulator," *IEEE Transactions on Energy Conversion*, vol. 15, no. 2, pp. 197–202, June 2000.
- [3.9] E. Uz-Logoglu, O. Salor, and M. Ermis, "Online characterization of interharmonics and harmonics of ac electric arc furnaces by multiple synchronous reference frame analysis," *IEEE Transactions on Industry Applications*, vol. 52, no. 3, pp. 2673–2683, May 2016.
- [3.10] P. C. Krause, "Method of multiple reference frames applied to the analysis of symmetrical induction machinery," *IEEE Transactions on Power Apparatus and Systems*, vol. PAS-87, no. 1, pp. 218–227, Jan 1968.
- [3.11] E. Clarke, *Circuit Analysis of A-C Power Systems*. New York: Wiley, 1950.
- [3.12] P. García, M. Sumner, Á. Navarro-Rodríguez, J. M. Guerrero, and J. García, "Observer-based pulsed signal injection for grid impedance estimation in three-phase systems," *IEEE Transactions on Industrial Electronics*, vol. 65, no. 10, pp. 7888–7899, Oct 2018.
- [3.13] M. Saad, H. Ali, H. Liu, S. Khan, H. Zaman, B. M. Khan, D. Kai, and J. Yongfeng, "A dq-domain impedance measurement methodology for three-phase converters in distributed energy systems," *Energies*, vol. 11, no. 10, 2018. [Online]. Available: <http://www.mdpi.com/1996-1073/11/10/2732>
- [3.14] P. Rioual, H. Poulquen, and J. . Louis, "Regulation of a pwm rectifier in the unbalanced network state using a generalized model," *IEEE Transactions on Power Electronics*, vol. 11, no. 3, pp. 495–502, May 1996.
- [3.15] I. Etxeberria-Otadui, U. Viscarret, M. Caballero, A. Rufer, and S. Bacha, "New optimized pwm vsc control structures and strategies under unbalanced voltage transients," *IEEE Transactions on Industrial Electronics*, vol. 54, no. 5, pp. 2902–2914, Oct 2007.

- 
- [3.16] Yongsug Suh and T. A. Lipo, "Control scheme in hybrid synchronous stationary frame for pwm ac/dc converter under generalized unbalanced operating conditions," *IEEE Transactions on Industry Applications*, vol. 42, no. 3, pp. 825–835, May 2006.
  - [3.17] Hong-Seok Song and Kwanghee Nam, "Dual current control scheme for pwm converter under unbalanced input voltage conditions," *IEEE Transactions on Industrial Electronics*, vol. 46, no. 5, pp. 953–959, Oct 1999.
  - [3.18] K. Ma, W. Chen, M. Liserre, and F. Blaabjerg, "Power controllability of a three-phase converter with an unbalanced ac source," *IEEE Transactions on Power Electronics*, vol. 30, no. 3, pp. 1591–1604, March 2015.



## Chapter 4

# Grid Impedance Estimation Considering Passive Loads

### 4.1 Introduction

Measurement of the unbalanced components in an electric grid, i.e. negative and zero sequence voltages and currents, for compensation purposes is a challenging task. Two options are currently used, each of those having an important drawback. The first one consist in relaying on the voltages at the point of common coupling (PCC), which can be greatly affected by the grid impedance value; however, if the converter is coupled to a strong grid, the resulting impedance may yield the negative and zero sequence voltage values to be within the resolution limits of the voltage sensors [4.1]. Alternatively, current sensors can be used for the measurement of the converter negative and zero sequence currents. Unfortunately, to comply with compensation tasks, additional current sensors need to be placed either at the load or at the grid side.

In the previous chapter, a modelling technique, which enables the definition of a generic impedance model based on the voltage that feeds the system, was presented. In the present one, a technique, based on the aforementioned algorithm, is introduced as a tool for impedance estimation, without the need of devoted sensors into the system. Identification of the negative and zero sequence under unbalanced conditions is achieved and a method for compensating the unbalance is presented. Simulations and experimental results are shown as a proof of the consistency of the method.

The chapter begins with a brief introduction of the system configuration and with an analysis of the limitations to identify the impedance of the system based on the data available. The data acquisition technique presented in this chapter is based on the injection of a high frequency signal, followed by the adaptation of that information to grid frequency. A compensation technique is proposed based on the estimation technique. The proposed technique is tested by simulations and experimental results; moreover, a solution for the identification and compensation of the negative sequence component is extensively demonstrated. Finally the chapter is closed with the conclusions drawn from the results of the method.

## 4.2 System Description

A 3-phase system with neutral connection is considered in Fig. 4.1. A VSC is connected to the PCC together with  $n$  loads. Upstream from the PCC, the grid is represented by a voltage source with a short-circuit impedance given by  $L_{sc}$  and  $R_{sc}$ , which feeds a distribution transformer. The feeder which interconnects the transformer with the PCC is represented by a series impedance,  $L_{feeder}$  and  $R_{feeder}$ .

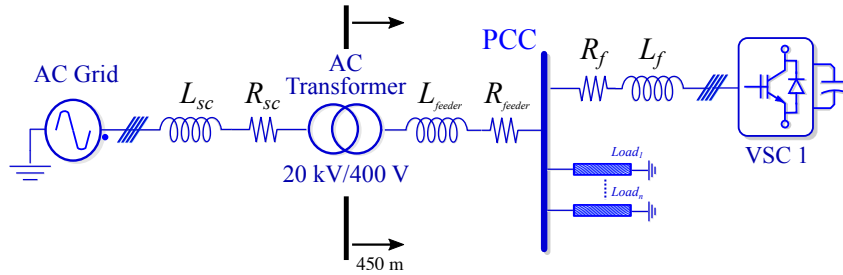


**Figure 4.1:** Real system interconnection of the 3-phase grid elements

The system in Fig. 4.1 can be approximated by the schematic shown in Fig. 4.2, where the load represents an equivalent model for all loads connected at PCC and  $L_g$  and  $R_g$  stands for the resistive and inductive components of the grid, respectively.

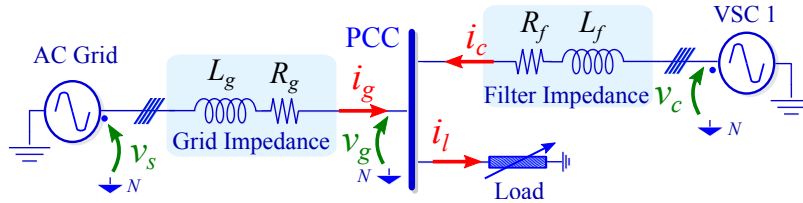


**Figure 4.2:** Equivalent schematic from system in Fig. 4.1

From the point of view the converter, the voltage at PCC,  $v_g$ , and the current  $i_c$  are known variables, however, an unbalance load causes negative and zero sequence components which potentially jeopardize the grid supplied voltages.

Converter VSC 1 should be responsible for estimating the magnitude of the unbalance based on the equivalent impedance resulting from it. Compensation might be done by injecting negative and zero sequence currents in opposition to the respective unbalanced currents [4.2]. However, isolating and further eliminating the negative sequences is not a straightforward task. Based on the solutions already presented in Chapter 2, impedance estimation methods consisting on HFSI are the ones which offer a wider range of possibilities from the point of view of the THD induced into the system and the reliability of the algorithm.

Moreover, the possibility of using the power converter to inject a low-magnitude and high-frequency signal at the PCC, makes HFSI methods an attractive solution to implement the algorithm already presented in Chapter 3.

### 4.2.1 Problem Statement

In the following, the impedance of the system is defined as the ratio between the voltage at the PCC and the current flowing into the system, as was previously stated in (3.5). This value,  $Z$ , is taken as a generic grid impedance, independently of the number of loads and their magnitude. Obtaining this impedance just from the voltage and current measurements obtained at the converter side is not enough to perform an accurate model of the system and thus, additional sensors are required at the load or at the grid side. This will be proved based on the impedance calculation results shown in Fig. 4.3. The test setup and all the laboratory aspects required to perform the experimental verification are presented in Appendix E.

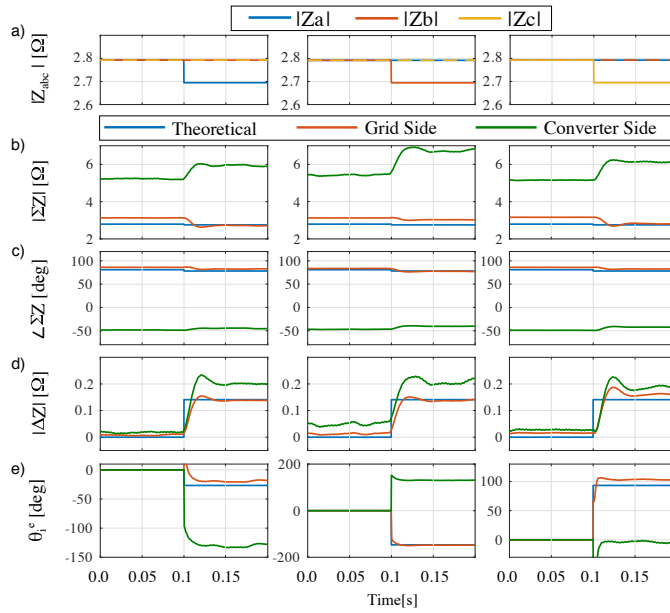


**Figure 4.3:** Experimental Results. Equivalent grid impedance at the PCC measured at 50Hz. From left to right: Unbalance induced in phase  $a$ , phase  $b$  and phase  $c$ . From top to bottom: a) phase impedances, b)  $|\Sigma Z|$  component, c) phase of  $\Sigma Z$ , d)  $|\Delta Z|$  component and e)  $\theta_i^e$ , which corresponds to the unbalance angle.

Being the system under evaluation the one shown in Fig. 4.2 and under balanced conditions, three set of experiments have been performed, one per each phase. Each of these tests consist in inducing a load unbalance by changing the impedance of the load at each phase at instant 0.1 s. Calculation of the impedance terms at 50 Hz are based on expressions (3.11), (3.12) and (3.13), which are shown in blue trace in Fig. 4.3 a)-e). These theoretical results have been compared with the terms obtained from evaluating expressions (3.40) and (3.41) with real measurements, at both grid and converter side. For the case of the grid side, expressions (3.40) and (3.41) are particularized in (4.1) and (4.2), being the ones labelled as *Grid Side*.

$$\Sigma Z_g^{\alpha\beta} = \frac{(v_{g\alpha\beta}^+ - v_{c\alpha\beta}^+) \cdot i_{g\alpha\beta}^+ - (v_{g\alpha\beta}^- - v_{c\alpha\beta}^-) \cdot i_{g\alpha\beta}^-}{(i_{g\alpha\beta}^+)^2 - (i_{g\alpha\beta}^-)^2} \quad (4.1)$$

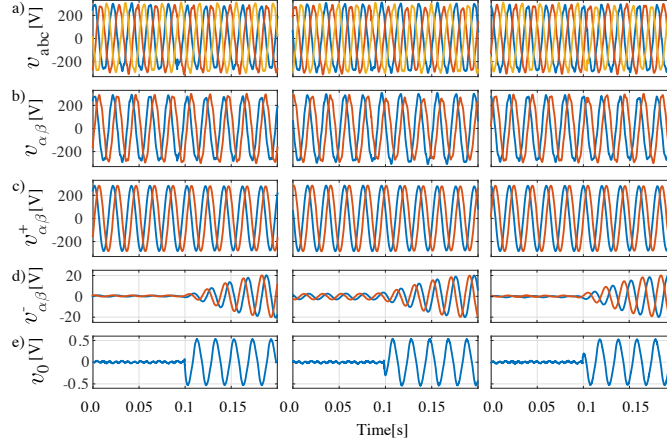


**Figure 4.4:** Experimental results. Voltage measurements at the PCC, under three different unbalance conditions as a consequence of a change in the load impedance. Unbalance is induced by connecting a parallel  $18 \Omega$  load at 0.1 s, to the  $18 \Omega$  balanced load at the PCC. From left to the right: Unbalance induced in phase  $a$ , unbalance induced in phase  $b$  and unbalance induced in phase  $c$ . From top to bottom: a) phase voltages, b)  $\alpha, \beta$  components, c), d) and e) are the positive, negative and zero sequence components of the voltage vector.

$$\Delta Z_g^{\alpha\beta} = \frac{(v_{g\alpha\beta}^- - v_{c\alpha\beta}^-) \cdot i_{g\alpha\beta}^+ - (v_{g\alpha\beta}^+ - v_{c\alpha\beta}^+) \cdot i_{g\alpha\beta}^-}{(i_{g\alpha\beta}^+)^2 - (i_{g\alpha\beta}^-)^2} \quad (4.2)$$

where  $v_{g\alpha\beta}$  and  $i_{g\alpha\beta}$  are the PCC voltage and the grid current and  $v_{c\alpha\beta}$  and  $i_{c\alpha\beta}$  are the voltage and current at the converter side.

For the three cases, the VSC 1 is operated in STATCOM mode, where  $d$ -axis is devoted to maintaining the DC-link at nominal voltage and the remaining level of freedom is used to inject a constant current of 10 A in the  $q$ -axis. The VSC is commanded to inject current to illustrate the effect of the load unbalance over the converter current.

At initial time, the impedance load at the PCC is balanced and equal for the three phases ( $Z_a = Z_b = Z_c = 18 \Omega$ ). As expected, neither negative nor zero components are present within the system. Figure 4.4 gathers voltage measurements at the PCC of the system according to the configuration shown in Fig. 4.2 for the three set of experiments. Similarly, the measured currents from the grid and converter sides are shown in Figs. 4.5 and 4.6, respectively. At instant 0.1 s, a  $18 \Omega$  load is connected in parallel to phase  $a$ , decreasing the initial impedance value at this phase by 50 %. Voltage unbalance arises at the PCC, where a negative sequence voltage value of 14.4 V is measured, as it is shown in Fig. 4.4. The presence of the unbalance is also reflected in both Figs. 4.5 and 4.6 where 11.2 A of zero sequence current starts flowing through the system. Similarly, 1.2 A of negative sequence current is measured from the converter side and 5.2 A, from the grid side.

The test is repeated by inducing the same unbalance in the other two phases (results from unbalance in phase  $b$  and  $c$  are shown in the middle and right columns, respectively). Similar results are obtained in the measurements of the voltage and current magnitudes.

The interesting aspect of this set of experiments lies on the comparison of the unbalance angle,  $\theta_e^i$ , already defined in (3.13), which depends on the phase affected by the unbalance (see

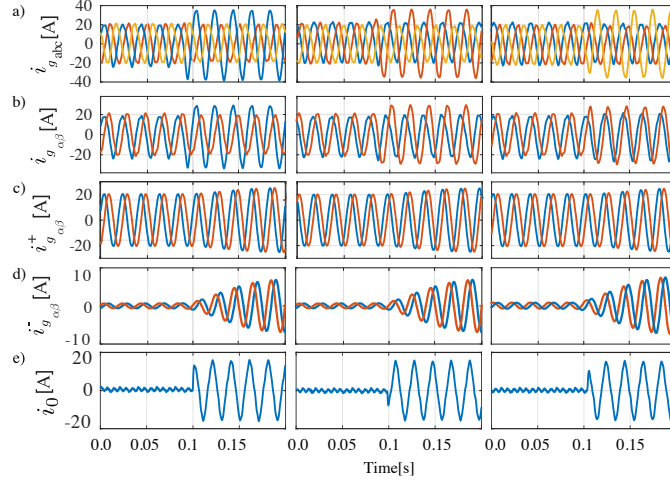


**Figure 4.5:** Experimental results. Grid current measurement, under the three different unbalance conditions described in Fig. 4.4. From left to right: Unbalance induced in phase  $a$ , unbalance induced in phase  $b$  and unbalance induced in phase  $c$ . From top to bottom: a) phase currents, b)  $\alpha, \beta$  components, c), d) and e) are the positive, negative and zero components of the current vector.

Fig. 4.3 e)). In the first case, the impedance angle changes from 0 deg to  $-26.67$  deg. In the second case, where the unbalance takes place in phase  $b$ ,  $\theta_i^c$  changes from 0 deg to  $-148.3$  deg. Notice that this result is 120 deg delayed with respect to the unbalance in phase  $a$ , ideally should be  $\theta_b = -26.67 - 120 = -146.67$  deg. The difference between the theoretical result and the experimental one is considered within the tolerance error. For the unbalance in phase  $c$ , the change is from 0 deg to  $93.33$  deg, which corresponds to  $\theta_c = 120 - 26.67 = 93.33$  deg. The remaining variables depicted in Fig. 4.3 are not dependent on the phase unbalance but only on the magnitude of the unbalance. For this reason,  $|\Sigma Z|$  decreases from  $2.8 \Omega$  to  $2.7 \Omega$  and  $|\Delta Z|$  increases at instant 0.1 s from 0 to  $0.15 \Omega$ .

As shown in Fig. 4.3, there are evident differences between the impedance results obtained from the converter side (green line) and those observed from the grid side (red line). This proves that an extra sensor is required. This clear inaccuracy is a consequence of the lack of information on the unbalance contained in the converter side currents. As it has been already pointed out, requiring an extra sensor for the grid side current,  $i_{g,\alpha\beta}$ , is undesirable, and thus, an impedance estimation method capable of doing without it would be a serious improvement.

This situation may be solved by the addition of a high frequency signal at the converter side. This is theoretically supported by Fig. 4.7, which shows a schematic simplification from the system of Fig. 4.2. By applying the *superposition theorem* [4.3], the original circuit can be split into two: one at grid frequency, 50 Hz, which includes the grid voltage source, and the other one at the high frequency of the added signal. At 50 Hz, the presence of the grid voltage source affects the voltage seen by the converter at the PCC, making impossible to estimate the current load without additional sensors (whether at the load or grid side). However, an analysis of the circuit at the frequency of the high-frequency signal, allows an estimation based on the information gathered just by the converter sensors. Notice that, at this frequency, the voltage provided by the converter is the only source in the circuit.

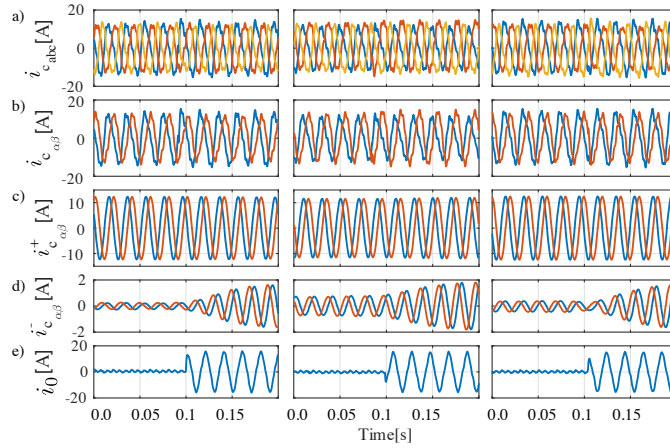


**Figure 4.6:** Experimental results. Converter current measurement at the PCC, under the three different unbalance conditions described in Fig. 4.4. From left to right: Unbalance induced in phase  $a$ , phase  $b$  and phase  $c$ . From top to bottom: a) phase currents, b)  $\alpha, \beta$  components, c), d) and e) are the positive, negative and zero components of the current vector.

In the following section, an approach to unbalance estimation based on the injection of a high frequency signal is proposed. The proposed method will enable the estimation of grid impedance based exclusively on converter side values, thus becoming a sensorless procedure.

## 4.3 High Frequency Signal Injection

As mentioned in Chapter 2, HFSI methods are based on the injection of a low voltage signal into the system and the subsequent analysis of the system response. The voltage signal might be commanded within the current control of the VSC, however, the selection of the magnitude of this signal as well as its frequency is not a despicable aspect, being affected by several factors.

### 4.3.1 Frequency Selection

The selection of the frequency to perform the injection as well as the magnitude of the signal has to be done based on the following considerations:

- i. The current control loop of the VSC might react and compensate the injected signal if the bandwidth of the controller (typically in a range of 100-500 Hz [4.4]) is above of the signal injection frequency. A solution to avoid this inconvenience might be to choose the frequency of injection above the bandwidth of the current controller. Complementary, a possible solution could be to install a notch filter in the current feedback tuned at the frequency of the injections. In this way, the controller would become insensitive to the high frequency signal.

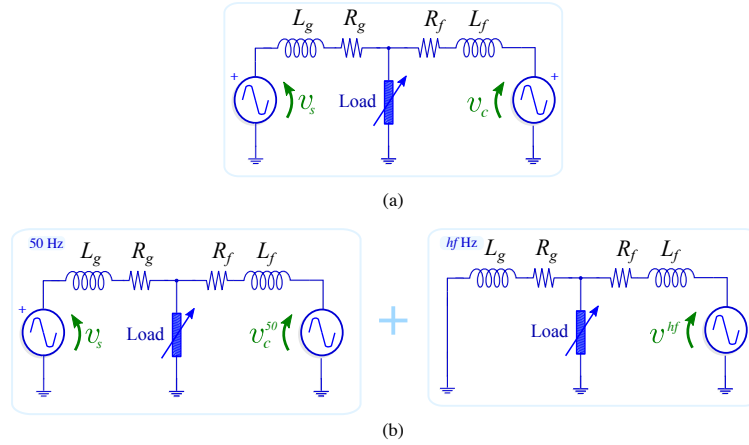


**Figure 4.7:** (a) Equivalent circuit of Fig. 4.2 (b) Equivalent circuit at different frequencies according to the Superposition Theorem

- ii. The resulting signal derived from the injection,  $\mathbf{i}_{\alpha\beta}^{hf}$ , will have positive and negative components since they are complex vectors. It has to be kept under consideration that filtering negative sequence current from the positive one is easier at higher frequencies, since there is more spectral separation. This fact allows to increase the resolution of the system at light unbalance conditions
- iii. The magnitude and frequency values can be tuned separately. From a power quality perspective, increasing the frequency and reducing the magnitude is preferred. However, this reduces the signal to noise ratio of the method [4.5]. Moreover, the selection of the frequency should provide enough spectral separation from the current controller bandwidth and, according to Nyquist Theorem, should not be higher than half the switching frequency if synchronous sampling is to be used.
- iv. The interharmonic frequency should be selected, not to interfere with possible additional shunt-connected converters at the PCC, which may compensate the injected signal in case of being an integer multiple of the fundamental frequency [4.6]
- v. The selection of the frequency of the excitation signal should avoid frequency bands typically affected by other compensating systems which may be present in the grid (e.g.  $-5^{th}$ ,  $7^{th}$ ).
- vi. In order to avoid resonance issues, when the converter is interfaced with the grid through an LCL filter, its resonance frequency should be considered. Typically, this value falls between ten times grid frequency and one-half of the switching frequency [4.7]. In this case, considering a switching frequency of 10 kHz, the resonance frequency should lie between 0.5 and 5 kHz.

Based on the enumerated considerations, the voltage excitation magnitude was chosen to be 10 V and the excitation frequency was selected to be far enough from the multiple harmonics of the grid and above 250 Hz. The following set of frequencies are all valid for the aim of this study: 333; 433; 633; 763 Hz. Note that the developed model does not take any assumption

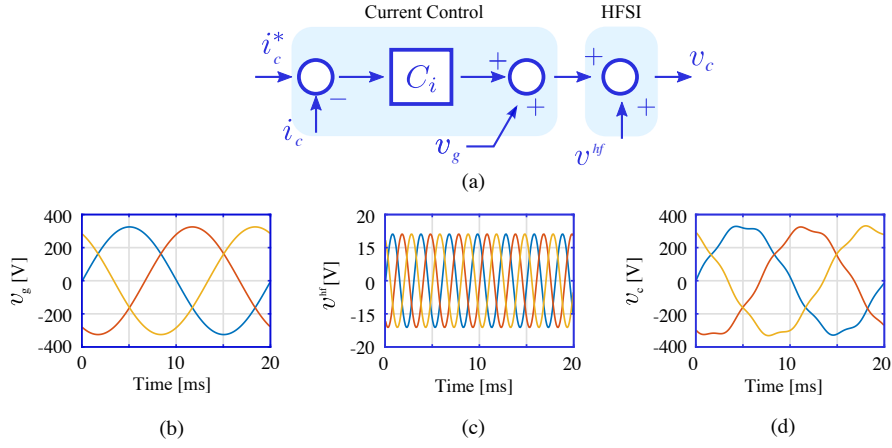


**Figure 4.8:** (a) HFSI schematic implemented within the current control of the VSC; (b) Voltage at the PCC which is added at the output of the conventional current control; (c) High frequency signal injected just after the output of the current loop; (d) Resulting voltage which will be synthesized at the output of the VSC

about the excitation frequency, and thus, it can be used to any fix frequency excitation just changing the  $\omega_{hf}$  variable by the frequency of interest.

### 4.3.2 Method Implementation

If a balanced high frequency ( $\omega_{hf}$ ) carrier-signal voltage,  $\mathbf{v}_{\alpha\beta}^{hf}$ , as denoted by (4.3), is added to the converter voltage command, as it is depicted in Fig. 4.8, it will induce a high frequency current given by (4.4).

$$\mathbf{v}_{\alpha\beta}^{hf} = V^{hf} e^{j\omega_{hf}t} \quad (4.3)$$

$$\mathbf{i}_{\alpha\beta}^{hf} = V^{hf} \sum_{i=1}^n \left[ \Sigma Y_i^{hf} e^{j\omega_{hf}t} + \Delta Y_i^{hf} e^{j(-\omega_{hf}t + \theta_e^i)} \right] \quad (4.4)$$

According to the modelling procedure already presented in Chapter 3, this high frequency current includes a high-frequency negative sequence component determined by the impedance unbalance, that can be modelled as in (4.5).

$$\begin{aligned} \mathbf{i}_{\alpha\beta}^{hf} = & V_{\alpha\beta}^{hf+} \sum_{i=1}^n \left[ \Sigma Y_i e^{j\omega_{hf}t} - \Delta Y_i e^{-j(\omega_{hf}t + \theta_{hf}^i)} \right] \\ & + V_{\alpha\beta}^{hf-} \sum_{i=1}^n \left[ \Sigma Y_i e^{-j\omega_{hf}t} - \Delta Y_i e^{j(\omega_{hf}t - \theta_{hf}^i)} \right] \end{aligned} \quad (4.5)$$

Figure 4.8 shows a schematic of the high frequency signal injection into the current control loop of the VSC. The high frequency signal ( $v^{hf}$ ) is injected at the output of the current

control, just after the grid voltage feedback ( $v_g$ ). The feedback current,  $i_c$  in Fig. 4.8, has been filtered not to include the high frequency signal inside the controller. The expression of the resulting high frequency current provided by (4.5), is based on (3.32). Notice that the latter equation is valid for any excitation voltage with fixed frequency. However, two important differences arises when compared with the expression at grid frequency:

- i. As the high frequency voltage is created by the converter and superimposed to the fundamental voltage, the resulting high frequency converter current,  $i_c^{hf}$ , contains the unbalance information. Hence, measuring the current at the load,  $i_l$ , or grid side,  $i_g$ , is not needed to proceed with the compensation.
- ii. Isolating the negative sequence current from the positive one is easier at higher frequencies, since there is more spectral separation. This allows to increase the resolution of the system, making it feasible to deal even with light unbalance conditions.

The fact that current in (4.5) provides information about the unbalance and the admittance of the system allows its use as a sensorless impedance estimation tool, in combination with the modelling technique presented in the previous chapter.

### 4.3.3 Equivalent Impedance Terms at High Frequency

The model presented in Chapter 3 has been proved to be an alternative solution to define the impedance of any system. Based on the expressions (3.40) and (3.41), it is possible to determine the impedance terms at a certain frequency for any system in real time. Thus, if a voltage signal is injected at 333 Hz, (4.6) and (4.7) are valid expressions to identify  $\Sigma Z_{eq}$  and  $\Delta Z_{eq}$  at that frequency, since it is the only excitation present in the system at that frequency as it has been reflected in Fig. 4.7.

$$\Sigma Z_{eq}^{hf} = \frac{v_{\alpha\beta}^{hf+} \cdot i_{\alpha\beta}^{hf+} - v_{\alpha\beta}^{hf-} \cdot i_{\alpha\beta}^{hf-}}{\left(i_{\alpha\beta}^{hf+}\right)^2 - \left(i_{\alpha\beta}^{hf-}\right)^2} \quad (4.6)$$

$$\Delta Z_{eq}^{hf} = \frac{v_{\alpha\beta}^{hf-} \cdot i_{\alpha\beta}^{hf+} - v_{\alpha\beta}^{hf+} \cdot i_{\alpha\beta}^{hf-}}{\left(i_{\alpha\beta}^{hf+}\right)^2 - \left(i_{\alpha\beta}^{hf-}\right)^2} \quad (4.7)$$

However, for such case, since the estimation is performed at a different frequency from the one from the grid, the magnitudes of  $\Sigma Z_{eq}^{\alpha\beta}$  and  $\Delta Z_{eq}^{\alpha\beta}$  components obtained at 333 Hz are different to the ones expected at 50 Hz.

Moreover the phase impedance of the load will be different from the equivalent one seen by the converter, since the latter is affected by grid impedance, as it is shown in Fig. 4.7(b). Based on this fact, the next section studies the performance of the method according to the frequency injection and the connection of the load to the PCC.

## 4.4 Equivalent Impedance of Passive Loads

The high frequency method has been initially adapted to identify the impedance of a system loaded by passive loads. Considering as passive loads, such elements that present a



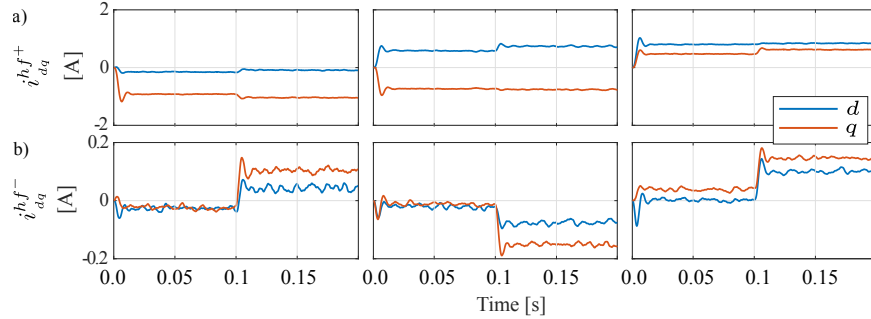


**Figure 4.10:** Experimental results. High frequency converter current. Each column presents the results considering an unbalance in a different phase, left column: unbalance in phase  $a$ , in the middle: unbalance in phase  $b$  and column at the right: unbalance in phase  $c$ . From top to bottom: a) Positive sequence of the high frequency current signal in the  $dq$  reference frame at 333 Hz, b) Negative sequence in the  $dq$  reference frame at 333 Hz.

A comparison of the impedance terms, similar to the one presented in the previous section, is shown in Fig. 4.11. In this case, it consists of a comparison of the results obtained from the Matlab/Simulink<sup>®</sup> simulation, the results extracted from the theoretical expressions at high frequency (3.11)-(3.12), based on the phase impedance terms, and the results from evaluating expressions (4.6)-(4.7) with real measurements, from Fig. 4.9 and 4.10.

The sequence of the experiment is similar to the one explained above in Fig. 4.3. Under balanced conditions, at instant 0.1 s, an additional load of 18  $\Omega$  is connected to one of the phases of the load, inducing an unbalance in the system. According to this, every impedance term is calculated only based on the converter side measurements. The same experiment is repeated for every phase and each column of the figures represents the unbalance in one of the phases.

The results in real time are shown in Fig. 4.11, however, to facilitate the analytical analysis, the numerical results are also provided in Table 4.1, which summarizes the RMS current values, at 50 Hz and 333 Hz ( $hf$  superscript), of the model, the simulation and the experimental results. In this table,  $t_1$  and  $t_2$ , represent the instants before and after the connection of the additional load causing the unbalance. The left columns show the current values that are obtained by applying the mathematical model presented in (3.32). The middle and right columns of Table 4.1 provide the results obtained from a MATLAB/Simulink<sup>®</sup> model, and from the experimental results, respectively. The results are shown, in rows, for each of the phases, and the error is provided as a percentage of the results obtained from the model.

The current values presented in Table 4.1 are calculated based on the equivalent impedance of the system in Fig. 4.2, both at 50 Hz and 333 Hz. As it was stated above, grid currents,  $I_{g\alpha\beta}^+$  and  $I_{g\alpha\beta}^-$ , are produced by the interaction of both grid and converter voltages. These estimated grid currents are supported by the results presented in Fig. 4.5(c) and (d). On the contrary,  $I_{\alpha\beta}^{hf+}$  and  $I_{\alpha\beta}^{hf-}$  result from the high frequency excitation signal provided by the converter, according to (4.3). Thus, for this case, only the converter voltage at 333 Hz needs to be considered. Clearly, there is a close agreement among the proposed model, the simulation and the experimental results for all the tested conditions. Nevertheless, small deviations are perceived in the experimental results, due to the fact that the simulations are conducted using

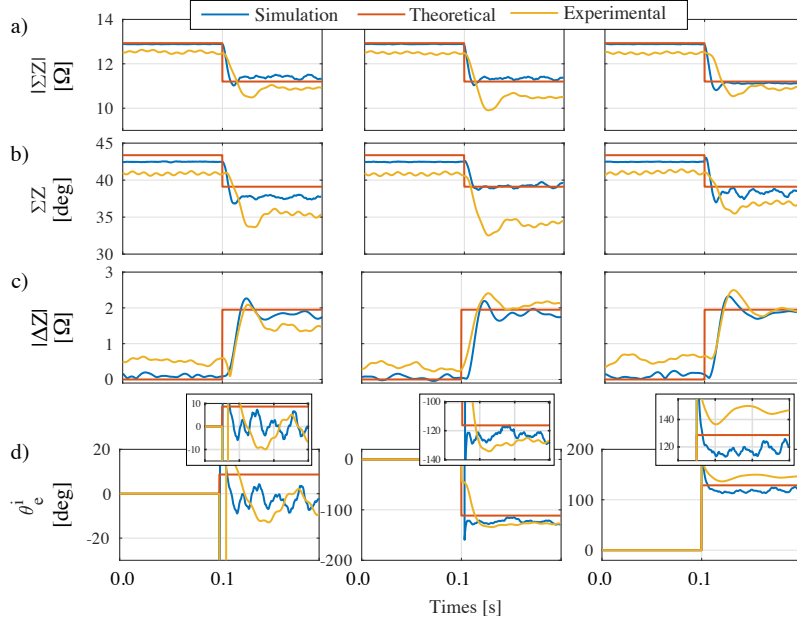


**Figure 4.11:** Experimental Results: Comparison of the results obtained in simulation (blue line), theoretical expression (red line) and experimental results (yellow line) of the presented method. Each column presents the results considering an unbalance in a different phase, left column: unbalance in phase  $a$ , in the middle: unbalance in phase  $b$  and column at the right: unbalance in phase  $c$ . From top to bottom: a) Equivalent value of  $\Sigma Z$ , b) Angle in deg. of the  $\Sigma Z$ , c) Equivalent value of  $\Delta Z$  and d)  $\theta_e^i$ .

an ideal voltage source. This might not be the case in the experimental tests, where a real grid is taken as PCC, thus including non-ideal voltage conditions. Besides that fact, calibration differences among the three current and voltage sensors are possible causes of the error which, in any case, remains below 9% for all the conducted tests.

In order to achieve the proposed sensorless unbalance compensation, the equivalent differential admittance/impedance at the PCC, as seen by the AC network at the fundamental frequency, should be determined. With this aim, these values must be related with those previously obtained at the high-frequency injected by the power converter. With the definition of variables used in Fig. 4.2, (3.32) can be represented in compact form as (4.8), whereas (4.4) is given by (4.9).

$$I_{g\alpha\beta}^{\omega_e} = Y_{eq\alpha\beta}^{\omega_e} \cdot (V_{s\alpha\beta}^{\omega_e} - V_{\alpha\beta}^{\omega_e}) \quad (4.8)$$

$$I_{\alpha\beta}^{\omega_{hf}} = Y_{eq\alpha\beta}^{\omega_{hf}} \cdot (V_{\alpha\beta}^{\omega_{hf}} - V_{s\alpha\beta}^{\omega_{hf}}) \quad (4.9)$$

In (4.8) and (4.9),  $\omega_e$  is the fundamental frequency and  $\omega_{hf}$  the high-frequency. The  $Y_{eq}$  is the equivalent admittance at the PCC, determined from the parallel connection of the grid and the load impedances as:  $Y_{eq} = Y_g + Y_l$  and can be determined using (3.37). By analyzing (4.8) and (4.9), it is clear that the equivalent admittance can be determined, at the two different frequencies, from both expressions. In traditional unbalance compensation approaches, (4.8) is used, although, as it has been already pointed out, that requires an additional current sensor for the grid or load current. On the contrary, in the method proposed in this section, only the

**Table 4.1:** RMS Current Values Comparison

	Model		Simulation		Experimental	
	(A)		error (%)		error (%)	
<i>a</i>	<i>t</i> <sub>1</sub>	<i>t</i> <sub>2</sub>	<i>t</i> <sub>1</sub>	<i>t</i> <sub>2</sub>	<i>t</i> <sub>1</sub>	<i>t</i> <sub>2</sub>
$I_{g_{\alpha\beta}}^+$	14.42	17.68	1.05	0.34	0.0	1.2
$I_{g_{\alpha\beta}}^-$	0.0149	4.288	0.0	5.2	0.0	7.87
$I_{\alpha\beta}^{hf+}$	0.6632	0.7501	1.01	4.81	0.48	5.01
$I_{\alpha\beta}^{hf-}$	0.0197	0.1258	0.0	3.11	0.05	3.8
<i>b</i>	<i>t</i> <sub>1</sub>	<i>t</i> <sub>2</sub>	<i>t</i> <sub>1</sub>	<i>t</i> <sub>2</sub>	<i>t</i> <sub>1</sub>	<i>t</i> <sub>2</sub>
$I_{g_{\alpha\beta}}^+$	14.33	17.13	0.49	1.42	0.21	2.78
$I_{g_{\alpha\beta}}^-$	0.044	4.238	0.0	3.5	0.54	7.46
$I_{\alpha\beta}^{hf+}$	0.6679	0.7442	2.5	4.9	0.83	8.95
$I_{\alpha\beta}^{hf-}$	0.0196	0.125	0.0	3.01	3.16	3.73
<i>c</i>	<i>t</i> <sub>1</sub>	<i>t</i> <sub>2</sub>	<i>t</i> <sub>1</sub>	<i>t</i> <sub>2</sub>	<i>t</i> <sub>1</sub>	<i>t</i> <sub>2</sub>
$I_{g_{\alpha\beta}}^+$	14.26	17.36	1.68	1.48	0.08	3.77
$I_{g_{\alpha\beta}}^-$	0.0043	4.303	0.0	3.2	0.0	7.80
$I_{\alpha\beta}^{hf+}$	0.6675	0.741	2.5	5.1	0.3	5.34
$I_{\alpha\beta}^{hf-}$	0.0198	0.1198	0.0	3.09	1.10	8.85

converter current is measured, and thus, the compensation will be determined from (4.9). It is worth noting that, assuming that the grid voltage is represented as an ideal voltage source upstream the grid impedance, the high-frequency component of the grid voltage ( $V_{s_{\alpha\beta}}^{\omega_{hf}}$ ) turns out to be zero.

In the next section, a feasible solution to identify the unbalance at the grid frequency based on the gathered information from high frequency, is presented.

#### 4.4.2 Impedance Estimation at Fundamental Frequency

Under the conditions described in the previous section, an additional expression that engages the impedance expressions at grid and high frequency is required. An approach might consist in the injection of a dual high frequency signal at two different frequencies, which may allow to establish a correlation between the magnitudes and frequencies of the impedance terms. The ratio between the terms at different frequencies needs to be calculated in real time by using converter measurements. This correlation might be expressed according

to (4.10)-(4.13), where  $\omega_{hf}$  and  $\omega_{hf'}$  are the two frequencies of injection.

$$\Delta R_\alpha = \frac{\omega_{hf'} \cdot \omega_{hf}}{\omega_{hf} - \omega_{hf'}} \left( \frac{\Re\{\Delta Z_{eq}^{hf'}\}}{\omega_{hf'}} - \frac{\Re\{\Delta Z_{eq}^{hf}\}}{\omega_{hf}} \right) \quad (4.10)$$

$$\Delta R_\beta = \frac{\omega_{hf'} \cdot \omega_{hf}}{\omega_{hf'} - \omega_{hf}} \left( \frac{\Im\{\Delta Z_{eq}^{hf'}\}}{\omega_{hf}} - \frac{\Im\{\Delta Z_{eq}^{hf'}\}}{\omega_{hf'}} \right) \quad (4.11)$$

$$\Delta L_\alpha = \frac{\Im\{\Delta Z_{eq}^{hf'}\} - \Im\{\Delta Z_{eq}^{hf}\}}{\omega_{hf'} - \omega_{hf}} \quad (4.12)$$

$$\Delta L_\beta = \frac{\Re\{\Delta Z_{eq}^{hf'}\} - \Re\{\Delta Z_{eq}^{hf}\}}{\omega_{hf} - \omega_{hf'}} \quad (4.13)$$

These expressions allow to establish a correlation between the terms obtained in real time and the ones defined according to expressions (3.46) and (3.47). Moreover, combination of  $\Delta R_{\alpha\beta}$ ,  $\Delta L_{\alpha\beta}$  terms with a certain frequency,  $\omega_n$ , allows to establish an expression for  $\Delta Z_{eq}^{\alpha\beta}$  at that frequency. This is synthesized in expression (4.14), which is particularized for the case of 50 Hz and assuming an inductive profile.

$$\Delta Z_{50}^{\alpha\beta} = \Delta R_\alpha - \omega_e \Delta L_\beta + j(\omega_e \cdot \Delta L_\alpha + \Delta R_\beta) \quad (4.14)$$

From expression (4.14) it is possible to determine the corresponding  $\Sigma Z_{eq}^{\alpha\beta}$  term, at 50 Hz, based on the definition from (3.22) and (3.23).

Once the model has been defined as bidirectional, it is possible to determine the negative sequence current component resulting from the load unbalance. The procedure of estimation and later on compensation is described in the following sections.

It has to be highlighted that this approach provides information of the negative sequence present under the unbalanced conditions. It is not determining the amount of energy demanded by every single load. In this matter, it has been included in Fig. 4.12 an analysis of the equivalent impedance seen by the converter side against the frequency. A resistive load, of 18  $\Omega$ , is connected in parallel with the grid inductance. It can be seen that at high frequencies the grid side is equivalent to an open circuit from the converter side. On the contrary, at lower frequencies the equivalent impedance is a short-circuit. This aspect will be afforded in more detail in Chapter 6.

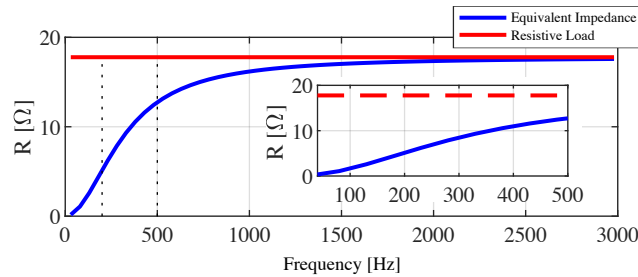


Figure 4.12: Deviation from frequency

## 4.5 Negative Sequence Current Estimation

Based on the exposition presented in the previous section, the estimation of the impedance term at 50 Hz is the first step to determine the negative sequence current induced under unbalanced conditions. A HFSI strategy is proposed to determine those unbalance conditions. Traditionally, HFSI techniques are devoted to islanding detection, requiring the injection of a single high-frequency signal. However, in the present approach, identification of the unbalanced conditions and its later on compensation, requires the injection of two high-frequency signals. Consequently, the complexity of the control loop is increased, since obtaining the control signal requires to process additional data and a filtering system that allows to isolate the signal of interest. This dynamic filtering system is a key aspect of the estimation technique. If the injected voltage signals and their resulting currents are not well isolated from the ones at grid frequency, the current controller of the VSC may react against them, frustrating any impedance estimation possibility.

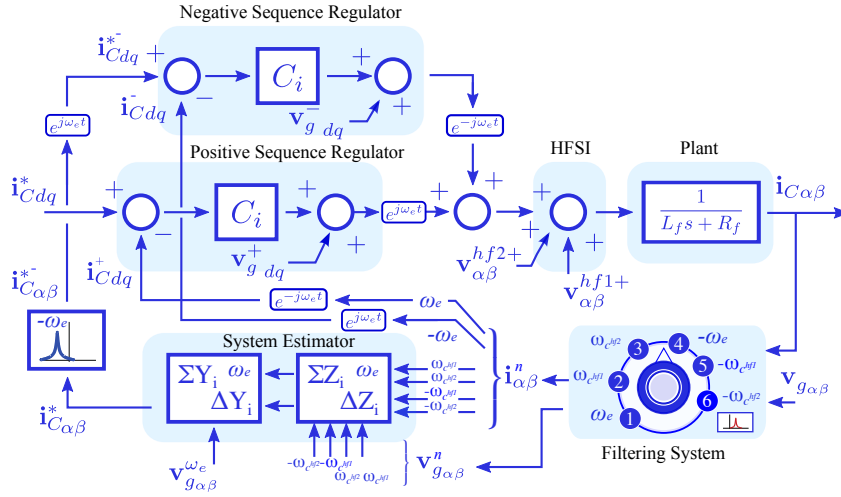
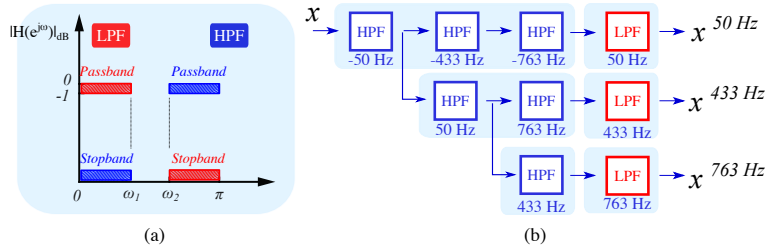


Figure 4.13: Control loop schematic

The proposed negative sequence compensation scheme is described in Fig. 4.13. Two positive sequence high frequency (433 and 763 Hz) carrier voltages,  $\mathbf{v}_{C\alpha\beta}^{hf1+}$  and  $\mathbf{v}_{C\alpha\beta}^{hf2+}$ , are added to the converter voltage command, inducing two negative sequence components in the converter current at the same frequencies,  $\mathbf{i}_{C\alpha\beta}^{hf1-}$  and  $\mathbf{i}_{C\alpha\beta}^{hf2-}$ , when an unbalance condition exist. The filtering system is responsible for isolating both the positive and negative components of the voltage and current signals at the frequencies of interest (fundamental,  $hf1$  and  $hf2$ ). Using that information and according to (4.10)-(4.14), the system unbalance at grid frequency, 50 Hz, can be estimated. Once the equivalent impedance at 50 Hz has been obtained from the impedance model, the required negative sequence current compensation can be determined using (3.32) and the voltage at the PCC,  $\mathbf{v}_{g\alpha\beta}^{\omega_e}$ . Finally, the resulting current is used as a reference driven to a negative sequence current controller.

### 4.5.1 Filtering System Description

The proper performance of the estimation technique is based on the accuracy of the filtering system to isolate each component. Voltage and current signals, at their respective frequencies, will be used to feed the estimation algorithm, and then, provide an accurate impedance value, which will be used to determine the negative sequence current term. The filtering structure designed is composed of cascaded High Pass Filters (HPF) banks (one per frequency) and an additional Low Pass Filter (LPF) at the frequency of interest. The filtering system is schematically depicted in Fig. 4.13. However; its real configuration resembles the model shown in Fig. 4.14(b). The filtering process is synthesized as follows: the measured signal,  $X$ , is used to feed the filter bank. Since fundamental frame coordinate rotation provides a frequency shift of  $-\omega_e$ , harmonic orders  $k = n \pm 1$  become  $k = n$ , where  $n$  assumes integer values. Consequently, in this frame, the positive and negative sequence harmonics of one pair are of the same order, and both can be simultaneously voided by a single HPF at that particular frequency. This fact allows to reduce the number of filters.



**Figure 4.14:** (a) Band frequencies for a HPF and LPF. (b) Schematic of the cascade filtering system for the converter voltage and current signals, according to the fundamental and the two injection frequencies.

The filters are tuned at fixed frequencies, as shown in Fig. 4.14(a). This means, the signal is rotated to each frequency and then the respective filter is applied. Fig. 4.14(b) shows the filters for the positive sequence signals. An equivalent procedure is required to isolate the negative sequences. The last LPF is responsible to erase the remaining energy from the frequency of interest. The equations of the HPFs and LPFs are shown in (4.15) and (4.16), respectively.

$$HPF(s) = \frac{s^2}{s^2 + 2\omega_0\xi s + \omega_0^2} \quad (4.15)$$

$$LPF(s) = \frac{\omega_n^2}{s^2 + \omega_n s + \omega_n^2} \quad (4.16)$$

The bandwidth of the filters is  $\omega_n = 2\pi 10$  rad/s and  $\omega_0 = 2\pi 5$  rad/s. The damping factor,  $\xi$ , has been selected to be  $\sqrt{2}$ . In order to evaluate the filter performance, the input signal has to be rotated to the corresponding reference frame, by using (4.17),

$$X_{f_o} = X_{C_{\alpha\beta}} \cdot e^{-j(\omega_i - \omega_o)} \quad (4.17)$$

where,  $\omega_i - \omega_o$  corresponds to the frequency difference between the frequencies. Then, the corresponding expression, (4.15)-(4.16), is applied to the rotated signal.

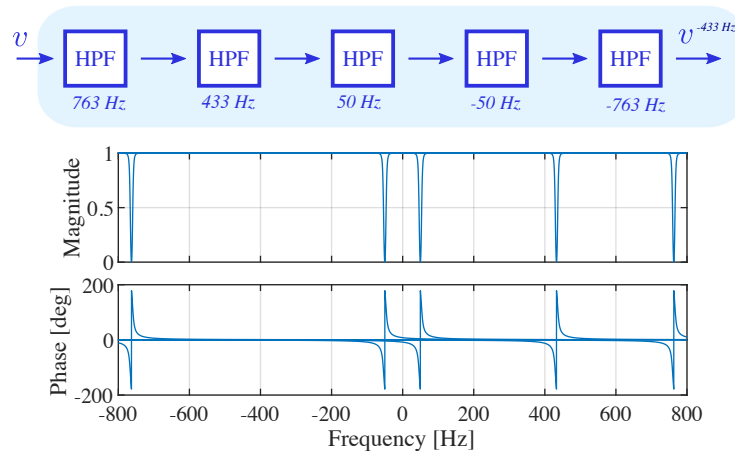
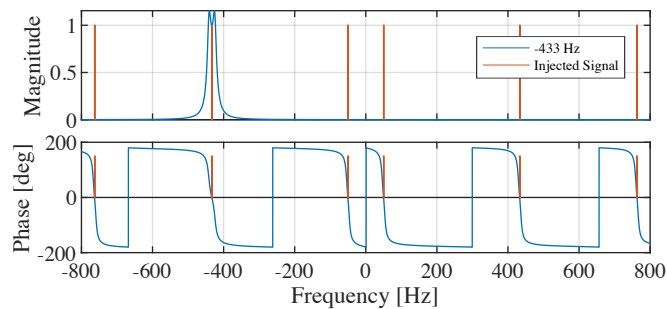


**Figure 4.15:** Isolation of the  $-433$  Hz signal after applying the HPF at the rest of frequencies

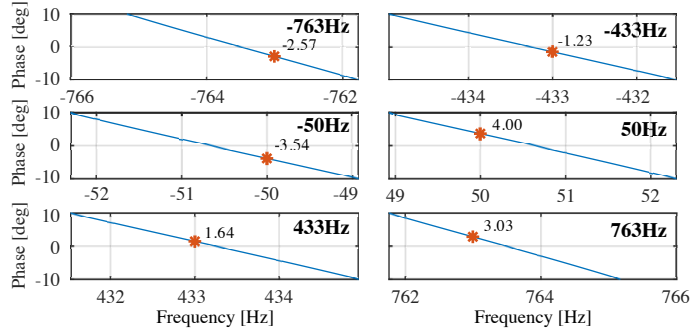
The proposed filtering structure induces changes and delays in the phase of the system, which can lead to instabilities in the control. Therefore, once the filtering bank is established, the frequency response of the system should be analysed to assure the control stability. To illustrate the procedure, the isolation of one of the negative sequence signal (at  $-433$  Hz) is analysed. Identical procedure can be carried out for the other frequencies.

Figure 4.15 shows the spectrum of the aforementioned signal, after the application of the HPFs at the different frequencies. For this case, it can be observed how the filter chain is attenuating all the frequencies of injection except for the one at  $-433$  Hz. For the sake of clarity, the LPF filter at  $-433$  Hz has not been included in Fig. 4.15. Including this last filter results in the full elimination of the rest of components, as it is shown in Fig. 4.16. In this figure, the location of the frequencies of interest has been highlighted using red bars. As expected, the spectral content at the frequencies of the HPFs has been virtually removed. This fact is corroborated by the shape of the phase trace in the angle axis, where the angle jumps from  $180$  to  $-180$  deg, in the frequencies where a HPF is applied.

Consequently, according to the number of filtering stages, a set of six voltage signals



**Figure 4.16:** Frequency spectrum obtained after the isolation of a  $-433$  Hz signal



**Figure 4.17:** Phase delay induced by the filtering chain at the frequencies of interest.

and six current signals must be obtained from the application of this methodology. The isolated components of current and voltage at grid frequency are used by the positive and negative sequence current controllers of the converter. On the other hand, the rest of isolated components are employed to obtain the equivalent impedance terms.

If the filtering chain was perfectly isolated, the zero crossing at the phase diagram of Fig. 4.16 should take place at the exact HPFs frequencies. Since the filters are not isolated, cross-coupling exist, inducing angle delays that must be compensated in order to accommodate the current signal used for the control. Those angles need to be compensated at the output of every filtering chain, within the phase of the specific signal. To determine the exact frequency-crossing, a polynomial approximation of 4<sup>th</sup> order for the phase angle trace at the frequency of interest has been done. In this manner, the exact value of the trace at that frequency can be determined. Evaluating each polynomial at the frequency of interest, the angle delays can be obtained.

Based on the configuration presented above for the six filters, the resulting phase-angle delays at each frequency are shown in Fig. 4.17. The highlighted point corresponds with the exact phase value at the frequency of interest. The delay compensation is carried out by subtracting those angles from the phase of the filtered signals.

## 4.5.2 Current Estimation at Fundamental Frequency

The filtering and isolation of the high frequency signals allow to obtain the equivalent impedance of the system according to (4.14). This expression corresponds to the one obtained from the *block estimator* in the schematic shown in Fig. 4.13. Combining the resulting expression of  $\Delta Z_{\alpha\beta}^{50}$  with the ones presented in (3.32) makes it possible to obtain the negative sequence current caused by the unbalance.

To illustrate the performance of the algorithm, a simulation based on the configuration shown in Fig. 4.2 was carried out. The estimated currents are shown in Fig. 4.18. From the beginning, a 3-phase balanced resistive load is connected at the PCC and at instant  $t = 2$  s two single phase loads with the same per-phase impedance are connected to two of the phases, thus inducing an unbalance in the system. The estimator is able to extract both the positive and negative sequence currents based on the information provided by the high frequency

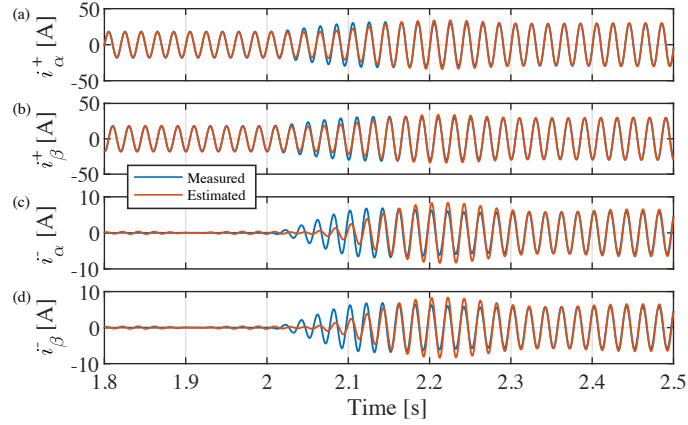


**Figure 4.18:** Simulation results: blue traces correspond to the measured variables and orange to the estimated ones (3.32) (a)  $\alpha$  positive sequence current; (b)  $\beta$  positive sequence current; (c)  $\alpha$  negative sequence current; (d)  $\beta$  negative sequence current.

signals. As it can be seen, Fig. 4.18, the tracking of the negative sequence components takes few fundamental cycles, fast enough to be used as a feedback signal for the negative sequence compensator.

Similarly, using (3.33), it is possible to estimate the zero-sequence current. Same experiment as the one exposed previously has been performed to estimate the zero-sequence current. The results are shown in Fig. 4.19. As in the case of the  $\alpha\beta$  terms, the zero-sequence current closely matched the original signal.

## 4.6 Unbalance Compensation

Once it has been proved that the proposed method is able to determine the negative and zero sequence current components resulting from an unbalance condition, the next step is to demonstrate the feasibility of using the estimation for compensation purposes. In Section 4.6.2, the compensation of the negative sequence component is addressed, while in Section 4.6.3 zero sequence compensation is considered. For the negative sequence compensation, the design of the current controller shown in Fig. 4.13 is firstly addressed.

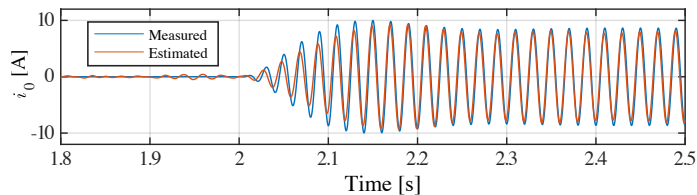


**Figure 4.19:** Simulation results: The blue trace corresponds to the measured zero-sequence current resulting under the unbalance and the orange corresponds to the zero-sequence current obtained from expression (3.33).

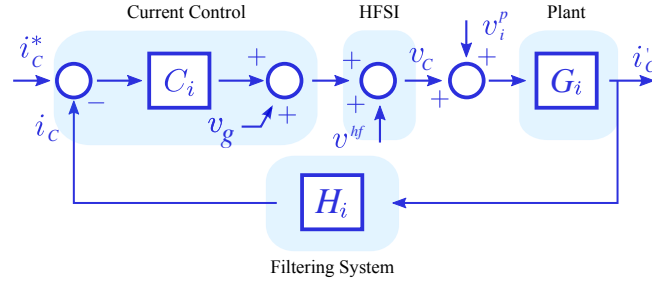


**Figure 4.20:** Current control loop of the system considering the HFSI technique used for impedance estimation

### 4.6.1 Stability Analysis

Considering the control system of the VSC the one shown in Fig. 4.20, the use of the filter chain in the feedback path could potentially reduce the close-loop phase margin and trigger stability problems. Thus, the design of the current controller has to consider its effect. A PI compensator in ideal form, assuming both the positive and negative control loops are implemented in their respective synchronous reference frame is assumed (4.18). For the positive sequence controller, the plant is referred to the positive-sequence reference frame, according to (4.19). It has to be highlighted that since the filter bank is the same in both positive and negative branches, the stability analysis is valid for both positive and negative controllers. However, to avoid redundancies only the positive sequence will be explained in detail, being the whole study valid for both controllers.

$$C_i = K_p \cdot \left( 1 + \frac{1}{T_i \cdot s} \right) \quad (4.18)$$

$$G_i = \frac{1}{L_f(s - j\omega_e) + R_f} \quad (4.19)$$

The magnitude  $K_p$  can be determined as  $K_p = 2\pi L_f b_w$  and  $K_i = \frac{K_p}{T_i}$ , where,  $T_i = \frac{L_f}{R_f}$  to achieve pole-zero cancellation. Initially, it was assumed a bandwidth for the controller of  $b_w = 100$  Hz. This assumption is valid in case the feedback gain is unitary (i.e  $H_i = 1$ ). However, the presence of the filtering chain adds extra poles to the close-loop system, which could potentially lead to system instability and thus requiring a new design of the current controller.

Fig. 4.21 shows the location of the poles of the plant in open loop and the position of the poles and zeros considering the effect of the filter in the feedback loop, without any controller in both cases. As it can be seen in Fig. 4.21, the design theory is to place the zero added by the controller approximately on top of the plant pole. This is analogous to the classical control pole/zero cancellation methodology. In this manner, all terms are placed in the negative part of the semi-plane, proving the system to be stable. It has to be highlighted that a LPF is not included in the filter chain of the positive and negative sequence at  $\omega_e = 2\pi 50$  rad/s. The controller itself suffice to filter out the non-interesting frequencies.

Command tracking, i.e., the output to reference ratio, (4.20), is a useful tool to evaluate the performance of the current regulator design. Similarly, the disturbance rejection capability of

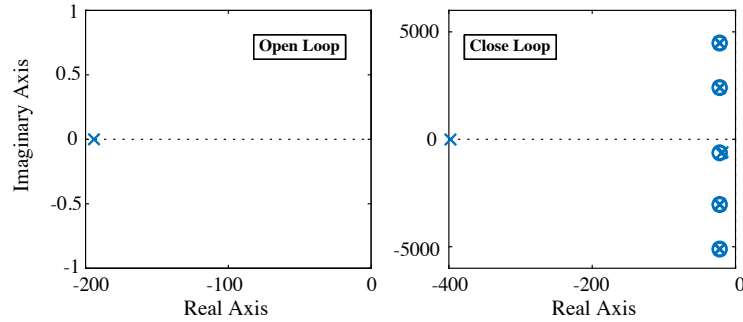


**Figure 4.21:** (a) Pole-zero location of the plant (4.19); (b) Pole-zero location of the close-loop system described in Fig. 4.20 without the controller

the controller can be evaluated according to (4.21), where  $v_i^p$  corresponds to the disturbance signal, as reflected in Fig. 4.24. Both transfer functions are defined in this section in the synchronous reference frame.

$$\frac{i_c'}{i_c^*} = \frac{C_i G_i}{1 + C_i G_i H_i} \quad (4.20)$$

$$\frac{i_c'}{v_i^p} = \frac{G_i}{1 + C_i G_i H_i} \quad (4.21)$$

Figure 4.22 shows the evaluation of expressions (4.20) and (4.21), based on its frequency response. Linear scale is used for the  $y$ -axis. This evaluation is made based on the study presented in Section 4.5.1, which considers both positive and negative frequencies, since variables are evaluated using complex vector quantities. According to Fig. 4.22 (a), the controller has a gain equal to one at zero frequency, which means that the VSC will have zero error in steady state, in the synchronous reference frame. Similarly, Fig. 4.22 (b) shows that the synchronous reference frame controller provides an adequate disturbance rejection at the fundamental frequency. However, this capability decreases rapidly as the frequency departs from zero. This means that proper grid-synchronization and signal isolation is required to accurately compensate for any system disturbance.

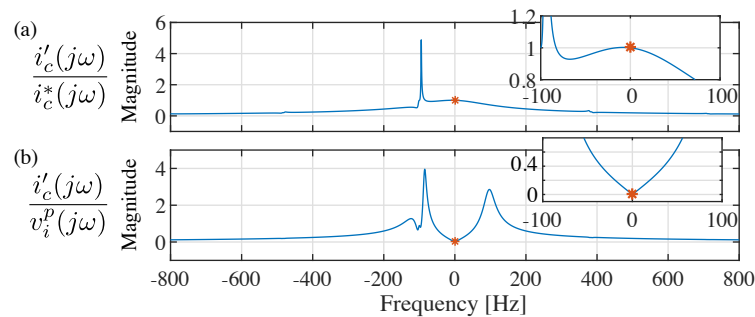


**Figure 4.22:** (a) Frequency response of the magnitude of the transfer function from (4.20); (b) Frequency response of the magnitude of the transfer function from (4.21)

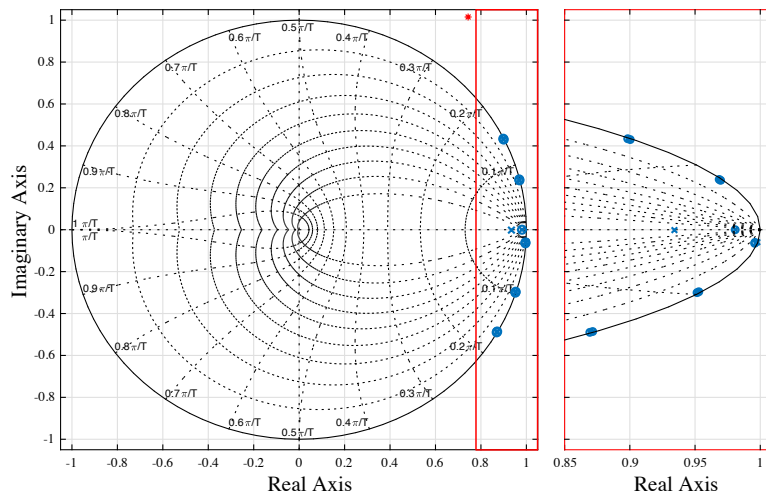


**Figure 4.23:** Pole-zero location of the discretized model from (4.20)

Until this point, this study has been conducted in the continuous time domain. However; its implementation requires the analysis to be extended to the discrete domain. Since the model needs a high accuracy at the specific frequencies of interest (positive and negative high-frequency components), the discretization method must match the frequencies of interest at the discrete domain. Several options exist for this constraint, including exact discretization and match zero-pole. Considering the relative margin among the high-frequency components and the sampling frequency (10 kHz), the Tustin approximation is also a good candidate. In this case, the Tustin transform including prewrapping has been used.

Figure 4.23 shows the resulting zero-pole location of the system after the discretization of (4.20). Since the location of all elements are within the unity circle, the system is considered stable. However, the location of the poles are in the vicinity of the stable zone, meaning that system might become unstable if the proportional term of the controller is increased above  $K_p = 1.3351$ , which results for a frequency bandwidth of 126 rad/s.

Once the stability of the controller has been validated, the behaviour of the whole system is tested through simulation in the next section.

## 4.6.2 Negative Sequence Compensation

Unbalance compensation is achieved by injecting negative and zero sequence currents in opposition phase to the respective unbalanced currents [4.8]. There are several methods proposed in the literature to compensate for this, all of them requiring to separate (filter) the negative and zero sequences from the positive one, and to cancel them out by using negative and zero sequence current controllers [4.8, 4.9]. In this thesis, the estimated negative-sequence current using the high-frequency information is used.

The performance of the current control and the compensation strategy has been tested by simulation results. The same setup configuration from Fig. 4.2 is considered, where a

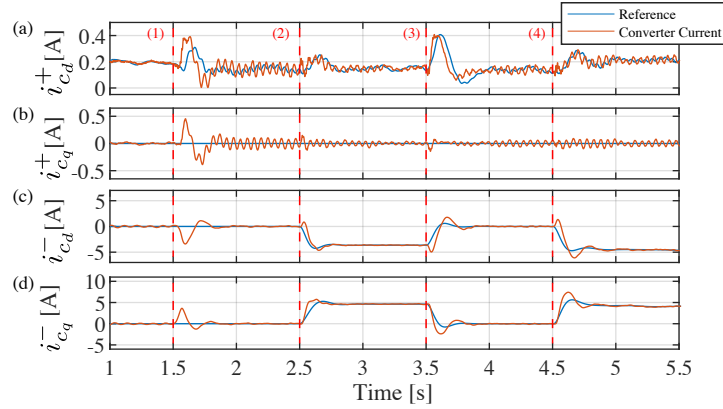


**Figure 4.24:** Simulation results: (a) Positive sequence reference current for the  $d$  component of the converter, in blue trace is the reference established by the voltage control and orange the corresponding current; (b) Positive sequence reference current for the  $q$  component of the converter; (c) Negative sequence reference current for the  $d$  component of the converter, based on the steps defined in the document; (d) Negative sequence reference current for the  $q$  component of the converter.

resistive load is connected to the PCC. At the beginning of the simulation a balanced system condition is established, being the converter operated in STATCOM mode. The rest of the converter current references are set to zero. To validate the performance of the current control, Fig. 4.24 shows the reference and commanded currents in both sequences of the VSC. Similarly, Fig. 4.25 shows the grid, load and VSC currents as a proof of the compensation method. The compensation strategy will provide the negative sequence current during the time that the unbalance is present. To do so, the estimation method described in Section 4.5.2 will provide the converter negative sequence reference current, and thus compensating the currents at the PCC.

The events in the simulation are marked in red numbers in Fig. 4.25 and are as follows: at  $t = 1$  s, the load is balanced and no negative sequence is present within the system. At  $t = 1.5$  s, the unbalance is produced. This is brought about by the connection of the two single phase impedances at the PCC at two different phases with a similar value of the one provided by the balanced original load. The negative sequence reference of the controller is set to zero, so no compensation is still provided from the converter and thus, the grid provides the 5.8 A of negative sequence current demanded by the unbalanced load.

In the second event of the simulation, at instant 2.5 s, the negative sequence of the load current is used as reference for the negative sequence converter current. From this instant, the converter is providing all the negative sequence current demanded by the load and, consequently, the negative sequence current from the grid goes to zero. At  $t = 3.5$  s, the reference of the negative sequence current of the converter is again set to zero and the negative sequence current at the grid side increases again.

Finally, at instant  $t = 4.5$  s, the controller is fed with the compensating signal obtained by applying the method proposed in this work. The results demonstrate that the behaviour is similar to the one obtained by using the load current unbalance, though in this proposal, this current is not directly measured. The results demonstrate compensation strategy is functionally feasible.

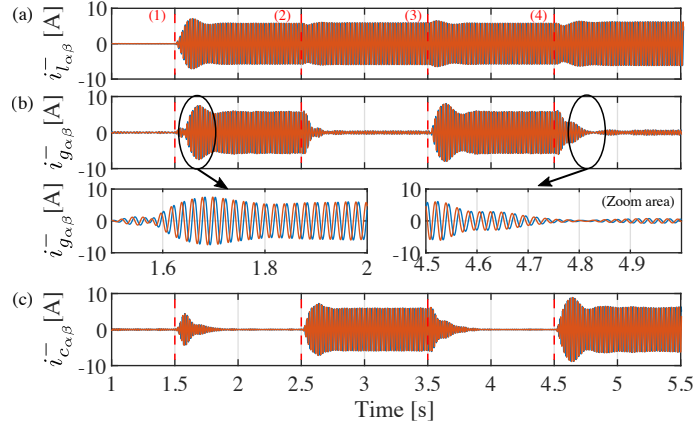


**Figure 4.25:** Simulation results: (a) Negative Sequence current at the load side in the  $\alpha\beta$  reference frame; (b) Negative Sequence current at the grid side in the  $\alpha\beta$  reference frame; (c) Negative Sequence current provided by the converter in the  $\alpha\beta$  reference frame;

In a similar way, the compensation of the zero sequence current may be achieved by combining the negative sequence expression obtained from the estimation. In the following section further details of the zero-sequence current control are explained.

### 4.6.3 Zero Sequence Compensation

For the designing of the zero-sequence current control, a compensation system based on resonant controllers has been proposed instead of the PI regulators previously described. This solution can be directly applied to AC signals, as it is the case of the zero sequence component and offers some advantages in terms of noise sensibility and signal processing requirements in comparison with the synchronous frame demodulation approaches. The plant is considered the same as in (4.19) and the control loop is shown in Fig. 4.26.

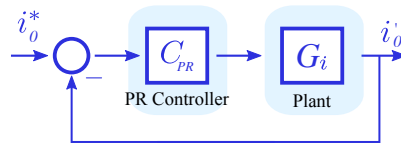


**Figure 4.26:** Current control for the zero sequence current

The designing principle consists in transform a desired DC variable compensation network into an equivalent AC one, so that it has the same frequency response characteristic in the bandwidth of concern, [4.10]. This transformation can be achieved according to (4.22).

$$H_{AC}(s) = \frac{H_{DC}(s + j\omega_0) + H_{DC}(s - j\omega_0)}{2} \quad (4.22)$$

where  $H_{AC}$  stands for the AC transfer function,  $H_{DC}$  for the DC one and  $\omega_0$  corresponds to the grid frequency at 50 Hz.

A feasible designing procedure might consist in transforming a DC compensator that achieves zero phase and magnitude error into an equivalent AC compensator. According to the results shown in Section 4.6, PI controller (4.18) achieves the desired objective of zero steady-state error. Thus, by frequency transformation of the controller transfer function (4.18) using (4.22), yields to (4.23).

$$C_{PR}(s) = K_p + \frac{2K_i s}{s^2 + \omega_0^2} \quad (4.23)$$

$C_{PR}(s)$  is a resonant controller, which provides infinite gain in open loop at the resonant frequency  $\omega_0$  and that assures perfect tracking for components that oscillate at that frequency when implemented in closed loop. The closed loop transfer function for the linear model of Fig. 4.26 with compensator (4.23) is given by (4.24) and the bode diagram of the open loop is shown in Fig. 4.27. The zoom area shows a cross-frequency with a phase margin of 48 deg proving the system to be stable for a value of  $K_p = 0.534$  and  $K_i = 0.0194$ .

$$\frac{i'_0}{i_0^*} = \frac{C_{PR}G_i}{1 + C_{PR}G_i} \quad (4.24)$$

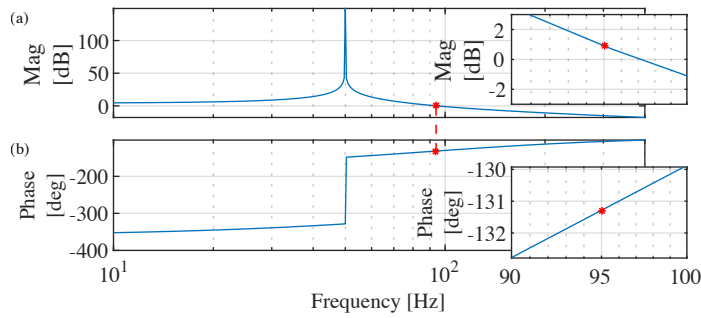


**Figure 4.27:** Bode diagram of the open loop system from Fig. 4.26

The close-loop reference tracking response given by (4.24) is shown in Fig. 4.28. In there, it can be seen that the controller achieves zero state error at the stationary reference frame (50 Hz), having an equivalent behaviour to (4.18) at the synchronous reference frame.

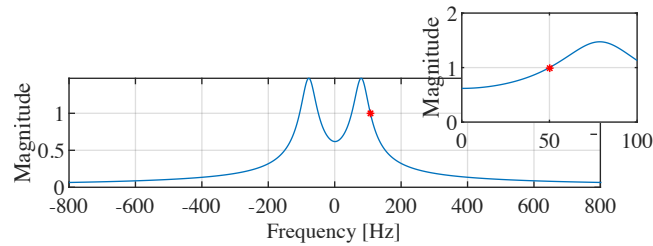


**Figure 4.28:** Frequency response of the magnitude of the transfer function from (4.23)

Figure 4.29 shows the (4.24) command tracking, for the same conditions described in the previous section: at  $t = 1.5$  s two single phase impedances are connected at the PCC inducing

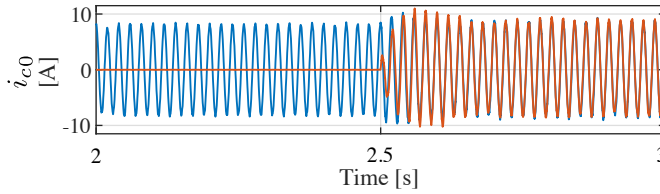


**Figure 4.29:** Simulation results. Command tracking response of (4.24) to a zero sequence current reference resulted from the presence of an unbalance in the conditions described in Section 4.6.2

the unbalanced conditions. The controller is enabled at instant  $t = 2.5$  s. As it can be seen in Fig. 4.29, proper reference tracking with zero steady state error is achieved.

The zero-sequence currents arise in the LV distribution system as a consequence of both unbalanced and non-linear loads. The local compensation of zero-sequence currents in order to avoid their propagation upstream from the PCC is a desirable ancillary service for power converters, though only four-wire topologies are valid to comply with this function. This task can be easily done by measuring the zero-sequence current at the grid side and implementing a closed loop strategy for compensating it. Unfortunately, this requires not only an additional sensor but also the connection or communication between distant points. The proposed algorithm can be used instead of the additional sensors to estimate the magnitude of the unbalance and thus provide a compensation current.

In Fig. 4.30, the compensation of the zero sequence component is demonstrated. Simulation conditions are kept the same as previously described: the load is balanced until  $t = 1.5$  s, where two single-phase loads with same magnitude are connected in parallel to two of the phases of the PCC. At this instant, 8.7 A of zero-sequence current start flowing from the neutral wire. Fig. 4.30(a) shows the current flowing from the grid side, corresponding with the same as the one demanded by the load Fig. 4.30(b). The estimated zero-sequence current is then provided as a reference for the converter zero sequence controller, which starts the injection at 2.5 s, Fig. 4.30(c), leading to a fast compensation of grid neutral current.

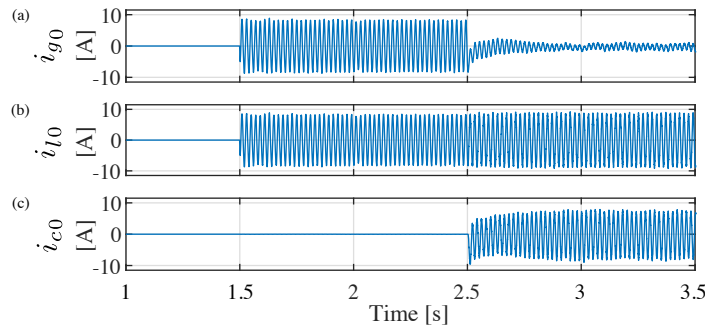


**Figure 4.30:** Simulation results. Zero sequence compensation. (a) neutral current at the grid side ( $i_{g0}$ ), (b) neutral current at the load side ( $i_{l0}$ ), and (c) current at the converter neutral leg ( $i_{c0}$ ).

The explanation of the zero sequence compensation has been performed independently from the negative sequence one, since different aspects of the controller design have been

addressed. However, the unbalance compensation has to be done considering both sequences at the same time. Consequently, the results shown are considering the effect of all compensation sequences and thus, the simulation events take place at the same instant.

## 4.7 Conclusion

This chapter introduces the problem of estimating the impedance seen by a grid-connected VSC in a system with multiple loads connected to the same PCC. With this aim, an estimation technique based on HFSI is presented which is capable of evaluating the impedance at a different frequency from the grid one,  $\omega_e$ , based on the impedance model presented in Chapter 3.

This high frequency demonstrates its capability to provide an accurate response at the frequency of estimation. However, it does not yield to the equivalent impedance at grid frequency. To do so, an updated technique consisting on the addition of a second high frequency signal has been proposed. This second signal, together with the algorithm presented in this work, makes it possible to determine the equivalent impedance of the system at grid frequency.

Once the impedance is determined, an estimation of the negative sequence current is obtained. This current is used as the reference for the negative sequence current compensator. A similar approach is used by the zero sequence current controller, thus virtually eliminating the unbalance from the grid side.

The main contributions of this chapter are summarized as:

- A reliable technique to determine the impedance of the system based on the injection of high frequency signals generated by the converter, which has been demonstrated and supported by simulations and experimental results.
- A criteria to determine the frequency of injection of a excitation signal with a magnitude which accomplishes with the THD of the system.
- A control system strategy based both on the estimation technique and the expressions presented in Chapter 3, able to compensate the negative sequence induced under an unbalance situation.
- A study of the filtering system required to isolate the signals used for the impedance estimation, including an analysis of the response of the high and low pass filters.
- A current control stability analysis which combines both the traditional current control of a VSC and the filtering system placed at the feedback of the current controller.
- An evaluation of the performance of the system under simulated conditions, where the model is able to determine the impedance of the system, the negative and zero sequence demanded by the unbalanced load and the compensation of both sequence currents present in the grid side.

## References

- [4.1] A. Luna, J. Rocabert, J. I. Candela, J. R. Hermoso, R. Teodorescu, F. Blaabjerg, and P. Rodríguez, "Grid voltage synchronization for distributed generation systems under grid fault conditions," *IEEE Transactions on Industry Applications*, vol. 51, no. 4, pp. 3414–3425, July 2015.
- [4.2] M. Savaghebi, A. Jalilian, J. C. Vasquez, and J. M. Guerrero, "Autonomous voltage unbalance compensation in an islanded droop-controlled microgrid," *IEEE Transactions on Industrial Electronics*, vol. 60, no. 4, pp. 1390–1402, April 2013.
- [4.3] A. C. K and M. N. O. Sadiku, *Fundamentals of electric circuits*, 7th ed. Boston: McGraw-Hill Higher Education, 2007.
- [4.4] F. Briz, P. García, M. W. Degner, D. Díaz-Reigosa, and J. M. Guerrero, "Dynamic behavior of current controllers for selective harmonic compensation in three-phase active power filters," *IEEE Transactions on Industry Applications*, vol. 49, no. 3, pp. 1411–1420, May 2013.
- [4.5] A. Suárez-González, P. García, Á. Navarro-Rodríguez, G. Villa, and J. M. Cano, "Sensorless unbalance modeling and estimation as an ancillary service for lv four-wire/three-phase power converters," *IEEE Transactions on Industry Applications*, vol. 55, no. 5, pp. 4876–4885, Sep. 2019.
- [4.6] S. Bifaretti, P. Zanchetta, A. Watson, L. Tarisciotti, and J. C. Clare, "Advanced power electronic conversion and control system for universal and flexible power management," *IEEE Transactions on Smart Grid*, vol. 2, no. 2, pp. 231–243, June 2011.
- [4.7] M. Liserre, F. Blaabjerg, and S. Hansen, "Design and control of an lcl-filter-based three-phase active rectifier," *IEEE Transactions on Industry Applications*, vol. 41, no. 5, pp. 1281–1291, Sep. 2005.
- [4.8] M. Savaghebi, A. Jalilian, J. Vasquez, and J. Guerrero, "Autonomous voltage unbalance compensation in an islanded droop-controlled microgrid," *IEEE Transactions on Industrial Electronics*, vol. PP, no. 99, p. 1, 2012.
- [4.9] C. Po-Tai, C. Chien-An, L. Tzung-Lin, and K. Shen-Yuan, "A cooperative imbalance compensation method for distributed-generation interface converters," *IEEE Transactions on Industry Applications*, vol. 45, no. 2, pp. 805–815, 2009.
- [4.10] D. N. Zmood and D. G. Holmes, "Stationary frame current regulation of pwm inverters with zero steady-state error," *IEEE Transactions on Power Electronics*, vol. 18, no. 3, pp. 814–822, 2003.

## Chapter 5

# Grid Impedance Estimation Considering Grid-tied Power Converters

### 5.1 Introduction

Chapter 4 addressed the estimation of system equivalent impedance considering only passive loads connected at the PCC. The modelling technique proposed in Chapter 3, together with the injection of high frequency signals, was used to achieve this objective. In the present chapter, the estimation of the equivalent impedance when multiple VSCs are parallel connected is tackled. A modification of the developed expressions presented in Chapter 3 to include the VSC power references is here considered. A pulsed signal injection (PSI) technique is proposed instead of the high-frequency signal injection. This approach has advantages when considering multiple converters as it can mitigate the interference of current regulators. The gathered data is evaluated under a recursive least square (RLS) algorithm which will be compared with the results obtained using the modelling approach developed in Chapter 3. The comparison of the results pursues a dual objective: 1) to prove the performance of the RLS based estimation technique and 2) to extend the technique proposed in Chapter 3 to those cases considering parallel-operation of power converters.

The chapter begins with a description of the power system configuration, as well as with a description of the constraints induced by a multiple converter scenario. The proposed model is supported by simulation and experimental results. A generalization of the equivalent impedance considering the contribution from the converter power references is provided and evaluated by simulation results. Then, the impedance estimation using an RLS algorithm is developed. Finally, the conclusions are presented.

## 5.2 System Description

The system under study is shown in Fig. 5.1. The grid-feeding converter VSC 2, is responsible to provide active and reactive power to the grid. The current injected depends on its power references, and thus, it resembles a variable impedance from the point of view of main AC-Grid. The converter VSC 1 is the responsible for the impedance estimation. Both converters are paralleled connected at the PCC, and this, in turn, connected to the AC-grid.

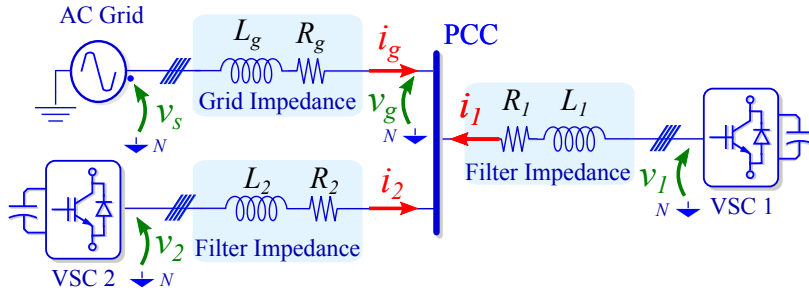


**Figure 5.1:** System schematic. Two power converters are considered connected to the PCC. VSC 1 is responsible for the impedance estimation and VSC 2 is commanding power references.

Grid-feeding converters behave as a current source with a high output impedance. As a consequence, VSC 2 can be considered as a variable impedance in parallel with the grid impedance, and thus, according to the Thevenin theorem, the system from Fig. 5.1 can be represented from the point of view of VSC 1 as an equivalent impedance,  $Z_{th}$ , in series with a voltage source  $V_{th}$ , as shown in Fig. 5.2.

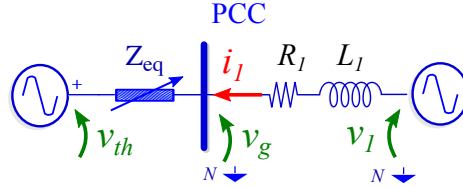


**Figure 5.2:** Thevenin equivalent circuit of Fig. 5.1.

Based on this, the voltage across the equivalent impedance can be expressed as (5.1), where  $v_{th}$  is the Thevenin equivalent voltage and  $v_g$  is the voltage at the PCC.

$$\mathbf{v}_{zeq}^{\alpha\beta} = \mathbf{v}_g^{\alpha\beta} - \mathbf{v}_{th}^{\alpha\beta} = \mathbf{R}_{\alpha\beta} \mathbf{i}_1^{\alpha\beta} + \mathbf{L}_{\alpha\beta} \frac{d\mathbf{i}_1^{\alpha\beta}}{dt} \quad (5.1)$$

Consequently,  $\mathbf{L}_{\alpha\beta}$  and  $\mathbf{R}_{\alpha\beta}$  are, respectively, the equivalent inductive and resistive terms of the impedance  $Z_{eq}$ . Notice, that  $Z_{eq}$  is also considering the equivalent impedance of converter VSC 2, which depend on its power references. Since VSC 2 can operate in the four quadrants, it should be more adequate to define the equivalent impedance in the form of (5.2), as it was already explained in Chapter 3. In case the impedance is balanced, diagonal terms ( $Z_{\alpha\alpha}$  and

$Z_{\beta\beta}$ ) are equal and cross-coupling between phases, represented by non diagonal terms ( $Z_{\alpha\beta}$ ), are not present.

$$\mathbf{Z}_{\alpha\beta} = \begin{pmatrix} Z_{\alpha\alpha} & Z_{\alpha\beta} \\ Z_{\alpha\beta} & Z_{\beta\beta} \end{pmatrix} \quad (5.2)$$

Expression (5.2) may be rotated to a common  $\alpha\beta$  reference frame, with  $n$  impedance elements, according to the reasoning explained in Chapter 3, leading to expression (5.3).

$$\begin{aligned} \mathbf{Z}_{\alpha\beta} &= \Sigma Z + \Delta Z \\ &= (\Sigma R + \Delta R) \pm j(\Sigma X + \Delta X) \end{aligned} \quad (5.3)$$

Equation (5.3) is expressed in terms of resistive and reactance components to consider both the reactive and capacitive behaviour of the equivalent impedance. Consequently, the impedance is considered inductive for positive values of  $X$  and capacitive for the negative ones. Thereby, the method can be used to account for four quadrant operation of power converters.

### 5.3 Impedance Modelling of Active Loads

Impedance identification in those applications considering power converters, as shown in Fig. 5.1, requires analysing the effect of the converter operating point in the equivalent impedance. Without loss of generality, VSC 2 is considered to be operated in P-Q mode, thus commanding different current levels in the  $d$  and  $q$  axis. The equivalent converter impedance, which can be expressed as a function of its average and differential values according to (5.3), is measured using the converter side current and the voltage at the PCC. These relationships can be determined by particularizing (3.40)-(3.41) for the converter VSC 2 connected at the PCC of the system in Fig. 5.1. This case yields to (5.4)-(5.5), which are proved to be enough to determine the equivalent system impedance (5.3), as exposed in Chapters 3 and 4, depending on the converter operation.

$$\Sigma Z_{VSC2}^{\alpha\beta} = \frac{v_{g_{\alpha\beta}}^+ \cdot i_{2_{\alpha\beta}}^+ - v_{g_{\alpha\beta}}^- \cdot i_{2_{\alpha\beta}}^-}{(i_{2_{\alpha\beta}}^+)^2 - (i_{2_{\alpha\beta}}^-)^2} \quad (5.4)$$

$$\Delta Z_{VSC2}^{\alpha\beta} = \frac{v_{g_{\alpha\beta}}^- \cdot i_{2_{\alpha\beta}}^+ - v_{g_{\alpha\beta}}^+ \cdot i_{2_{\alpha\beta}}^-}{(i_{2_{\alpha\beta}}^+)^2 - (i_{2_{\alpha\beta}}^-)^2} \quad (5.5)$$

This relationship between sequences is illustrated in Fig. 5.3. As said, under balanced situation, only  $\Sigma Z$  term is interacting at main frequency, but the  $\Delta Z$  term is contributing to the cross-term element under unbalanced conditions.

The evaluation of expressions (5.4) and (5.5) is carried out based on a simulation where converters VSC 1 is disconnected and VSC 2 is commanding different levels of power according the configuration shown in Fig. 5.1. Fig. 5.4 shows the operation of VSC 2 in the four quadrants along with the positive/negative voltage and current sequences. Different values for the active and reactive power components (5 A, 10 A, 20 A, 30 A) are considered, including both positive and negative sequences. Notice that the components shown in Fig. 5.4 are represented in the synchronous frame to facilitate the analysis.

Expressions (5.4) and (5.5) are evaluated considering  $v_{gdq}$  and  $i_{2dq}$  and according to the values shown in Fig. 5.4. The resulting terms from this evaluation are exposed in Fig. 5.5. In

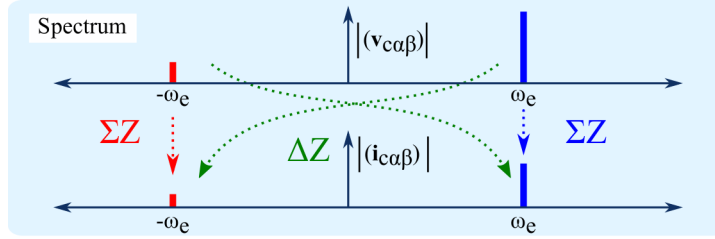


**Figure 5.3:** Relationship between voltage and current, in frequency domain, according to expression of the equivalent impedance  $\Sigma Z$  and  $\Delta Z$ .

this figure, the results from (5.4)-(5.5) are also compared with a virtual impedance which would provide the same values of  $\Sigma Z$  and  $\Delta Z$  terms. This comparison might appear redundant, however, it is a way to proof the reversibility of the modelling method, providing an equivalent value of the impedance according to the operating conditions of converter VSC 2. The values of the virtual phase impedances, which are obtained from (5.3) according to the procedure described in Chapter 3, are shown in Fig. 5.6.

Based on the exposition from Chapter 3, the current from converter VSC 2 can be ex-

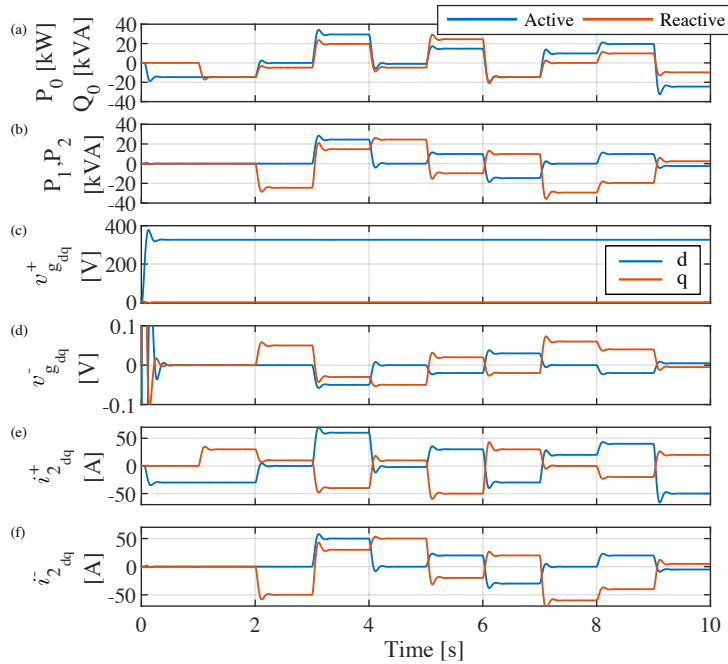


**Figure 5.4:** Simulation results. (a)  $P_0$  (blue) and  $Q_0$  (orange) power components; (b) Pulsating terms  $P_1$  (blue) and  $P_2$  (orange) resulted from the negative sequence injection; (c) Positive Sequence voltage of  $v_g$  in  $dq$  reference frame; (d) Negative Sequence voltage of  $v_g$  in  $dq$  reference frame; (e) Positive Sequence current of VSC 2 in  $dq$  reference frame; (f) Negative Sequence current of VSC 2 in  $dq$  reference frame.

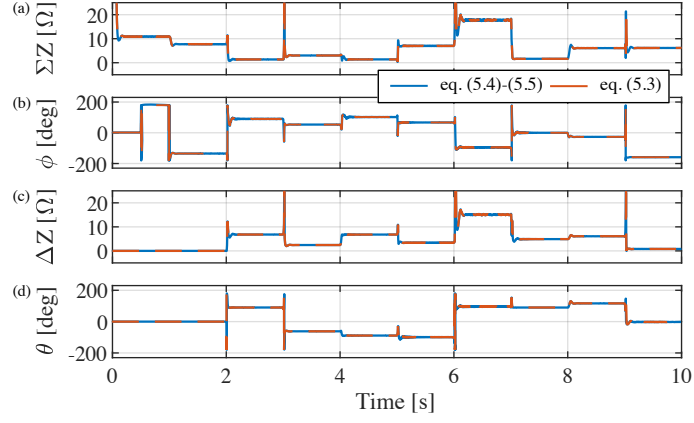


**Figure 5.5:** Simulation results of the comparison between the equivalent impedance terms obtained from evaluating the currents from simulation according to (5.4)-(5.5) and the ones obtained from an equivalent phase impedance that produces the same impedance values based on (5.3). (a)  $\Sigma Z$  term; (b) Equivalent angle from term  $\Sigma Z$ ; (c)  $\Delta Z$  term; (d)  $\Delta Z$  angle, corresponding with the unbalanced angle,  $\theta$ .

pressed in terms of the impedance according to  $\Sigma Z$  and  $\Delta Z$ , leading to obtain a relation between positive and negative sequence components and the system impedance, as (5.6).

$$\mathbf{i}_{2\alpha\beta} = \underbrace{\frac{\Sigma Z}{\Sigma Z^2 - \Delta Z^2}}_{\Sigma Y} \cdot V_{g\alpha\beta} e^{j\omega t} - \underbrace{\frac{\Delta Z}{\Sigma Z^2 - \Delta Z^2}}_{\Delta Y} \cdot V_{g\alpha\beta} e^{-j(\omega t + \theta)} \quad (5.6)$$

Expression (5.6) can be rewritten in matrix form as (5.7), where both positive and negative instantaneous voltages and real and imaginary admittance terms are considered, following the same procedure as in (3.36).

$$\begin{bmatrix} i_{2\alpha}^+ \\ i_{2\beta}^+ \\ i_{2\alpha}^- \\ i_{2\beta}^- \end{bmatrix} = \begin{bmatrix} \Sigma Y_\alpha & -\Sigma Y_\beta & -\Delta Y_\alpha & \Delta Y_\beta \\ \Sigma Y_\beta & \Sigma Y_\alpha & \Delta Y_\beta & \Delta Y_\alpha \\ \Delta Y_\alpha & -\Delta Y_\beta & \Sigma Y_\alpha & -\Sigma Y_\beta \\ -\Delta Y_\beta & -\Delta Y_\alpha & \Sigma Y_\beta & \Sigma Y_\alpha \end{bmatrix} \cdot \begin{bmatrix} v_{g\alpha}^+ \\ v_{g\beta}^+ \\ v_{g\alpha}^- \\ v_{g\beta}^- \end{bmatrix} \quad (5.7)$$

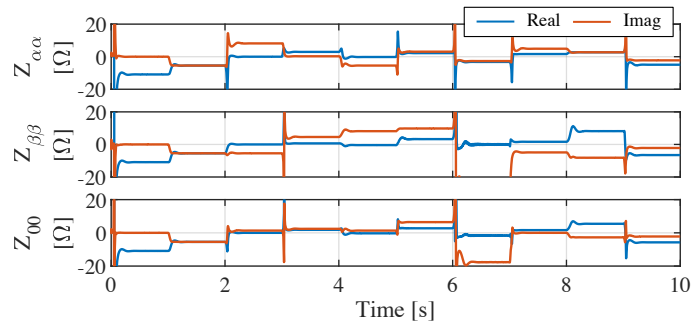


**Figure 5.6:** Simulation results. Virtual phase impedances: (a)  $Z_{\alpha\alpha}$ ; (b)  $Z_{\beta\beta}$ ; (c)  $Z_{00}$ .

Assuming that the converter references are provided as power commands, it is insightful to rewrite (5.7) based on the active and reactive power of the device. Based on expression (3.57), it can be particularized as (5.8).

$$\begin{bmatrix} P_0 \\ Q_0 \\ P_1 \\ P_2 \end{bmatrix} = \frac{3}{2} \begin{bmatrix} v_{g\alpha}^+ & v_{g\beta}^+ & v_{g\alpha}^- & v_{g\beta}^- \\ -v_{g\beta}^+ & v_{g\alpha}^+ & -v_{g\beta}^- & v_{g\alpha}^- \\ v_{g\alpha}^- & v_{g\beta}^- & v_{g\alpha}^+ & v_{g\beta}^+ \\ v_{g\beta}^- & -v_{g\alpha}^- & -v_{g\beta}^+ & v_{g\alpha}^+ \end{bmatrix} \begin{bmatrix} i_{2\alpha}^+ \\ i_{2\beta}^+ \\ i_{2\alpha}^- \\ i_{2\beta}^- \end{bmatrix} \quad (5.8)$$

Where  $P_0$  and  $Q_0$  are the average part of the real and imaginary power and  $P_1$  and  $P_2$  result from the positive and negative terms interaction under unbalanced conditions, according to the instantaneous power theory [5.1]. Combination of (5.7) and (5.8) allows to establish a relationship between the admittance terms and power components, leading to expression (5.9). It is important to remark that  $P_0$  and  $Q_0$  terms do not depend on the system unbalance.

$$\begin{bmatrix} P_0 \\ Q_0 \\ P_1 \\ P_2 \end{bmatrix} = \frac{3}{2} \left[ \Sigma Y_{\alpha i} \begin{pmatrix} v_{g\alpha}^+ & v_{g\beta}^+ & v_{g\alpha}^- & v_{g\beta}^- \\ 0 & 0 & 0 & 0 \\ v_{g\alpha}^- & v_{g\beta}^- & v_{g\alpha}^+ & v_{g\beta}^+ \\ v_{g\beta}^- & -v_{g\alpha}^- & -v_{g\beta}^+ & v_{g\alpha}^+ \end{pmatrix} \right. \quad (5.9) \\ \left. + \Sigma Y_{\beta i} \begin{pmatrix} 0 & 0 & 0 & 0 \\ v_{g\beta}^+ & -v_{g\alpha}^+ & v_{g\beta}^- & -v_{g\alpha}^- \\ 0 & 0 & 0 & 0 \\ 0 & 0 & 0 & 0 \end{pmatrix} + \Delta Y_{\alpha i} \begin{pmatrix} 0 & 0 & 0 & 0 \\ 0 & 0 & 0 & 0 \\ v_{g\alpha}^+ & -v_{g\beta}^+ & -v_{g\alpha}^- & v_{g\beta}^- \\ -v_{g\beta}^+ & -v_{g\alpha}^+ & -v_{g\beta}^- & -v_{g\alpha}^- \end{pmatrix} \right. \\ \left. + \Delta Y_{\beta i} \begin{pmatrix} 0 & 0 & 0 & 0 \\ 0 & 0 & 0 & 0 \\ -v_{g\beta}^+ & -v_{g\alpha}^+ & v_{g\beta}^- & v_{g\alpha}^- \\ -v_{g\alpha}^+ & v_{g\beta}^+ & -v_{g\alpha}^- & v_{g\beta}^- \end{pmatrix} \right] \begin{bmatrix} v_{g\alpha}^+ \\ v_{g\beta}^+ \\ v_{g\alpha}^- \\ v_{g\beta}^- \end{bmatrix}$$

The evaluation of (5.9) is carried out using the voltage and current measurements represented in Fig. 5.4. The results are shown in Fig. 5.7(a)-(d). To prove the consistence of the expression, these results have been compared with the ones obtained from evaluating expression (5.8) with same measurements. As shown, both expressions provide remarkably close results, which is used as a prove of their equivalence.

By additional algebraic manipulation, the average and differential admittance components can be expressed as a function of the power terms and the converter positive and negative sequence voltages. The resulting expression is shown in (5.10). This expression highlights how the average active ( $P_0$ ) and reactive ( $Q_0$ ) terms are related with the average admittances while  $P_1$  and  $P_2$  are related with the differential.

$$\begin{bmatrix} \Sigma Y_{\alpha} \\ \Sigma Y_{\beta} \\ \Delta Y_{\alpha} \\ \Delta Y_{\beta} \end{bmatrix} = \frac{1}{(v_{g\alpha}^+)^2 + (v_{g\beta}^+)^2 + (v_{g\alpha}^-)^2 + (v_{g\beta}^-)^2} \begin{bmatrix} P_0 \\ Q_0 \\ P_1 \\ P_2 \end{bmatrix} \quad (5.10)$$

The numerical evaluation of the equation is shown in Fig. 5.7(e)-(h). These results have been also included in same Fig. 5.7 to make more evident how the changes in the power references are affecting the rest of the power components and vice versa. The steps in the pulsating terms of the powers,  $P_1$ ,  $P_2$ , correspond with the changes in the  $\Delta Y$  term. A zoom at every change is included for comparison purposes.

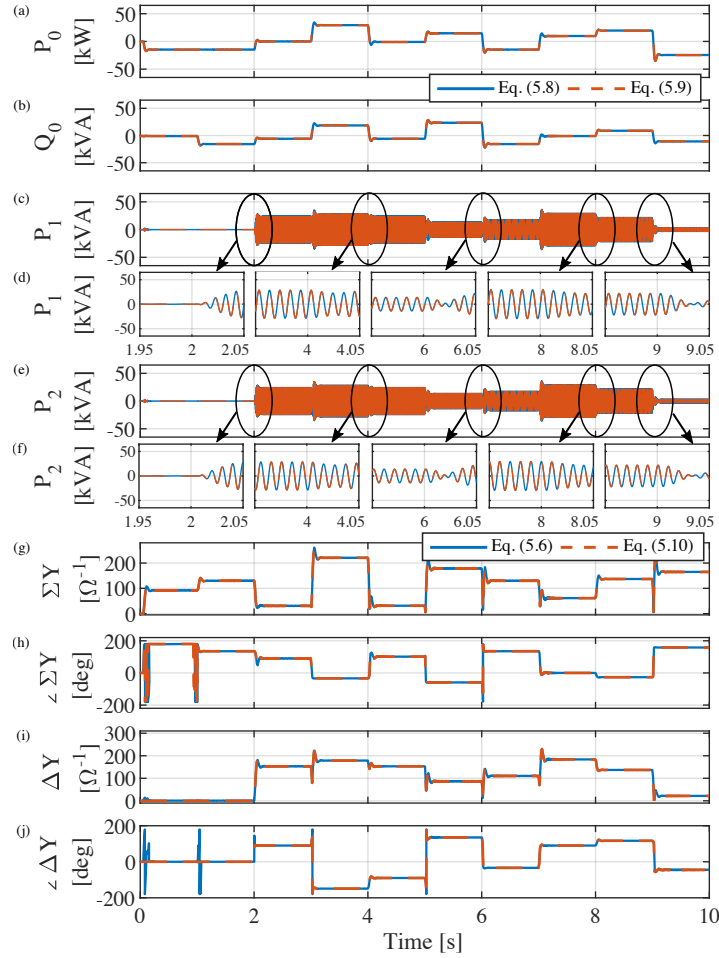


**Figure 5.7:** Simulations results. Comparison between the results obtained from (5.8) and (5.9); (a) Average part of the real power component  $P_0$ ; (b) Average part of the imaginary power component  $Q_0$ ; (c) First pulsating term associated with the term  $P_1$ ; (d) Zoom areas of the highlighted areas from  $P_1$  component; (e) Second pulsating term associated with the component  $P_2$ ; (f) Zoom areas of the highlighted areas from  $P_2$  component; (g) Comparison of the absolute value of the  $\Sigma Y$  term according to expression (5.6) and (5.10); (h) Angle of the  $\Sigma Y$  term; (i) Comparison of the absolute value of  $\Delta Y$ ; (j) Angle of  $\Delta Y$ .

## 5.4 Equivalent Impedance Estimation Based on a RLS Algorithm

Section 5.3 has described the procedure to obtain the equivalent impedance of the VSC based on the modelling technique proposed in Chapter 3. Relying on the results provided in [5.2], this section presents a solution based on a Recursive Least Square (RLS) algorithm which provides an impedance estimation technique based on a Pulsed Signal Injection (PSI). The algorithm will be used to provide an estimation of the converter operation according to the aforementioned modelling tool. As opposed to the signal employed in Chapter 4, this technique is based on the injection of a short duration voltage pulse superimposed to the power converter output voltage. This strategy has some advantages in those environments where several converters are operating at the same time, as it has the potential to mitigate the interferences in current regulators.

### 5.4.1 Pulsed Signal Injection Technique

The proposed method uses a grid excitation technique based on the injection of a short duration voltage spike into the voltage supply. The duration of this transient is limited in order to maintain the voltage distortion of the system as low as possible. According to the parameters of the injected signal, there are multitude of PSI strategies which can be implemented, that range from a modification of the amplitude of phase voltages to their complete inhibition at those instants close to their zero crossing. The method selected in this implementation is conducted directly in the  $dq$  reference frame, thus matching the domain used in the controller. The PLL is responsible to track the voltage signal and detect the zero crossing of the voltage components in the  $dq$  reference frame. The voltage signal is intentionally inhibited symmetrically with respect to the zero crossing instants in order to avoid any dc component.

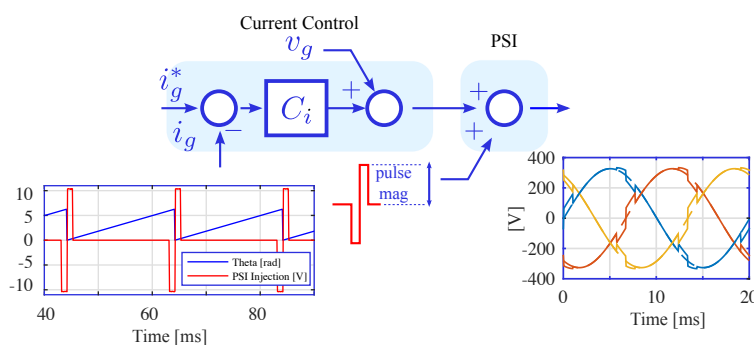


**Figure 5.8:** PSI Loop implementation. The pulse injection is synchronized with respect to the grid voltage zero crossing and it is added in the  $q$  component.

Specifically, the pulses are injected by modifying the duty cycle provided by the current controller within the  $q$  component of the fundamental voltage. This is intentionally implemented in this way, in order not to perturb the performance of the DC-link which is usually

controlled through the  $d$  current component of the VSC. The magnitude and duration of the pulse may contribute to ease the detection of the impedance but also might increase the current THD, for this reason it is convenient to establish a trade-off between duration and also magnitude. The values presented in Table E.2 have been used. Fig. 5.8 shows a detailed view about the injection mechanism and the resulting voltage waveforms.

### 5.4.2 RLS Algorithm Implementation

This section describes the RLS algorithm employed in the estimation of the impedance terms, which is based in the works previously presented in [5.2–5.4]. Considering the equivalent impedance from circuit in Fig. 5.2 to be aligned with the spatial angle of the impedance, and according to the reasoning presented in Chapter 3, the equivalent grid impedance can be expressed as in matrix form as (5.2), where non diagonal terms ( $Z_{\alpha\beta}$ ) are zero in case of balanced situation. Similarly, (5.2) can be expressed according to (5.11), Once again, by considering the overall grid impedance dominated by the resistive and inductive terms.

$$\mathbf{Z}_{\alpha\beta} = \left[ (\Sigma R + j\omega_e \Sigma L) \begin{pmatrix} 1 & 0 \\ 0 & 1 \end{pmatrix} + (\Delta R + j\omega_e \Delta L) \begin{pmatrix} \cos \theta_e & -\sin \theta_e \\ -\sin \theta_e & -\cos \theta_e \end{pmatrix} \right] \quad (5.11)$$

From here, gathering expressions (5.1) and (5.11), and according to [5.5], the discrete approximation of the grid current in  $\alpha\beta$  reference frame, employing Tustin method and a sample time,  $T_s$ , is given by (5.12)-(5.13),

$$i_{g[k]}^\alpha = a_1^\alpha \cdot i_{g[k-1]}^\alpha + a_2^\alpha \cdot i_{g[k]}^\beta + a_3^\alpha \cdot i_{g[k-1]}^\beta + b_0^\alpha (v_{\alpha[k]} + v_{\alpha[k-1]}) \quad (5.12)$$

$$i_{g[k]}^\beta = a_1^\beta \cdot i_{g[k-1]}^\beta + a_2^\beta \cdot i_{g[k]}^\alpha + a_3^\beta \cdot i_{g[k-1]}^\alpha + b_0^\beta (v_{\beta[k]} + v_{\beta[k-1]}) \quad (5.13)$$

where

$$\begin{aligned} a_1^\alpha &= \frac{\frac{2}{T_s} L_{\alpha\alpha} - R_{\alpha\alpha}}{\frac{2}{T_s} L_{\alpha\alpha} + R_{\alpha\alpha}}, & a_2^\alpha &= -\frac{\frac{2}{T_s} L_{\alpha\beta} + R_{\alpha\beta}}{\frac{2}{T_s} L_{\alpha\alpha} + R_{\alpha\alpha}} \\ a_3^\alpha &= \frac{\frac{2}{T_s} L_{\alpha\beta} + R_{\alpha\beta}}{\frac{2}{T_s} L_{\alpha\alpha} + R_{\alpha\alpha}}, & b_0^\alpha &= \frac{1}{\frac{2}{T_s} L_{\alpha\alpha} + R_{\alpha\alpha}} \\ a_1^\beta &= \frac{\frac{2}{T_s} L_{\beta\beta} - R_{\beta\beta}}{\frac{2}{T_s} L_{\beta\beta} + R_{\beta\beta}}, & a_2^\beta &= -\frac{\frac{2}{T_s} L_{\alpha\beta} + R_{\alpha\beta}}{\frac{2}{T_s} L_{\beta\beta} + R_{\beta\beta}} \\ a_3^\beta &= \frac{\frac{2}{T_s} L_{\alpha\beta} - R_{\alpha\beta}}{\frac{2}{T_s} L_{\beta\beta} + R_{\beta\beta}}, & b_0^\beta &= \frac{1}{\frac{2}{T_s} L_{\beta\beta} + R_{\beta\beta}} \end{aligned}$$

and  $v_\alpha, v_\beta$  represent the components of the voltage term  $\mathbf{v}_z^{\alpha\beta}$ , which is the difference between the PCC and the grid voltages. From (5.12), (5.13) the values for the resistance and inductance terms can be obtained as (5.14).

$$\begin{aligned} R_{xx} &= \frac{1 - a_1^x}{2b_0^x}, & L_{xx} &= \frac{T_s}{4} \frac{1 + a_1^x}{b_0^x}, \\ R_{xy} &= -\frac{a_2^x + a_3^x}{2b_0^x}, & L_{xy} &= \frac{T_s}{4} \frac{a_3^x - a_2^x}{b_0^x} \end{aligned} \quad (5.14)$$

where  $x, y$  could be either  $\alpha$  or  $\beta$ .

The RLS algorithm allows to estimate the resistances and inductances in (5.14) by determining the values of the coefficients  $a_i^x$  and  $b_j^x$ . The grid voltage is assumed to be stiff enough not to be affected by the pulse injection. Thus, it is possible to decouple the unknown grid voltage  $\mathbf{v}_s^{\alpha\beta}$ , by only considering the current induced by the pulse injection.

The least squares problem is formulated in recursive form as in [5.5], using the equations (5.15)-(5.18). The system equations are represented by defining the variables and coefficients vectors,  $\mathbf{X}_{[k]}^x$ ,  $\mathbf{W}_{[k]}^x$ , as (5.19) and (5.20), respectively, where superscript  $x$  could be either  $\alpha$  or  $\beta$ . The estimated RLS current,  $\hat{i}_{g[k]}^x$ , is determined by the product  $\mathbf{W}_{[k-1]}^x \cdot \mathbf{X}_{[k]}^x$  in (5.15). All the names of the variables are referred to those shown in Fig. 5.1.

$$\alpha_{[k]}^x = i_{g[k]}^x - \mathbf{W}_{[k-1]}^x \cdot \mathbf{X}_{[k]}^x \quad (5.15)$$

$$\mathbf{g}_{[k]}^x = \mathbf{P}_{[k-1]}^x \cdot \mathbf{X}_{[k]}^x \cdot \left[ \lambda + \mathbf{X}_{[k]}^{xT} \cdot \mathbf{P}_{[k-1]}^x \cdot \mathbf{X}_{[k]}^x \right]^{-1} \quad (5.16)$$

$$\mathbf{P}_{[k]}^x = \lambda^{-1} \cdot \mathbf{P}_{[k-1]}^x - \mathbf{g}_{[k]}^x \cdot \mathbf{X}_{[k]}^{xT} \lambda^{-1} \cdot \mathbf{P}_{[k-1]}^x \quad (5.17)$$

$$\mathbf{W}_{[k]}^x = \mathbf{W}_{[k-1]}^x + (\alpha_{[k]}^x \cdot \mathbf{g}_{[k]}^x)^T \quad (5.18)$$

$$\mathbf{X}_{[k]}^x = \left[ i_{g[k-1]}^x, i_{g[k]}^y, i_{g[k-1]}^y, v_{g[k]}^x, v_{g[k-1]}^x \right]^T \quad (5.19)$$

$$\mathbf{W}_{[k]}^x = [a_{1[k]}^x, a_{2[k]}^x, a_{3[k]}^x, b_{0[k]}^x, b_{0[k]}^x] \quad (5.20)$$

In (5.15)-(5.18),  $\mathbf{P}_{(5 \times 5)}$  stands for the covariance matrix and it is initialized to  $\mathbf{P} = 0.01 \cdot \mathbf{I}_{(5 \times 5)}$ ;  $\mathbf{g}_{(5 \times 1)}$  is the adaptation gain, and  $\lambda = [0, 1]$  is the forgetting factor, which need to be selected as a trade-off of the expected estimation bandwidth and the signal to noise ratio. Values between 0.95 and 1 are often selected. For this study, the values shown in Table E.2 have been used. After the injection of a new pulse, the estimation of the  $\mathbf{W}$  components for both the  $\alpha$  and the  $\beta$  components is updated and a new estimation for  $\mathbf{R}_{\alpha\beta}$  and  $\mathbf{L}_{\alpha\beta}$  is obtained using (5.14). The algorithm has demonstrated to be fast enough to be implemented on medium performance digital signal controllers as it is shown in [5.5].

### 5.4.3 RLS Accuracy Evaluation

To compare the accuracy of the RLS estimation method with the proposed modelling technique for defining the equivalent impedance of a grid-tied converter, the following study is proposed, where it has been considered only the operation of VSC 2. In this evaluation converter VSC 2 is interconnected with an ideal voltage source responsible to establish the voltage at the PCC,  $v_g$ , and also to inject the pulse to obtain the data for the estimation. The ideal voltage source is interconnected with converter VSC 2 by a filter as the one described in Fig. 5.1, with  $L = 1.7$  mH and  $R = 0.33$   $\Omega$ . The simulation results comparing the performance of the RLS and the modelling technique are illustrated in Fig. 5.9. In blue trace the results obtained according to (5.4) and (5.5) and in orange the ones from the RLS method.

As shown, active and reactive commands for covering the four quadrant operation are considered. The current commands for the VSC are established based on the approach described in [5.6] and according to (5.3) and (5.4)-(5.5), the equivalent terms of the converter impedance can be obtained following the procedure described in Section 5.3. The results show a close agreement between both solutions.

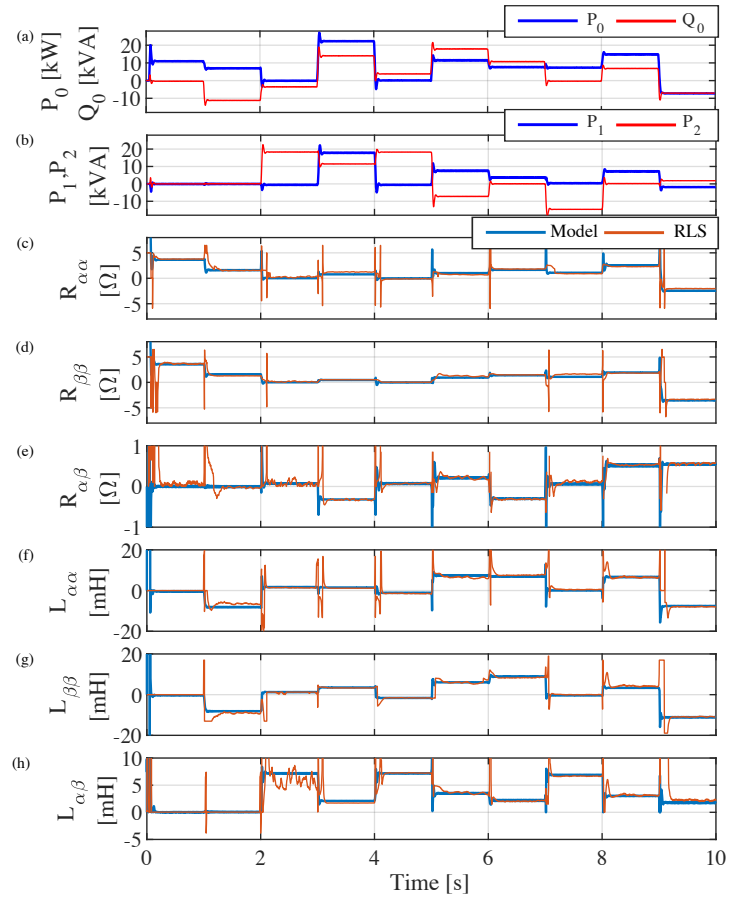


**Figure 5.9:** Simulation results. Comparison between the RLS method (orange) and the model components (blue) according to the modelling approach presented in section 5.3, using the power references in (a) and (b). (a) Active (blue) and reactive (orange) power references; (b) Pulsating terms resulted from the presence of negative sequence currents; (c) Resistive term,  $R_{\alpha\alpha}$  of the equivalent grid impedance, RLS results in blue and the ones from the modelling technique in orange; (d) Inductive term,  $L_{\alpha\alpha}$ , of the equivalent grid impedance; (e) Resistive term  $R_{\beta\beta}$ ; (f) Inductive term  $L_{\beta\beta}$ ; (g) Resistive term  $R_{\alpha\beta}$ ; (h) Inductive term  $L_{\alpha\beta}$ .

An additional simulation has been carried out considering the operation of converter VSC 2 within the system from Fig. 5.1. In this case, the converter VSC 1 is also responsible for the estimation and thus to implement the PSI strategy. The results are shown in Fig. 5.10. In this case, both converters are parallel connected with the main grid. Thus to estimate the equivalent impedance of the system, it has to be considered the impedance from the grid side. The results from the RLS algorithm has been compared with the ones obtained from the isolated operation of converter VSC 2 shown in Fig. 5.9, considering a grid impedance of  $R_g = 0.33 \Omega$  and  $L_g = 11 \text{ mH}$ .

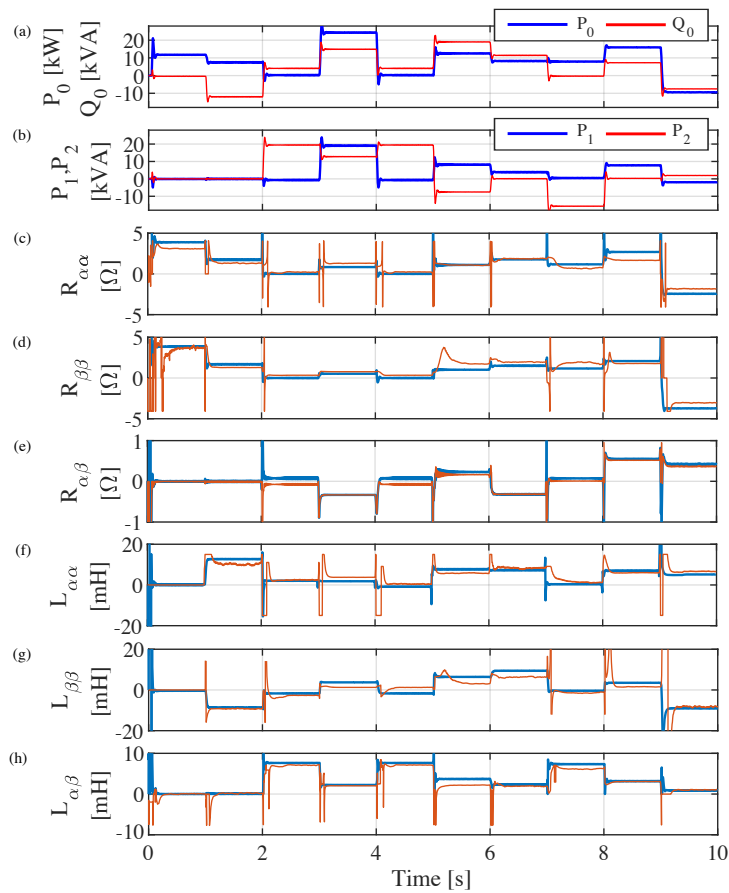


**Figure 5.10:** Simulation results. Comparison between the RLS method (orange) and the model components (blue) considering the system configuration from Fig. 5.1, using the power references in (a) and (b). (a) Active (blue) and reactive (orange) power references; (b) Pulsating terms resulted from the presence of negative sequence currents; (c) Resistive term,  $R_{\alpha\alpha}$  of the equivalent grid impedance, RLS results in blue and the ones from the modelling technique in orange; (d) Inductive term,  $L_{\alpha\alpha}$ , of the equivalent grid impedance; (e) Resistive term  $R_{\beta\beta}$ ; (f) Inductive term  $L_{\beta\beta}$ ; (g) Resistive term  $R_{\alpha\beta}$ ; (h) Inductive term  $L_{\alpha\beta}$ .

### 5.4.4 Experimental Results

To test the performance of the RLS method, an initial test without considering the operation of converter VSC 2 was carried out. The purpose of this is to establish an evaluation frame between the estimation provided by the RLS algorithm and the modelling technique. The modelling technique provides, straightforwardly, the equivalent impedance of the converter VSC 2. However, the RLS technique determines the impedance of the converter by estimating the *Thevenin* equivalent between the converter and the grid impedance, according to Fig. 5.2, thus grid impedance has to be decoupled from the RLS estimation, in order to compare these results with the ones from the modelling technique.

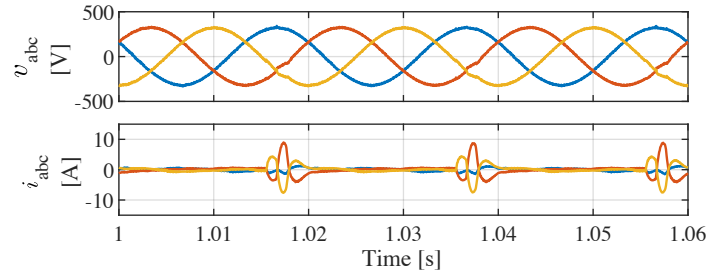


**Figure 5.11:** Experimental results. (a) Voltage waveforms of VSC 1 with the PSI; (b) Current waveforms of VSC 1 with the PSI.

To determine the grid impedance through the RLS method, an initial test has been performed, where converter VSC 2 is not commanding any power reference and converter VSC 1 is injecting the PSI signal to obtain the grid data. The estimation is performed at instant  $t = 1$  s, when VSC 1 starts injecting the pulses. Fig. 5.11 shows the experimental current injection and the resulting voltage after the start of the pulse injection. As it can be seen, fewer distortion is induced, in comparison with the previous HFSI method, and although current control may react against the pulses, their presence on the voltage is still noticeable. This also presents the benefit that stability analysis is not required. Before the RLS estimation, the grid voltage,  $\mathbf{v}_s^{\alpha\beta}$  is subtracted from the one measured at the PCC,  $\mathbf{v}_g^{\alpha\beta}$  and  $\mathbf{i}_1$  is used for the estimation. Fig. 5.12 shows a comparison between the simulated results from converter VSC 1 injecting the pulses as described in Fig. 5.8 and an experiment under same conditions.

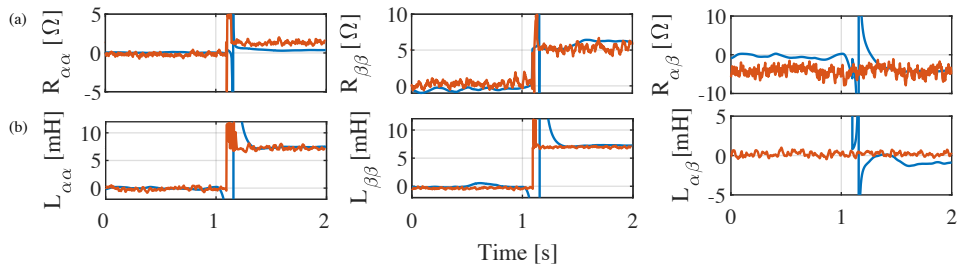


**Figure 5.12:** Experimental results. Comparison of RLS method between simulation results (in blue) and experimental results (in orange). (a) Resistive terms of the equivalent grid impedance, from left to right:  $R_{\alpha\alpha}, R_{\beta\beta}, R_{\alpha\beta}$ ; (b) Inductive terms of the equivalent grid impedance, from left to right:  $L_{\alpha\alpha}, L_{\beta\beta}, L_{\alpha\beta}$ .

There is a close concordance between the simulation and the experimental results, which can be used as a prove of the accuracy of the method. These values are achieved for a grid impedance of  $L = 9$  mH and  $R = 6$   $\Omega$ . The grid impedance characteristic has been considered the same for the rest of the analysis, and thus, to evaluate only the equivalent impedance of converter VSC 2 it has to be decoupled from the results.

An additional experiment has been evaluated to prove the performance of the RLS in a real environment. Fig. 5.13 shows the estimation of the grid impedance during different power converter transients, comparing experimental and simulated results. For this case, in a setup similar to the one shown in Fig. 5.1, converter VSC 2 is commanding 2.5 kVA of positive and negative reactive power and VSC 1 is responsible for implementing the PSI strategy and the RLS estimation. The impedance values are filtered with a 5 Hz low pass filter to remove the high frequency noise affecting the  $a_i$  and  $b_j$  values. The results show a close concordance between the terms from simulation with the experimental setup.

The magnitude of the inductive terms are similar for the positive and negative power reference, differing on the direction on the  $L_{\beta\beta}$  term, which makes sense with the conditions

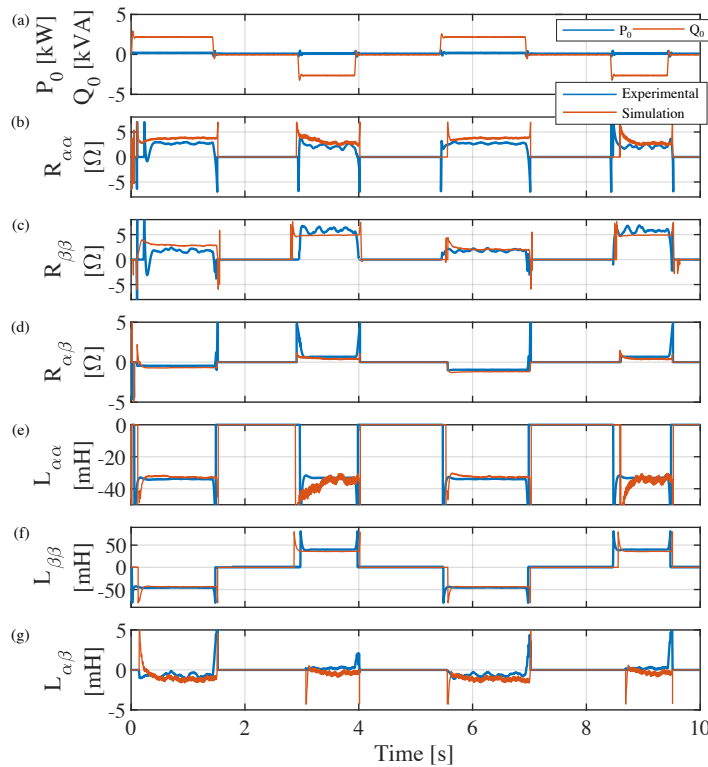


**Figure 5.13:** Experimental results. Comparison of RLS method between simulated and experimental results in two transients. (a) Active (blue) and reactive (orange) power references of converters VSC 2; (b) Resistive term,  $R_{\alpha\alpha}$  of the equivalent grid impedance, simulated results in blue and experimental ones in orange; (c) Resistive term  $R_{\beta\beta}$ ; (d) Resistive term  $R_{\alpha\beta}$ ; (e) Inductive term,  $L_{\alpha\alpha}$ , of the equivalent grid impedance; (f) Inductive term  $L_{\beta\beta}$ ; (g) Inductive term  $L_{\alpha\beta}$ .

of the experiment. The fluctuation in the resistive terms result from the losses in the filter. Additionally, there is a slight variation between the  $R_{\alpha\alpha}$  and the  $R_{\beta\beta}$  terms which depends on the direction of the current, being the module of the equivalent impedance term  $Z_{\alpha\alpha}$  and  $Z_{\beta\beta}$  equal in both cases.

## 5.5 Conclusion

In this chapter, the problem of impedance estimation in grids with embedded grid-tied converters has been addressed. The equivalent modelling of the converter, based on the technique developed in Chapter 3, has been presented. Additionally, a RLS algorithm based on a PSI technique has been applied to the online impedance estimation problem.

A simulated comparison between the modelling technique and the RLS estimation has been carried out. For the validation, the power converter has been required to inject/absorb different levels of active/reactive power. The results derived from the simulation prove that the RLS converge to close values when compared with the proposed modelling.

Experimental results have been also provided, validating the conclusions driven from the simulation tests. The contributions of this chapter may be summarized as follows:

- The validation of the model presented in Chapter 3 to determine the equivalent impedance of a VSC depending on its power references. Proving to be a valid tool to define the system conditions in the four quadrant operation as well as with balance and unbalance conditions.
- An alternative excitation technique based on a PSI method has been proposed to be implemented within the controller of the VSC. This technique has been presented as an alternative to the one proposed on Chapter 4, inducing fewer distortion than HFSI solutions and with no need of additional stability analysis.
- The performance of an online impedance estimation technique based on the aforementioned PSI excitation method has been tested working in parallel with an RLS algorithm. The performance of this technique has been compared with the results from the modelling technique showing a close agreement between them.
- The proposed estimation technique has been evaluated under preliminary experimental conditions, within a real environment with a VSC commanding different levels of active and reactive power. These experimental results have been compared with the equivalent impedance terms determined by simulation under the same conditions and proving a close agreement.

## References

- [5.1] P. Rioual, H. Pouliquen, and J. . Louis, "Regulation of a pwm rectifier in the unbalanced network state using a generalized model," *IEEE Transactions on Power Electronics*, vol. 11, no. 3, pp. 495–502, May 1996.
- [5.2] P. García, M. Sumner, Á. Navarro-Rodríguez, J. M. Guerrero, and J. García, "Observer-based pulsed signal injection for grid impedance estimation in three-phase systems," *IEEE Transactions on Industrial Electronics*, vol. 65, no. 10, pp. 7888–7899, Oct 2018.
- [5.3] A. Arriagada, J. Espinoza, J. Rodriguez, and L. Moran, "On-line filtering reactance identification in voltage-source three-phase active-front-end rectifiers," in *The 29th Annual Conference of the IEEE Industrial Electronics Society, 2003. IECON '03*, vol. 1, Nov. 2003, pp. 192–197 vol.1.
- [5.4] M. Cespedes and J. Sun, "Adaptive control of grid-connected inverters based on online grid impedance measurements," *IEEE Transactions on Sustainable Energy*, vol. 5, no. 2, pp. 516–523, April 2014.
- [5.5] P. García, J. M. Guerrero, J. García, A. Navarro-Rodríguez, and M. Sumner, "Low frequency signal injection for grid impedance estimation in three phase systems," in *2014 IEEE Energy Conversion Congress and Exposition (ECCE)*, Sept 2014, pp. 1542–1549.
- [5.6] K. Ma, W. Chen, M. Liserre, and F. Blaabjerg, "Power controllability of a three-phase converter with an unbalanced ac source," *IEEE Transactions on Power Electronics*, vol. 30, no. 3, pp. 1591–1604, March 2015.

## Chapter 6

# Variable Switching Frequency Control of Distributed Resources for Improved System Efficiency

### 6.1 Introduction

Efficiency of power converters has gained interest and importance over the past years. The increased installation of distributed generation and the seeking for a maximization of the renewable generation energy have motivated an increased interest on efficiency aspects. However, this is a sensitive matter in the sense that it has to be analysed as a whole, concerning the application, the regulatory conditions and the technical constrains.

Power converters are feasible solutions for interconnecting renewable energy sources with the energy power system (EPS). Nevertheless, in prevailing applications, such as solar and wind, they are operated rarely at rated values, being the efficiency at light loads a source of great concern. Semiconductor switching losses can be cut down by a reduction of the switching frequency. On the other hand, a reduction of the switching frequency may result in an increase of the presence of harmonics in the system, not conforming with regulation [6.1], which limits the harmonic current injected at the PCC. Thus, it is necessary to establish a trade-off between the losses of the DR and the switching frequency that allows to accomplish with regulation at the local EPS, maintaining a good system efficiency profile. In most cases, once verified that the selected switching frequency (SF) complies with the harmonic emission limits, it is maintained constant at any operating condition. Adapting the SF according to the operating conditions leaves room for a global optimization of the power losses. Moreover, this is proposed as a convenient approach for LV applications in which the large impedance of the transformer at high frequencies allows to assume that most of the power losses are under the

responsibility of the distributed resource (DR) owner and increasing the switching frequency might result in the reduction of the distortion losses in the local grid.

Chapter 2 summarizes the most common modulation schemes for three-phase systems as well as their main challenges, oriented to extend the linear modulation range and obtain larger power density, improving the efficiency of the converters. Selective harmonic mitigation techniques could find a way to reduce low-order harmonic amplitudes at low frequency modulation indices [6.2, 6.3]. Also, different modulation schemes, which allows to increase system efficiency by reducing the number of switches operating at a time, like discontinuous PWM techniques, may be a way to enhance system efficiency [6.4, 6.5]. Additionally, variable switching frequency techniques are feasible solutions for the aforementioned applications, due to their possibility of adapting the SF to the operating conditions.

In the previous sections, the impact of impedance estimation in endowing power converters with the possibility of providing reactive power and unbalance compensation features has been studied. In the present one, impedance estimation is presented as a key aspect to enhance the efficiency of the power system, by a dynamic optimization of the SF depending on the load level of the converter. The chapter introduces the regulatory limits of a system with LV DRs, starting with the study of the effect of the SF on the harmonic emission in three-phase VSC. Two-level inverters with first-order inductive filters are considered, as one of the preferred technologies in LV applications. The evaluation of inverter losses, based on the switching frequency conditions and including thermal constraints, is presented. An analysis of the estimation of distortion losses caused by the inverter in the local grid is also included. The proposed method for the on-line optimization of the SF is described then, as well as the case study designed to demonstrate the validity of the proposal with their experimental results. Finally, the conclusions drawn from the study close the chapter.

## 6.2 Efficiency Constrains

As it has been previously mentioned, converter efficiency is highly dependant of the switching operation, being possible to enhance it by adapting the frequency based on the system conditions. However, converter operation is limited by a series of regulatory and technical constrains. In this section, the limitations faced to enhance system efficiency, and the aspects that might be addressed to improve converter performance are studied.

### 6.2.1 Switching Frequency and Current Harmonics

As a general rule, increasing the SF leads to a displacement of the harmonic spectrum of the voltage at the converter terminals to a higher frequency range. Consequently, the inductive behavior of the filter and grid upstream yields to a reduction in the induced current harmonics due to the higher impedance of these inductances at the new frequencies. However, it is important to note that the dead-time of the IGBTs limits the validity of the said statement, leading to the emergence of low-frequency harmonics (mainly 5<sup>th</sup> and 7<sup>th</sup> order) [6.6, 6.7] with a growing impact at higher SFs. Nevertheless, this effect can be mitigated by current regulators, whose bandwidth use to fall within these values. Fig. 6.1 shows the current distortion of an inverter given by the parameters shown in Table E.3 as a function of the SF.

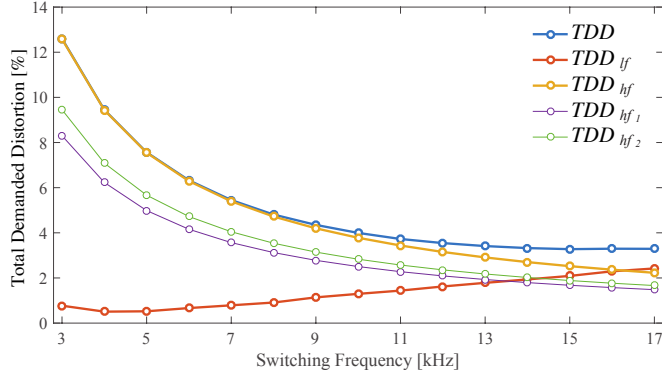


**Figure 6.1:** Current  $TDD$  as a function of the SF for different frequency bands. Effect of the dead-time in low-frequency harmonics

According to the standard, [6.1], this value has been reported as the total demanded distortion ( $TDD$ ),

$$TDD = \frac{\sqrt{\sum I_i^2}}{I_n}, \quad (6.1)$$

which can be defined as the total root-sum-square of the current harmonics injected by the DR unit,  $I_i$ , divided by the rated current capacity of that unit,  $I_n$ . In Fig. 6.1,  $TDD$  has been split in two terms,  $TDD_{lf}$  and  $TDD_{hf}$  using the 40<sup>th</sup> harmonic included in [6.8] as a limit between low and high frequencies. Thus, those parameters can be related as

$$TDD = \sqrt{TDD_{lf}^2 + TDD_{hf}^2}, \quad (6.2)$$

which allows to show the different behavior of the theoretical PWM harmonics and the non-idealities induced by the dead-time. As it is shown in Fig. 6.1, the effect of the dead-time reaches such an importance in  $TDD$  that increasing the SF over a certain limit becomes counterproductive. The use of dead-time compensation techniques [6.9, 6.10] could potentially raise this limit. It is also interesting to point out that the results shown in Fig. 6.1 are independent of the load of the converter, as only the fundamental component varies on a significant scale with the SF. On the contrary, and especially in weak grids, the values shown in this graph can be affected to some extent by the impedance of the system upstream from the converter terminals. This suggests that an online measurement of harmonic distortion will provide better results than a theoretical estimation. Nonetheless, the simplicity of this estimation can be valuable in most cases.

## 6.2.2 Converter Losses and Thermal Limits

Converter losses,  $P_{VSC}$ , are mainly determined by switching losses,  $P_{sw}$ , and conduction losses,  $P_{cd}$  [6.11–6.13]. Other issues should be considered when assessing the efficiency of these devices, such as cooling power; however, as they are not normally affected by the SF, they will not be considered in this work. Switching losses are strongly influenced by the SF,  $f_{sw}$ , as well as by the load level of the converter,  $c$ , defined as the ratio between the actual and rated

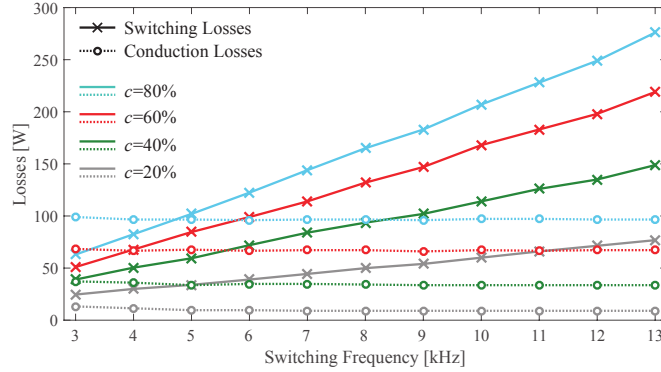


Figure 6.2: Converter switching and conduction losses as a function of the SF

current. Even if the power factor of the converter also affects this parameter due to variations in the commutation phenomenon, this effect is hardly noticeable and can be neglected with little error for the aim of this study. As increasing the SF results in a proportional rise of switching events, the relationship between SF and switching losses is almost linear. Conduction losses, for its part, are mainly affected by the load of the converter, and in a more subtle way, by the SF due to the increased current distortion that arises at lower frequencies. Taking these facts into consideration, an approach to the converter losses, with  $c$  and  $f_{sw}$  as parameters, can be obtained by using expression (6.3).

$$P_{VSC}(c, f_{sw}) = P_{sw}(c, f_{sw}) + P_{cd}(c, f_{sw}). \quad (6.3)$$

The assessment of the aforementioned power losses for the specific IGBT power modules mounted in the converter used for the experimental validation is shown in Fig. 6.2. To obtain the said graph, a PLECS model of the converter was implemented [6.14]. This model includes the thermal performance of the IGBT power modules, which allows to depict the operational constraints of the converter in terms of SF. Thus, the imperative derating of the device is shown in Fig. 6.3. This figure was calculated for each SF by assessing the load level of the converter at which the junction temperature of the solid state devices equals the temperature reached at rated values. The inclusion of these data in a two-dimensional look-up table (LUT), together with the use of interpolation, is enough to obtain a good estimation of converter losses as a function of  $c$  and  $f_{sw}$  in the optimization scheme proposed in this work. The exploitation of this table for control purposes by operating the converter at variable SF is analyzed in Section 6.3. In any case, it is clear from Fig. 6.3 that, if the SF command  $f_{sw}^*$  lies on the forbidden area of the graph, it has to be reduced to the nearest feasible value,  $f_{sw}^{**}$ .

### 6.2.3 Distortion Losses in the Local Grid

Regulation provides practical guidelines to comply with regulation, [6.8], which considers the first 40 harmonics of the spectrum. This implies to operate converters at a SF typically higher than 3 kHz, limiting the range of harmonics present at PCC. However, even if limited

by regulation, the injection of current harmonics into the distribution grid can cause significant power losses which may be classified in two categories:

1. Copper losses in the distribution line and distribution transformer;
2. Power losses in local loads.

Notice that additional losses could exist upstream from the distribution transformer which are not on the local EPS owner's responsibility. However, this term can be neglected, not only because of the low value of the resistive contribution from the MV level when compared with the LV side, but also because of the low capability of high-order current harmonics to travel deep into the EPS.

Fig. 6.4 shows a layout of the benchmark system considered in this work. A full description of the components required for the physical implementation is provided in the Appendix E. The local EPS, with embedded DRs, is connected to the Area EPS through a distribution transformer, being the metering devices connected either in the MV or LV side according to the ownership of this piece of equipment. Both the DRs and the local loads are connected to the distribution line. Those local loads located close to the power converters are more prone to suffer from distortion losses. In Fig. 6.4, a local load is connected directly to the DR point of coupling (PC) to highlight this phenomenon. The effect of the distortion power in local loads is different according to the type of device (motor, lighting, heating, etc.) and its nature (linear/non-linear). In any case, distortion power can be, as a general rule, considered undesirable [6.15].

Different types of penalization criteria could be considered in order to take into account the harmful effects of higher levels of injected current distortion in particular loads, e.g. cost associated to the loss of life. However, in this work only the cost associated with the power transmitted at non-fundamental frequency is taken into account. A pure resistive load is considered in this contribution as the easiest way to underline the benefits of the proposal.

A precise calculation of the power transmitted by the converter at harmonic frequencies

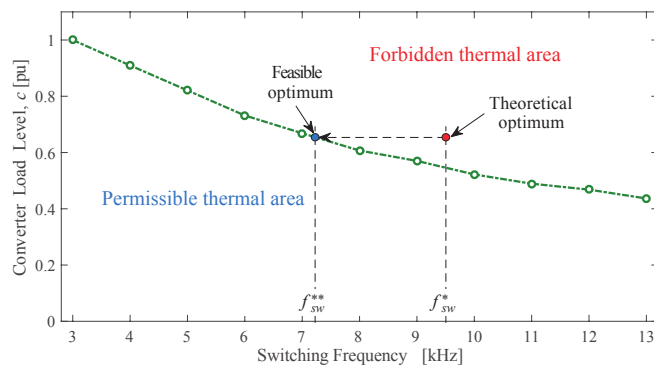


**Figure 6.3:** Thermal constraints for variable SF operation

can be done by assessing the expression (6.4).

$$P_{losses} = Re\left\{\sum_{i=2}^N \mathbf{v}_{PCi} \cdot \mathbf{i}_{conv i}^*\right\}, \quad (6.4)$$

where  $\mathbf{i}_{conv i}$  and  $\mathbf{v}_{PCi}$  are the power invariant space vector harmonic components of the converter current and voltage at its point of coupling, obtained by applying the Direct Fourier Transform (DFT).

For the practical implementation of (6.4), natural sampling of voltages and currents at SF is not enough due to Nyquist limit, but oversampling can help in complying with these requirements. In any case, other simplified methods such as Goertzel algorithm [6.16] are better suited for on-line applications [6.17, 6.18]. In this numerically efficient method, just a selected set of harmonics are identified, which can be enough to calculate the resistive component of system impedance,  $R_{eq}$ , at the most relevant bands of the spectrum. This reduced set of values can be used, together with the expected injection of current harmonics given in Fig. 6.1, to formulate a good estimation of the said power losses.

Fig. 6.5 shows the value of  $R_{eq}$  for the installation depicted in Fig. 6.4 considering the parameters shown in Table E.4. The identification of just three impedance values, one at the low-frequency range (5<sup>th</sup> or 7<sup>th</sup>) and two at the two lowest PWM frequency bands (e.g.  $f_{sw} - 2f_m$  and  $2f_{sw} - f_m$ ,  $f_m$  being the modulation frequency), can be enough to estimate distortion losses by using expression (6.5).

$$P_{losses} \approx 3I_n^2 \cdot (R_{eq}^{5f_m} \cdot TDD_{lf}^2 + R_{eq}^{f_{sw}-2f_m} \cdot TDD_{hf1}^2 + R_{eq}^{2f_{sw}-f_m} \cdot TDD_{hf2}^2). \quad (6.5)$$

Notice that with this aim,  $TDD_{hf}$  has been segregated in two components:  $TDD_{hf1}$ , for the harmonic band around the SF and  $TDD_{hf2}$ , for the rest of higher frequency values. The specific contribution of each of these components can be observed in Fig. 6.1.

It is important to highlight that the effect of a variation in the power demand,  $P$ , of the loads connected to the local EPS, on the harmonic power losses at the line and local loads,  $P_{losses}$ , is not obvious. As a consequence, neither is the effect of this variation on the resulting

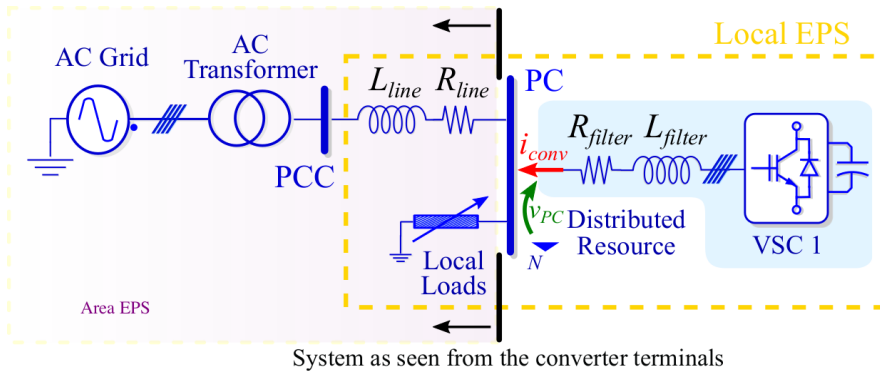
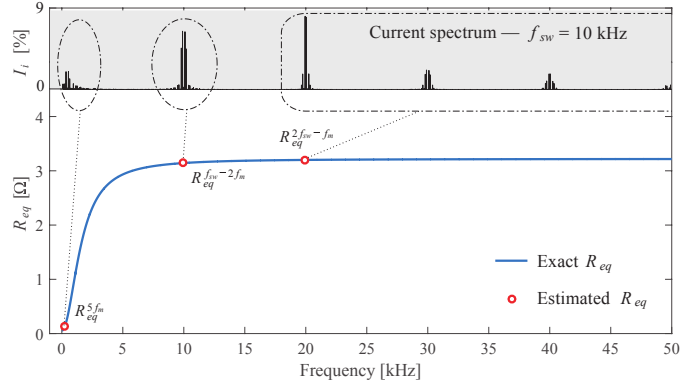


Figure 6.4: Local EPS with embedded DRs



**Figure 6.5:** Estimation of the resistive component of system impedance at the PC as a function of frequency

optimum SF. The value of the resistive components of system impedance for the benchmark system shown in Fig. 6.4 are the result of the parallel equivalent represented by the RL branch of the line and transformer and the resistive branch represented by the local loads.

For the data shown in Table E.4, the value of these resistive components for the frequencies of interest is depicted in Fig. 6.6 as a function of  $P$ . At low power demand levels, the connection of new loads increases harmonic power losses. On the contrary, beyond a certain power demand, 4.47 kW in the present case, the connection of new loads decreases the resistive value of system impedance, and thus, harmonic power losses. For this reason, if the DR is working at a fixed load level,  $c$ , with a low power demand of local loads, the connection of new loads drives the optimum SF to higher values in search for a lower level of harmonic losses. Conversely, up from the stated power demand value, the connection of new loads leads to a reduction of the optimum SF value, as higher harmonic losses can be admitted in the search for a global optimum.

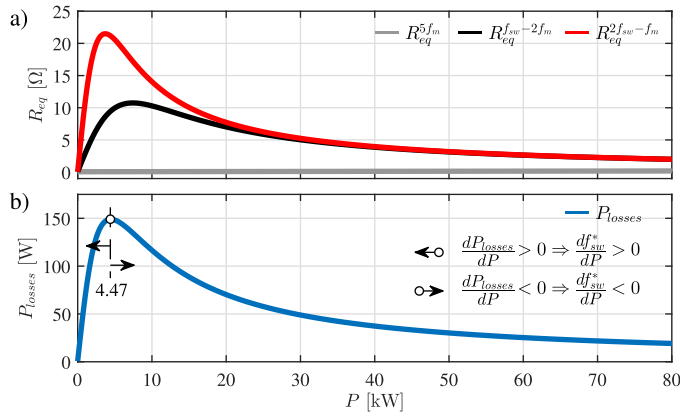


**Figure 6.6:** Effect of the power demand of local loads in harmonic power losses. (a) resistive component for the frequencies of interest ( $f_{sw}=10$ kHz,  $f_m=50$ Hz) and (b) harmonic power losses

### 6.3 On-line Optimization of the Switching Frequency

The fundamentals of the on-line optimization of the SF proposed in this study are schematically summarized in Fig. 6.7. The inputs for the algorithm are:

1. The space vector of the converter current, which is already available as calculated from current samples for the operation of its inner controller;
2. The resistive component of system impedance for the different frequency bands considered in Section 6.2.3.

The application of a set of look-up tables together with a SF sweep allows the on-line calculation of a curve, relating the losses at the local EPS,  $P_{Local\_EPS}$ , with the SF,  $f_{sw}$ , for the present operating point. With this aim, the converter losses,  $P_{VSC}$ , are obtained from a 2D-look-up table built by adding the conduction and switching losses of the specific converter according to 6.3.

A set of three 1D-look-up tables, built from the distortion data depicted in Fig. 6.1, provides the  $TDD$  of the converter at the different frequency bands for each SF used in the sweep. From these results, the losses at the line and local loads,  $P_{losses}$ , are obtained by using (6.5). The addition of both converter losses and line and local load losses at each SF leads to the desired curve. Then, the minimum of this curve is identified, which gives the optimum losses at the local EPS and, even more important, the optimum SF for the current operating point. Notice that the bandwidth of the SF command,  $f_{sw}^*$ , must be much lower than the one used in the inner controllers of the inverter not to interfere with its dynamic performance. As a consequence, a low update rate of this command is acceptable and the required computational burden can be assumed by the controller without a significant effort either in a synchronous or asynchronous scheme. In order to avoid the effect of noise in the sampled parameters, as well as steep frequency variations due to sudden changes in the inverter load level or in the system impedance – due to the connection/disconnection of local loads, a first-order low-pass (FLP) filter is used to smooth the frequency command.

Although not depicted in Fig. 6.7 for the sake of clarity, the frequency command,  $f_{sw}^*$ , should pass a final limitation stage in order to make the control compatible with the thermal constraints shown in Fig. 6.3. As already stated in Section 6.2.2, if the pair  $(f_{sw}^*, c)$  lies in the forbidden area of this graph, the SF command is reduced to the maximum SF compatible with the present converter load level,  $f_{sw}^{**}$ .

### 6.4 Case Study

In this section, a case study is used to illustrate the advantages of using an overall efficiency optimization of the DR within its local EPS. With this aim, the LV distribution feeder and the distributed generator (DG) depicted in Fig. 6.4 are considered. The parameters of the grid infrastructure are shown in Table E.4 while those from the inverter-based DG are given in Table E.3 (except for the system impedance, that for this case study is derived from Table E.4).

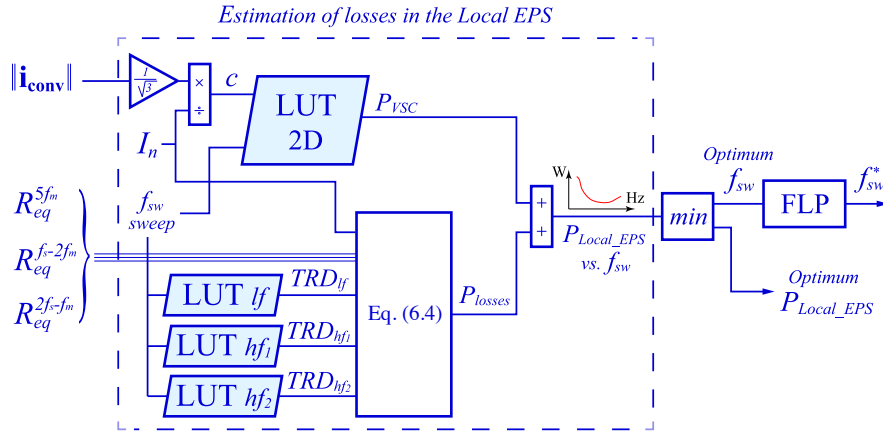


Figure 6.7: On-line method for the optimization of the switching frequency

Fig. 6.8 shows the total losses in the local EPS, together with its different components, i.e. converter losses and grid & local loads losses for a DR working at 20% of its rated power with unity power factor. It is concluded from this drawing that increasing the SF from the design parameter, 3 kHz, to 9 kHz, reduces the local EPS losses in a 44.6%, and improves the overall efficiency at this load level (i.e. the ratio between the local EPS losses and the power delivered by the converter) in 1.20%.

Fig. 6.9 expands the analysis to different load levels of the DR. As it is depicted in this figure, connecting the values of the minimum local EPS losses at each converter load level,  $c$ , leads to the optimum trajectory of the inverter SF. Furthermore, the thermal limit of the device is also given in Fig. 6.9. This limit is established by calculating the maximum acceptable SF at each load level, which is determined by the frequency that leads to the design temperature (i.e. the one obtained at 3 kHz and rated power). From the said graph, it can be concluded that for the device under test, a variable SF mode with optimization of

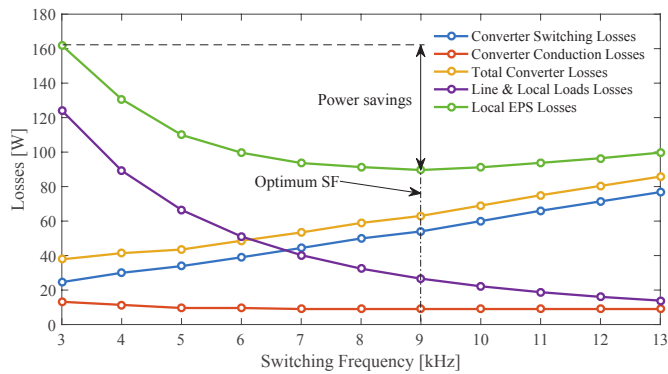


Figure 6.8: Local EPS losses as a function of SF -  $c = 20\%$

losses is only feasible for loads lighter than 80% of rated power. Moreover, it is also observed that the benefit of the proposal is much more relevant at light loads: e.g. the saved power is higher at 20% than at 80% on both relative and absolute terms (72 W vs. 21 W and 1.20% vs. 0.09%).

Fig. 6.10 shows simulation results of the application of the on-line optimization method proposed in Section 6.3 to the present case study. An update rate of 10 ms was used for the SF command and a bandwidth of 0.6 Hz was selected for the FLP filter. The SF sweep included in the algorithm is conducted with a resolution of 100 Hz in order to limit the computational burden. As it is shown in Fig. 6.10 (a), the converter load level is started at  $c = 20\%$  and increased to  $c = 80\%$  after 2 s, always with unity power factor. Moreover, the local loads stay at rated power according to Table E.4 and are reduced to 50% of this value, i.e. 25 kW, at 4 s. Fig. 6.10 (b) shows the effect of the steep variation on the resistive components of system impedance induced by the local load reduction. After the load variation, slight modifications can be still observed on these values, which are caused by the SF drift along the process, due to the influence of reactive components on the resistive equivalent. The optimum SF value obtained by the algorithm along with the final SF command, i.e. after the FLP, is depicted in Fig. 6.10 (c). The converter is started with a conservative SF value of 5 kHz and, from this instant, the algorithm competently tracks the optimum SF increasing the efficiency of the installation. As predicted in Fig. 6.6, the reduction of the power demand of local loads from 50 kW to 25 kW at 4 s leads to a rise of the optimum SF. In Fig. 6.10 (d) the optimum and real power savings, compared to a traditional operation of the DR at constant SF, are depicted. As expected, greater power savings are obtained with the converter working at light loads as well as with an increased value of the resistive component of system impedance.

## 6.5 Experimental Results

Two sets of experimental tests were carried out in this work: the first one is aimed to prove the power saving potential of the stated proposal, and the second, to demonstrate the validity of the on-line SF optimization method described in Section 6.3.

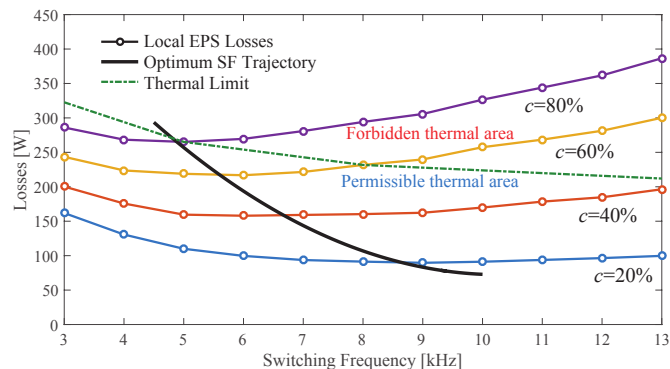
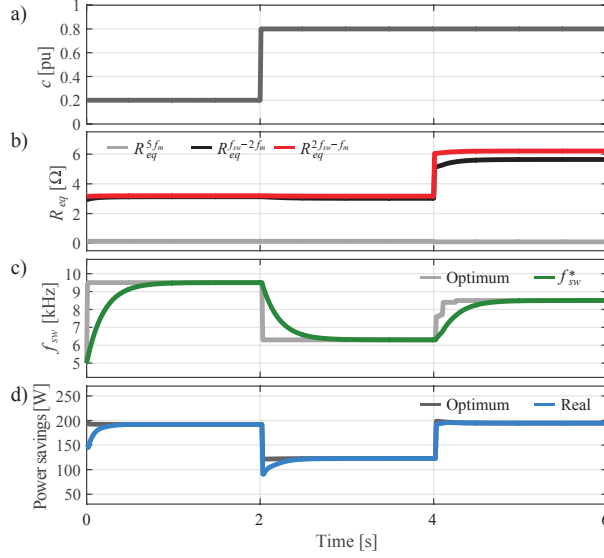


Figure 6.9: Optimum trajectory of the SF as a function of converter load



**Figure 6.10:** Application of the optimization method to the proposed case study. (a) converter load profile, (b) system impedance, (c) SF command, and (d) power savings

### 6.5.1 STATCOM Mode

The test setup used in this case is shown in Fig. E.3. A 4-quadrant grid simulator, TC.ACS by Regatron, is used to emulate the electric system, 400 V – 50 Hz, and a 0.32 mH inductor,  $L_1$ , is used to emulate the LV line and transformer according to Fig. 6.4. An almost purely resistive air-heating system with a rated power of 9 kW is used to emulate the local loads according to the said figure. Finally, a custom-made three-phase two-level VSC, with a rated power of 30 kVA and a design SF of 6 kHz, is coupled to the grid through a 0.88 mH inductor,  $L_2$ , to play the role of the DR.

During this test the converter is operated in STATCOM mode at a light load, 10 kVA (i.e.  $c = 33\%$ ), delivering reactive power to the LV grid. Similar results are expected from other operation modes, due to the small influence of the power factor in converter losses, as it was stated in Section 6.2.1. The three-phase voltages and currents at the point of coupling of the DR, PC in Fig. 6.4, were registered in steady-state for different SFs within the range 6 kHz to 16 kHz. An off-line handling of these measurements were carried out to calculate their DFT, and subsequently, the losses at harmonic frequencies at the line and local loads (i.e. those caused by the air-heating system and parasitic resistance of  $L_1$ ) were calculated by the application of (6.4). For the particular case of the STATCOM operation mode, including the term at the fundamental frequency in (6.4) leads directly to the converter losses, so finally, the losses at the local EPS can be computed in a simple way as

$$\begin{aligned}
 P_{Local.EPS} &= Re\{\sum_{i=2}^N \mathbf{v}_{PCi} \cdot i_{conv i}^*\} - Re\{\sum_{i=1}^N \mathbf{v}_{PCi} \cdot i_{conv i}^*\} \\
 &= -Re\{\mathbf{v}_{PC1} \cdot i_{conv 1}^*\}.
 \end{aligned} \tag{6.6}$$

Notice that this is just a particular result, valid only for STATCOM operation mode. As

**Table 6.1:** Experimental results –  $c = 33\%$

SF	Losses			Pwr. savings
	Converter	Line&Loads	Local EPS	
6 kHz	781.2 W	253.8 W	1035.0 W	0.0 W
8 kHz	790.5 W	178.4 W	968.9 W	66.1 W
10 kHz	814.0 W	139.8 W	953.8 W	81.1 W
12 kHz	836.3 W	111.2 W	947.6 W	87.5 W
14 kHz	868.1 W	91.6 W	959.7 W	75.3 W
16 kHz	896.9 W	76.9 W	973.8 W	61.2 W

stated in Section 6.2.2, in a more general scheme, with the DR participating in the active power flow (inverter/rectifier mode), a look-up table with and estimation of converter losses as a function of the SF and the converter load level is to be used.

The results of the test are presented in Table 6.1 and Fig. 6.11. Thus, the spectra of the power invariant space vectors of voltage and current, at the point of coupling of the DR, are shown in the said figure for selected key SFs, such as 8 kHz, 12 kHz and 16 kHz. Both the positive and negative sequence components are displayed in this image. The most significant harmonics, located in bands around one and two times  $f_{sw}$ , are shifted to higher frequencies as the SF increases. Also, a clear reduction in the injection of harmonic currents can be observed at higher SFs. In Table 6.1 the computed values for converter losses, line and load losses and local EPS losses for each of the analyzed SFs are displayed, together with the resulting power savings. Specifically, harmonic power losses at the line and loads are calculated by using (6.4), while the application of (6.6) allows the computation of the local EPS losses. Both equations take the voltage and current harmonics of Fig. 6.11 as an input. Finally, the difference between the results from (6.6) and (6.4) gives the value of converter losses. As expected, an optimum SF is obtained, capable of achieving the minimization of system losses. As it is highlighted in the said table, the operation at 12 kHz reduces the overall system losses in 87.5 W when compared with the operation at the design value. This means a reduction of around 8.4% of the losses at this operation point ( $c = 33\%$ ), and thus, an improvement of the local EPS efficiency, which increases from 89.65% to 90.52%.

### 6.5.2 Inverter Mode

Slight changes are introduced in the test setup for this case. The 30 kVA converter is now operated in inverter mode to effectively replicate the performance of a DR. With this aim the DC-bus of the converter is fed from the Li-Ion battery shown in Fig. E.3 through a DC-DC stage. Furthermore, the converter is now coupled to the utility grid, 400 V – 50 Hz, through a dedicated distribution line and transformer according to the values shown in Table E.4. Three separate air-heating systems, each with a rated power of 9 kW, are used to emulate the local loads. The connection/disconnection of these systems allows to test the effect of a sudden change in system impedance.

The custom-made converter is operated through a controller using a TI C2000 Delfino™ TMS320F28335 MCU. The algorithm described in Section 6.3 was included in the firmware with the LUT system embedded in non-volatile RAM memory. Moreover, a variable SF inner

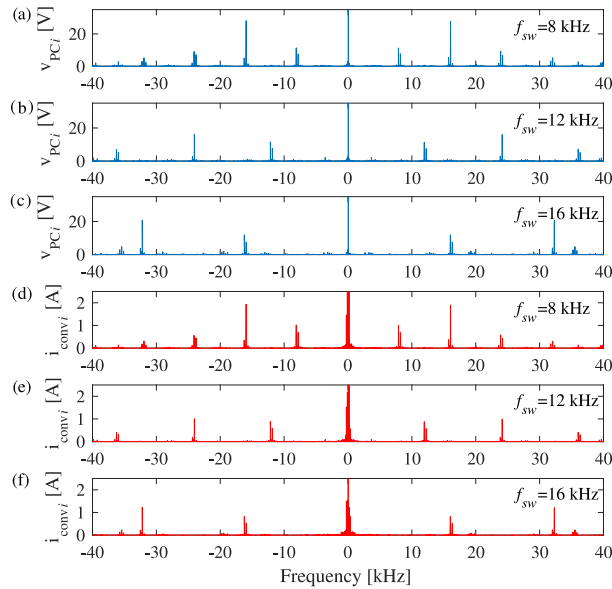


**Figure 6.11:** Spectrum of signals measured at the PC for different SFs. a), b) and c): voltage space vector for 8 kHz, 12 kHz and 16 kHz, respectively; and d), e) and f): current space vector for 8 kHz, 12 kHz and 16 kHz, respectively. Note: Fundamental components are truncated for the sake of clarity.

current controller for the converter was specifically designed for this test, including an adaptive tuning of the associated regulators.

During the test the DC-DC converter is commanded with different power steps, as shown in Fig. 6.12(d), while the VSC fixes a constant DC bus voltage value of 800 V and a constant power factor of 0.6. The test is started at a light load, 7.5 kVA (i.e.  $c = 25\%$ ), thus delivering 4.5 kW to the grid, while two of the 9 kW air-heating devices stay connected to emulate the local loads. After 2 s the converter load level increases to 12 kVA (i.e.  $c = 40\%$ ) and then to 27 kVA (i.e.  $c = 90\%$ ) at time 4 s, so that up to 16.2 kW are injected into the local grid. Fig. 6.12 shows the phase current of the VSC during these variations together with the performance of the SF in reaction to those load step changes. Finally, at time 6 s one air-heating system is added to the two devices already connected to the local grid, thus shifting the local demand from 18 kW to 27 kW.

As predicted in Fig. 6.6, the consequent change in system impedance at the converter point of coupling causes a reduction of harmonic power losses which leads to a fall in the optimum value of the SF.

Fig. 6.12, shows the measurements of the power supplied by the Li-Ion battery along the test, together with the power supplied by the VSC to the local grid. Thus, in Fig. 6.12(e) the VSC losses are obtained. The value of line and local load losses are calculated from voltage and current measurements for each step (considering steady state intervals) through Fast Fourier Transform (FFT) analysis, being 92.5 W, 137.6 W, 192.0 W and 180.6 W, respectively. As expected, during the first three steps, the decreasing switching frequencies lead to increasing line and local load losses. In the fourth step, even if the switching frequency is further

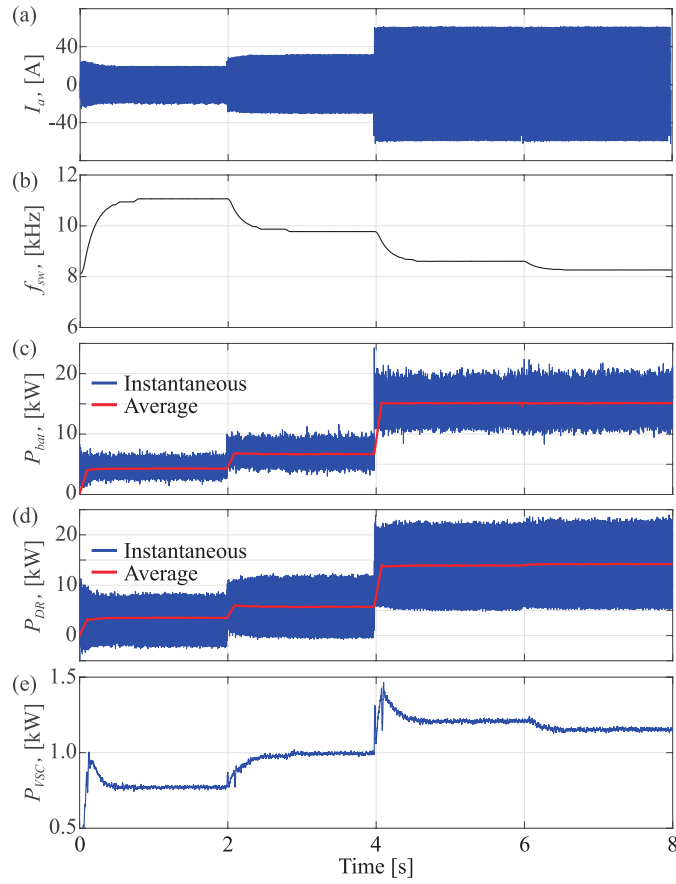


**Figure 6.12:** On-line SF optimization test: (a) converter ac current - phase  $a$ , (b) converter SF, (c) power supplied by the Li-Ion battery - DC-DC converter output side, (d) power supplied to the grid, and (e) converter losses

reduced, the decline of the Thevenin impedance of the system at the converter PC, due to the connection of a new load, overcomes this effect.

A comparison of the losses at the first step of the test, i.e. the one conducted with a lighter load,  $c = 25\%$ , with those obtained for the same conditions in a fix switching frequency scheme of 6 kHz, reveals that up to 132 W can be saved using the proposed operating mode. This means increasing the efficiency in 1.7% at the present operating point and in 0.4% if referred to the rated power of the converter.

## 6.6 Conclusion

In this chapter, an improved system efficiency of the local EPS is achieved by the optimization of the switching frequency of the converter to the current operation point. The technical and regulatory constraints which may limit the selection of the SF have been also considered. An online optimization strategy for the SF adaptation based on the load conditions and system impedance has been proposed, supported both with simulations and experiments. Contributions may be summarized as follows:

- The contribution demonstrates the interest of considering the converter losses together with the induced harmonic losses in the local line and loads when the ownership/operation of both assets is held by the same entity.
- The proposed method can be applied to DRs relying only on local intelligence but also to those in charge of system-level controllers.
- The thermal limits of the power modules used in the inverter are taken as a constraint in order to assure a safe operation of the device beyond its design SF when working at light loads. A LUT-based system, valid for an on-line implementation, was designed to provide the DR with a smart regulation of its SF. The results demonstrate that an improvement of the overall efficiency of the system at light converter loads by about 1% is readily achieved with the proposed method.
- This improvement is especially important for applications in which the grid-tied converter works often under rated power. This is the usual case of widespread technologies such as PV systems and small wind turbines.

## References

- [6.1] “IEEE standard for interconnecting distributed resources with electric power systems,” *IEEE Std 1547-2003*, pp. 1–28, July 2003.
- [6.2] J. Pontt, J. Rodriguez, and R. Huerta, “Mitigation of noneliminated harmonics of shepwm three-level multipulse three-phase active front end converters with low switching frequency for meeting standard ieee-519-92,” *IEEE Transactions on Power Electronics*, vol. 19, no. 6, pp. 1594–1600, 2004.
- [6.3] M. Sharifzadeh, H. Vahedi, R. Portillo, L. G. Franquelo, and K. Al-Haddad, “Selective harmonic mitigation based self-elimination of triplen harmonics for single-phase five-level inverters,” *IEEE Transactions on Power Electronics*, vol. 34, no. 1, pp. 86–96, 2019.
- [6.4] O. Ojo, “The generalized discontinuous pwm scheme for three-phase voltage source inverters,” *IEEE Transactions on Industrial Electronics*, vol. 51, no. 6, pp. 1280–1289, 2004.
- [6.5] L. Dalessandro, S. D. Round, U. Drofenik, and J. W. Kolar, “Discontinuous space-vector modulation for three-level pwm rectifiers,” *IEEE Transactions on Power Electronics*, vol. 23, no. 2, pp. 530–542, 2008.
- [6.6] C. Wu, W.-H. Lau, and H.-H. Chung, “Analytical technique for calculating the output harmonics of an H-bridge inverter with dead time,” *Circuits and Systems I: Fundamental Theory and Applications, IEEE Transactions on*, vol. 46, no. 5, pp. 617–627, May 1999.
- [6.7] S. Kaitwanidvilai, W. Khan-ngern, and M. Panarut, “The impact of deadtime effect on unwanted harmonics conducted emission of PWM inverters,” in *Environmental Electromagnetics, 2000. CEEM 2000. Proceedings. Asia-Pacific Conference on*, May 2000, pp. 232–237.
- [6.8] “IEEE standard conformance test procedures for equipment interconnecting distributed resources with electric power systems,” *IEEE Std 1547.1-2005*, pp. 1–62, July 2005.
- [6.9] S.-G. Jeong and M.-H. Park, “The analysis and compensation of dead-time effects in PWM inverters,” *Industrial Electronics, IEEE Transactions on*, vol. 38, no. 2, pp. 108–114, Apr 1991.
- [6.10] D.-H. Lee and J.-W. Ahn, “A simple and direct dead-time effect compensation scheme in PWM-VSI,” *Industry Applications, IEEE Transactions on*, vol. 50, no. 5, pp. 3017–3025, Sept 2014.
- [6.11] L. K. Mestha and P. D. Evans, “Analysis of on-state losses in PWM inverters,” *IEE Proceedings B - Electric Power Applications*, vol. 136, no. 4, pp. 189–195, July 1989.
- [6.12] J. W. Kolar, H. Ertl, and F. C. Zach, “Influence of the modulation method on the conduction and switching losses of a PWM converter system,” in *Industry Applications Society Annual Meeting, 1990., Conference Record of the 1990 IEEE*, vol. 1, Oct 1990, pp. 502–512.
- [6.13] S. Hazra, S. Madhusoodhanan, G. K. Moghaddam, K. Hatua, and S. Bhattacharya, “Design considerations and performance evaluation of 1200-V 100-A SiC MOSFET-based two-level voltage source converter,” *IEEE Transactions on Industry Applications*, vol. 52, no. 5, pp. 4257–4268, Sept 2016.
- [6.14] *Piece-wise Linear Electrical Circuit Simulation (PLECS), User Manual, Version 4.1*, Plexim GmbH, 2017, [Online]. Available: <http://www.plexim.com>.

- 
- [6.15] “IEEE recommended practices and requirements for harmonic control in electrical power systems,” *IEEE Std 519-1992*, pp. 1–112, April 1993.
  - [6.16] G. Goertzel, “An algorithm for the evaluation of finite trigonometric series,” *The American Mathematical Monthly*, vol. 65, no. 1, pp. 34–35, 1958.
  - [6.17] J.-H. Kim, J.-G. Kim, Y.-H. Ji, Y.-C. Jung, and C.-Y. Won, “An islanding detection method for a grid-connected system based on the Goertzel algorithm,” *Power Electronics, IEEE Transactions on*, vol. 26, no. 4, pp. 1049–1055, April 2011.
  - [6.18] R. Peña-Alzola, M. Liserre, F. Blaabjerg, M. Ordonez, and T. Kerekes, “A self-commissioning notch filter for active damping in a three-phase LCL-filter-based grid-tie converter,” *IEEE Transactions on Power Electronics*, vol. 29, no. 12, pp. 6754–6761, Dec 2014.



# Chapter 7

## Conclusion and Future Work

### 7.1 Conclusiones

El presente trabajo se centra en la operación de convertidores de potencia conectados a red en microrredes de corriente alterna. Se ha prestado especial atención al problema de la variabilidad de la impedancia equivalente de la red aguas arriba del punto de conexión en baja tensión de estos convertidores, relacionándolo con el impacto que ocasiona en el comportamiento dinámico del sistema de control de estos dispositivos. Las soluciones propuestas, basadas en técnicas de estimación de impedancia, permiten implementar sistemas de control que reaccionan a cambios en la red y logran la compensación en tiempo real de condiciones de desequilibrio. Para llevar a cabo esta tarea, sólo precisan de la información de variables eléctricas medidas en el punto de conexión, haciendo uso de la flexibilidad de los convertidores para generar señales de excitación superpuestas a la componente fundamental. Además, la estimación de parámetros de red brinda oportunidades relacionadas con la mejora de la eficiencia del sistema, por lo que también se han propuesto soluciones de optimización basadas en la operación de convertidores de potencia a frecuencia variable.

La disertación se basa en el trabajo de investigación publicado en [JC1-JC3], [JP1-JP2]. Comprende una revisión del estado del arte, una descripción de las contribuciones de los autores a lo largo de los Capítulos 3-6 y cuatro apéndices con información adicional sobre los antecedentes teóricos y la configuración experimental utilizada para la validación de estas contribuciones.

Los principales esfuerzos de investigación se han dirigido hacia la definición y el análisis de una técnica de modelado de la impedancia/admitancia de la red. Esta técnica permite determinar la evolución temporal de tensión/corriente en cualquier bus considerando terminales de distribución en 4 hilos para baja tensión que funcionan en condiciones desequilibradas. En el Capítulo 3, el método ha sido completamente descrito y validado utilizando la teoría de la potencia instantánea. La técnica de modelado propuesta permite establecer una conexión entre los términos de impedancia y los componentes de potencia, lo que permite su aplicación cuando el convertidor de potencia está integrado en la red. El modelo se ha utilizado con

éxito en el problema de identificación de impedancia, que puede llevarse a cabo a partir de mediciones locales de tensión y corriente tomadas en el PCC del convertidor.

La aplicación del modelo antes mencionado para la estimación de la impedancia de la red no es una tarea sencilla si se deben considerar las cargas conectadas en paralelo en el PCC. Como se destaca en el Capítulo 4, la presencia del voltaje principal de la red dificulta la estimación de la impedancia del sistema equivalente para la frecuencia de red si hay un número limitado de sensores disponibles. Por lo tanto, se ha propuesto una técnica de estimación, basada en la inyección de señales de alta frecuencia. Estas señales de excitación se superponen a la referencia principal del convertidor. La estimación de la impedancia a alta frecuencia a partir de la información proporcionada por el valor de la tensión local y las mediciones de corriente es una tarea directa cuando se utiliza la técnica de modelado propuesta.

Sin embargo, la inclusión de una señal adicional a una frecuencia diferente de la principal da como resultado dos problemas principales que deben abordarse: 1) la señal de excitación del convertidor causa una mayor distorsión, y 2) la información recopilada en la frecuencia tiene que estar relacionada con la estimación de la impedancia de la red a la frecuencia fundamental. Para abordar el primer problema, se ha proporcionado una lista de consideraciones, útiles para determinar la frecuencia y magnitud óptimas de la señal de excitación para minimizar el impacto en la calidad de la energía. Las frecuencias seleccionadas están por encima del ancho de banda del controlador actual y también evitan que las bandas de frecuencia afecten a otros sistemas de compensación. Además, se ha propuesto la instalación de un banco de filtrado en la retroalimentación actual para hacer que el controlador sea insensible a la señal de excitación. En cuanto a la magnitud de la señal, se ha seleccionado lo suficientemente grande como para extraer información de la red, manteniendo lo más bajo posible el nivel de THD del sistema. El segundo problema está relacionado con el hecho de que los términos reales y complejos de la impedancia dependen de la frecuencia de excitación. Como consecuencia, una derivación directa del componente fundamental de los valores de alta frecuencia no es factible. Para superar este problema, se ha propuesto la inyección de una segunda señal de alta frecuencia. Esta segunda señal proporciona un conjunto adicional de ecuaciones al problema, lo que permite aislar los términos de impedancia independientemente de la frecuencia de inyección. De esta manera, la identificación de la impedancia en la frecuencia fundamental se puede lograr con éxito.

Una vez que se identifican los términos de impedancia/admitancia, se pueden determinar los componentes de corriente/tensión de secuencia positiva, negativa y cero en el PCC. Se ha propuesto un método de compensación basado en la secuencia negativa estimada y las corrientes de secuencia cero. Esta técnica permite la compensación al confiar solo en los sensores de corriente del lado del convertidor y las mediciones de tensión en el PCC. Por lo tanto, se evita la instalación de sensores de corriente adicionales del lado de la red o del lado de la carga. Además, también se ha incluido un estudio del ancho de banda del compensador, basado en el efecto de la cadena de filtrado necesaria para el aislamiento de los diferentes componentes de la secuencia. Para este propósito, se analizó la función de transferencia de valor complejo resultante y se aisló su contribución al desfase de la señal.

El Capítulo 5 aborda la extensión de la técnica de modelado de impedancia presentada en el Capítulo 3, a aquellos sistemas con varios convertidores funcionando en paralelo. Esto se ha logrado considerando el convertidor conectado a la red como una impedancia variable, que se adapta dinámicamente según sus referencias de potencia. Por lo tanto, se ha determinado un modelo equivalente del convertidor, definido de acuerdo con las expresiones desarrolladas en el Capítulo 3. Las nuevas expresiones han sido validadas en los cuatro cuadrantes, considerando

un convertidor de potencia que ordena diferentes niveles de corrientes activas/reactivas positivas/negativas.

También se ha abordado la utilidad del modelo extendido propuesto para la estimación de impedancia. Para eso, se ha empleado un algoritmo RLS que funciona conjuntamente con un método de inyección de señal de pulso. Se ha demostrado que este método de excitación mantiene un bajo nivel de distorsión y ofrece algunas ventajas en sistemas con presencia de múltiples convertidores, debido a su capacidad para mitigar la interferencia de los reguladores de corriente. El método RLS ha sido probado en condiciones experimentales y simuladas, demostrando ser una solución fiable para determinar la impedancia equivalente de un sistema desde el PCC. Los resultados extraídos de la comparación entre la técnica de modelado y el método de estimación resaltan la validez del modelo para definir la impedancia equivalente de un convertidor vinculado a la red en los cuatro cuadrantes. Estos resultados abren la puerta a futuras estrategias de cooperación entre convertidores, basadas en métodos de control por droop, que permiten adaptar las condiciones de operación en función de la impedancia estimada de la red.

Se ha propuesto otro uso de la identificación de impedancia de red en el Capítulo 6. En este capítulo, se realizó un estudio de la eficiencia global de un EPS local, considerando en conjunto las pérdidas de potencia del convertidor y del sistema. Al considerar los requisitos de regulación con respecto al THD, que se dan a la potencia nominal del convertidor, se demuestra que se puede derivar una eficiencia global mejorada a partir de una reducción de la frecuencia de conmutación del convertidor a bajos niveles de carga. De hecho, en estas condiciones de operación, la reducción de las pérdidas de conmutación del convertidor puede compensar los efectos de un aumento del THD actual en el sistema local, sin violar los requisitos de conexión a la red. La implementación de la operación de frecuencia de conmutación variable requiere el conocimiento de la impedancia equivalente en el PCC del convertidor, que puede obtenerse mediante las técnicas de estimación de impedancia propuestas. Se ha realizado un análisis para determinar las restricciones físicas que limitan la aplicación del método, considerando la compensación entre la distorsión adicional inducida por el convertidor en el EPS local al reducir la frecuencia de conmutación y la reducción de las pérdidas del convertidor. Se ha propuesto una tabla de búsqueda basada en los límites térmicos de los semiconductores y las pérdidas del convertidor para determinar el punto de funcionamiento óptimo del convertidor. Los resultados de la técnica de optimización han sido validados tanto en simulación como en análisis experimental.

Finalmente, como resumen, las siguientes contribuciones y logros pueden destacarse como las principales conclusiones de esta disertación:

- Una expresión elegante y compacta que relaciona las secuencias de tensión y corriente con la impedancia de la red, válida para redes de 4 hilos que funcionan en condiciones desequilibradas [JC2], [JP2].
- Una técnica de estimación de impedancia de red sin sensores, válida para 4 hilos, en los cuatro cuadrantes y operación en condiciones desequilibradas [JC2], [JP2].
- Una solución de compensación de desequilibrio basada en una técnica de estimación de impedancia de red [JC2], [JP2].
- Una técnica confiable para determinar la impedancia de red equivalente considerando la operación de los convertidores conectados a la red, y capaz de operar en los cuatro cuadrantes, así como en condiciones desequilibradas [JC3].

- Un modo de operación de convertidores de potencia a bajos niveles de carga que utiliza una frecuencia de conmutación variable para la optimización de la eficiencia global basada en la impedancia equivalente del sistema [JC1], [JP1].

## 7.2 Conclusion

This doctoral dissertation focuses on the operation of grid-tied power converters in the context of AC microgrids. Special attention has been paid to the problem of the equivalent impedance variability of the network upstream from the low voltage connection point of these converters, relating this issue to the impact on the dynamic behaviour of the control system of these devices. The proposed solutions, based on impedance estimation techniques, allow the implementation of control systems that react to changes in the grid, achieving real-time compensation of unbalanced conditions. To carry out this task, only the information of electrical variables measured at the connection point is needed, using the power converters to generate excitation signals superimposed to the fundamental component. Additionally, the estimation of network parameters triggers opportunities related to the improvement of system efficiency, so optimization solutions based on the operation of power converters at variable frequency have also been proposed.

The dissertation is based on the research work published in [JC1-JC3], [JP1-JP2]. It comprises a review of the state of the art, a description of the authors contributions along Chapters 3-6 and four appendices with additional information regarding the theoretical background and the experimental setup used for the validation of these contributions.

The main research efforts have been directed towards the definition and analysis of a modelling technique of the grid impedance/admittance. This technique allows to determine the temporal evolution of voltage/current at any bus considering terminal 4-wires distribution low voltage grids working under unbalanced conditions. In Chapter 3, the method has been fully described and validated using the instantaneous power theory. The proposed modelling technique allows to establish a connection between the impedance terms and the power components, which enables its application when power converter are embedded into the grid. The model has been successfully used in the impedance identification problem, which can be carried out from local voltage and current measurements taken at the converter PCC.

The application of the aforementioned model for grid-impedance estimation is not a straightforward task if loads connected in parallel at the PCC are to be considered. As it is highlighted in Chapter 4, the presence of the main voltage from the AC grid hinders the estimation of the equivalent system impedance at grid frequency if a limited number of sensors are available. Thus, an estimation technique, based in the injection of high-frequency signals, has been proposed. These excitation signals are superimposed to the main reference of the converter. The estimation of the impedance at high-frequency from the information provided by local voltage and current measurements is a direct task when using the proposed modelling technique.

Nevertheless, the inclusion of an additional signal at a different frequency from the main one, results in two main issues that have to be addressed: 1) an increased distortion is caused by the converter excitation signal, and 2) the information gathered at high-frequency has to be related to the estimation of the grid impedance at the fundamental frequency. To tackle the first problem, a list of considerations, useful to determine the optimum frequency

and magnitude of the excitation signal to minimize the impact on power quality, has been provided. The selected frequencies are above the current controller bandwidth and also avoid frequency bands affecting by other compensating systems. Additionally, it has been proposed the installation of a filtering bank in the current feedback to make the controller insensitive to the excitation signal. Regarding the magnitude of the signal, it has been selected large enough to extract the grid information but maintaining a low level of THD. The second problem is related with the fact that the real and complex terms of the impedance are dependent on the excitation frequency. As a consequence, a direct derivation of the fundamental component from the high-frequency values is not feasible. To overcome this issue, the injection of a second high-frequency signal has been proposed. This second signal provides an additional set of equations to the problem, which allows to isolate the impedance terms independently of the injection frequency. In this way, the identification of the impedance at the fundamental frequency can be successfully achieved.

Once the impedance/admittance terms are identified, the positive, negative and zero sequence current/voltage components at the PCC can be determined. A compensation method based on the estimated negative sequence and zero sequence currents has been proposed. This technique allows the compensation by relying only on the converter-side current sensors and voltage measurements at the PCC. Thus, the installation of additional grid-side or load-side current sensors is avoided. Additionally, a study of the compensator bandwidth, based on the effect of the filtering chain needed for the isolation of the different sequence components, has been also included. For this purpose, the resulting complex-value transfer function has been analysed and its contribution to the phase lag isolated.

Chapter 5 addresses the extension of the impedance modelling technique presented in Chapter 3, to those systems with several converters operating in parallel. This has been accomplished by considering the grid-tied converter as a variable impedance, which is dynamically adapted depending on its power references. Thus, an equivalent model of the converter, defined according to the expressions developed in Chapter 3 has been determined. The new expressions have been validated in the four quadrants, considering a power converter commanding different levels of positive/negative active and reactive currents.

The usefulness of the proposed extended model for impedance estimation has also been addressed. For that, a RLS algorithm working together with a pulse signal injection method has been employed. This excitation method has been proved to maintain a low level of distortion and offers some advantages in systems with multiple converters, due to its capability to mitigate the interference of current regulators. The RLS method has been tested under experimental and simulated conditions, proving to be a reliable solution to determine the equivalent impedance of a system from the PCC. The results drawn from the comparison between the modelling technique and the estimation method highlight the validity of the model to define the equivalent impedance of a grid-tied converter in the four quadrants. These results open the door for future cooperative strategies between converters, based on droop control methods, which allow to adapt the operating conditions based on the estimated grid impedance.

Another use of the grid-impedance identification has been proposed in Chapter 6. In this chapter, a study of the global efficiency of a local EPS, considering together converter and system power losses, has been conducted. By considering the regulation requirements regarding the THD, which are given at the converter rated power, it is demonstrated that an improved global efficiency can be derived from a reduction of the switching frequency of the converter at low load levels. Indeed, in this operating conditions, the reduction of

converter switching losses can compensate the effects of an increase of the current THD in the local system, without violating the grid-connection requirements. The implementation of the variable switching frequency operation requires the knowledge of the equivalent impedance at the PCC of the converter, which can be obtained by the proposed impedance estimation techniques. An analysis to determine the physical constraints that limit the application of the method, considering the trade-off between the additional distortion induced by the converter in the local EPS when lowering the SF and the reduction in converter losses has been conducted. A lookup table based on the thermal limits of the semiconductors and the converter losses has been proposed to determine the optimal operating point of the converter. Results from the optimization technique have been validated both in simulation and experimental analysis.

Finally, as a summary, the following contributions and achievements can be highlighted as the main conclusions of this dissertation:

- An elegant and compact expression that links the voltage and current sequences with the grid impedance, valid for 4-wire networks working under unbalanced conditions [JC2], [JP2].
- An online sensorless grid impedance estimation technique, valid for 4-wire, four quadrants and operation under unbalanced conditions [JC2], [JP2].
- An unbalance compensation solution based on a grid impedance estimation technique [JC2],[JP2].
- A reliable technique to determine the equivalent grid impedance considering the operation of grid-tied converters, and able to operate in the four quadrants as well as under unbalanced conditions [JC3].
- An operation mode of power converters at low load levels which uses variable switching frequency for the optimization of the global efficiency based on the equivalent impedance of the system [JC1], [JP1].

### 7.3 Future Work

Based on the research experience gathered along this work, the following researching lines are proposed:

- I. Current controllers are often tuned considering the filter impedance to dominate the overall equivalent grid impedance. This assumption is valid for those cases in which the power converter is interconnected with a strong grid. However, this might not be the case in weak grids, resulting in stability problems within the controller. In the literature, the use of the virtual-impedance concept is proposed for mitigating this problem. A feasible alternative can be implemented by using the proposed grid impedance estimation technique for developing either adaptive or robust control approaches based on the real-time estimation of the grid impedance. Also a comparative evaluation on the performance of alternative control structures based on PR regulators can be addressed. These regulators require less computational efforts since signal transformation from AC to DC is not required.

- 
- II. The proposed impedance modelling technique has been implemented in this document for AC systems. However, an in-depth study of the possibility of adapting this methodology to hybrid DC/AC microgrids has still not been conducted. Thus, the extension of the technique to this kind of hybrid grids is proposed, which should comprise the development of a compact modelling for the representation of equivalent DC/AC impedances/admittances able to predict power flows in the two electrical domains.
  - III. The estimation of the equivalent impedance of a power converter from another converter operated in the same microgrid has been reported by restricting the analysis to the fundamental frequency. The study of more complex grid conditions, considering multiple and different nature of non-linear loads and converters operated at the same time has not been studied in depth. Similarly, it is possible to use the proposed identification technique as the root for building a complex-valued droop control, in which the relationship between the active and reactive power and the grid voltage and frequency (or power angle) is adapted depending on the estimated grid impedance in real-time. This opens the door to a solution for the traditional problem presented in the literature regarding to the selection of the droop approach, i.e.  $P/f$ ,  $Q/V$  for inductive lines and  $P/V$ ,  $Q/f$  for resistive ones, to a more general one that relates the apparent complex power with the voltage and the power angle.
  - IV. Voltage synchronization in weak grids is a source of instabilities from the point of view of the converter operation. The increased distortion, characteristic of these kind of grids, makes synchronization a much difficult task. The knowledge of the grid impedance can be employed to build a model of the grid at the PCC. This model can be embedded into an observer that allows for the decoupling of the grid impedance to determine a cleaner voltage used for phase tracking.
  - V. The global efficiency improvement was proposed in a scenario which considers only resistive loads connected to the local EPS. Further studies considering inductive/capacitive loads embedded in the local system can be conducted. Moreover, the modelling technique for the estimation of the losses in the system, as described in the optimization method proposed in Chapter 6, can be further studied.



# Appendix A

## Harmonic Emission Normative

### A.1 Introduction

In this Appendix, the tables which gather information about current harmonic emission limits for equipment connected to the public system are introduced. Since this issue is only marginally under the scope of this work, only a brief introduction and a mere citation of the norms are provided in here.

### A.2 IEC-61000-2-5 [[A.1](#)]

This part of the norm from the International Electrotechnical Commission (IEC) deals with electromagnetic phenomena and provides a definition of the different types of events included into this concept. It serves as a guidance for those in charge of dealing with immunity requirements. A list of the main phenomena causing electromagnetic disturbances are gathered in Table A.1.

### A.3 IEC-61000-3-2 [[A.2](#)]

This part of the international norm IEC-61000 sets limits for the maximum harmonic currents that can be injected into the public power system. It applies to all equipment with a rated current below 16 A per phase. As can be seen in Fig. A.1, the norm establishes four classes of devices according to the type of load, rated power and unbalance characteristics. The harmonic emission limits for each of these classes are shown in Table A.2, Table A.3 and Table A.4. The harmonic emission limits for Class B equipment are obtained by multiplying by 1.5 the limits for Class A.

**Table A.1:** Principal phenomena causing electromagnetic disturbances as classified by [A.1]

Low Frequency Phenomena	
Conducted	Radiated
Harmonics, interharmonics Signal systems (power line carrier) Voltage fluctuations Voltage dips and interruptions Voltage imbalance Power-frequency variations Induced low-frequency voltages DC in AC networks	Magnetic fields Electric fields
High Frequency Phenomena	
Conducted	Radiated
Induced continuous wave (CW) voltages or currents Unidirectional transients Oscillatory transients	Magnetic fields Electric fields Electromagnetic fields Continuous waves Transients
Electrostatic discharge phenomena (ESD)	
Nuclear electromagnetic pulse (NEMP)	

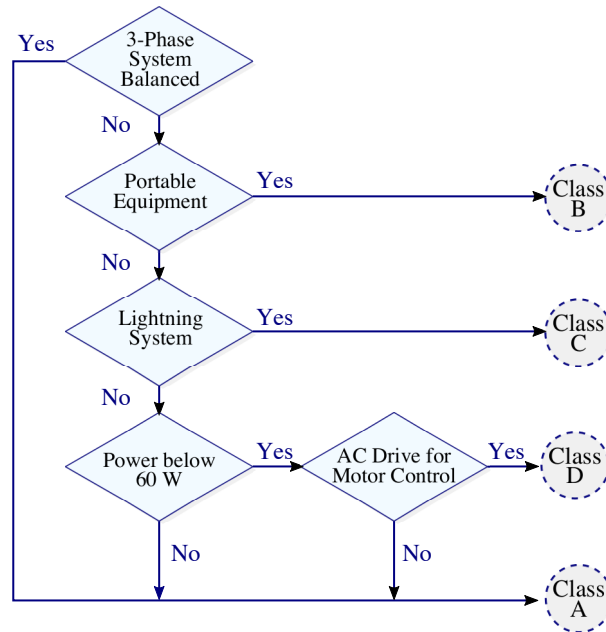


**Figure A.1:** Classification of the equipment Class according [A.2]

**Table A.2:** Current Limits for Class A Equipment

Odd Harmonics		Even Harmonics	
Harmonic	Max. Current	Harmonic	Max. Current
n	(A)	n	(A)
3	2.30	2	1.08
5	1.14	4	0.43
7	0.77	6	0.30
9	0.40	$8 \leq n \leq 40$	$0.23 \frac{8}{n}$
11	0.33		
13	0.21		
$15 \leq n \leq 39$	$0.15 \frac{15}{n}$		

**Table A.3:** Current Limits for Class C Equipment

Harmonic	Max. Current*
n	(%)
2	2
3	$30 \cdot \cos(\phi)^{**}$
5	10
7	7
9	5
$11 \leq n \leq 39$	3
(Only odd harmonics)	

\* In % respect to the fundamental one  
\*\*  $\cos(\phi)$  of the circuit

## A.4 IEC-61000-3-12 [A.3]

This part of the international norm IEC 61000 sets limits for the maximum harmonic currents that can be injected into the public power system. It applies to all equipment with a rated current over 16 A and below or equal to 75 A per phase, with a rated voltage of 240 V in case of single phase equipment and until 690 V in case of three-phase devices.

The norm provides a set of definitions in order to accomplish with the requirements. They are described below:

- **The Total Harmonic Current (THC)** is defined as (A.1), where  $I_h$  is the current harmonic component in RMS:

$$THC = \sqrt{\sum_{h=2}^{40} I_h^2} \quad (\text{A.1})$$

- **The Partial Weighted Harmonic Current (PWHC)** is a weighted assessment of a selected group of high order current harmonics within the range 14 to 40. The partial

**Table A.4:** Current Limits for Class D Equipment

Harmonic n	Max. Current per watt (mA/W)	Max. Current A
3	3.4	2.30
5	1.90	1.14
7	1.00	0.77
9	0.50	0.40
11	0.35	0.33
$13 \leq n \leq 39$ (Only odd harmonics)	$\frac{3.85}{n}$	$0.15 \frac{15}{n}$

weighted harmonic current is employed in order to ensure that the effects of the higher order harmonic currents on the results are reduced sufficiently and individual limits need not be specified. It is defined according to (A.2).

$$PWHC = \sqrt{\sum_{h=14}^{40} h \cdot I_h^2} \quad (\text{A.2})$$

- **The rated power of the equipment connected at the PCC ( $S_{equ}$ )** is calculated based on the current provided by the manufacturer, ( $I_{equ}$ ), and the nominal voltage at the PCC, it might be the phase-to-neutral voltage ( $U_p$ ) or the line voltage ( $U_i$ ).
  1.  $S_{equ} = U_p I_{equ}$ ; for single-phase system.
  2.  $S_{equ} = U_i I_{equ}$ ; for a phase-phase system.
  3.  $S_{equ} = \sqrt{3} U_i I_{equ}$ ; for a three-phase system.
  4.  $S_{equ} = \sqrt{3} U_i I_{equ}^{max}$ ; for a non-balanced system, where  $I_{equ}^{max}$  is the maximum current that flows through the phases.
- **The short-circuit ratio ( $R_{sce}$ )** is the ratio between the short-circuit power at the PCC ( $S_{sc}$ ) and the rated power of the equipment ( $S_{equ}$ ). It can be calculated as in (A.3).

$$R_{sce} = \begin{cases} \frac{S_{sc}}{3S_{eq}}, & \text{Single-Phase} \\ \frac{S_{sc}}{2S_{eq}}, & \text{Phase-Phase} \\ \frac{S_{sc}}{S_{eq}}, & \text{Three-Phase} \end{cases} \quad (\text{A.3})$$

Tables A.5 and A.6 gather the information corresponding to the harmonic current limits.

## A.5 IEEE-519-2014 [A.4]

This guidance, published by the Institute of Electrical and Electronics Engineers (IEEE), provides limits for harmonic voltage distortion and harmonic current injection. They are

**Table A.5:** Current Limits for Three-phases non-balanced Equipment

Minimum $R_{scc}$	Maximum Harmonic Current *						Harmonic Parameters **	
	%						%	
	$I_3$	$I_5$	$I_7$	$I_9$	$I_{11}$	$I_{13}$	$\frac{\text{THC}}{I_{\text{ref}}}$	$\frac{\text{PWHC}}{I_{\text{ref}}}$
33	21.6	19.7	7.2	3.8	3.1	2	23	23
66	24	13	8	5	4	3	26	26
120	27	15	10	6	5	4	30	30
250	35	20	13	8	8	6	40	40
$\geq 350$	41	24	15	12	10	8	47	47

\*  $I_n$  % respect to the fundamental one

\*\*  $I_{\text{ref}}$  is the reference current

**Table A.6:** Current Limits for Three-phases Balanced Equipment

Minimum $R_{scc}$	Maximum Harmonic Current *				Harmonic Parameters **	
	%				%	
	$I_5$	$I_7$	$I_{11}$	$I_{13}$	$\frac{\text{THC}}{I_{\text{ref}}}$	$\frac{\text{PWHC}}{I_{\text{ref}}}$
33	10.7	7.2	3.1	2	13	22
66	14	9	5	3	16	25
120	19	12	7	4	22	28
250	31	20	12	7	37	38
$\geq 350$	40	25	15	10	48	46

\*  $I_n$  % respect to the fundamental one

\*\*  $I_{\text{ref}}$  is the reference current

shown in Table A.7 and Table A.8, where the following definitions are included:

- **Total Harmonic Distortion (THD):** The ratio of the RMS of the harmonic content, considering harmonic components up to the 50<sup>th</sup> order and specifically excluding interharmonics, expressed as a percent of the fundamental.
- **Total Demand Distortion (TDD):** The ratio of the RMS of the harmonic content, considering harmonic components up to the 50<sup>th</sup> order and specifically excluding interharmonics, expressed as a percent of the maximum demand current.

**Table A.7:** Voltage Distortion Limits according to *IEEE-519-2014*

Bus Voltage at PCC	Individual Harmonic %	THD %
$V \leq 1$ kV	5.0	8.0
$1$ kV $< V \leq 69$ kV	3.0	5.0
$69$ kV $< V \leq 161$ kV	1.5	2.5
$V < 161$ kV	1.0	1.5

**Table A.8:** Current Distortion Limits for systems rated 120 V through 69 kV according to *IEEE-519-2014*

Max. Current Distortion in percent of $I_L$						
Individual Harmonic Order (Odd Harmonics)						
$I_{sc}/I_L$	$3 \leq h < 11$	$11 \leq h < 17$	$17 \leq h < 23$	$23 \leq h < 35$	$35 \leq h < 50$	TDD
$< 20$	4.0	2.0	1.5	0.6	0.3	5.0
$20 < 50$	7.0	3.5	2.5	1.0	0.5	8.0
$50 < 100$	10.0	4.5	4.0	1.5	0.7	12.0
$100 < 1000$	12.0	5.5	5.0	2.0	1.0	15.0
$100 > 1000$	15.0	7.0	6.0	2.5	1.4	20.0

*Even harmonics are limited to 25% of the odd harmonics limits above*

Where

$I_{sc}$  = Maximum short-circuit current at PCC

$I_L$  = Maximum demand load current at the PCC

TDD = Total Demand Distortion

## References

- [A.1] IEC-61000-2-5:2017: "Electromagnetic compatibility (EMC) - part 2-5: Environment - description and classification of electromagnetic environments," IEC, Tech. Rep., 2017.
- [A.2] IEC-61000-3-2:2018: "Electromagnetic compatibility (EMC) - part 3-2: Limits - limits for harmonic current emissions (equipment input current below 16 a per phase)," IEC, Tech. Rep., 2018.
- [A.3] IEC-61000-3-12:2011: "Electromagnetic compatibility (EMC) - part 3-12: Limits - limits for harmonic currents produced by equipment connected to public low-voltage systems with input current over 16 a and below 75 a per phase," IEC, Tech. Rep., 2011.
- [A.4] IEEE Standard, "Ieee recommended practice and requirements for harmonic control in electric power systems," IEEE, Tech. Rep., June 2014.

## Appendix B

# Review of the Fourier Series

The notion of periodic functions was initially developed by the mathematician *Jean Baptiste Joseph Fourier (1768-1830)*, to decompose a periodic signal into an infinite set of sinusoidal waveforms. *Fourier* developed the technique in a thermal application; however, the technique can be extended to many different fields. In particular, under the electromagnetic field, it can be used to analyse the response of an electric circuit under the excitation of a periodic non-sinusoidal signal. This procedure allows to determine the response of the grid at every frequency of every sinusoidal waveform that composed the original waveform. Lately, superposition theorem allows to obtain the full response of the circuit to arbitrary periodic input signals [B.1]. The importance of the Appendix relies on the relation of voltages and currents in the frequency and time domain required to establish the impedance and admittance ratio required for the modelling tool from Chapter 3.

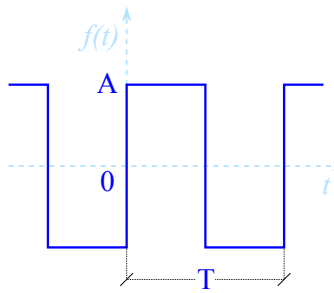
### B.1 Periodic Signals

A signal is considered periodic when it is repeated every  $T$  seconds. It can be expressed algebraically as (B.1). Where  $n$  is an integer and  $T$  is the period of the function.

$$f(t) = f(t + nT) \quad (\text{B.1})$$

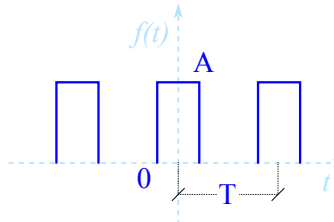
The frequency  $f_0$  of the function  $f$  is the number of cycles per second and it is measured in *Hertz*. Fig. B.1 shows some examples of periodic signals, where the period is highlighted. The angular frequency of the signals is defined as

$$\omega_0 = 2\pi f_0 = \frac{2\pi}{T} [\text{rad/s}] \quad (\text{B.2})$$



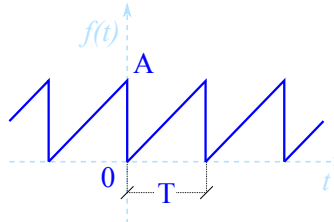
$$f(t) = \frac{4A}{\pi} \sum_{n=1}^{\infty} \frac{1}{2n-1} \sin(2n-1)\omega_0 t$$

(a)



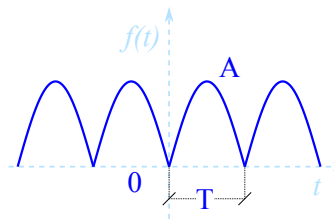
$$f(t) = \frac{4\tau}{T} + \frac{2A}{T} \sum_{n=1}^{\infty} \frac{1}{n} \sin\left(\frac{n\pi\tau}{T}\right) \cos(n\omega_0 t)$$

(b)



$$f(t) = \frac{A}{2} - \frac{A}{\pi} \sum_{n=1}^{\infty} \frac{\sin(n\omega_0 t)}{n}$$

(c)



$$f(t) = \frac{2A}{\pi} - \frac{4A}{\pi} \sum_{n=1}^{\infty} \frac{1}{4n^2-1} \cos(n\omega_0 t)$$

(d)

**Figure B.1:** Fourier series expansion for some common functions.

## B.2 Trigonometric Functions

*Fourier* demonstrated that a periodic signal  $f$  is suitable to be decomposed into an infinite series of periodic sinusoidal functions. The mathematical representation is shown in (B.3).

$$f = \frac{a_0}{2} + a_1 \cos(\omega_0 t) + a_2 \cos(2\omega_0 t) + \dots + a_n \cos(n\omega_0 t) + \dots \\ b_1 \sin(\omega_0 t) + \dots + b_2 \sin(2\omega_0 t) + \dots + b_n \sin(n\omega_0 t) + \dots \quad (\text{B.3})$$

It can be synthesized in a more compact way as (B.4).

$$f = \underbrace{\frac{a_0}{2}}_{\text{dc-term}} + \underbrace{\sum_{n=1}^{\infty} (a_n \cos(n\omega_0 t) + b_n \sin(n\omega_0 t))}_{\text{ac-term}} \quad (\text{B.4})$$

In Fig. B.1 there are some graphical representations of common Fourier functions. According to expressions (B.3) and (B.4), term  $a_0$  is a constant and the sinus and cosinus of the multiple integers of  $\omega_0$  are named as harmonics, being the term  $n$  the order of the harmonic. The signal  $f$  to be represented as a Fourier series must comply with the following:

1.  $f$  has to be continuous in the time period  $T$ .
2.  $f$  has a finite number of finite discontinuities in any one period.
3.  $f$  has a finite number of maxima and minima in any one period.
4. The integral  $\int_{t_0}^{t_0+T} |f(t)| dt < \infty$  for any  $t_0$ .

Consequently, the resolution of the Fourier series lies on the identification of the coefficients  $a_n$  and  $b_n$ , which comes from the integration of every term in the following expression:

$$\int_0^T f dt = \int_0^T \frac{a_0}{2} dt + \int_0^T \left[ \sum a_n \cos(n\omega_0 t) \right] dt + \int_0^T \left[ \sum b_n \sin(n\omega_0 t) \right] dt \quad (\text{B.5})$$

Terms  $a_n$  and  $b_n$  might be expressed according to (B.6).

$$a_n = \frac{2}{T} \int_{t_0}^{t_0+T} f \cos(n\omega_0 t) dt \quad (\text{B.6a})$$

$$b_n = \frac{2}{T} \int_{t_0}^{t_0+T} f \sin(n\omega_0 t) dt \quad (\text{B.6b})$$

Considering the symmetry concept within the representation of the functions, it can be established the following:

$$f(t) = f(-t): \quad \text{Even symmetry function.} \\ f(-t) = -f(t): \quad \text{Odd symmetry function.}$$

According to this, (B.4) may be expressed as (B.7).

$$f = a_0 + \underbrace{\sum_{n=1}^{\infty} a_n \cos(n\omega_0 t)}_{\text{even}} + \underbrace{\sum_{n=1}^{\infty} b_n \sin(n\omega_0 t)}_{\text{odd}} = f_e + f_o \quad (\text{B.7})$$

### B.3 Circuit Applications

In practice, many circuits are driven by non-sinusoidal periodic functions. To obtain the steady-state response of a circuit to a non-sinusoidal periodic excitation requires the application of a Fourier series, AC phasor analysis, and the superposition principle. The procedure usually involves the following steps:

1. Express the excitation as a Fourier series.
2. Transform the circuit from time domain into frequency domain.
3. Find response of the dc and ac components in the Fourier series.
4. To combine every single response using superposition theorem.

Considering the excitation voltage signal as (B.8).

$$v = V_m \cos(\omega_0 t + \phi) \quad (\text{B.8})$$

According to what exposed above, (B.8) may be expressed as a series Fourier as (B.9).

$$v = V_{m0} + \sum_{n=1}^{\infty} V_{mn} \cos(n\omega_0 t + \phi_n) \quad (\text{B.9})$$

Additionally, to facilitate evaluating the complex voltage vector associated with the excitation, instantaneous voltage (B.8) may be expressed as the sum of two complex exponentials (B.10).

$$\cos(n\omega_0 t) = \frac{1}{2} [e^{jn\omega_0 t} + e^{-jn\omega_0 t}] \quad (\text{B.10a})$$

$$\sin(n\omega_0 t) = \frac{1}{2j} [e^{jn\omega_0 t} - e^{-jn\omega_0 t}] \quad (\text{B.10b})$$

Consequently, voltage in (B.8) can be expressed as the sum of two complex conjugated terms, where the dc term is zero and the rest of the ac terms are evaluated at  $n = 1$ , as (B.11), [B.2].

$$\mathbf{v} = \frac{1}{2} [V_m e^{j(\omega_0 t + \phi)} + V_m e^{-j(\omega_0 t + \phi)}] \quad (\text{B.11})$$

If the exponential term involving  $V_m$  is then combined with the voltage amplitude to form the conventional peak value phasor voltage, equation (B.11) may be expressed as (B.12).

$$\mathbf{v} = \frac{\sqrt{2}}{2} [\vec{V} e^{j(\omega_0 t)} + \vec{V}^* e^{-j(\omega_0 t)}] \quad (\text{B.12})$$

where

$$\vec{V} = \frac{V_m}{\sqrt{2}} \cdot e^{j\phi} = V \angle \phi \quad (\text{B.13})$$

Application of (B.12) into a polyphasial circuit allows to obtain the magnitude of the positive, negative and zero sequence of the voltages and currents under unbalanced conditions as it will explain in more detail in Appendix C.

Additionally to the previous reasoning, excitation voltage (B.8) can be expressed in to the frequency domain based on the *Euler's Identity* as (B.14):

$$v = \Re\left(\frac{V_m}{\sqrt{2}} \cdot e^{j(\omega_0 t + \phi)}\right) = \Re(\vec{V} \cdot e^{j\omega_0 t}) \quad (\text{B.14})$$

$\vec{V}$  is thus, the phasor representation of the sinusoid  $v$ , which consists on a complex representation of the magnitude and the phase of a sinusoid. A graphical representation of the phasor concept is shown in Fig. B.2.

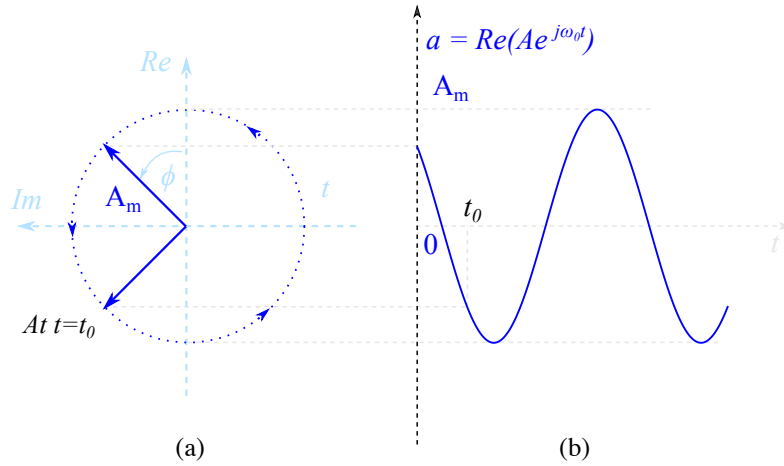


**Figure B.2:** Graphical Representation of  $\vec{A}e^{j\omega t}$ . (a): Phasor representation (b) Projection on the real axis.

The reasoning behind the equations (B.8) through (B.13), is that to represent a sinusoidal signal, first it is expressed in the cosine form, so the signal may be expressed as the real part of a complex number. Then, removing the time factor  $e^{j\omega t}$ , what is left corresponds to the phasor of the sinusoid. By making this suppression, the sinusoid is transform from the time to the frequency domain. It can be summarized as (B.15).

$$v = V_m \cos(\omega_0 t + \phi) \Leftrightarrow \vec{V} = V \angle \phi \quad (\text{B.15})$$

(Time-Domain)                      (Frequency-Domain)

Note that in the phasor domain representation, frequency is not explicitly shown, because  $\omega$  is constant; however its calculation depends on it. For this reason is known as frequency domain. Consequently, (B.8) may be expressed:

$$\begin{aligned} \frac{dv}{dt} &= -\omega_0 V_m \sin(\omega_0 t + \phi) = -\omega_0 V_m \cos(\omega_0 t + \phi + 90^\circ) \\ &= \Re(\omega_0 V_m e^{j\omega_0 t} e^{j\phi} e^{j90^\circ}) = \Re(j\omega_0 \vec{V} e^{j\omega_0 t}) \end{aligned} \quad (\text{B.16})$$

It can be concluded similarly:

$$\begin{aligned} \frac{dv}{dt} &\Leftrightarrow j\omega \vec{V} \\ \int v dt &\Leftrightarrow \frac{\vec{V}}{j\omega} \end{aligned} \quad (\text{B.17})$$

(Time-Domain)                      (Frequency-Domain)

These relationships are valid for steady state analysis and at  $\omega$  constant.

Once the system is at the frequency domain, the response of each term in the series can be obtained. The DC components are calculated by setting  $n = 0$  and  $\omega = 0$ . The ac components are calculated based on the impedance  $Z(n\omega_0)$  or admittance  $Y(n\omega_0)$  of the grid at such frequency.

Finally, by applying superposition, the resulting current can be obtained by adding all individual responses, as in (B.18).

$$\begin{aligned} i &= i_0 + i_1 + i_2 + \dots + \\ &= I_0 + \sum_{n=1}^{\infty} |\vec{I}_n| \cos(n\omega_0 t + \Psi_n) \end{aligned} \quad (\text{B.18})$$

## References

- [B.1] C. Alexander and M. Sadiku, *Fundamentals of Electric Circuits*, 4th ed. McGraw Hill Higher Education, 2008.
- [B.2] G. C. Paap, "Symmetrical components in the time domain and their application to power network calculations," *IEEE Transactions on Power Systems*, vol. 15, no. 2, pp. 522–528, 2000.

## Appendix C

# Space Vector Transformations of Three-Phase Systems

### C.1 Introduction

A generic three-phase system is a polyphase circuit, consisting of three voltages and three currents interacting with each others to deliver power. The phase voltages and line currents are considered balanced if they are sinusoidal, equal in magnitude and displaced between each other by equal phase angle, in practical  $120^\circ$ . Similarly, a polyphase system is balanced if both voltage and currents are balanced and sinusoidal at same circuit. If one of the conditions is not achieved, then the system is considered unbalanced. This is the result either the set of phase voltage or the set of lines currents are not symmetrical. The reason might by the appearance of a fault in the line or because the impedance of the line is not equal in the three phases.

The expressions required to define an unbalance according to the symmetrical components are developed along this appendix. This study is the basis of the proposed modelling tool from Chapter 3 and the estimation and compensation proposals from Chapter 4 and 5. Additionally, the expressions required for variable transformation into the stationary and the synchronous reference frame are analysed in here, considering in all the cases the zero sequence component present in the neutral wire connection under an unbalanced condition.

### C.2 Symmetrical Components

According to the theorem proposed from Fortescue [C.1], any unsymmetrical polyphase circuit of  $n$  elements might be decomposed in the sum of  $n$  symmetrical components by the application of the superposition theorem. The following transformations are applied for both voltages and currents.

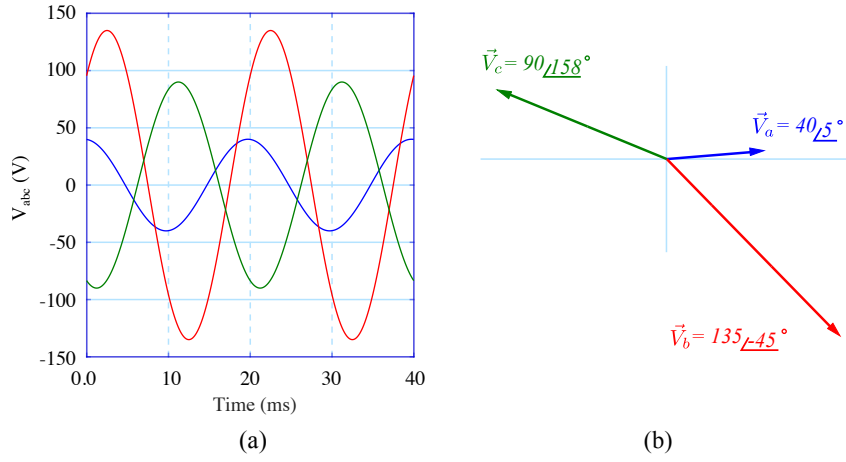


**Figure C.1:** (a) Instantaneous voltage waveforms; (b) Phase Voltage phasors

Considering the three voltage phasors of an unbalanced system represented in Fig. C.1, it can be mathematically expressed as (C.1).

$$\tilde{\mathbf{V}}_{abc} = \begin{bmatrix} \vec{V}_a \\ \vec{V}_b \\ \vec{V}_c \end{bmatrix} = \begin{bmatrix} V_a \angle \theta_a \\ V_b \angle \theta_b \\ V_c \angle \theta_c \end{bmatrix} \quad (\text{C.1})$$

According to the symmetrical components theorem, voltage phasors  $\tilde{\mathbf{V}}_{abc}$  are suitable to be decomposed into a set of three phasors (C.2), with same magnitude and phase between them, where  $a = e^{-j2\pi/3} = 1 \angle -120^\circ$ .

$$[\vec{V}_a^{+-0}] = [F] \cdot [\vec{V}_{abc}]; \quad \begin{bmatrix} \vec{V}_a^+ \\ \vec{V}_a^- \\ \vec{V}_a^0 \end{bmatrix} = \begin{bmatrix} 1 & a & a^2 \\ 1 & a^2 & a \\ 1 & 1 & 1 \end{bmatrix} \cdot \begin{bmatrix} \vec{V}_a \\ \vec{V}_b \\ \vec{V}_c \end{bmatrix} \quad (\text{C.2})$$

The relation between sequence phasors and voltage phasors for the three phases is given by (C.3).

$$\begin{aligned} \vec{V}_a &= \vec{V}_a^+ + \vec{V}_a^- + \vec{V}_a^0 \\ \vec{V}_b &= \vec{V}_b^+ + \vec{V}_b^- + \vec{V}_b^0 \\ \vec{V}_c &= \vec{V}_c^+ + \vec{V}_c^- + \vec{V}_c^0 \end{aligned} \quad (\text{C.3})$$

Figure C.2 illustrates the resultant voltages in the time domain, where the positive terms rotates in counter-clockwise and negative terms do it clockwise.

Similarly, it is possible to obtain the relation between voltage phasors, based on the sequence phasors, according to (C.4) and taking as reference the phase  $a$ .

$$\begin{aligned} \vec{V}_b^+ &= a^2 \vec{V}_a^+; & \vec{V}_b^- &= a \vec{V}_a^-; \\ \vec{V}_c^+ &= a \vec{V}_a^+; & \vec{V}_c^- &= a^2 \vec{V}_a^- \end{aligned} \quad (\text{C.4})$$

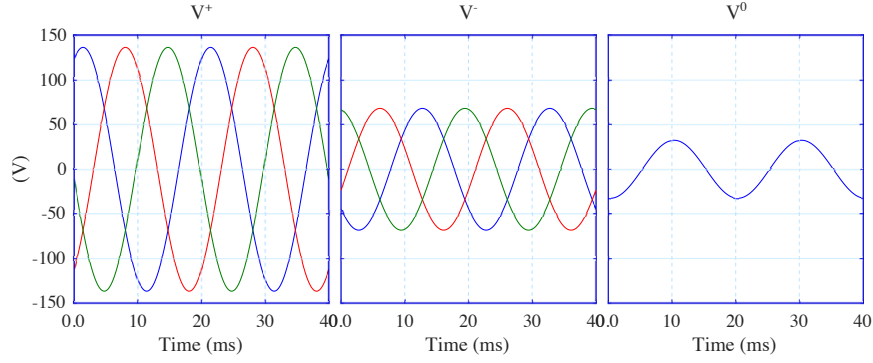


**Figure C.2:** Instantaneous voltage representation of the positive, negative and zero sequences

Additionally, the phasor voltages are extracted based on the sequence voltages by taking the inverse of (C.2), leading to (C.5)

$$\begin{bmatrix} \vec{V}_a \\ \vec{V}_b \\ \vec{V}_c \end{bmatrix} = \begin{bmatrix} 1 & 1 & 1 \\ a^2 & a & 1 \\ a & a^2 & 1 \end{bmatrix} \cdot \begin{bmatrix} \vec{V}_a^+ \\ \vec{V}_a^- \\ \vec{V}_a^0 \end{bmatrix} \quad (\text{C.5})$$

Based on the extended work of the Fortescue Theorem, proposed by [C.2], the symmetrical component theorem is suitable to be applied into the time domain. Considered the instantaneous voltage waveforms presented in (C.6).

$$\mathbf{v}_{abc} = \begin{bmatrix} v_a \\ v_b \\ v_c \end{bmatrix} = \begin{bmatrix} V_a \cdot \cos(\omega t) \\ V_b \cdot \cos(\omega t - 2\pi/3) \\ V_c \cdot \cos(\omega t + 2\pi/3) \end{bmatrix} \quad (\text{C.6})$$

Where  $v$  denotes the instantaneous value and  $V$  the RMS of the phase voltage. Considering the relation  $\cos(\sigma) = \frac{e^{j\sigma} + e^{-j\sigma}}{2}$  and according to [C.3], expression (C.6) can be defined as the sum of two complex conjugated terms, (C.7).

$$\mathbf{v}_{abc} = \frac{1}{2} \begin{bmatrix} \vec{V}_a e^{j\omega t} + \vec{V}_a^* e^{-j\omega t} \\ \vec{V}_b e^{j\omega t} + \vec{V}_b^* e^{-j\omega t} \\ \vec{V}_c e^{j\omega t} + \vec{V}_c^* e^{-j\omega t} \end{bmatrix} \quad (\text{C.7})$$

Expression (C.7) is suitable to be transformed into the symmetrical components according to the transformation presented in (C.2), the result yields to (C.8)

$$\begin{bmatrix} \mathbf{v}^+ \\ \mathbf{v}^- \\ \mathbf{v}^0 \end{bmatrix} = \frac{1}{2} \begin{bmatrix} \vec{V}^+ e^{j\omega t} + \vec{V}^{-*} e^{-j\omega t} \\ \vec{V}^- e^{j\omega t} + \vec{V}^{+*} e^{-j\omega t} \\ \vec{V}^0 e^{j\omega t} + \vec{V}^{0*} e^{-j\omega t} \end{bmatrix} \quad (\text{C.8})$$

where the phasors  $\vec{V}^{+-0}$  are obtained based on (C.9).

$$\begin{bmatrix} \vec{V}^+ \\ \vec{V}^- \\ \vec{V}^0 \end{bmatrix} = \frac{1}{\sqrt{3}} \begin{bmatrix} 1 & a & a^2 \\ 1 & a^2 & a \\ 1 & 1 & 1 \end{bmatrix} \cdot \begin{bmatrix} \vec{V}_a \\ \vec{V}_b \\ \vec{V}_c \end{bmatrix} \quad (\text{C.9})$$

The terms  $v^{+-0}$  are time-dependent, meanwhile,  $\vec{V}^{+-0}$  are the steady-state phasors. As results of (C.2) and (C.9), it can be concluded, that the negative component  $v^-$  is the complex conjugate of the positive sequence component  $v^+$  and is for then superfluous, however the steady-state phasor  $\vec{V}^-$  is independent from  $\vec{V}^+$  and it is only present in the case the system is unbalanced. These values should not be mistaken for the positive and negative sequence voltage vectors. These values are linked according to equation (C.10)

$$\begin{aligned} v_{abc} &= \begin{bmatrix} v_a \\ v_b \\ v_c \end{bmatrix} = v_{abc}^+ + v_{abc}^- + v_{abc}^0 \\ &= V_m^+ \begin{bmatrix} \cos(\omega t) \\ \cos(\omega t - 2\pi/3) \\ \cos(\omega t + 2\pi/3) \end{bmatrix} + V_m^- \begin{bmatrix} \cos(\omega t) \\ \cos(\omega t + 2\pi/3) \\ \cos(\omega t - 2\pi/3) \end{bmatrix} + V_m^0 \begin{bmatrix} \cos(\omega t) \\ \cos(\omega t) \\ \cos(\omega t) \end{bmatrix} \end{aligned} \quad (\text{C.10})$$

Since operator  $a = -\frac{1}{2} + j\frac{\sqrt{3}}{2}$  is in the frequency domain, it can not be applied over  $v_{abc}$ , which are instantaneous and time dependent values. It is possible to obtain the instantaneous voltage sequences by translating the operator  $a$  to the time domain by a filter,  $\alpha$ , which introduces a  $90^\circ$  delay, associated with  $j$  term, according to [C.4].

$$\begin{bmatrix} v_a^+ \\ v_b^+ \\ v_c^+ \end{bmatrix} = \frac{1}{3} \begin{bmatrix} 1 & \alpha & \alpha^2 \\ \alpha^2 & 1 & \alpha \\ \alpha & \alpha^2 & 1 \end{bmatrix} \cdot \begin{bmatrix} v_a \\ v_b \\ v_c \end{bmatrix} \quad (\text{C.11})$$

$$\begin{bmatrix} v_a^- \\ v_b^- \\ v_c^- \end{bmatrix} = \frac{1}{3} \begin{bmatrix} 1 & \alpha^2 & \alpha \\ \alpha & 1 & \alpha^2 \\ \alpha^2 & \alpha & 1 \end{bmatrix} \cdot \begin{bmatrix} v_a \\ v_b \\ v_c \end{bmatrix} \quad (\text{C.12})$$

Similar results can be obtained from the frequency domain by applying related equations and calculating the instantaneous value of the voltage sequence (C.13) - (C.16).

$$[\vec{V}_{abc}^+] = [F_+] \cdot [\vec{V}_{abc}]; \Rightarrow \begin{bmatrix} \vec{V}_a^+ \\ \vec{V}_b^+ \\ \vec{V}_c^+ \end{bmatrix} = \frac{1}{3} \begin{bmatrix} 1 & a & a^2 \\ a^2 & 1 & a \\ a & a^2 & 1 \end{bmatrix} \cdot \begin{bmatrix} \vec{V}_a \\ \vec{V}_b \\ \vec{V}_c \end{bmatrix} \quad (\text{C.13})$$

$$\begin{bmatrix} v_a^+ \\ v_b^+ \\ v_c^+ \end{bmatrix} = \begin{bmatrix} V_a^+ \cos(\theta_a^+) \\ V_b^+ \cos(\theta_b^+) \\ V_c^+ \cos(\theta_c^+) \end{bmatrix} \quad \begin{aligned} \vec{V}_a^+ &= V_a^+ \angle \theta_a^+; \\ \vec{V}_b^+ &= V_b^+ \angle \theta_b^+; \\ \vec{V}_c^+ &= V_c^+ \angle \theta_c^+; \end{aligned} \quad (\text{C.14})$$

$$[\vec{V}_{abc}^-] = [F_-] \cdot [\vec{V}_{abc}]; \Rightarrow \begin{bmatrix} \vec{V}_a^- \\ \vec{V}_b^- \\ \vec{V}_c^- \end{bmatrix} = \frac{1}{3} \begin{bmatrix} 1 & a^2 & a \\ a & 1 & a^2 \\ a^2 & a & 1 \end{bmatrix} \cdot \begin{bmatrix} \vec{V}_a \\ \vec{V}_b \\ \vec{V}_c \end{bmatrix} \quad (\text{C.15})$$

$$\begin{bmatrix} v_a^- \\ v_b^- \\ v_c^- \end{bmatrix} = \begin{bmatrix} V_a^- \cos(\theta_a^-) \\ V_b^- \cos(\theta_b^-) \\ V_c^- \cos(\theta_c^-) \end{bmatrix} \quad \begin{aligned} \vec{V}_a^- &= V_a^- \angle \theta_a^-; \\ \vec{V}_b^- &= V_b^- \angle \theta_b^-; \\ \vec{V}_c^- &= V_c^- \angle \theta_c^-; \end{aligned} \quad (\text{C.16})$$

### C.3 Stationary Reference Frame Transformation

As stated above, from the transformation of the three real variables  $v_a, v_b, v_c$ , in (C.8), there are only three independent real components:  $\Re(\mathbf{v}^+)$ ,  $\Im(\mathbf{v}^+)$  and  $v^0$ , which can be combined as (C.17).

$$\begin{bmatrix} \Re(\mathbf{v}^+) \\ \Im(\mathbf{v}^+) \\ v^0 \end{bmatrix} = \frac{1}{3} \begin{bmatrix} 1 & \Re(a) & \Re(a^2) \\ 1 & \Im(a) & \Im(a^2) \\ 1 & 1 & 1 \end{bmatrix} \begin{bmatrix} v_a \\ v_b \\ v_c \end{bmatrix} \quad (\text{C.17})$$

This combination yields to the widely used Clarke transformation, for time-dependent variables, based on the work presented in [C.5]. This transformation might be rewritten as (C.18), where  $\mathbf{A}$  is the *Clark Transformation Matrix*. Expressing (C.18) in matrix form leads to (C.19) and (C.20).

$$\mathbf{v}_{\alpha\beta 0} = \mathbf{A} \cdot \mathbf{v}_{abc} \quad (\text{C.18})$$

$$\begin{bmatrix} v_\alpha \\ v_\beta \\ v_0 \end{bmatrix} = k_p \begin{bmatrix} 1 & -\frac{1}{2} & -\frac{1}{2} \\ 0 & \frac{\sqrt{3}}{2} & -\frac{\sqrt{3}}{2} \\ \frac{1}{\sqrt{2}} & \frac{1}{\sqrt{2}} & \frac{1}{\sqrt{2}} \end{bmatrix} \begin{bmatrix} v_a \\ v_b \\ v_c \end{bmatrix} \quad (\text{C.19})$$

$$\begin{bmatrix} v_\alpha \\ v_\beta \\ v_0 \end{bmatrix} = k_m \begin{bmatrix} 1 & -\frac{1}{2} & -\frac{1}{2} \\ 0 & \frac{\sqrt{3}}{2} & -\frac{\sqrt{3}}{2} \\ \frac{1}{2} & \frac{1}{2} & \frac{1}{2} \end{bmatrix} \begin{bmatrix} v_a \\ v_b \\ v_c \end{bmatrix} \quad (\text{C.20})$$

Where the  $\alpha$  element is the projection over the real axes of the voltage vector representation and the  $\beta$  element is the projection over the imaginary axes. Graphical representation of the transformation is depicted in Fig. C.3, where the homopolar component is orthogonal to the  $\alpha\beta$  plane.

In (C.19), the  $k_p$  term is a proportional value that might turn  $\sqrt{\frac{2}{3}}$  and the ratio  $[A]^{-1} = [A]^T$  is fulfilled. In this case the transformation of the system is considered power invariant, where the following is accomplished.

$$v_\alpha^2 + v_\beta^2 + v_0^2 = v_a^2 + v_b^2 + v_c^2 \quad (\text{C.21})$$

Consequently as result, when transformation is applied to the voltage and currents of a three-phase system, the resulting power relationship is as follows in (C.22).

$$p = v_{\alpha\beta 0} \cdot i_{\alpha\beta 0} = v_{abc} \cdot i_{abc} \quad (\text{C.22})$$

On the contrary, in (C.20)  $k_m = \frac{2}{3}$ , which means the transformation is magnitude invariant and then the sinusoidal signals are equal in magnitude, fulfilling  $V_\alpha = V_a$ .

### C.4 Synchronous Reference Frame Transformation

A particular widely used transformation in the analysis of electrical machines and, more general, circuits is the *Park* transformation or synchronous transformation, which is based

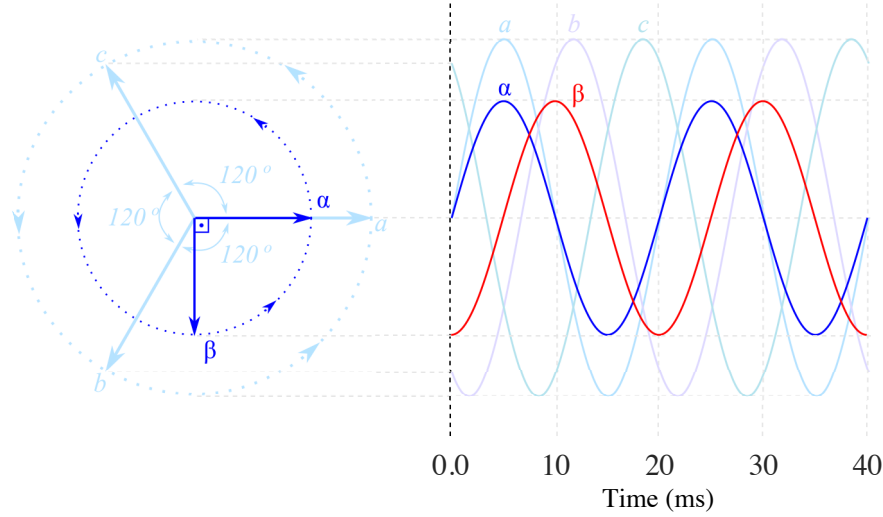


**Figure C.3:** Instantaneous representation of the  $\alpha\beta$  reference frame

on two orthogonal  $dq$ -axes that rotates at constant frequency,  $\omega_e$ , which corresponds to the grid frequency. The  $dq$ -axes are located at an angular position respect to  $\alpha\beta$  reference frame, which corresponds to the  $\theta = \omega_e t$ . Graphical representation of the relation between axes is depicted in Fig. C.4.

The transformation may be simply defined as (C.23), where in both reference frames, voltage is defined as a complex vector.

$$\mathbf{v}_{dq} = \mathbf{v}_{\alpha\beta} \cdot e^{-j\theta} \quad (\text{C.23})$$

According to (C.23), matrix transformation which links both reference frame is shown in (C.24).

$$\begin{bmatrix} v_d \\ v_q \\ v_0 \end{bmatrix} = k \begin{bmatrix} \cos(\theta) & \sin(\theta) & 0 \\ -\sin(\theta) & \cos(\theta) & 0 \\ 0 & 0 & 1 \end{bmatrix} \begin{bmatrix} v_\alpha \\ v_\beta \\ v_0 \end{bmatrix} \quad (\text{C.24})$$

However, this transformation may be considered from the sinus waveform transformation, depending on the alignment desired. Eq. (C.23) might become (C.25).

$$\mathbf{v}_{dq} = \mathbf{v}_{\alpha\beta} \cdot e^{-j(\theta - \frac{\pi}{2})} \quad (\text{C.25})$$

considering the relation  $e^{-j(\theta - \frac{\pi}{2})} = \sin(\omega t) - j \cos(\omega t)$ ; which leads to a matrix transformation (C.26)

$$\begin{bmatrix} v_d \\ v_q \\ v_0 \end{bmatrix} = k \begin{bmatrix} \sin(\theta) & -\cos(\theta) & 0 \\ \cos(\theta) & \sin(\theta) & 0 \\ 0 & 0 & 1 \end{bmatrix} \begin{bmatrix} v_\alpha \\ v_\beta \\ v_0 \end{bmatrix} \quad (\text{C.26})$$

Similarly, it is also possible to transform the  $abc$  variables into the synchronous reference





# Appendix D

## Instantaneous Power Theory

### D.1 Introduction

This power theory review serves as a reference frame for the modelling technique proposed in Chapter 3, which has been extended to the impedance/admittance characteristic of a generic system, based on the theories gathered in this appendix.

### D.2 Instantaneous Power Theory

Under generic grid conditions, a generic excitation voltage might be defined according to the symmetrical components theory as (D.1).

$$\begin{aligned} v &= \sum_{n=1}^{\infty} (v_n^+ + v_n^- + v_n^0) \\ &= \sum_{n=1}^{\infty} \left\{ V_n^+ \begin{bmatrix} \cos(n\omega t + \phi_n^+) \\ \cos(n\omega t - \frac{2\pi}{3} + \phi_n^+) \\ \cos(n\omega t + \frac{2\pi}{3} + \phi_n^+) \end{bmatrix} + V_n^- \begin{bmatrix} \cos(n\omega t + \phi_n^-) \\ \cos(n\omega t + \frac{2\pi}{3} + \phi_n^-) \\ \cos(n\omega t - \frac{2\pi}{3} + \phi_n^-) \end{bmatrix} + \right. \\ &\quad \left. V_n^0 \begin{bmatrix} \cos(n\omega t + \phi_n^0) \\ \cos(n\omega t + \phi_n^0) \\ \cos(n\omega t + \phi_n^0) \end{bmatrix} \right\} \end{aligned} \quad (D.1)$$

The current drawn downstream the PCC might be defined as (D.2).

$$i = \sum_{n=1}^{\infty} \left\{ I_n^+ \begin{bmatrix} \sin(n\omega t + \delta_n^+) \\ \sin(n\omega t - \frac{2\pi}{3} + \delta_n^+) \\ \sin(n\omega t + \frac{2\pi}{3} + \delta_n^+) \end{bmatrix} + I_n^- \begin{bmatrix} \sin(n\omega t + \delta_n^-) \\ \sin(n\omega t + \frac{2\pi}{3} + \delta_n^-) \\ \sin(n\omega t - \frac{2\pi}{3} + \delta_n^-) \end{bmatrix} + I_n^0 \begin{bmatrix} \sin(n\omega t + \delta_n^0) \\ \sin(n\omega t + \delta_n^0) \\ \sin(n\omega t + \delta_n^0) \end{bmatrix} \right\} \quad (D.2)$$

where superscripts  $+$ ,  $-$  and  $^0$  refer to the positive, negative and homopolar sequences [D.1, D.2]. In (D.2),  $n$  states for the different harmonics of voltage  $v$ . According to [D.3, D.4, D.5], the instantaneous power resulting from the interaction of the voltages and currents from (D.1) and (D.2) may be described as (D.3).

$$\begin{aligned} p &= \mathbf{v} \cdot \mathbf{i} \\ q &= |\mathbf{v} \times \mathbf{i}| \end{aligned} \quad (D.3)$$

These expressions are considered instantaneous since are the result from the inner and cross product of the instantaneous voltage and current vectors. This theory is applicable during transients and the physical meaning of both terms may be summarized as follow:

- The instantaneous active power  $p$  describes the total instantaneous energy flow between two systems.
- The imaginary power  $q$  is proportional to the quantity of energy that is being exchanged between the phases of the system but it does not contribute to the energy transfer between the source and the load.

Under generic conditions, which may include harmonic distortion and/or unbalance, (D.3) may be decomposed in:

$$p = \bar{p} + \tilde{p}; \quad (D.4)$$

$$q = \bar{q} + \tilde{q}; \quad (D.5)$$

$$p_0 = \bar{p}_0 + \tilde{p}_0; \quad (D.6)$$

where  $\bar{p}$ ,  $\bar{q}$  and  $\bar{p}_0$  equal the average part of every power term, representing the result from the interaction of voltage and current components with the same frequency and sequence. The oscillating terms  $\tilde{p}$ ,  $\tilde{q}$  and  $\tilde{p}_0$  represent the oscillating energy flow, resulting from the interaction of the harmonic distortion and the negative sequence caused by the unbalance, [D.2]. Those oscillating terms have a zero average value, denoting an additional amount of power flow in the system without effective contribution to the energy transfer. The amplitude of every term is calculated according to:

$$\bar{p} = \frac{3}{2} \sum_{n=1}^{\infty} [V_n^+ I_n^+ \cos(\phi_n^+ - \delta_n^+) + V_n^- I_n^- \cos(\phi_n^- - \delta_n^-)] \quad (D.7)$$

$$\bar{q} = \frac{3}{2} \sum_{n=1}^{\infty} [V_n^+ I_n^+ \sin(\phi_n^+ - \delta_n^+) - V_n^- I_n^- \sin(\phi_n^- - \delta_n^-)] \quad (D.8)$$

$$\bar{p}_0 = \frac{3}{2} \sum_{n=1}^{\infty} V_n^0 I_n^0 \cos(\phi_n^0 - \delta_n^0) \quad (\text{D.9})$$

$$\begin{aligned} \tilde{p} = \frac{3}{2} & \left\{ \sum_{\substack{m=1 \\ m \neq n}}^{\infty} \left[ \sum_{n=1}^{\infty} V_m^+ I_n^+ \cos((\omega_m - \omega_n)t + \phi_m^+ - \delta_n^+) \right] \right. \\ & + \sum_{\substack{m=1 \\ m \neq n}}^{\infty} \left[ \sum_{n=1}^{\infty} V_m^- I_n^- \cos((\omega_m - \omega_n)t + \phi_m^- - \delta_n^-) \right] \\ & + \sum_{m=1}^{\infty} \left[ \sum_{n=1}^{\infty} -V_m^+ I_n^- \cos((\omega_m + \omega_n)t + \phi_m^+ + \delta_n^-) \right] \\ & \left. + \sum_{m=1}^{\infty} \left[ \sum_{n=1}^{\infty} -V_m^- I_n^+ \cos((\omega_m + \omega_n)t + \phi_m^- + \delta_n^+) \right] \right\} \quad (\text{D.10}) \end{aligned}$$

$$\begin{aligned} \tilde{q} = \frac{3}{2} & \left\{ \sum_{\substack{m=1 \\ m \neq n}}^{\infty} \left[ \sum_{n=1}^{\infty} V_m^+ I_n^+ \sin((\omega_m - \omega_n)t + \phi_m^+ - \delta_n^+) \right] \right. \\ & + \sum_{\substack{m=1 \\ m \neq n}}^{\infty} \left[ \sum_{n=1}^{\infty} V_m^- I_n^- \sin((\omega_m - \omega_n)t + \phi_m^- - \delta_n^-) \right] \\ & + \sum_{m=1}^{\infty} \left[ \sum_{n=1}^{\infty} -V_m^+ I_n^- \sin((\omega_m + \omega_n)t + \phi_m^+ + \delta_n^-) \right] \\ & \left. + \sum_{m=1}^{\infty} \left[ \sum_{n=1}^{\infty} -V_m^- I_n^+ \sin((\omega_m + \omega_n)t + \phi_m^- + \delta_n^+) \right] \right\} \quad (\text{D.11}) \end{aligned}$$

$$\begin{aligned} \tilde{p}_0 = \frac{3}{2} & \left\{ \sum_{\substack{m=1 \\ m \neq n}}^{\infty} \left[ \sum_{n=1}^{\infty} V_m^0 I_n^0 \sin((\omega_m - \omega_n)t + \phi_m^0 - \delta_n^0) \right] \right. \\ & \left. + \sum_{m=1}^{\infty} \left[ \sum_{n=1}^{\infty} -V_m^0 I_n^0 \sin((\omega_m - \omega_n)t + \phi_m^0 - \delta_n^0) \right] \right\} \quad (\text{D.12}) \end{aligned}$$

The operation of the system of Figure 3.1, under unbalanced grid conditions, can be studied by considering only the fundamental frequency in the previous power expressions, i.e. making  $m = n = 1$ . Authors in [D.6] proposed a combination of the variables, based on the *Park's* transformation, as follows:

$$p = P_0 + P_{c2} \cos(2\omega t) + P_{s2} \sin(2\omega t) \quad (\text{D.13})$$

$$q = Q_0 + Q_{c2} \cos(2\omega t) + Q_{s2} \sin(2\omega t) \quad (\text{D.14})$$

where  $P_0$  and  $Q_0$  represent the average value of the instantaneous active and reactive power, whereas the other terms are related to the oscillatory terms which does not contribute to the power transfer. The magnitude of these variables are calculated as follow:

$$P_0 = \frac{3}{2} (v_d^+ i_d^+ + v_q^+ i_q^+ + v_d^- i_d^- + v_q^- i_q^-) \quad (\text{D.15})$$

$$P_{c2} = \frac{3}{2} (v_d^- i_d^+ + v_q^- i_q^+ + v_d^+ i_d^- + v_q^+ i_q^-) \quad (\text{D.16})$$

$$P_{s2} = \frac{3}{2} (v_q^- i_d^+ - v_d^- i_q^+ - v_q^+ i_d^- + v_d^+ i_q^-) \quad (\text{D.17})$$

$$Q_0 = \frac{3}{2} (v_q^+ i_d^+ - v_d^+ i_q^+ + v_q^- i_d^- - v_d^- i_q^-) \quad (\text{D.18})$$

$$Q_{c2} = \frac{3}{2} (v_q^- i_d^+ - v_d^- i_q^+ + v_q^+ i_d^- - v_d^+ i_q^-) \quad (\text{D.19})$$

$$Q_{s2} = \frac{3}{2} (-v_d^- i_d^+ - v_q^- i_q^+ + v_d^+ i_d^- + v_q^+ i_q^-) \quad (\text{D.20})$$

where the terms are joint according to the terms link to sinus or cosinus in the *Park's* transformation. This approach is considerably interesting for the case of the active filtering, since it enables a clear distinction between the different elements involved in the power transfer.

Similarly, (D.15)-(D.20), may be expressed within the stationary reference frame as depicted in (D.21)

$$\begin{bmatrix} P_0 \\ P_1 \\ P_2 \\ Q_0 \\ Q_1 \\ Q_2 \end{bmatrix} = \frac{3}{2} \begin{bmatrix} v_\alpha^+ & v_\beta^+ & v_\alpha^- & v_\beta^- \\ v_\alpha^- & v_\beta^- & v_\alpha^+ & v_\beta^+ \\ v_\beta^- & -v_\alpha^- & -v_\beta^+ & v_\alpha^+ \\ v_\beta^+ & -v_\alpha^+ & v_\beta^- & -v_\alpha^- \\ v_\beta^- & -v_\alpha^- & v_\beta^+ & -v_\alpha^+ \\ -v_\alpha^- & -v_\beta^- & v_\alpha^+ & v_\beta^+ \end{bmatrix} \cdot \begin{bmatrix} i_\alpha^+ \\ i_\beta^+ \\ i_\alpha^- \\ i_\beta^- \end{bmatrix} \quad (\text{D.21})$$

Since the algorithm has been defined according to the  $\alpha\beta$  reference frame, this set of equations is the one used in this document.

## References

- [D.1] G. C. Paap, "Symmetrical components in the time domain and their application to power network calculations," *IEEE Transactions on Power Systems*, vol. 15, no. 2, pp. 522–528, May 2000.
- [D.2] R. Teodorescu, M. Liserre, and P. Rodriguez, *Control of Grid Converters under Grid Faults*. IEEE, 2007, pp. 237–287. [Online]. Available: <https://ieeexplore.ieee.org/document/5732935>
- [D.3] M. A. Hirofumi Akagi, Edson Hirokazu Watanabe, *Instantaneous Power Theory and Applications to Power Conditioning*. Wiley-IEEE Press, March 2007.
- [D.4] H. Akagi, Y. Kanazawa, and A. Nabae, "Instantaneous reactive power compensators comprising switching devices without energy storage components," *IEEE Transactions on Industry Applications*, vol. IA-20, no. 3, pp. 625–630, May 1984.

- 
- [D.5] Fang Zheng Peng, G. W. Ott, and D. J. Adams, "Harmonic and reactive power compensation based on the generalized instantaneous reactive power theory for three-phase four-wire systems," *IEEE Transactions on Power Electronics*, vol. 13, no. 6, pp. 1174–1181, Nov 1998.
- [D.6] P. Rioual, H. Pouliquen, and J. . Louis, "Regulation of a pwm rectifier in the unbalanced network state using a generalized model," *IEEE Transactions on Power Electronics*, vol. 11, no. 3, pp. 495–502, May 1996.



# Appendix E

## Simulation and Laboratory Setup

### E.1 Introduction

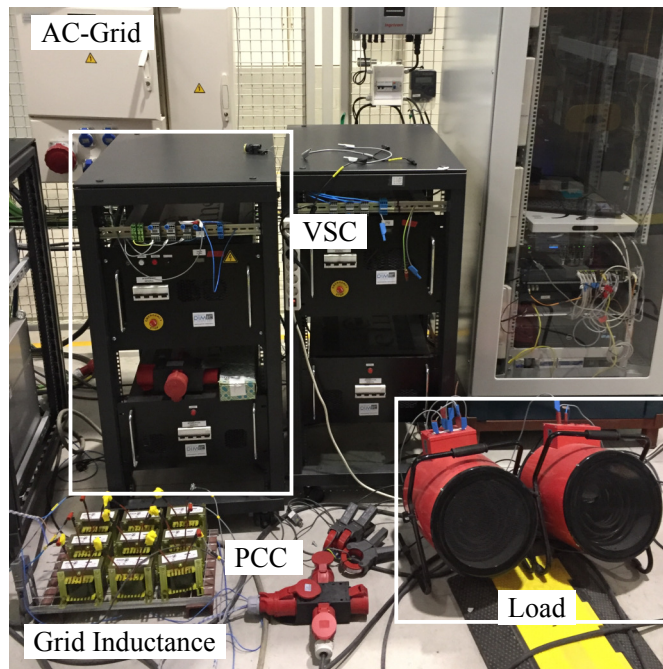
This appendix provides additional information related to the simulation, facilities and laboratory setup employed during the experimental verification of the present work. All experiments have been conducted in the Laboratory for Electrical Energy Management Unified Research (LEMUR), from the Universidad de Oviedo.

### E.2 Simulation and Experimental Setup of the HFSI Technique proposed in Chapter 4

The grid impedance estimation method proposed in Chapter 4 consists on the analysis of the response to a high frequency excitation signal injected from a converter. Simulations of the method have been carried out through Matlab/Simulink<sup>®</sup> software and the experimental setup is shown in Fig. E.1. The converter information and the technical data of the RL filter and the additional inductance,  $L_g$ , used to increase the inductive characteristic of the grid is included in Table E.1. The control system is implemented within a Texas Instruments Digital Signal Controller (F28335). Both simulation and experimental test were carried out with the same technical characteristics.

**Table E.1:** System parameters of the setup for the experiment described in E.2

Converter parameters	Value
Power (kW)	30
DC Link Voltage (V)	750
Max Current (A)	30
Switching frequency (kHz)	10
AC Filter	$L_f = 7 \text{ mH}, R_f = 0.33 \Omega$
Grid impedance	$L_g = 9 \text{ mH}, R_g = 0.02 \Omega$
DC bus capacitor ( $\mu\text{F}$ )	700
Loads	
Three phase balance load ( $\Omega$ )	$R_l = 18$
Single phase loads ( $\Omega$ )	$R_{ls} = 18$
Control	
Sampling control loop $T_c$ ( $\mu\text{s}$ )	100
DC voltage loop	$K_p = 0.088, K_i = 13.2$
Current control loop	$K_p = 5.341, K_i = 2221.4$
High frequency parameters	
Carrier voltage (V)	10.0
Carrier frequency (Hz)	333
Converter switching frequency (kHz)	10
Sampling frequency (kHz)	10

**Figure E.1:** Setup for experimental validation of the HFSI Technique proposed in Chapter 4. At the bottom left side the inductance bank used to emulate the impedance upstream from the PCC, where the STATCOM and local loads are connected.

### E.3 Experimental Setup of the LFSI Technique proposed in Chapter 5

The estimation technique proposed in Chapter 5 considers the operation of multiple grid-tied converters at the same PCC. Simulations have been carried out through Matlab/Simulink<sup>®</sup> software and the experimental setup is shown in Fig. E.2. The information of both converters as well as the technical data of the RL filter and the additional inductance,  $L_g$ , used to emulate the inductive characteristic of the grid is included in Table E.2. The control system is implemented within two Texas Instruments Digital Signal Controllers (F28335), one per converter.

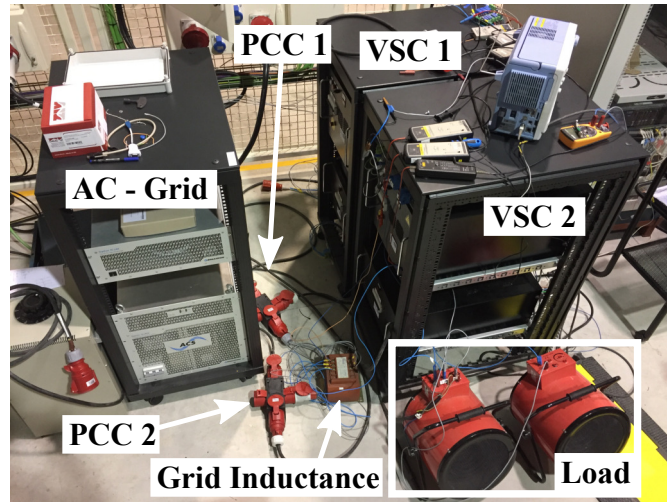


**Figure E.2:** Setup for experimental validation of the PSI Technique proposed in Chapter 5.

**Table E.2:** System parameters of the setup for the experiment described in E.3

<b>Hardware</b>	
Grid voltage	$V_{rms} = 400 \text{ V}, f = 50 \text{ Hz}$
Rated power/current	$S = 30 \text{ kVA}, I_n = 43.3 \text{ A}$
DC link	$v_{dc} = 750 \text{ V}, C = 350 \mu\text{F}$
Grid impedance	$L_g = 9 \text{ mH}$
Converter filter VSC 1 and VSC 2	$L_{filter} = 1.0 \text{ mH}, R_{filter} = 0.16 \text{ m}\Omega$
<b>Control</b>	
pulse mag.	20 V
pulse width.	2 ms
$\lambda$	0.9/0.8
SF at rated power	$f_{sw} = 1 \text{ kHz}$
Current reg. bandwidth	500 Hz

## E.4 Experimental Setup of the Variable SF Technique Proposed in Chapter 6

The efficiency study carried out in Chapter 6 is based on the switching frequency adaptation based on the operating conditions of the system. Simulations have been carried out through Matlab/Simulink<sup>®</sup> software and the experimental setup is shown in Fig. E.3. The information of the converter and the technical data is included in Table E.3. The information regarding the transformer, loads and distribution line to emulate the EPS environment is included in Table E.4. The control system is implemented within two Texas Instruments Digital Signal Controllers (F28335).

**Table E.3:** Converter parameters according to the experimental validation from E.4

Hardware	
Grid voltage	$V_{rms} = 400 \text{ V}, f = 50 \text{ Hz}$
Rated power/current	$S = 30 \text{ kVA}, I_n = 43.3 \text{ A}$
System impedance	See Table E.2
Coupling inductor	$L_{filter} = 1.0 \text{ mH}, R_{filter} = 0.16 \text{ m}\Omega$
DC link	$v_{dc} = 800 \text{ V}, C = 350 \mu\text{F}$
IGBT modules	2MBI200HH-120-50
Dead-time	$t_d = 1 \mu\text{s}$
Control	
PWM Type	Sym. regular sampled w/ 3 <sup>rd</sup> harm. injection
SF at rated power	$f_{sw} = 3 \text{ kHz}$
PLL	Dual 2 <sup>nd</sup> Order Generalized Integrator (SOGI)
Anti-aliasing filter	Butterworth 2 <sup>nd</sup> order, $f_c = f_{sw}/2$
Current reg. bandwidth	300 Hz
Power factor	1

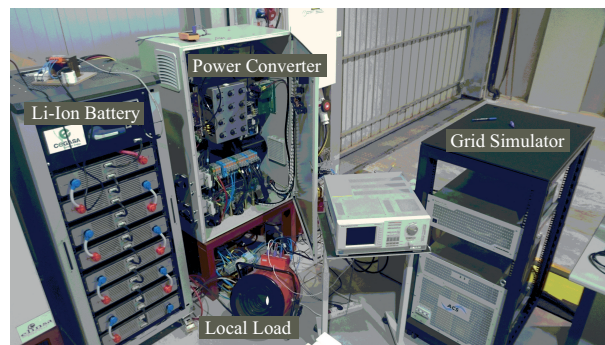


**Figure E.3:** Test setup for the experimental validation of the technique proposed in E.4

**Table E.4:** Installation parameters according to the experimental validation from E.4

<b>Transformer</b>	
Rated power	$S_n = 100$ kVA
Short-circuit impedance & resistance	$Z_{pu} = 0.06, R_{pu} = 0.01$
<b>Distribution Line</b>	
Length	$l = 200$ m
Resistance	$R_{line} = 0.2$ m $\Omega$ /m
X/R ratio	0.32
<b>Local Loads</b>	
Power factor	1
Active power	$P = 50$ kW

## E.5 Cascade Control Design

The structure of a VSC cascade control is generally composed by: an outer loop, which is devoted for controlling the DC-Link voltage and an inner control that is responsible of the current control. Current control loops are designed to provide high dynamic response of the system and no phase and amplitude errors, since fast response is the main issue. On the other hand, voltage control has longer settling times, since stability is the major concern. Three-phase converters are generally controlled by PI regulators, which achieve zero steady-state error with DC magnitudes. To do so, three-phase magnitudes require to be transformed into the  $dq$ -reference frame, synchronized with grid frequency  $\omega_e$ , and thus, the alternating terms become constant at 50 Hz. The dynamic characteristic of the output filter of the converter can be modelled as (E.1).

$$G = \frac{1}{L_f \cdot s + R_f} \quad (\text{E.1})$$

Accordingly, the transfer function of the PI, (E.2), is tuned to achieve zero/pole cancellation. The gains are set based on the magnitudes of the output filter as:  $K_p = 2\pi f_{bw} L_f$  and  $T_i = \frac{L_f}{R_f}$ , where  $f_{bw}$  is the bandwidth of the regulator.

$$C_i = \frac{v_{dq}^e}{e} = K_p \frac{s + 1/T_i}{s} = K_p + \frac{K_i}{s}; \quad (\text{E.2})$$

$$K_i = \frac{K_p}{T_i} \quad (\text{E.3})$$

A similar procedure of zero/pole cancellation is followed to design the PI voltage controller devoted to control the DC-link. In this case, the size of the capacitor will determine the location of the pole, by setting  $K_p = 2\pi f_{bw} C$ , considering a bandwidth ten times slower than the current controller, then, the  $K_i$  term is selected in order to cancel the poles of the closed loop system.



## Appendix F

# Journal Publications



## **F.1 Sensorless Unbalance Modeling and Estimation as an Ancillary Service for LV Four-Wire/Three- Phase Power Converters**



# Sensorless Unbalance Modeling and Estimation as an Ancillary Service for LV Four-Wire/Three-Phase Power Converters

Andrés Suárez-González , Student Member, IEEE, Pablo García , Member, IEEE, Ángel Navarro-Rodríguez , Student Member, IEEE, Geber Villa , Student Member, IEEE, and Jose M. Cano , Member, IEEE

**Abstract**—This paper describes a method to provide low-voltage four-wire three-phase power converters with the capability of unbalance estimation as an ancillary service to the main role that they play in the distribution system (distributed generator, energy storage system, drive, etc.). Typically, dedicated grid/load current sensors are needed to effectively comply with unbalance compensation tasks, increasing system cost and reducing reliability. This is due to the difficulties that arise in the extraction of the zero- and negative-voltage components from the voltages at the point of common coupling, such as the inadequate resolution of full-scaled voltage sensors and limited spectral separation. In this paper, the proposed method does not rely on additional sensors to those typically used in voltage-source converters, and in any case, those sensors are limited to the point of connection of the power converter. Impedance estimation only using converter-side current sensors is implemented by adding a high-frequency voltage excitation over the fundamental command. A new model approach is proposed for the real-time extraction of system impedance using a complex-valued compact form. Considering the voltage source at that frequency to be unique in the grid, it will be proved that the impedance and, thus, the resulting negative-sequence current, which is used for unbalance compensation, can be estimated. For the zero sequence, a special arrangement of the converter voltage sensors together with a repetitive controller is used.

**Index Terms**—Active filter, dc-ac power conversion, distributed resources, four-wire systems, impedance estimation, unbalanced load.

Manuscript received December 31, 2018; revised March 29, 2019; accepted May 15, 2019. Date of publication May 20, 2019; date of current version August 14, 2019. Paper 2018-IPCC-1033.R1, presented at the 2017 IEEE Energy Conversion Congress and Exposition, Cincinnati, OH, USA, Oct. 1-5, and approved for publication in the IEEE TRANSACTIONS ON INDUSTRY APPLICATIONS by the Industrial Power Converter Committee of the IEEE Industry Applications Society. This work was supported in part by the predoctoral grants program Severo Ochoa for the formation in research and university teaching of Principado de Asturias PCTI-FICYT under Grant ID BP14-135, in part by the Research, Technological Development, and Innovation Program Oriented to the Society Challenges of the Spanish Ministry of Economy and Competitiveness under Grant ENE2016-77919-R and Grant DPI2017-89186-R, in part by the Government of the Principality of Asturias under Grant FC-GRUPIN-IDI/2018/000241, and in part by the European Union through ERFD Structural Funds (FEDER). (Corresponding author: Andrés Suárez-González.)

The authors are with the Department of Electrical, Computer and Systems Engineering, University of Oviedo, 33204 Gijón, Spain (e-mail: suarezandres@uniovi.es; garciafpablo@uniovi.es; navarroangel@uniovi.es; villageber@uniovi.es; jmciano@uniovi.es).

Color versions of one or more of the figures in this paper are available online at <http://ieeexplore.ieee.org>.

Digital Object Identifier 10.1109/TIA.2019.2918046

## I. INTRODUCTION

THE adoption of distributed generation has been increased in the past few years due to both political and economic regulations [1], [2] and emerging power electronics converter topologies, which allow us to improve network quality and reliability [3] and decrease in the costs for distributed generation. Power converters have been employed at the transmission network to improve power transmission capability, e.g., static synchronous compensator (STATCOM) [4], [5], static synchronous series compensator [6], and unified power flow controller [4], [7]. Similar topologies have been later integrated at distribution levels, e.g., active power filters (APFs) [8]–[11], allowing the increase of the distributed generation penetration and overcoming some problems related to the decentralized generation approach.

Among the problems related to the distributed generation paradigm [12], [13], current and/or voltage unbalances or sags have recently received much attention [7], [14]–[17]. There are several international standards that recommend maximum limits of the voltage unbalance: ANSI Standard C81.1 requires to keep it lower than 3% [18], and the International Electrotechnical Commission and the European Committee for Electrotechnical Standardization recommend the limit of 2% [19], [20].

Unbalance compensation can be achieved by shunt [21], series [22], or series/shunt combination of the power converter [23], [24]. Among the three structures, series/shunt allows for an optimal [25], [26] sharing of the voltage/current compensation. However, it requires a dedicated converter for the compensation problem. Solely shunt converter compensation can lead to high compensation currents through the converters, reducing the active/reactive power supply capability, and thus, some sharing mechanism among the APF is needed [14]. Sharing of unbalance can be done either by exchanging information among the microgrid converters or by an autonomous method, which is implemented in the form of a droop control [14], [15], [17].

Measurement of the unbalanced components, i.e., negative- and zero-sequence voltages and currents, is a challenging task. Two options are currently used, each of those having an important drawback. When relaying on the voltages at the point of common coupling (PCC), they are greatly affected by the grid impedance value. In those cases, where the converter is coupled



low-voltage (LV) distribution networks have, generally, a negligible value compared to the phase impedances [32]. The main characteristic of this reference frame is the matrix being diagonal, thus noticeably easing the needed algebra for the modeling

$$\mathbf{Z}_{\alpha\beta 0i} = \begin{pmatrix} Z_{\alpha\alpha i} & 0 & 0 \\ 0 & Z_{\beta\beta i} & 0 \\ 0 & 0 & Z_{00i} \end{pmatrix}. \quad (5)$$

In (5), each load is represented by the subscript  $i$ . For the case the load is balanced,  $Z_{\alpha\alpha i} = Z_{\beta\beta i} = Z_{00i}$ . Rotating the impedance matrix to the  $\alpha\beta 0$  reference frame and considering  $n$  loads leads to

$$\mathbf{Z}_{\alpha\beta 0} = \sum_{i=1}^n \left[ \Sigma Z_i \begin{pmatrix} 1 & 0 & 0 \\ 0 & 1 & 0 \\ 0 & 0 & 1 \end{pmatrix} + |\Delta Z_i| \begin{pmatrix} \cos \theta_e^i & -\sin \theta_e^i & \sqrt{2} \cos \theta_e^i \\ -\sin \theta_e^i & -\cos \theta_e^i & \sqrt{2} \sin \theta_e^i \\ \sqrt{2} \cos \theta_e^i & \sqrt{2} \sin \theta_e^i & 0 \end{pmatrix} \right]. \quad (6)$$

In (6),  $\Sigma Z_i$  and  $\Delta Z_i$  can be defined in (7) and (8), respectively:

$$\Sigma Z_i = \frac{Z_{\alpha\alpha i} + Z_{\beta\beta i}}{2} = \frac{Z_a + Z_b + Z_c}{3} \quad (7)$$

$$\Delta Z_i = \frac{Z_{\alpha\alpha i} - Z_{\beta\beta i}}{2} = \frac{Z_a + a \cdot Z_b + a^2 \cdot Z_c}{3} \quad (8)$$

$$\theta_e^i = \tan^{-1}(\Delta Z_i) \quad (9)$$

where  $\theta_e^i$  is the impedance unbalance angle and  $a = e^{-j2\pi/3}$ . For example, for single-phase loads at phases  $a$ ,  $b$ , and  $c$ ,  $\theta_e^i$  equals  $0$ ,  $2\pi/3$ , and  $4\pi/3$ , respectively. It is worth noting that for the case of single-phase loads, in which the impedances at the two remaining phases are infinity, expressions (7) and (8) will also be evaluated as infinity.

By substituting (6) into the voltage equation (1) expressed in the  $\alpha\beta 0$  reference frame, and considering steady-state conditions, the resulting current vector ( $\mathbf{i}_{\alpha\beta}$ ) and the homopolar component ( $i_0$ ) are given by (10) and (11), respectively, as

$$\mathbf{i}_{\alpha\beta} = V_{\alpha\beta}^+ \sum_{i=1}^n \left[ \Sigma Y_i e^{j\omega_e t} - \Delta Y_i e^{-j(\omega_e t + \theta_e^i)} \right] + V_{\alpha\beta}^- \sum_{i=1}^n \left[ \Sigma Y_i e^{-j\omega_e t} - \Delta Y_i e^{j(\omega_e t - \theta_e^i)} \right] \quad (10)$$

$$i_0 = V_0 \sum_{i=1}^n \left[ \frac{1}{\Sigma Z_i} \sin(\omega_e t + \phi_e) \right] + V_{\alpha\beta}^+ \sum_{i=1}^n \left[ \frac{\Delta Y_i^2}{\Sigma Y_i} \sqrt{2} \left( e^{j\omega_e t} - \frac{\Sigma Y_i}{\Delta Y_i} e^{j(\omega_e t + \theta_e^i)} \right) \right] + V_{\alpha\beta}^- \sum_{i=1}^n \left[ \frac{\Delta Y_i^2}{\Sigma Y_i} \sqrt{2} \left( e^{-j\omega_e t} - \frac{\Sigma Y_i}{\Delta Y_i} e^{-j(\omega_e t - \theta_e^i)} \right) \right] \quad (11)$$

where  $\Sigma Y_i = \frac{\Sigma Z_i}{\Sigma Z_i^2 - \Delta Z_i^2}$ ,  $\Delta Y_i = \frac{\Delta Z_i}{\Sigma Z_i^2 - \Delta Z_i^2}$ ,  $\omega_e$  is the grid frequency,  $\phi_e = \tan^{-1}(\mathbf{v}_{\alpha\beta})$ , and  $V_{\alpha\beta}^+$ ,  $V_{\alpha\beta}^-$ , and  $V_0$  are the positive-, negative-, and zero-sequence magnitudes of the voltage vector.

The proposed model allows obtaining a compact expression in time domain for the  $\alpha\beta 0$  terms of the current vector depending on the equivalent impedance, as seen from a voltage source. This will be used later for isolating different parameters in real time, having applications from impedance estimation to unbalance compensation. In order to compare the proposed model with the traditional symmetrical component approach, the following equation provides the expression for the positive, negative, and zero components derived from (10) and (11):

$$\begin{pmatrix} I_{\alpha\beta}^+ \\ I_{\alpha\beta}^- \\ I_0 \end{pmatrix} = \sum_{i=1}^n \left[ \Sigma Y_i \begin{pmatrix} 1 & 0 & 0 \\ 0 & 1 & 0 \\ 0 & 0 & 1 \end{pmatrix} - \Delta Y_i \begin{pmatrix} 0 & e^{j\theta_e^i} & 0 \\ e^{j\theta_e^i} & 0 & 0 \\ \sqrt{2}(e^{j\theta_e^i} - \frac{\Delta Y_i}{\Sigma Y_i}) & \sqrt{2}(e^{j\theta_e^i} - \frac{\Delta Y_i}{\Sigma Y_i}) & \frac{\Delta Y_i}{\Sigma Y_i} \end{pmatrix} \right] \begin{pmatrix} V_{\alpha\beta}^+ \\ V_{\alpha\beta}^- \\ V_0 \end{pmatrix}. \quad (12)$$

Equations (10)–(12) build the proposed model by adding together all the admittances at the PCC using the superposition theorem. The equivalent admittance at the PCC, later used for the impedance identification, can be defined as

$$Y_{\text{eq}}^{\alpha\beta} = \sum_{i=1}^n \left[ \frac{1}{\Sigma Z_i^2 - \Delta Z_i^2} \left( \Sigma Z_i \begin{pmatrix} 1 & 0 \\ 0 & 1 \end{pmatrix} + |\Delta Z_i| \begin{pmatrix} -\cos \theta_i & \sin \theta_i \\ \sin \theta_i & \cos \theta_i \end{pmatrix} \right) \right] = \frac{1}{\Sigma Z_{\text{eq}}^2 - \Delta Z_{\text{eq}}^2} \left( \Sigma Z_{\text{eq}} \begin{pmatrix} 1 & 0 \\ 0 & 1 \end{pmatrix} + |\Delta Z_{\text{eq}}| \begin{pmatrix} -\cos \theta_{\text{eq}} & \sin \theta_{\text{eq}} \\ \sin \theta_{\text{eq}} & \cos \theta_{\text{eq}} \end{pmatrix} \right). \quad (13)$$

For the online estimation of the equivalent impedance, the equivalent admittance is used instead. This is to avoid any division by zero when the current is zero. The equivalent mean and differential admittances can be obtained using (14) and (15). Clearly, the two equations can be solved in real time with a really low computational burden, thus allowing for a simple identification method. Equivalent expressions for the impedance terms are also included in (16) and (17), respectively:

$$\Sigma Y_{\text{eq}}^{\alpha\beta} = \frac{i_{\alpha\beta}^+ \cdot v_{\alpha\beta}^+ - i_{\alpha\beta}^- \cdot v_{\alpha\beta}^-}{(v_{\alpha\beta}^+)^2 - (v_{\alpha\beta}^-)^2} \quad (14)$$

$$\Delta Y_{\text{eq}}^{\alpha\beta} = \frac{i_{\alpha\beta}^- \cdot v_{\alpha\beta}^+ - i_{\alpha\beta}^+ \cdot v_{\alpha\beta}^-}{(v_{\alpha\beta}^+)^2 - (v_{\alpha\beta}^-)^2} \quad (15)$$

$$\Sigma Z_{\text{eq}}^{\alpha\beta} = \frac{v_{\alpha\beta}^+ \cdot i_{\alpha\beta}^+ - v_{\alpha\beta}^- \cdot i_{\alpha\beta}^-}{(i_{\alpha\beta}^+)^2 - (i_{\alpha\beta}^-)^2} \quad (16)$$

$$\Delta Z_{\text{eq}}^{\alpha\beta} = \frac{v_{\alpha\beta}^- \cdot i_{\alpha\beta}^+ - v_{\alpha\beta}^+ \cdot i_{\alpha\beta}^-}{(i_{\alpha\beta}^+)^2 - (i_{\alpha\beta}^-)^2}. \quad (17)$$

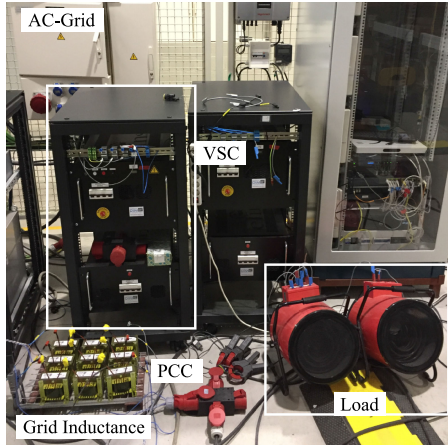


Fig. 3. Experimental setup according to the schematic shown in Fig. 1. At the bottom left side, the inductance bank is used to emulate the impedance upstream from the PCC, where the STATCOM and local loads are connected.

TABLE I  
SYSTEM PARAMETERS

Converter parameters	Value
Power (kW)	100
DC Link Voltage (V)	850
Max Current (A)	200
Switching frequency (kHz)	10
AC Filter	$L_f = 7\text{mH}, R_f = 0.33\Omega$
Grid impedance	$L_g = 9\text{mH}, R_g = 0.02\Omega$
DC bus capacitor ( $\mu\text{F}$ )	700
Loads	
Three phase balance load	$R_l = 18\Omega$
Single phase loads	$R_{ls} = 18\Omega$
Control tuning	
Sampling control loop $T_c$ ( $\mu\text{s}$ )	100
DC voltage loop	$K_p = 0.088, K_i = 13.2$
Current control loop	$K_p = 5.341, K_i = 2221.4$
High frequency parameters	
Carrier voltage (V)	10.0
Carrier frequency (Hz)	333
Converter switching frequency (kHz)	10
Sampling frequency (kHz)	10

The proposed model has been validated by numerical simulation and experimental tests. For that, different step changes in the load impedance values ( $z_a, z_b, z_c$ ) have been applied, and the predicted model values for the current and impedances have been compared with respect to the simulation and experimental results. A real setup is presented in Fig. 3, following the same topology as the schematic in Fig. 1. A four-wire/three-phase VSC of 30 kVA has been used to perform the experiments with the system parameters depicted in Table I. The control system is implemented within a Texas Instruments digital signal controller (F28335). The VSC was operated in the STATCOM mode, where the  $d$ -axis is devoted to maintaining the dc link at a nominal voltage. A constant reference of 10 A is set in the  $q$ -axis.

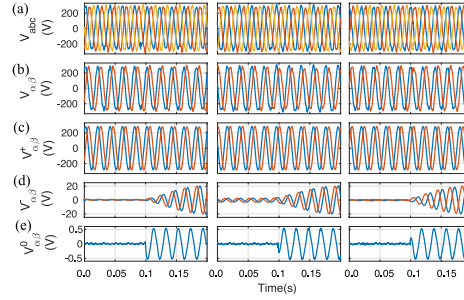


Fig. 4. Experimental results. Voltage measurements at the PCC, under three different unbalance conditions as a consequence of a change in the load impedance. Unbalance is induced by connecting a parallel  $18\text{-}\Omega$  load at 0.1 s to the  $18\text{-}\Omega$  balanced load at the PCC. From left to the right: unbalance induced in phase  $a$ , unbalance induced in phase  $b$ , and unbalance induced in phase  $c$ . From top to bottom: (a) phase voltages, (b)  $\alpha, \beta$  components, and (c)–(e) the positive, negative, and zero components of the voltage vector.

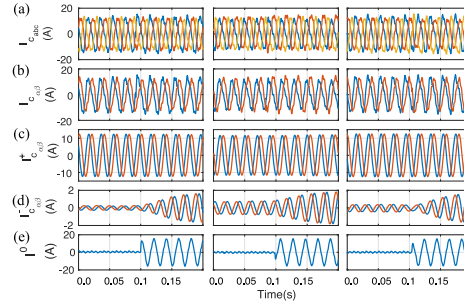


Fig. 5. Experimental results. Converter current measurement at the PCC, under the three different unbalance conditions described in Fig. 4. From left to right: unbalance induced in phases  $a, b$ , and  $c$ . From top to bottom: (a) phase currents, (b)  $\alpha, \beta$  components, and (c)–(e) the positive, negative, and zero components of the current vector.

The reason behind the VSC being injecting current is to illustrate the effect of the load unbalance over the converter current. At initial time, the load impedance is balanced and equal for the three phases ( $Z_a = Z_b = Z_c = 18\Omega$ ). As expected, neither negative nor homopolar component is observed.

Figs. 4–6 show the experimental results in the  $\alpha\beta 0$  reference frame for the converter voltage, converter current, and grid voltage at the PCC, respectively, under different load unbalance conditions in each phase. At instant 0.1 s, an  $18\text{-}\Omega$  load is connected in parallel to phase  $a$ , decreasing its nominal value by 50%. Voltage distortion is present at the PCC, where 14.4 V of negative sequence is measured, as shown in Fig. 4. The presence of the unbalance is also reflected in both Figs. 5 and 6, where a homopolar current of 11.2 A starts flowing through the system. Similarly, a negative-sequence current of 1.2 A is measured from the converter side and 5.2 A from the grid side. The

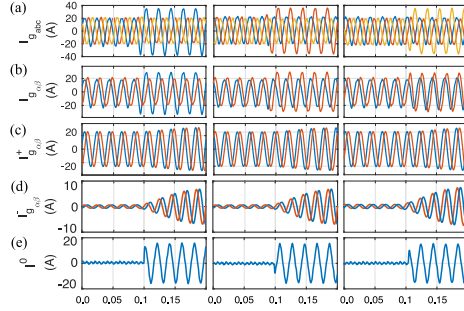


Fig. 6. Experimental results. Grid current measurement, under the three different unbalance conditions described in Fig. 4. From left to right: unbalance induced in phase  $a$ , unbalance induced in phase  $b$ , and unbalance induced in phase  $c$ . From top to bottom: (a) phase currents, (b)  $\alpha, \beta$  components, and (c)–(e) the positive, negative, and zero components of the current vector.

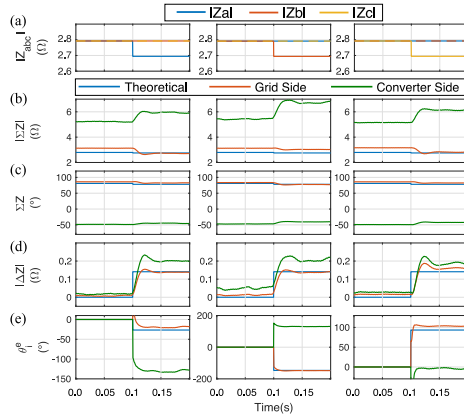


Fig. 7. Experimental results. Equivalent grid impedance at the PCC measured at 50 Hz. From left to right: unbalance induced in phases  $a$ ,  $b$ , and  $c$ . From top to bottom: (a) phase impedances, (b)  $|\Sigma Z|$  component, (c) phase of  $\Sigma Z$ , (d)  $|\Delta Z|$  component, and (e)  $\theta_e^i$ , which corresponds to the unbalance angle.

same test is repeated in the other two phases (results from unbalance in phase  $b$  and  $c$  are shown in the middle and right columns), obtaining similar results in the voltage and current magnitudes.

Fig. 7 compares the impedance values according to (7)–(9) and the ones obtained from the experimental measurements, at both grid and converter sides, in order to support the proposed model and ease the explanation. The interesting aspect of the test lies in the comparison of the unbalance angle  $\theta_e^i$ , which is rotating depending on the phase where the unbalance is located. In the first case, the impedance angle changes from  $0^\circ$  to  $-26.67^\circ$ . The second case, where the unbalance takes place in phase  $b$ ,  $\theta_e^i$  changes from  $0^\circ$  to  $-148.3^\circ$ . Note that this result is  $120^\circ$  delayed with respect to the previous unbalance in phase

$a$  and ideally should be  $\theta_b = -26.67^\circ - 120^\circ = -146.67^\circ$ . The difference between the expected result and the real one is considered within the error tolerance. For the unbalance in phase  $c$ , the change is from  $0^\circ$  to  $93.33^\circ$ , which corresponds to  $\theta_c = 120^\circ - 26.67^\circ = 93.33^\circ$ . The remaining variables depicted in Fig. 7 are not dependent on the phase unbalance, but only on the magnitude of the unbalance. For this reason,  $|\Sigma Z|$  decreases from 2.8 to 2.7  $\Omega$  and  $|\Delta Z|$  increases at instant 0.1 s from 0 to 0.15  $\Omega$ .

From (10), it is clear that the load unbalances will cause negative- and zero-sequence currents to appear, which potentially will create an unbalance in the grid supplied voltages. Compensation can be done by injecting a negative- and zero-sequence currents in opposition to the respective unbalanced currents [14]. There are several methods proposed in the literature to compensate for this, all of them requiring to separate (filter) the negative and zero sequences from the positive one and to cancel them out by using negative- and zero-sequence current controllers [14], [15]. For the measurement, extra current sensors for the load or the grid currents are required. The need for these extra sensors is demonstrated according to the results presented in Fig. 7, where the impedance observed from the converter side (green line) and the one observed from the grid side (red one) are represented. This clear inaccuracy in the results is due to the lack of information from the converter-side currents. Impedances are calculated according to (16) and (17), resulting in

$$\Sigma Z_g^{\alpha\beta} = \frac{(v_{g\alpha\beta}^+ - v_{c\alpha\beta}^+) \cdot i_{g\alpha\beta}^+ - (v_{g\alpha\beta}^- - v_{c\alpha\beta}^-) \cdot i_{g\alpha\beta}^-}{(i_{g\alpha\beta}^+)^2 - (i_{g\alpha\beta}^-)^2} \quad (18)$$

$$\Delta Z_g^{\alpha\beta} = \frac{(v_{g\alpha\beta}^- - v_{c\alpha\beta}^-) \cdot i_{g\alpha\beta}^+ - (v_{g\alpha\beta}^+ - v_{c\alpha\beta}^+) \cdot i_{g\alpha\beta}^-}{(i_{g\alpha\beta}^+)^2 - (i_{g\alpha\beta}^-)^2} \quad (19)$$

where  $v_{g\alpha\beta}$  and  $i_{g\alpha\beta}$  are the PCC voltage and the grid current, respectively, and  $v_{c\alpha\beta}$  and  $i_{c\alpha\beta}$  are the voltage and current at the converter side, respectively. The required extra sensor for the  $i_{g\alpha\beta}$  current is an undesired component, and thus, it is desirable to obtain an impedance estimation without it. However, as evidenced in Fig. 7, the use of the converter current at the fundamental frequency is not an option. In the following section, an approach for the unbalance estimation based on the injection of an HFS is proposed. The method will enable the measurement of the grid impedance from the converter side currents, thus leading to a sensorless compensation.

### III. HFS INJECTION AND ONLINE MEASUREMENT OF EQUIVALENT IMPEDANCE AT THE PCC

As discussed previously, the existence of unbalances both in the impedance and in the voltages will generate negative- and zero-sequence components in the current vector (10), (11). The developed model did not take any assumption about the excitation frequency, and thus, it can be used to any fixed-frequency excitation just changing the  $\omega_e$  variable by the frequency of interest. If a balanced high-frequency ( $\omega_{hf}$ ) carrier-signal voltage  $v_{\alpha\beta}^{hf+}$ , as denoted by (20), is added to the converter voltage command, it will induce a high-frequency current (21) that

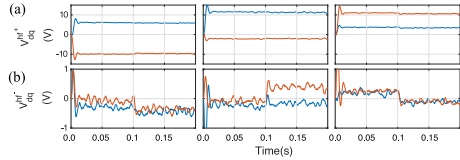


Fig. 8. Experimental results. High-frequency PCC voltage. Each column presents the results under one phase unbalanced: left column: unbalance in phase  $a$ ; middle column: unbalance in phase  $b$ ; and right column: unbalance in phase  $c$ . From top to bottom: (a) Positive sequence of the high-frequency voltage signal in the  $dq$  reference frame at 333 Hz; (b) negative sequence in the  $dq$  reference frame at 333 Hz.

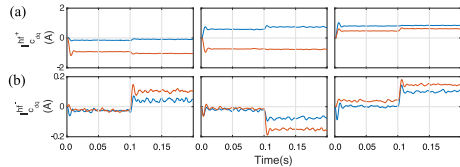


Fig. 9. Experimental results. High-frequency converter current. Each column presents the results under one phase unbalanced: left column: unbalance in phase  $a$ ; middle column: unbalance in phase  $b$ ; and right column: unbalance in phase  $c$ . From top to bottom: (a) Positive sequence of the high-frequency current signal in the  $dq$  reference frame at 333 Hz; (b) negative sequence in the  $dq$  reference frame at 333 Hz.

includes a high-frequency negative-sequence component determined by the impedance unbalance. However, two fundamental differences exist compared to the fundamental excitation: 1) as the high-frequency voltage is created by the converter and superimposed to the fundamental voltage, the resulting high-frequency converter current  $i_C^{hf}$  contains the unbalance information; hence, measuring the current at the load,  $i_l$ , or at the grid side,  $i_g$ , is not needed to proceed with the compensation (see Fig. 1). The same concern implies the selection of the excitation signal frequency, which should be selected with enough spectral separation from the current controller bandwidth and not higher than half the switching frequency when synchronous sampling is used, according to the Nyquist theorem. The selection of an interharmonic is done to not interfere with possible additional shunt-connected converters at the PCC; and 2) filtering the negative-sequence current from the positive one is easier at higher frequencies, since there is more spectral separation. This will allow us to increase the resolution of the system to light unbalanced conditions. Figs. 8 and 9 show, respectively, the experimental high-frequency voltage at the PCC and current signals injected by the converter to calculate the equivalent grid impedance. To clarify and ease the understanding, the signals are presented in the synchronous reference frame at 333 Hz. At instant  $t = 0.1$  s, the unbalance is produced. As expected, both the negative voltage and current sequences have information about the unbalance

$$\mathbf{v}_{\alpha\beta}^{hf} = V^{hf} e^{j\omega_{hf}t} \quad (20)$$

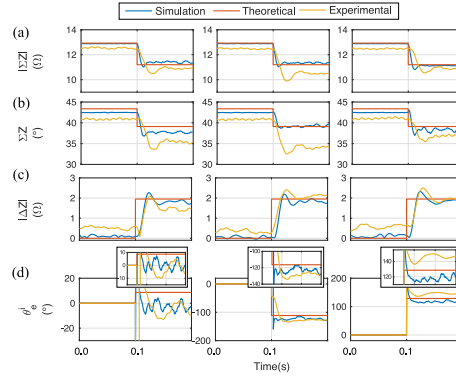


Fig. 10. Comparison of the results obtained in the simulation (blue line), theoretical expression (red line), and experiment (yellow line) of the presented method. Each column presents the results under one phase unbalanced: left column: unbalance in phase  $a$ ; middle column: unbalance in phase  $b$ ; right column: unbalance in phase  $c$ . From top to bottom: (a) Equivalent value of  $\Sigma Z$ , (b) angle in degrees of  $\Sigma Z$ , (c) equivalent value of  $\Delta Z$ , and (d)  $\theta_e^*$ .

$$i_{\alpha\beta}^{hf} = V^{hf} \sum_{i=1}^n \left[ \Sigma Y_i^{hf} e^{j\omega_{hf}t} + \Delta Y_i^{hf} e^{j(-\omega_{hf}t + \theta_e^*)} \right]. \quad (21)$$

The proposed HFS injection for the estimation of the model parameters has been tested by both simulation and experimental results. The simulation parameters are gathered in Table I. In Fig. 10, the proposed model is verified using MATLAB/Simulink for different steps in the load connected at the PCC.

Fig. 10 gathers the results obtained in the simulation, the theoretical expression, and the experiment of the method. The sequence of the experiment is the same as the one explained above in Fig. 7. A load unbalance is induced in every phase of the system at 0.1 s, and every impedance term is calculated only with the converter-side measurements.

Table II summarizes the rms current values, at 50 and 333 Hz (hf superscript), of the presented model, the simulation, and the experimental results. In this table,  $t_1$  and  $t_2$  represent the instants before and after the unbalance takes place. Model columns show the current values resulted from applying the mathematical model presented in (10) with the same grid impedance values from Table I, before and after the unbalance conditions. Simulation and experimental columns show the results obtained from a MATLAB/Simulink model and from the experiment, respectively. The results are shown, in rows, for each of the phases, and as a percentage error with respect to the model results. The current values presented in Table II are calculated based on the equivalent impedance of the system in Fig. 1, both at 50 and 333 Hz. As stated above, grid currents  $I_{g\alpha\beta}^+$  and  $I_{g\alpha\beta}^-$  are produced by the interaction of both grid and converter voltages. These estimated grid currents are supported as well as by the results presented in Fig. 6(c) and (d). On the contrary,  $I_{\alpha\beta}^{hf+}$  and

TABLE II  
 COMPARISON OF RMS CURRENT VALUES

	Model		Simulation		Experimental	
	$t_1$	$t_2$	error (%)	error (%)	$t_1$	$t_2$
$a$						
$I_{g\alpha\beta}^+$	14.42	17.68	1.05	0.34	0.0	1.2
$I_{g\alpha\beta}^-$	0.0149	4.288	0.0	5.2	0.0	7.87
$I_{c\alpha\beta}^{hf+}$	0.6632	0.7501	1.01	4.81	0.48	5.01
$I_{c\alpha\beta}^{hf-}$	0.0197	0.1258	0.0	3.11	0.05	3.8
$b$						
$I_{g\alpha\beta}^+$	14.33	17.13	0.49	1.42	0.21	2.78
$I_{g\alpha\beta}^-$	0.044	4.238	0.0	3.5	0.54	7.46
$I_{c\alpha\beta}^{hf+}$	0.6679	0.7442	2.5	4.9	0.83	8.95
$I_{c\alpha\beta}^{hf-}$	0.0196	0.125	0.0	3.01	3.16	3.73
$c$						
$I_{g\alpha\beta}^+$	14.26	17.36	1.68	1.48	0.08	3.77
$I_{g\alpha\beta}^-$	0.0043	4.303	0.0	3.2	0.0	7.80
$I_{c\alpha\beta}^{hf+}$	0.6675	0.741	2.5	5.1	0.3	5.34
$I_{c\alpha\beta}^{hf-}$	0.0198	0.1198	0.0	3.09	1.10	8.85

$I_{c\alpha\beta}^{hf-}$  result from the high-frequency excitation signal (20), provided by the converter, so for this case, only the converter voltage at 333 Hz needs to be considered. Clearly, there is a close agreement among the proposed model, the simulation, and the experimental results for all the tested conditions. Nevertheless, small deviations are perceived in the experimental results, due to the fact that the simulations are conducted using an ideal voltage source. This might not be the case in the experimental tests, where a real grid is taken as the PCC, and thus, nonideal voltage conditions are included. Besides that fact, calibration differences among the three current and voltage sensors are candidates for the error, being below 9% for all the conducted tests.

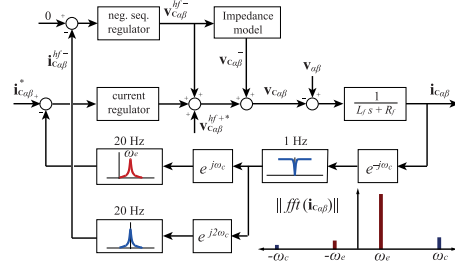
#### IV. HFS-BASED UNBALANCE COMPENSATION

In order to achieve the proposed sensorless unbalance compensation, it is needed to determine the equivalent differential admittance/impedance at the PCC as seen by the ac network at the fundamental frequency and to relate it to the equivalent high-frequency injected from the power converter. With the definition of variables used in Fig. 1, (10) can be represented in compact form as (22), whereas (21) is given by (23):

$$I_{g\alpha\beta}^{\omega_c} = Y_{eq\alpha\beta}^{\omega_c} \cdot (V_{g\alpha\beta}^{\omega_c} - V_{c\alpha\beta}^{\omega_c}) \quad (22)$$

$$I_{c\alpha\beta}^{\omega_{hf}} = Y_{c\alpha\beta}^{\omega_{hf}} \cdot (V_{c\alpha\beta}^{\omega_{hf}} - V_{g\alpha\beta}^{\omega_{hf}}) \quad (23)$$

where  $\omega_c$  is the fundamental frequency and  $\omega_{hf}$  is the high frequency.  $Y_{eq}$  is the equivalent admittance at the PCC, determined from the parallel connection of the grid and the load impedances as:  $Y_{eq} = Y_g + Y_l$  and can be determined using (13). By analyzing (22) and (23), it is clear that the equivalent admittance can be determined, at the two different frequencies, from both expressions. In traditional unbalance compensation approaches, (22) is used. However, it requires an additional current sensor for the grid or load current. In the method proposed in this paper, only the converter current is measured, and thus, the compensation


 Fig. 11. HFS injection and signal processing. Spectrum showing the main components of the converter current ( $i_c$ ) is shown in the lower right corner.

will be determined from (23). It is worth noting that, assuming that the grid voltage is represented as an ideal voltage source upstream the grid impedance, the high-frequency component of the grid voltage ( $V_{g\alpha\beta}^{\omega_{hf}}$ ) could be assumed to be zero. Compensating the circulating high-frequency negative-sequence current requires to inject a high-frequency negative-sequence voltage. Being the goal of the proposed high-frequency injection to determine the needed compensation voltage at the fundamental frequency, the idea is to first determine the needed voltage for the high-frequency excitation and, then, obtain the corresponding fundamental frequency component. By applying (10) to the high-frequency components and making the two terms to generate a negative-sequence current to cancel out, an expression for the required negative-sequence high-frequency voltage is given by

$$v_{c\alpha\beta}^{hf-} = -v_{c\alpha\beta}^{hf+} \frac{\sum_{i=1}^n \Delta Y_i^{hf} e^{-j\theta_i}}{\sum Y_i^{hf}}. \quad (24)$$

As the information of the load unbalance is still included in  $v_{c\alpha\beta}^{hf-}$ , the proper correction action at the grid frequency can be derived from this value.

In regard to the high-frequency excitation signal, its magnitude and frequency values can be tuned separately. From a power quality perspective, increasing the frequency and reducing the magnitude is preferred. However, this reduces the signal-to-noise ratio of the method. Additionally, the injected frequency should not be a harmonic of the fundamental frequency, in order to avoid the reaction of any existing harmonic compensator connected to the grid [33]. For this paper, the values shown in Table I have been chosen.

The control scheme shown in Fig. 11 is used to compensate for the negative-sequence current at grid frequency. A positive-sequence high-frequency (333 Hz) carrier voltage  $v_{C\alpha\beta}^{hf+}$  is added to the converter voltage, causing a negative-sequence component to appear in the converter current at the same frequency  $i_{C\alpha\beta}^{hf-}$ . Provided that the grid side is free from this frequency component and mostly balanced, this negative-sequence component is the same as could be observed at the load, i.e.,  $i_{C\alpha\beta}^{hf-} = -i_{\alpha\beta}^{hf-}$ . This negative-sequence current is obtained from the converter current and controlled to be zero by using two PI regulators,

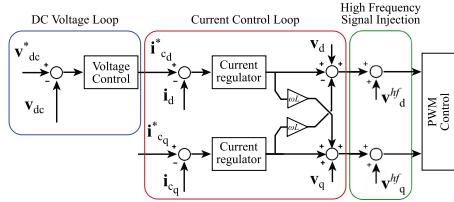


Fig. 12. Conventional cascade control combined with the high-frequency excitation signal. HFS is injected as a voltage signal over the current-loop control action.

one per each axis. The output of this regulator,  $v_{C\alpha\beta}^{hf-}$ , is used to estimate the negative sequence to be added at the grid frequency to the converter voltage,  $v_{C\alpha\beta}^-$ , in order to achieve the compensating objective. An unbalance impedance model is used to relate injections at both frequencies, provided that a linear load is connected to the PCC. The unbalance impedance model shown in Fig. 11, which relates the fundamental frequency to the high-frequency compensation, can be obtained by calculating the differential admittance at the high frequency corrected by the relationship between the magnitude of the ideal grid voltage (assumed here to be 1 p.u.) and the injected high-frequency voltage. The relationship is given by

$$v_{c\alpha\beta}^- = \Delta Y_{eq}^{hf} \cdot \frac{V_g}{V_c} \cdot v_{c\alpha\beta}^{hf}. \quad (25)$$

In Fig. 12 it is shown the schematic of the practical implementation of the high frequency signal injection within the converter cascade control.

## V. ZERO-SEQUENCE COMPENSATION

Zero-sequence currents arise in the LV distribution system as a consequence of both unbalanced and nonlinear loads. The local compensation of zero-sequence currents in order to avoid their propagation upstream from the PCC is a desirable ancillary service for power converters, though only four-wire topologies are valid to comply with this function. This task can be easily done by measuring the zero-sequence current at the grid side and implementing a closed-loop strategy for compensating it. Unfortunately, this requires not only an additional sensor, but also the connection or communication between distant points. A theoretical alternative comes from the compensation of the zero-sequence voltage at the PCC, which could be calculated from the grid phase-voltage sensors of the VSC. However, the use of three voltage sensors ranged at full scale to measure the voltages at the PCC makes it difficult to provide a suitable resolution in the calculation of this value, and it can be even impossible in the interconnection to strong power systems. The arrangement proposed in Fig. 13 for a four-leg topology is used in this paper to solve this adversity. Two full-scale sensors are combined with a third one, ranged at a much lower scale. The latter

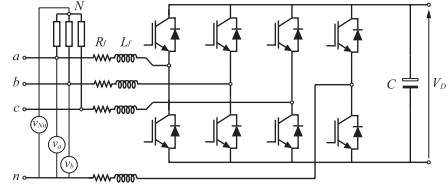


Fig. 13. Zero-sequence voltage compensation. The proposed sensor arrangement for the measurement of the zero-sequence component.

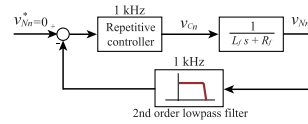


Fig. 14. Zero-sequence voltage compensation. Control loop modeling based on the use of an RC.

sensor is devoted to measure the zero-sequence voltage component directly, by connecting it between the grounded neutral point of the installation and the artificial neutral point of a three-phase balanced high-impedance load, intentionally located at the PCC. The analytical expression for the zero-sequence voltage is given by

$$v_{Nn} = \frac{1}{3} (v_a + v_b + v_c) = v^0. \quad (26)$$

After applying a second-order low-pass filter to remove the high-frequency components of  $v_{Nn}$ , a simple resonant controller could be used to cancel the fundamental frequency zero-sequence component seen from the grid side. Nevertheless, an RC was selected for this application in order to also remove other zero-sequence frequencies. This is of special interest in this type of installations, in which the massive use of single-phase nonlinear loads can cause a significant flow of triplen current harmonics. Fig. 14 shows the control loop, which cancels the zero-sequence components by adding the proper signal to the modulation of the neutral leg of the converter. Note that, although the total modulation of this leg contains other zero-sequence components to counteract the effect of the traditional zero-sequence injection in the other legs, only the added output of the RC appears in  $v_{Cn}$ . In Fig. 15, the proper compensation of the zero-sequence component is demonstrated. The neutral current at the load ( $i_{nload}$ ) is presented in Fig. 15(a). As can be seen, two single-phase loads are connected to phase *a* at time 0.05 s, and one of them is disconnected at time 0.2 s to test transient performance. The application of the RC proposed in this paper together with the special arrangement of voltage sensors leads to a fast compensation of grid neutral current ( $i_{ngrid}$ ) in Fig. 15(c) by the converter ( $i_{nconv}$ ), which starts the injection at 0.1 s.

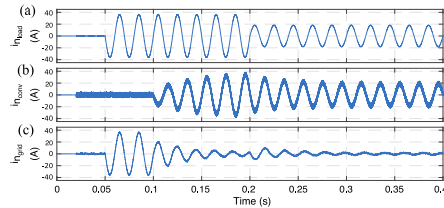


Fig. 15. Simulation results. Zero-sequence compensation. (a) Neutral current at the load ( $i_{nload}$ ). (b) Current at the converter neutral leg ( $i_{ncom}$ ). (c) Neutral current at the grid side ( $i_{ngrid}$ ).

VI. CONCLUSION

In this paper, a method for measuring and compensating unbalance currents for four-wire three-phase converters is presented. An HFS injection is used for the negative-sequence component and an RC for zero-sequence components. Both strategies allow a sensorless high-resolution alternative for unbalance compensation. A model considering unbalance loads and voltages has been developed. This model allows us to estimate the negative-sequence currents generated by the unbalance loads, as well as by the cross-coupling terms. From the general model, a high-frequency model that shows the resulting high-frequency current in the presence of unbalance conditions has been obtained.

REFERENCES

[1] R. Lasseter, "Microgrids," in *Proc. IEEE Power Eng. Soc. Winter Meeting*, 2002, vol. 1, pp. 305–308.  
 [2] R. Lasseter and P. Paigi, "Microgrid: A conceptual solution," in *Proc. IEEE 35th Annu. Power Electron. Spec.*, Jun. 2004, vol. 6, pp. 4285–4290.  
 [3] J. M. Guerrero, "Editorial special issue on power electronics for microgrids—Part II," *IEEE Trans. Power Electron.*, vol. 26, no. 3, pp. 659–663, Mar. 2011.  
 [4] N. G. Hingorani and L. Gyugyi, *Understanding FACTS: Concepts and Technology of Flexible AC Transmission Systems*. New York, NY, USA: IEEE Press, 2000.  
 [5] B. Singh, R. Saha, A. Chandra, and K. Al-Haddad, "Static synchronous compensators (STATCOM): A review," *IET Power Electron.*, vol. 2, no. 4, pp. 297–324, Jul. 2009.  
 [6] L. Gyugyi, C. Schauder, and L. Sen, "Static synchronous series compensator: A solid-state approach to the series compensation of transmission lines," *IEEE Trans. Power Del.*, vol. 12, no. 1, pp. 406–417, Jan. 1997.  
 [7] V. Khadkikar, "Enhancing electric power quality using UPQC: A comprehensive overview," *IEEE Trans. Power Electron.*, vol. 27, no. 5, pp. 2284–2297, May 2012.  
 [8] B. Singh, K. Al-Haddad, and A. Chandra, "A review of active filters for power quality improvement," *IEEE Trans. Ind. Electron.*, vol. 46, no. 5, pp. 960–971, Oct. 1999.  
 [9] V. Corasaniti, M. Barbieri, P. Arnera, and M. Valla, "Comparison of active filters topologies in medium voltage distribution power systems," in *Proc. IEEE Power Energy Soc. Gen. Meeting—Converters. Del. Elect. Energy 21st Century*, Jul. 2008, pp. 1–8.  
 [10] H. Fujita and H. Akagi, "The unified power quality conditioner: The integration of series and shunt-active filters," *IEEE Trans. Power Electron.*, vol. 13, no. 2, pp. 315–322, Mar. 1998.  
 [11] P.-T. Cheng and T.-L. Lee, "Distributed active filter systems (DAFSs): A new approach to power system harmonics," *IEEE Trans. Ind. Appl.*, vol. 42, no. 5, pp. 1301–1309, Sep. 2006.

[12] F. Bastiao, P. Cruz, and R. Fiteiro, "Impact of distributed generation on distribution networks," in *Proc. 5th Int. Conf. Eur. Elect. Market*, May 2008, pp. 1–6.  
 [13] R. Walling, R. Saint, R. Dugan, J. Burke, and L. Kojovic, "Summary of distributed resources impact on power delivery systems," *IEEE Trans. Power Del.*, vol. 23, no. 3, pp. 1636–1644, Jul. 2008.  
 [14] M. Savaghebi, A. Jalilian, J. Vasquez, and J. Guerrero, "Autonomous voltage unbalance compensation in an islanded droop-controlled microgrid," *IEEE Trans. Ind. Electron.*, vol. 60, no. 4, pp. 1390–1402, Apr. 2013.  
 [15] P. Cheng, C. Chen, T. Lee, and S. Kuo, "A cooperative imbalance compensation method for distributed-generation interface converters," *IEEE Trans. Ind. Appl.*, vol. 45, no. 2, pp. 805–815, Mar./Apr. 2009.  
 [16] C. J. Melhorn, T. D. Davis, and G. E. Beam, "Voltage sags: Their impact on the utility and industrial customers," *IEEE Trans. Ind. Appl.*, vol. 34, no. 3, pp. 549–558, May/Jun. 1998.  
 [17] A. Tuladhar, T. Unger, and K. Mauch, "Control of parallel inverters in distributed ac power systems with consideration of line impedance effect," *IEEE Trans. Ind. Appl.*, vol. 36, no. 1, pp. 131–138, Jan./Feb. 2000.  
 [18] *American National Standard for Electrical Power Systems and Equipment, Voltage Ratings (60 Hertz)*, ANSI c84.1-1995, 1995.  
 [19] *Voltage Characteristics of Electricity Supplied by Public Distribution Systems*, EN50160, 2011.  
 [20] *Electromagnetic Compatibility (EMC) Part 4-30: Testing and Measurement Techniques and Power Quality Measurement Methods*, IEC 61004-30, 2003.  
 [21] J. P. R. A. Mello, C. B. Jacobina, and M. B. d. Rossiter Corrêa, "Three-phase four-wire inverters based on cascaded three-phase converters with four and three legs," *IEEE Trans. Ind. Appl.*, vol. 53, no. 6, pp. 5539–5552, Nov./Dec. 2017.  
 [22] M. Bongiorno, J. Svensson, and A. Sannino, "An advanced cascade controller for series-connected VSC for voltage dip mitigation," *IEEE Trans. Ind. Appl.*, vol. 44, no. 1, pp. 187–195, Jan./Feb. 2008.  
 [23] V. Khadkikar and A. Chandra, "UPQC-S: A novel concept of simultaneous voltage sag/swell and load reactive power compensations utilizing series inverter of UPQC," *IEEE Trans. Power Electron.*, vol. 26, no. 9, pp. 2414–2425, Sep. 2011.  
 [24] V. Khadkikar and A. Chandra, "A novel structure for three-phase four-wire distribution system utilizing unified power quality conditioner (UPQC)," *IEEE Trans. Ind. Appl.*, vol. 45, no. 5, pp. 1897–1902, Sep./Oct. 2009.  
 [25] A. Al-Zamil and D. Torrey, "A passive series, active shunt filter for high power applications," *IEEE Trans. Power Electron.*, vol. 16, no. 1, pp. 101–109, Jan. 2001.  
 [26] G. A. D. A. Carlos, C. B. Jacobina, and E. C. dos Santos, "Investigation on dynamic voltage restorers with two dc links and series converters for three-phase four-wire systems," *IEEE Trans. Ind. Appl.*, vol. 52, no. 2, pp. 1608–1620, Mar./Apr. 2016.  
 [27] A. Luna *et al.*, "Grid voltage synchronization for distributed generation systems under grid fault conditions," *IEEE Trans. Ind. Appl.*, vol. 51, no. 4, pp. 3414–3425, Jul./Aug. 2015.  
 [28] A. Suárez-González, P. García, Á. Navarro-Rodríguez, G. Villa, and J. M. Cano, "Sensorless unbalance correction as an ancillary service for LV 4-wire/3-phase power converters," in *Proc. IEEE Energy Convers. Congr. Expo.*, Oct. 2017, pp. 4799–4805.  
 [29] J. C. Vasquez, J. M. Guerrero, M. Savaghebi, J. Eloy-Garcia, and R. Teodorescu, "Modeling, analysis, and design of stationary-reference-frame droop-controlled parallel three-phase source inverters," *IEEE Trans. Ind. Electron.*, vol. 60, no. 4, pp. 1271–1280, Apr. 2013.  
 [30] G. C. Paap, "Symmetrical components in the time domain and their application to power network calculations," *IEEE Trans. Power Syst.*, vol. 15, no. 2, pp. 522–528, May 2000.  
 [31] P. García, M. Sumner, Á. Navarro-Rodríguez, J. M. Guerrero, and J. García, "Observer-based pulsed signal injection for grid impedance estimation in three-phase systems," *IEEE Trans. Ind. Electron.*, vol. 65, no. 10, pp. 7888–7899, Oct. 2018.  
 [32] M. Saad *et al.*, "A dq-domain impedance measurement methodology for three-phase converters in distributed energy systems," *Energies*, vol. 11, no. 10, 2018, Art. no. 2732. [Online]. Available: <http://www.mdpi.com/1996-1073/11/10/2732>  
 [33] F. Briz, P. García, M. W. Degner, D. Díaz-Reigosa, and J. M. Guerrero, "Dynamic behavior of current controllers for selective harmonic compensation in three-phase active power filters," *IEEE Trans. Ind. Appl.*, vol. 49, no. 3, pp. 1411–1420, May/Jun. 2013.



**Andrés Suárez-González** (S'16) received the M.Sc. degree in electrical engineering from the University of Oviedo, Gijón, Spain, in 2011, and the M.Sc. degree in wind power systems from Aalborg University, Aalborg, Denmark, in 2012. He is working toward the Ph.D. degree in electrical engineering with the LEMUR Research Team, University of Oviedo.

From 2012, he was a Research Assistant with the University of Oviedo until 2013, when he joined the Department of Smart Grids of Iberdrola Ingeniería y Construcción, as R&D Engineer. In 2015, he joined LEMUR Research Team, University of Oviedo. His research interests include control of power converters, parameter estimation, microgrids, and power quality.



**Pablo García** (S'01–A'06–M'09) received the M.S. and Ph.D. degrees in electrical engineering and control from the University of Oviedo, Gijón, Spain, in 2001 and 2006, respectively.

In 2004, he was a Visitor Scholar with the Electric Machines and Power Electronics Consortium, University of Madison–Wisconsin, Madison, WI, USA. In 2013, he was a Visiting Scholar with the University of Nottingham, Nottingham, U.K. He has coauthored more than 20 IEEE journals and 50 international conferences. He is currently an Associate Professor with the Department of Electrical, Electronics, Computer, and Systems Engineering, University of Oviedo. His research interests include control of grid-tied converters, parameter estimation, energy conversion, ac drives, sensorless control, ac machine diagnostics, and signal processing.



**Ángel Navarro-Rodríguez** (S'15) received the B.Sc. (Hons.) degree in telecommunications engineering from the University of Castilla–La Mancha, Ciudad Real, Spain, in 2012, and the M.Sc. degree in electrical energy conversion and power systems from the University of Oviedo, Gijón, Spain, in 2014. He is currently working toward the Ph.D. degree with the Department of Electrical, Computer, and Systems Engineering, University of Oviedo, granted by the Government of Principado de Asturias.

Since 2014, he has been a part of the LEMUR Research Team, University of Oviedo. His research interests include energy storage systems, control systems, electronics, power electronic converters, microgrids, power quality, and renewable energies.



**Geber Villa** (S'17) received the B.Sc. degree in electronics and control engineering, the M.Sc. degree in electrical energy conversion and power systems, and the M.Sc. degree in industrial engineering from the University of Oviedo, Gijón, Spain, in 2011, 2016, and 2017, respectively. He is currently working toward the Ph.D. degree in electrical engineering with the LEMUR Research Team, University of Oviedo.

He has coauthored several IEEE international conference papers. His research interests include analysis and control of power converters, energy storage systems, and microgrids.

Mr. Villa received the Spanish National Award for the Outstanding Graduate of the Year in 2014 and a Spanish Predoctoral Grant for the formation in university teaching (Formación de Profesorado Universitario) in 2017.



**Jose M. Cano** (M'98) was born in Oviedo, Spain, in 1971. He received the M.Sc. and Ph.D. degrees in electrical engineering from the University of Oviedo, Gijón, Spain, in 1996 and 2000, respectively.

In 1996, he joined the Department of Electrical Engineering, University of Oviedo, where he is currently an Associate Professor. In 2012 and 2014, he held appointments as a Visiting Associate Professor with the Department of Electrical and Computing Engineering, University of British Columbia, Vancouver, BC, Canada. His main research interests include power quality solutions for industry, power converters, distributed generation, and smart grids.

Dr. Cano has been an Associate Editor for *IET Power Electronics* since 2017.

## **F.2 Variable Switching Frequency Control of Distributed Resources for Improved System Efficiency**



## Variable Switching Frequency Control of Distributed Resources for Improved System Efficiency

José M. Cano , Member, IEEE, Ángel Navarro-Rodríguez , Student Member, IEEE, Andrés Suárez , Student Member, IEEE, and Pablo García , Member, IEEE

**Abstract**—This contribution explores the possibility of improving the global efficiency of three-phase inverter-based distributed resources (DR) embedded in low-voltage distribution feeders, by the adaptation of their switching frequency (SF) to the operation point of both the converter and local loads. The core of this proposal lies on the fact that in a good number of applications, in both service and residential sectors, the owner of the DR is also in charge of the losses caused in the local electric power system. This fact leaves room for a global optimization of the power losses, i.e., converter losses will be considered together with those losses caused by the current harmonics injected into the local grid. A dynamic adaptive SF frame of the DR is considered in this proposal to allow its operation beyond its rated frequency at light loads, subjected to the thermal constraints of the device. Simulation results obtained using PLECS software as well as an experimental validation of the method are included.

**Index Terms**—Distributed resources (DR), efficiency, power losses, variable switching frequency (SF), voltage source converters (VSCs).

### I. INTRODUCTION

THE SOARING use of inverters in distributed generation and energy storage applications has increased the attention paid to the efficiency of these devices in recent years. The efficiency of power converters interconnected to the energy power system (EPS) is influenced by regulations, such as [1], which states limits for the harmonic current injection of these devices at the point of common coupling (PCC). In prevailing applications, such as solar and wind, power converters operate rarely at rated values, being the efficiency at light loads a source of great concern [2], [3]. According to [4], the tests to comply with [1], takes only into account the first 40 harmonics. This

allows using relatively low switching frequencies (SFs), typically higher than 3 kHz, since the high-frequency harmonics induced by pulsewidth modulation (PWM) will be in this case over the stated limit.

The efficiency of the inverter as a separate unit is the only concern of the owner of the distributed resource (DR) when he is not responsible for the losses upstream. In this case, once verified that the selected SF complies with the harmonic emission limits, it can be maintained constant at any operating condition. In most cases, increasing the SF reduces the efficiency of the device due to the rise of the converter switching losses, while decreasing this parameter could make the device not conform with [4]. Notice that the tests must be conducted not just at 100% but also at 66% and 33% of the output rated current. Most of the efforts carried out in recent years by power electronics researchers in the quest for higher efficiency applications are founded on this concept that treats the DR as a separate unit. Thus, a good number of studies propose alternative power topologies for the grid-tie inverter or for the internal dc-dc stages of the DR, as a way of obtaining improved efficiency [5]–[7]. Other authors focus their approach in advance modulation schemes [8]–[10] or new power electronic devices [11], [12]. The improvement of the DR efficiency by optimizing the interaction between the grid-tie converter and the generation/storage stage is also a widely used approach, e.g., maximum power point tracking methods in wind turbines and photovoltaic (PV) solar systems [13], [14].

In a good number of common applications used in residential buildings and connected to the low-voltage (LV) grid, the owner of the DR is also responsible for the local losses caused by the inverter current harmonics both in line and local loads, up to the metering location at the distribution transformer (either on the LV or medium voltage (MV) side). In assessing the efficiency of the DR in this scenario, the inverter losses should be taken into account together with the distortion losses caused in the local grid [15]. The increasing penetration of DRs has driven power system researchers to deal with efficiency issues in their interconnection to the power grid. Thus, numerous studies can be found with the aim of optimizing the dispatch of these resources in the search of a coordinated behavior [16]–[19], and with the objective of optimizing their location in order to minimize power losses [20], [21]. However, the location of LV DRs is mostly driven by decentralized initiatives, so the assumption of a given site has to be considered in most of the scenarios. In the optimal dispatch approach, convenient active and reactive commands are provided to DRs based on a coordinated operation,

Manuscript received October 30, 2017; revised March 14, 2018; accepted May 9, 2018. Date of publication May 14, 2018; date of current version September 17, 2018. Paper 2017-IPCC-1126.R1, presented at the 2016 IEEE Energy Conversion Congress and Exposition, Milwaukee, WI, USA, Sep. 18–22, and approved for publication in the IEEE TRANSACTIONS ON INDUSTRY APPLICATIONS by the Industrial Power Converter Committee of the IEEE Industry Applications Society. This work was supported in part by the Spanish Government Innovation Development and Research Office (MEC) under research Grant ENE2014-52272-R, Grant ENE2016-77919-R, and Grant DPI2017-89186-R; and in part by the Predoctoral Grant ID BP14-135 under the program Severo Ochoa for the formation in research and university teaching of Principado de Asturias PCTI-FICYT. (Corresponding author: Jose M. Cano.)

The authors are with the Department of Electrical Engineering, University of Oviedo, Gijón 30204, Spain (e-mail: jmcano@uniovi.es; navarroangel@uniovi.es; suarezandres@uniovi.es; garciafpablo@uniovi.es).

Color versions of one or more of the figures in this paper are available online at <http://ieeexplore.ieee.org>.

Digital Object Identifier 10.1109/TIA.2018.2836365

but harmonic losses and, even less, internal operational features of the converters, such as the SF, are totally neglected. In this paper, the optimization of the efficiency of the DR within the local EPS, based on the adaptation of the SF used in the modulation scheme of the grid-tie converter, is analyzed. This is proposed as a convenient approach for LV applications in which the large impedance of the transformer at high frequencies allows to assume that most of the power losses are under the responsibility of the DR owner. This new approach has the potential to exist together with high-level controllers at the system level, or to be applied to standard converters just relying on local intelligence. Even if by design, a thermal constraint in the increment of the SF at rated power is likely to exist, the possibility of operating the device at higher frequencies when working at light loads is still there. Increasing the SF rises the converter switching losses but reduces the distortion losses in the local grid at the same time. This fact, together with the great advances carried out in recent years in the field of grid impedance estimation techniques [22]–[27], opens the door for a dynamic optimization of the SF capable of achieving an improved overall efficiency.

In Section II, a study of the effect of the SF on the harmonic emission in three-phase voltage source converters (VSCs) is carried out. Two-level inverters with first-order inductive filters are considered, as one of the preferred technologies in LV applications. The evaluation of inverter losses, considering thermal constraints, is presented in Section III. Section IV deals with the estimation of the distortion losses caused by the inverter in the local grid. The proposed method for the online optimization of the SF is described in Section V. Section VI presents a case study to demonstrate the validity of the proposal and experimental results are given in Section VII. Finally, the conclusions of the study are drawn in Section VIII.

## II. SF AND CURRENT HARMONICS

As a general rule, increasing the SF leads to a displacement of the harmonic spectrum of the voltage at the converter terminals to a higher frequency range. Consequently, the inductive behavior of the filter and grid upstream yields to a reduction in the induced current harmonics due to the higher impedance of these inductances at the new frequencies. However, it is important to note that the dead-time of the IGBTs limits the validity of the said statement, leading to the emergence of low-frequency harmonics (mainly 5th and 7th order) [28], [29] with a growing impact at higher SFs. Nevertheless, this effect can be mitigated by current regulators, whose bandwidth use to fall within these values. Fig. 1 shows the current distortion of an inverter given by the parameters shown in Table I as a function of the SF. According to the standard, [1], this value has been reported as the total rated-current distortion ( $TRD$ ), where

$$TRD = \frac{\sqrt{\sum I_i^2}}{I_n} \quad (1)$$

which can be defined as the total root sum square of the current harmonics injected by the DR unit  $I_i$ , divided by the rated current capacity of that unit,  $I_n$ . In Fig. 1, the  $TRD$  has been split in two terms,  $TRD_{lf}$  and  $TRD_{hf}$  using the 40th harmonic included

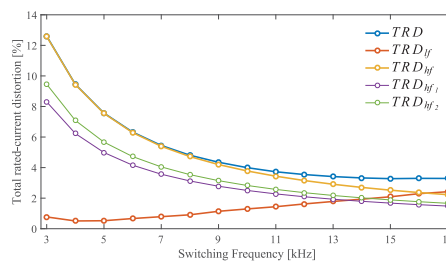


Fig. 1. Current  $TRD$  as a function of the SF for different frequency bands. Effect of the dead-time in low-frequency harmonics.

TABLE I  
CONVERTER PARAMETERS

Hardware	
Grid voltage	$V_{rms} = 400$ V, $f = 50$ Hz
Rated power/current	$S = 30$ kVA, $I_n = 43.3$ A
System impedance	Direct coupling to an ideal grid
Coupling inductor	$L_{filter} = 1.0$ mH, $R_{filter} = 0.16$ m $\Omega$
DC link	$v_{dc} = 800$ V, $C = 350$ $\mu$ F
IGBT modules	2MBI200HH-120-50
Dead-time	$t_d = 1$ $\mu$ s
Control	
PWM Type	Sym. regular sampled w/ 3 <sup>rd</sup> harm. injection
SF at rated power	$f_{sw} = 3$ kHz
PLL	Dual 2 <sup>nd</sup> Order Generalized Integrator (SOGI)
Anti-aliasing filter	Butterworth 2 <sup>nd</sup> order, $f_c = f_{sw}/2$
Current reg. bandwidth	300 Hz
Power factor	1

in [4] as a limit between low and high frequencies. Thus, those parameters can be related as

$$TRD = \sqrt{TRD_{lf}^2 + TRD_{hf}^2} \quad (2)$$

which allows us to show the different behavior of the theoretical PWM harmonics and the nonidealities induced by the dead-time. As it is shown in Fig. 1, the effect of the dead-time reaches such an importance in  $TRD$  that increasing the SF over a certain limit becomes counterproductive. The use of dead-time compensation techniques [30], [31] could potentially raise this limit. It is also interesting to point out that the results shown in Fig. 1 are independent of the load of the converter, as only the fundamental component varies on a significant scale with the SF. On the contrary, and especially in weak grids, the values shown in this graph can be affected to some extent by the impedance of the system upstream from the converter terminals, which is referred to as *system impedance* throughout this paper. This suggests that an online measurement of harmonic distortion will provide better results than a theoretical estimation. Nonetheless, the simplicity of this estimation can be valuable in most cases.

## III. CONVERTER LOSSES AND THERMAL LIMITS

Converter losses,  $P_{VSC}$ , are mainly determined by switching losses,  $P_{sw}$ , and conduction losses,  $P_{cd}$  [11], [32], [33]. Other issues should be considered when assessing the efficiency of

4614

IEEE TRANSACTIONS ON INDUSTRY APPLICATIONS, VOL. 54, NO. 5, SEPTEMBER/OCTOBER 2018

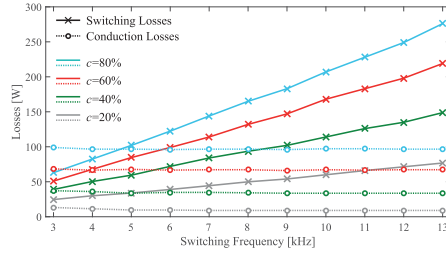


Fig. 2. Converter switching and conduction losses as a function of the SF.

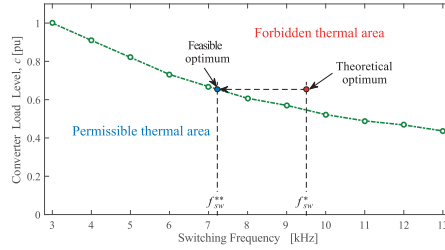


Fig. 3. Thermal constraints for variable SF operation.

these devices, such as cooling power; however, as they are not normally affected by the SF, they will not be considered in this paper. Switching losses are strongly influenced by the SF,  $f_{sw}$ , as well as by the load level of the converter  $c$ , defined as the ratio between the actual and rated current. Even if the power factor of the converter also affects this parameter due to variations in the commutation phenomenon, this effect is hardly noticeable and can be neglected with little error for the aim of this study. As increasing the SF results in a proportional rise of switching events, the relationship between the SF and switching losses is almost lineal. Conduction losses, for its part, are mainly affected by the load of the converter, and in a more subtle way, by the SF due to the increased current distortion that arises at lower frequencies. Taking these facts into consideration, an approach to the converter losses, with  $c$  and  $f_{sw}$  as parameters, can be obtained by using

$$P_{VSC}(c, f_{sw}) = P_{sw}(c, f_{sw}) + P_{cd}(c, f_{sw}). \quad (3)$$

The assessment of the aforementioned power losses for the specific IGBT power modules mounted in the converter used for the experimental validation included in Section VII is shown in Fig. 2. To obtain the graph, a PLECS model of the converter was implemented [34]. This model includes the thermal performance of the IGBT power modules, which allows to depict the operational constraints of the converter in terms of SF. Thus, the imperative derating of the device is shown in Fig. 3. This figure was calculated for each SF by assessing the load level of the converter at which the junction temperature of the solid

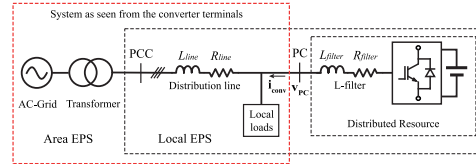


Fig. 4. Local EPS with embedded DRs.

state devices equals the temperature reached at rated values. The inclusion of these data in a two-dimensional (2-D) look-up table (LUT), together with the use of interpolation, is enough to obtain a good estimation of converter losses as a function of  $c$  and  $f_{sw}$  in the optimization scheme proposed in this paper. The exploitation of this table for control purposes by operating the converter at variable SF is analyzed in Section V. In any case, it is clear from Fig. 3 that, if the SF command  $f_{sw}^*$  lies on the forbidden area of the graph, it has to be reduced to the nearest feasible value,  $f_{sw}^{**}$ .

#### IV. DISTORTION LOSSES IN THE LOCAL GRID

Even if limited by regulations, the injection of current harmonics into the distribution grid can cause significant power losses that are classified in the following two categories: First, copper losses in the distribution line and distribution transformer, and second, power losses in local loads. Notice that additional losses could exist upstream from the distribution transformer that are not on the local EPS owner's responsibility. However, this term can be neglected, not only because of the low value of the resistive contribution from the MV level when compared with the LV side, but also because of the low capability of high-order current harmonics to travel deep into the EPS. Fig. 4 shows a layout of the benchmark system considered in this paper. The local EPS, with embedded DRs, is connected to the area EPS through a distribution transformer, being the metering devices connected either in the MV or LV side according to the ownership of this piece of equipment. Both the DRs and the local loads are connected to the distribution line. Those local loads located close to the power converters are more prone to suffer from distortion losses. In Fig. 4, a local load is connected directly to the DR point of coupling (PC) to highlight this phenomenon. The effect of the distortion power in local loads is different according to the type of device (motor, lighting, heating, etc.) and its nature (linear/nonlinear). In any case, distortion power can be, as a general rule, considered undesirable [35]. Different types of penalization criteria could be considered in order to take into account the harmful effects of higher levels of injected current distortion in particular loads, e.g., cost associated to the loss of life. However, in this paper, only the cost associated with the power transmitted at the non-fundamental frequency is taken into account. A pure resistive load is considered in this paper as the easiest way to underline the benefits of the proposal.

A precise calculation of the power transmitted by the converter at harmonic frequencies can be done by assessing the

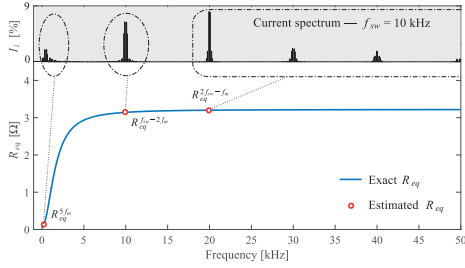


Fig. 5. Estimation of the resistive component of system impedance at the PC as a function of frequency.

TABLE II  
INSTALLATION PARAMETERS

<b>Transformer</b>	
Rated power	$S_n = 100$ kVA
Short-circuit impedance & resistance	$Z_{pu} = 0.06, R_{pu} = 0.01$
<b>Distribution Line</b>	
Length	$l = 200$ m
Resistance	$R_{line} = 0.2$ mΩ/m
X/R ratio	0.32
<b>Local Loads</b>	
Power factor	1
Active power	$P = 50$ kW

expression

$$P_{losses} = Re \left\{ \sum_{i=2}^N \mathbf{v}_{PCi} \cdot \mathbf{i}_{conv i}^* \right\} \quad (4)$$

where  $\mathbf{i}_{conv i}$  and  $\mathbf{v}_{PCi}$  are the power invariant space vector harmonic components of the converter current and voltage at its PC, obtained by applying the direct Fourier transform (DFT). For the practical implementation of (4), natural sampling of voltages and currents at SF is not enough due to Nyquist limit, but oversampling can help in complying with these requirements. In any case, other simplified methods, such as Goertzel algorithm [36], are better suited for online applications [37], [38]. In this numerically efficient method, just a selected set of harmonics are identified, which can be enough to calculate the resistive component of system impedance,  $R_{eq}$ , at the most relevant bands of the spectrum. This reduced set of values can be used, together with the expected injection of current harmonics given in Fig. 1, to formulate a good estimation of the aforementioned power losses. Fig. 5 shows the value of  $R_{eq}$  for the installation depicted in Fig. 4 considering the parameters shown in Table II. The identification of just three impedance values, one at the low-frequency range (5th or 7th) and two at the two lowest PWM frequency bands (e.g.,  $f_{sw} - 2f_m$  and  $2f_{sw} - f_m$ ,  $f_m$  being the modulation frequency), can be enough to estimate distortion losses by using

$$P_{losses} \approx 3I_n^2 \cdot \left( R_{eq}^{5f_m} \cdot TRD_{if}^2 + R_{eq}^{f_{sw}-2f_m} \cdot TRD_{hf_1}^2 + R_{eq}^{2f_{sw}-f_m} \cdot TRD_{hf_2}^2 \right). \quad (5)$$

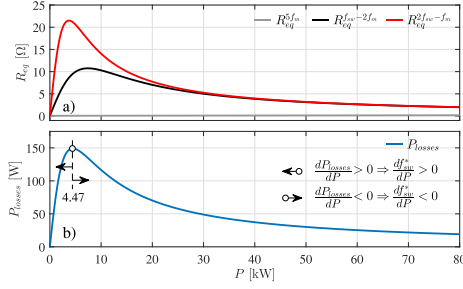


Fig. 6. Effect of the power demand of local loads in harmonic power losses. (a) Resistive component for the frequencies of interest ( $f_{sw} = 10$  kHz,  $f_m = 50$  Hz). (b) Harmonic power losses.

Notice that with this aim,  $TRD_{hf}$  has been segregated in two components:  $TRD_{hf_1}$ , for the harmonic band around the SF and  $TRD_{hf_2}$ , for the rest of higher frequency values. The specific contribution of each of these components can be observed in Fig. 1.

It is important to highlight that the effect of a variation in the power demand,  $P$ , of the loads connected to the local EPS, on the harmonic power losses at the line and local loads,  $P_{losses}$ , is not obvious. As a consequence, neither is the effect of this variation on the resulting optimum SF. The value of the resistive components of system impedance for the benchmark system shown in Fig. 4 are the result of the parallel equivalent represented by the RL branch of the line and transformer and the resistive branch represented by the local loads. For the data shown in Table II, the value of these resistive components for the frequencies of interest is depicted in Fig. 6 as a function of  $P$ . At low power demand levels, the connection of new loads increases harmonic power losses. On the contrary, beyond a certain power demand, 4.47 kW in the present case, the connection of new loads decreases the resistive value of system impedance, and thus, harmonic power losses. For this reason, if the DR is working at a fixed load level,  $c$ , with a low power demand of local loads, the connection of new loads drives the optimum SF to higher values in search for a lower level of harmonic losses. Conversely, up from the stated power demand value, the connection of new loads leads to a reduction of the optimum SF value, as higher harmonic losses can be admitted in the search for a global optimum.

## V. ONLINE OPTIMIZATION OF THE SF

The fundamentals of the online optimization of the SF proposed in this paper are schematically summarized in Fig. 7. The inputs for the algorithm are as follows: first, the space vector of the converter current, which is already available as calculated from current samples for the operation of its inner controller, and second, the resistive component of system impedance for the different frequency bands considered in Section IV. The application of a set of LUTs together with a SF sweep allows the

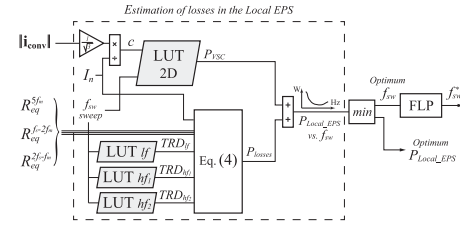


Fig. 7. Online method for the optimization of the SF.

online calculation of a curve, relating the losses at the local EPS,  $P_{\text{local\_EPS}}$ , with the SF,  $f_{\text{sw}}$ , for the present operating point. With this aim, the converter losses,  $P_{\text{VSC}}$ , are obtained from a 2-D-LUT built by adding the conduction and switching losses of the specific converter according to (3). A set of three 1-D-LUTs, built from the distortion data depicted in Fig. 1, provides the TRD of the converter at the different frequency bands for each SF used in the sweep. From these results, the losses at the line and local loads,  $P_{\text{losses}}$ , are obtained by using (5). The addition of both converter losses and line and local load losses at each SF leads to the desired curve. Then, the minimum of this curve is identified, which gives the optimum losses at the local EPS and, even more important, the optimum SF for the current operating point. Notice that the bandwidth of the SF command,  $f_{\text{sw}}^*$ , must be much lower than the one used in the inner controllers of the inverter not to interfere with its dynamic performance. As a consequence, a low update rate of this command is acceptable and the required computational burden can be assumed by the controller without a significant effort either in a synchronous or asynchronous scheme. In order to avoid the effect of noise in the sampled parameters, as well as steep frequency variations due to sudden changes in the inverter load level or in the system impedance—due to the connection/disconnection of local loads, a first-order low-pass (FLP) filter is used to smooth the frequency command.

Although not depicted in Fig. 7 for the sake of clarity, the frequency command,  $f_{\text{sw}}^*$ , should pass a final limitation stage in order to make the control compatible with the thermal constraints shown in Fig. 3. As already stated in Section III, if the pair  $(f_{\text{sw}}^*, c)$  lies in the forbidden area of this graph, the SF command is reduced to the maximum SF compatible with the present converter load level,  $f_{\text{sw}}^{**}$ .

VI. CASE STUDY

In this section, a case study is used to illustrate the advantages of using an overall efficiency optimization of the DR within its local EPS. With this aim, the LV distribution feeder and the distributed generator (DG) depicted in Fig. 4 are considered. The parameters of the grid infrastructure are shown in Table II while those from the inverter-based DG are given in Table I (except for the system impedance, that for this case study is derived from Table II). Fig. 8 shows the total losses in the local EPS, together with its different components, i.e., converter losses and

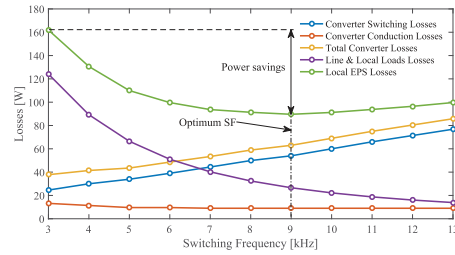


Fig. 8. Local EPS losses as a function of SF –  $c = 20\%$ .

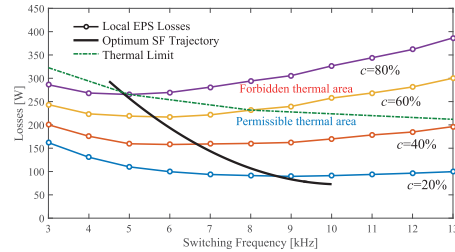


Fig. 9. Optimum trajectory of the SF as a function of converter load.

grid and local loads losses for a DR working at 20% of its rated power with unity power factor. It is concluded from this drawing that increasing the SF from the design parameter, 3 to 9 kHz, reduces the local EPS losses in a 44.6%, and improves the overall efficiency at this load level (i.e., the ratio between the local EPS losses and the power delivered by the converter) in 1.20%.

Fig. 9 expands the analysis to different load levels of the DR. As it is depicted in this figure, connecting the values of the minimum local EPS losses at each converter load level,  $c$ , leads to the optimum trajectory of the inverter SF. Furthermore, the thermal limit of the device is also given in Fig. 9. This limit is established by calculating the maximum acceptable SF at each load level, which is determined by the frequency that leads to the design temperature (i.e., the one obtained at 3 kHz and rated power). From the aforementioned graph, it can be concluded that for the device under test, a variable SF mode with optimization of losses is only feasible for loads lighter than 80% of rated power. Moreover, it is also observed that the benefit of the proposal is much more relevant at light loads: e.g., the saved power is higher at 20% than at 80% on both relative and absolute terms (72 W versus 21 W and 1.20% versus 0.09%).

Fig. 10 shows simulation results of the application of the online optimization method proposed in Section V to the present case study. An update rate of 10 ms was used for the SF command and a bandwidth of 0.6 Hz was selected for the FLP filter. The SF sweep included in the algorithm is conducted with a resolution of 100 Hz in order to limit the computational burden.

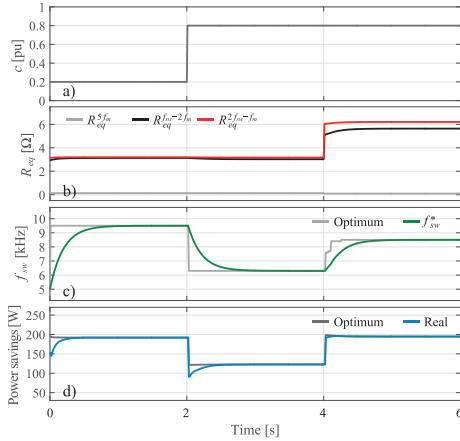


Fig. 10. Application of the optimization method to the proposed case study. (a) Converter load profile. (b) System impedance. (c) SF command. (d) Power savings.

As it is shown in Fig. 10(a), the converter load level is started at  $c = 20\%$  and increased to  $c = 80\%$  after 2 s, always with unity power factor. Moreover, the local loads stay at rated power according to Table II and are reduced to 50% of this value, i.e., 25 kW at 4 s. Fig. 10(b) shows the effect of the steep variation on the resistive components of system impedance induced by the local load reduction. After the load variation, slight modifications can be still observed on these values, which are caused by the SF drift along the process, due to the influence of reactive components on the resistive equivalent. The optimum SF value obtained by the algorithm along with the final SF command, i.e., after the FLP, is depicted in Fig. 10(c). The converter is started with a conservative SF value of 5 kHz and, from this instant, the algorithm competently tracks the optimum SF increasing the efficiency of the installation. As predicted in Fig. 6, the reduction of the power demand of local loads from 50 to 25 kW at 4 s leads to a rise of the optimum SF. In Fig. 10(d), the optimum and real power savings, compared to a traditional operation of the DR at constant SF, are depicted. As expected, greater power savings are obtained with the converter working at light loads as well as with an increased value of the resistive component of system impedance.

## VII. EXPERIMENTAL RESULTS

Two sets of experimental tests were carried out in this paper: the first one is aimed to prove the power saving potential of the stated proposal, and the second, to demonstrate the validity of the online SF optimization method described in Section V.

### A. Test 1

The test setup used in this case is shown in Fig. 11. A four-quadrant grid simulator, TC.ACS by Regatron, is used to

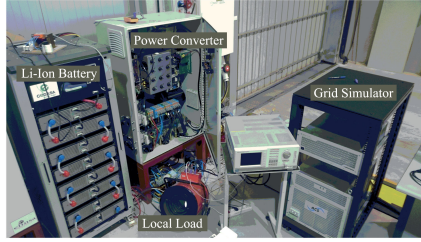


Fig. 11. Test setup.

emulate the electric system, 400 V – 50 Hz, and a 0.32 mH inductor,  $L_1$ , is used to emulate the LV line and transformer according to Fig. 4. An almost purely resistive air-heating system with a rated power of 9 kW is used to emulate the local loads according to the figure. Finally, a custom-made three-phase two-level VSC, with a rated power of 30 kVA and a design SF of 6 kHz, is coupled to the grid through a 0.88 mH inductor,  $L_2$ , to play the role of the DR.

During this test the converter is operated in STATCOM mode at a light load, 10 kVA (i.e.,  $c = 33\%$ ), delivering reactive power to the LV grid. Similar results are expected from other operation modes, due to the small influence of the power factor in converter losses, as it was stated in Section II. The three-phase voltages and currents at the PC of the DR, PC in Fig. 4, were registered in steady state for different SFs within the range 6 – 16 kHz. An offline handling of these measurements were carried out to calculate their DFT, and subsequently, the losses at harmonic frequencies at the line and local loads (i.e., those caused by the air-heating system and parasitic resistance of  $L_1$ ) were calculated by the application of (4). For the particular case of the STATCOM operation mode, including the term at the fundamental frequency in (4) leads directly to the converter losses, so finally, the losses at the local EPS can be computed in a simple way as

$$\begin{aligned}
 P_{Local.EPS} &= Re \left\{ \sum_{i=2}^N \mathbf{v}_{PCi} \cdot \mathbf{i}_{conv i}^* \right\} \\
 &\quad - Re \left\{ \sum_{i=1}^N \mathbf{v}_{PCi} \cdot \mathbf{i}_{conv i}^* \right\} \\
 &= -Re \left\{ \mathbf{v}_{PC1} \cdot \mathbf{i}_{conv 1}^* \right\}. \quad (6)
 \end{aligned}$$

Notice that this is just a particular result valid only for STATCOM operation mode. As stated in Section III, in a more general scheme in which the DR participates in the active power flow (inverter/rectifier mode), a LUT, with and estimation of converter losses as a function of the SF and the converter load level, ought to be used.

The results of the test are presented in Table III and Fig. 12. Thus, the spectra of the power invariant space vectors of voltage and current, at the PC of the DR, are shown in Fig. 12 for selected key SFs, such as 8, 12, and 16 kHz. Both the positive and negative sequence components are displayed in this image.

TABLE III  
EXPERIMENTAL RESULTS -  $c = 33\%$

SF	Losses			Pwr. savings
	Converter	Line&Loads	Local EPS	
6 kHz	781.2 W	253.8 W	1035.0 W	0.0 W
8 kHz	790.5 W	178.4 W	968.9 W	66.1 W
10 kHz	814.0 W	139.8 W	953.8 W	81.1 W
12 kHz	836.3 W	111.2 W	947.6 W	87.5 W
14 kHz	868.1 W	91.6 W	959.7 W	75.3 W
16 kHz	896.9 W	76.9 W	973.8 W	61.2 W

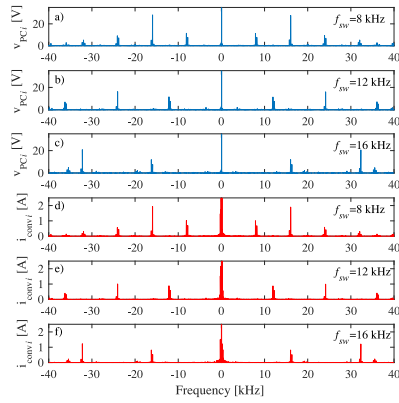


Fig. 12. Spectrum of signals measured at the PC for different SFs. (a), (b), and (c): Voltage space vector for 8, 12, and 16 kHz, respectively. (d), (e), and (f): Current space vector for 8, 12, and 16 kHz, respectively. Note: Fundamental components are truncated for the sake of clarity.

The most significant harmonics, located in bands around one and two times  $f_{sw}$ , are shifted to higher frequencies as the SF increases. Also, a clear reduction in the injection of harmonic currents can be observed at higher SFs. In Table III, the computed values for converter losses, line and load losses, and local EPS losses for each of the analyzed SFs are displayed, together with the resulting power savings. Specifically, harmonic power losses at the line and loads are calculated by using (4), while the application of (6) allows the computation of the local EPS losses. Both equations take the voltage and current harmonics of Fig. 12 as an input. Finally, the difference between the results from (6) and (4) gives the value of converter losses. As expected, an optimum SF is obtained, capable of achieving the minimization of system losses. As it is highlighted in Table III, the operation at 12 kHz reduces the overall system losses in 87.5 W when compared with the operation at the design value. This means a reduction of around 8.4% of the losses at this operation point ( $c = 33\%$ ), and thus, an improvement of the local EPS efficiency, which increases from 89.65% to 90.52%.

B. Test 2

Slight changes are introduced in the test setup for this case. The 30 kVA converter is now operated in inverter mode to effectively replicate the performance of a DR. With this aim, the

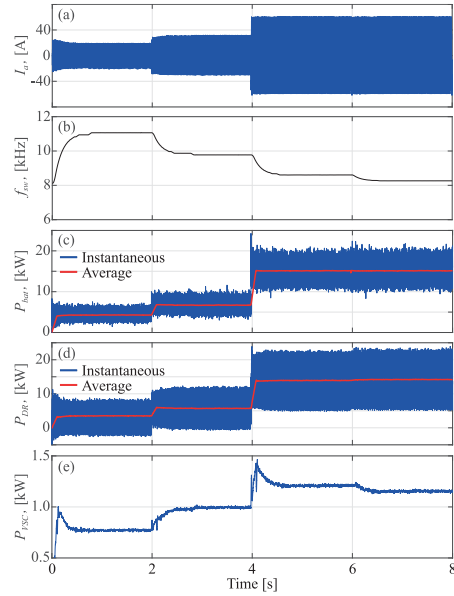


Fig. 13. Online SF optimization test. (a) Converter ac current—phase a. (b) Converter SF. (c) Power supplied by the Li-Ion battery—dc-dc converter output side. (d) Power supplied to the grid. (e) Converter losses.

dc bus of the converter is fed from the Li-Ion battery shown in Fig. 11 through a dc-dc stage. Furthermore, the converter is now coupled to the utility grid, 400 V -50 Hz, through a dedicated distribution line and transformer according to the values shown in Table II. Three separate air-heating systems, each with a rated power of 9 kW, are used to emulate the local loads. The connection/disconnection of these systems allows to test the effect of a sudden change in system impedance.

The custom-made converter is operated through a controller using a TI C2000 Delfino TMS320F28335 MCU. The algorithm described in Section V was included in the firmware with the LUT system embedded in nonvolatile RAM memory. Moreover, a variable SF inner current controller for the converter was specifically designed for this test, including an adaptive tuning of the associated regulators.

During the test, the dc-dc converter is commanded with different power steps, as shown in Fig. 13(d), while the VSC fixes a constant dc-bus voltage value of 800 V and a constant power factor of 0.6. The test is started at a light load, 7.5 kVA (i.e.,  $c = 25\%$ ), thus delivering 4.5 kW to the grid, while two of the 9-kW air-heating devices stay connected to emulate the local loads. After 2 s, the converter load level increases to 12 kVA (i.e.,  $c = 40\%$ ) and then to 27 kVA (i.e.,  $c = 90\%$ ) at time 4 s, so that up to 16.2 kW are injected into the local grid. Fig. 13 shows the phase current of the VSC during these variations together

with the performance of the SF in reaction to those load step changes. Finally, at time 6 s, one air-heating system is added to the two devices already connected to the local grid, thus shifting the local demand from 18 to 27 kW. As predicted in Fig. 6, the consequent change in system impedance at the converter PC causes a reduction of harmonic power losses that leads to a fall in the optimum value of the SF.

Fig. 13 shows the measurements of the power supplied by the Li-Ion battery along the test, together with the power supplied by the VSC to the local grid. Thus, in Fig. 13(c), the VSC losses are obtained. The value of line and local load losses are calculated from voltage and current measurements for each step (considering steady state intervals) through fast Fourier transform analysis, being 92.5, 137.6, 192.0, and 180.6 W, respectively. As expected, during the first three steps, the decreasing SFs lead to increasing line and local load losses. In the fourth step, even if the SF is further reduced, the decline of the Thevenin impedance of the system at the converter PC, due to the connection of a new load, overcomes this effect.

A comparison of the losses at the first step of the test, i.e., the one conducted with a lighter load,  $c = 25\%$ , with those obtained for the same conditions in a fix SF scheme of 6 kHz, reveals that up to 132 W can be saved using the proposed operating mode. This means increasing the efficiency in 1.7% at the present operating point and in 0.4% if referred to the rated power of the converter.

### VIII. CONCLUSION

This paper presents an operation strategy for DRs based on the use of an adaptive SF framework in the grid-tie converter with the aim of achieving an overall improvement of the efficiency within the local EPS. The contribution demonstrates the interest of considering the converter losses together with the induced harmonic losses in the local line and loads when the ownership/operation of both assets is held by the same entity. The proposed method can be applied to DRs relying only on local intelligence but also to those in charge of system-level controllers. The thermal limits of the power modules used in the inverter are taken as a constraint in order to assure a safe operation of the device beyond its design SF when working at light loads. A LUT-based system, valid for an online implementation, was designed to provide the DR with a smart regulation of its SF. The results demonstrate that an improvement of the overall efficiency of the system at light converter loads by about 1% is readily achieved with the proposed method. This improvement is especially important for applications in which the grid-tie converter works often under rated power. This is the usual case of widespread technologies, such as PV systems and small wind turbines.

### REFERENCES

- [1] *IEEE Standard for Interconnecting Distributed Resources With Electric Power Systems*, IEEE Std. 1547-2003, Jul. 2003.
- [2] Z. Chen, H. Wu, K. Sun, L. Ni, and Y. Xing, "Light-load efficiency optimization for module integrated converters in photovoltaic systems," in *Proc. IEEE Energy Convers. Congr. Expo.*, Sep. 2013, pp. 5560–5565.
- [3] V. R. K. Kanamarlapudi, B. Wang, N. K. Kandasamy, and P. L. So, "A new ZVS full-bridge dc-dc converter for battery charging with reduced losses over full-load range," *IEEE Trans. Ind. Appl.*, vol. 54, no. 1, pp. 571–579, Jan./Feb. 2017.
- [4] *IEEE Standard Conformance Test Procedures for Equipment Interconnecting Distributed Resources With Electric Power Systems*, IEEE Std. 1547.1-2005, Jul. 2005.
- [5] Y. H. Liao and C. M. Lai, "Newly-constructed simplified single-phase multistring multilevel inverter topology for distributed energy resources," *IEEE Trans. Power Electron.*, vol. 26, no. 9, pp. 2386–2392, Sep. 2011.
- [6] Y. Zhou and W. Huang, "Single-stage boost inverter with coupled inductor," *IEEE Trans. Power Electron.*, vol. 27, no. 4, pp. 1885–1893, Apr. 2012.
- [7] T. B. Soeiro and J. W. Kolar, "The new high-efficiency hybrid neutral-point-clamped converter," *IEEE Trans. Ind. Electron.*, vol. 60, no. 5, pp. 1919–1935, May 2013.
- [8] O. Onederra, I. Kortabarria, I. M. de Alegria, J. Andreu, and J. I. Grate, "Three-phase VSI optimal switching loss reduction using variable switching frequency," *IEEE Trans. Power Electron.*, vol. 32, no. 8, pp. 6570–6576, Aug. 2017.
- [9] D. Jiang and F. Wang, "Variable switching frequency PWM for three-phase converters based on current ripple prediction," *IEEE Trans. Power Electron.*, vol. 28, no. 11, pp. 4951–4961, Nov. 2013.
- [10] S. Bhattacharya, D. Mascarella, and G. Joos, "Space-vector-based generalized discontinuous pulsewidth modulation for three-level inverters operating at lower modulation indices," *IEEE J. Emerg. Sel. Topics Power Electron.*, vol. 5, no. 2, pp. 912–924, Jun. 2017.
- [11] S. Hazra, S. Madhusoodhanan, G. K. Moghaddam, K. Hatua, and S. Bhattacharya, "Design considerations and performance evaluation of 1200-V, 100-A SiC MOSFET-based two-level voltage source converter," *IEEE Trans. Ind. Appl.*, vol. 52, no. 5, pp. 4257–4268, Sep. 2016.
- [12] J. Rabkowski, D. Pefitis, and H. P. Nee, "Design steps toward a 40-kVA SiC JFET inverter with natural-convection cooling and an efficiency exceeding 99.5%," *IEEE Trans. Ind. Appl.*, vol. 49, no. 4, pp. 1589–1598, Jul./Aug. 2013.
- [13] S. A. M. Saleh, "Testing the performance of a resolution-level MPPT controller for PMG-based wind energy conversion systems," *IEEE Trans. Ind. Appl.*, vol. 53, no. 3, pp. 2526–2540, May 2017.
- [14] X. Li, H. Wen, L. Jiang, W. Xiao, Y. Du, and C. Zhao, "An improved MPPT method for PV system with fast-converging speed and zero oscillation," *IEEE Trans. Ind. Appl.*, vol. 52, no. 6, pp. 5051–5064, Nov. 2016.
- [15] J. M. Cano, A. Suárez, A. Navarro-Rodríguez, and P. García, "Improved efficiency of local EPS through variable switching frequency control of distributed resources," in *Proc. IEEE Energy Convers. Congr. Expo.*, Sep. 2016, pp. 1–7.
- [16] I. Kouveliotis-Lysikatos and N. Hatzigiorgi, "Fully distributed economic dispatch of distributed generators in active distribution networks considering losses," *IET Gener., Transmiss. Distrib.*, vol. 11, no. 3, pp. 627–636, 2017.
- [17] F. Yang and Z. Li, "Improve distribution system energy efficiency with coordinated reactive power control," *IEEE Trans. Power Syst.*, vol. 31, no. 4, pp. 2518–2525, Jul. 2016.
- [18] H. Karami, M. J. Sanjari, S. H. Hosseini, and G. B. Gharehpetian, "An optimal dispatch algorithm for managing residential distributed energy resources," *IEEE Trans. Smart Grid*, vol. 5, no. 5, pp. 2360–2367, Sep. 2014.
- [19] I. K. Song, W. W. Jung, J. Y. Kim, S. Y. Yun, J. H. Choi, and S. J. Ahn, "Operation schemes of smart distribution networks with distributed energy resources for loss reduction and service restoration," *IEEE Trans. Smart Grid*, vol. 4, no. 1, pp. 367–374, Mar. 2013.
- [20] D. K. Khatod, V. Pant, and J. Sharma, "Evolutionary programming based optimal placement of renewable distributed generators," *IEEE Trans. Power Syst.*, vol. 28, no. 2, pp. 683–695, May 2013.
- [21] K. Mahmoud, N. Yorino, and A. Ahmed, "Optimal distributed generation allocation in distribution systems for loss minimization," *IEEE Trans. Power Syst.*, vol. 31, no. 2, pp. 960–969, Mar. 2016.
- [22] H. Gu, X. Guo, D. Wang, and W. Wu, "Real-time grid impedance estimation technique for grid-connected power converters," in *Proc. IEEE Int. Symp. Ind. Electron.*, May 2012, pp. 1621–1626.
- [23] N. Hoffmann and F. Fuchs, "Minimal invasive equivalent grid impedance estimation in inductive-resistive power networks using extended Kalman filter," *IEEE Trans. Power Electron.*, vol. 29, no. 2, pp. 631–641, Feb. 2014.

- [24] L. Asiminoaei, R. Teodorescu, F. Blaabjerg, and U. Borup, "Implementation and test of an online embedded grid impedance estimation technique for PV inverters," *IEEE Trans. Ind. Electron.*, vol. 52, no. 4, pp. 1136–1144, Aug. 2005.
- [25] B. Arif, L. Tarisciotti, P. Zanchetta, J. Clare, and M. Degano, "Grid parameter estimation using model predictive direct power control," *IEEE Trans. Ind. Appl.*, vol. 51, no. 6, pp. 4614–4622, Nov. 2015.
- [26] J. G. Norniebla *et al.*, "Analytic and iterative algorithms for online estimation of coupling inductance in direct power control of three-phase active rectifiers," *IEEE Trans. Power Electron.*, vol. 26, no. 11, pp. 3298–3307, Nov. 2011.
- [27] P. García, J. Guerrero, J. García, A. Navarro-Rodríguez, and M. Sumner, "Low frequency signal injection for grid impedance estimation in three phase systems," in *Proc. IEEE Energy Convers. Congr. Expo.*, Sep. 2014, pp. 1542–1549.
- [28] C. Wu, W.-H. Lau, and H.-H. Chung, "Analytical technique for calculating the output harmonics of an H-bridge inverter with dead time," *IEEE Trans. Circuits Syst. I, Fundam. Theory Appl.*, vol. 46, no. 5, pp. 617–627, May 1999.
- [29] S. Kaitwanidvilai, W. Khan-ngern, and M. Panarut, "The impact of dead-time effect on unwanted harmonics conducted emission of PWM inverters," in *Proc. Asia-Pac. Conf. Environ. Electromagn.*, May 2000, pp. 232–237.
- [30] S.-G. Jeong and M.-H. Park, "The analysis and compensation of dead-time effects in PWM inverters," *IEEE Trans. Ind. Electron.*, vol. 38, no. 2, pp. 108–114, Apr. 1991.
- [31] D.-H. Lee and J.-W. Ahn, "A simple and direct dead-time effect compensation scheme in PWM-VSI," *IEEE Trans. Ind. Appl.*, vol. 50, no. 5, pp. 3017–3025, Sep. 2014.
- [32] L. K. Mestha and P. D. Evans, "Analysis of on-state losses in PWM inverters," *Inst. Elect. Eng. Proc. B-Elect. Power Appl.*, vol. 136, no. 4, pp. 189–195, Jul. 1989.
- [33] J. W. Kolar, H. Ertl, and F. C. Zach, "Influence of the modulation method on the conduction and switching losses of a PWM converter system," in *Proc. IEEE Ind. Appl. Soc. Annu. Meeting*, Oct. 1990, vol. 1, pp. 502–512.
- [34] Plexim GmbH, "Piece-wise Linear Electrical Circuit Simulation (PLECS) Version 4.1," 2017. [Online]. Available: <http://www.plexim.com>
- [35] *IEEE Recommended Practices and Requirements for Harmonic Control in Electrical Power Systems*, IEEE Std. 519-1992, Apr. 1993.
- [36] G. Goertzel, "An algorithm for the evaluation of finite trigonometric series," *Amer. Math. Monthly*, vol. 65, no. 1, pp. 34–35, 1958.
- [37] J.-H. Kim, J.-G. Kim, Y.-H. Ji, Y.-C. Jung, and C.-Y. Won, "An islanding detection method for a grid-connected system based on the Goertzel algorithm," *IEEE Trans. Power Electron.*, vol. 26, no. 4, pp. 1049–1055, Apr. 2011.
- [38] R. Peña-Alzola, M. Liserre, F. Blaabjerg, M. Ordóñez, and T. Kerekes, "A self-commissioning notch filter for active damping in a three-phase LCL-filter-based grid-tie converter," *IEEE Trans. Power Electron.*, vol. 29, no. 12, pp. 6754–6761, Dec. 2014.



**José M. Cano** (M'98) was born in Oviedo, Spain, in 1971. He received the M.Sc. and Ph.D. degrees in electrical engineering from the University of Oviedo, Gijón, Spain, in 1996 and 2000, respectively.

In 1996, he joined the Department of Electrical Engineering, University of Oviedo, where he is currently an Associate Professor. From 2012 to 2014, he held appointments as a Visiting Associate Professor with the Department of Electrical and Computing Engineering, University of British Columbia, Vancouver, BC, Canada. His main research interests include power quality solutions for industry, power converters, distributed generation, and smart grids.

Dr. Cano has been an Associate Editor for the IET Power Electronics since 2017.



**Ángel Navarro-Rodríguez** (S'15) received the B.Sc. degree (Hons.) in telecommunications engineering from the University of Castilla La-Mancha, Ciudad Real, Spain, in 2012, and the M.Sc. degree in electrical energy conversion and power systems from the University of Oviedo, Gijón, Spain, in 2014. He is currently working toward the Ph.D. degree at the Department of Electrical, Computer, and Systems Engineering, University of Oviedo, funded by the Government of Principado de Asturias.

Since 2014, he has been a part of the LEMUR Research Team and his research interests include energy storage systems, control systems, electronics, power electronic converters, microgrids, power quality, and renewable energies.



**Andrés Suárez** (S'16) received the M.Sc. degree in electrical engineering from the University of Oviedo, Gijón, Spain, in 2011, and the M.Sc. degree in wind power systems from Aalborg University, Aalborg, Denmark, in 2012. He is currently working toward the Ph.D. degree in electrical engineering with LEMUR Research Team, University of Oviedo.

From 2012 to 2013, he was a Research Assistant with the University of Oviedo. In 2013, he joined the Department of Smart Grids, Iberdrola Ingeniería y Construcción, where he was an R&D Engineer. In 2015, he joined LEMUR Research Team, University of Oviedo. His research interests include control of power converters, parameter estimation, microgrids, and power quality.



**Pablo García** (S'01–A'06–M'09) received the M.Sc. and Ph.D. degrees in electrical engineering and control from the University of Oviedo, Gijón, Spain, in 2001 and 2006, respectively.

In 2004, he was a Visitor Scholar with the Electric Machines and Power Electronics Consortium, University of Madison-Wisconsin, Madison, WI, USA. In 2013, he was a Visiting Scholar with The University of Nottingham, Nottingham, U.K. He has coauthored more than 20 IEEE journals and 50 international conferences. He is currently an Associate Professor with the Department of Electrical, Electronics, Computer, and Systems Engineering, University of Oviedo. His research interests include control of grid-tied converters, parameter estimation, energy conversion, ac drives, sensorless control, ac machines diagnostics, and signal processing.



**Appendix G**

**Conference Publications**



## **G.1 Online Impedance Estimation in AC Grids Considering Parallel-Connected Converters**



## Online Impedance Estimation in AC Grids Considering Parallel-Connected Converters

Andrés Suárez, Cristian Blanco, Pablo García, Ángel Navarro-Rodríguez, Jose Manuel Cano Rodríguez  
*Dept. of Electrical, Electronic, Computers and Systems Engineering*  
*University of Oviedo Gijón, 33204, Spain*

e-mail: suarezandres@uniovi.es, blancocristian@uniovi.es, garciafpablo@uniovi.es, navarroangel@uniovi.es, jmcano@uniovi.es

**Abstract**—This paper addresses the estimation of the grid impedance under unbalanced conditions in AC Grids with power converter operating in parallel. A Pulsed Signal Injection (PSI) approach is employed for online estimating the grid impedance using an Recursive Least Square (RLS) algorithm. The method proposed here extends previous works focused on the impedance measurement and identification for pure passive grids. The most important contribution of the proposal can thus be summarized as the presentation of an online impedance technique suitable to be used in distribution grids having other power converters connected near the Point of Common Coupling (PCC). The proposal is valid both for balanced and unbalanced conditions.

### I. INTRODUCTION

Interfacing Voltage Source Converters (VSC) with the AC grid requires a very precise design of the current controller in order to fulfill the currents requirements of the grid. For this reason it is critical to have a deep knowledge of the dynamic model between the converter output voltage and the resulting grid current. The dynamics of this model are affected by the filter topology, i.e. L, LC, LCL, and the disturbance decoupling capability depending on the number and the position of the voltage and current sensors [1], [2].

There are multitude methods for grid impedance estimation, an initial classification may be according to the ones that require additional dedicated hardware to perform the estimation and the ones that not. In first group [3], [4] use signal injection and frequency based techniques to estimate the impedance over a wide frequency range. Regarding the second group, impedance estimation could be implemented using two different approaches:

- **Model-based techniques**, where the transfer function between the voltage and the current is used for the estimation. Examples of these techniques are present in the literature, i.e. the use of the LCL filter resonance proposed in [5] for grid estimation. However the presence of two resonant frequencies when reactive power passive

The present work has been partially supported by the predoctoral grants program Severo Ochoa for the formation in research and university teaching of Principado de Asturias PCTI-FICYT under the grant ID BP14-135. This work also was supported in part by the Research, Technological Development and Innovation Program Oriented to the Society Challenges of the Spanish Ministry of Economy and Competitiveness under grant ENE2016-77919-R, ENE2014-52272-R, by the European Union through ERFD Structural Funds (FEDER) and by the government of Principality of Asturias, under IDEPA grant 2017 Thyssen SV-PA-17-RIS3-3.

is added at the PCC is the main limitation of this strategy. In [6] a experimentally supported method is proposed for estimating the equivalent inductance and resistance of the grid. It is based on the closed-loop transient response, nonetheless this method does not include the operation under unbalanced grid conditions and does not show the response to sudden changes on the grid impedance, which is critical for islanding detection. The use of Kalman filters for grid estimation are other solutions within this approach. In [7] grid impedance is estimated based on the grid harmonics and the impedance at different frequencies, this study is only supported with simulations. In [8] a similar approach is presented; the estimated coefficients are online updated using an adaptive linear neuron (ADALINE) algorithm, this model requires to measure grid current and voltages but it is experimentally demonstrated under balanced conditions. In [9], grid inductance is estimated using two consecutive samples of the grid current within a switching period. The estimation method is based on the discrete-time model at the grid frequency and, as recognized by the authors, the method is only valid for the inductive component. Moreover, the operation is only demonstrated for two different inductance values and unbalanced conditions are not considered.

- **Signal-injection based techniques** use an additional excitation for tracking the system response [10]–[17]. For the excitation signal, several approaches have been proposed:

- 1) Pulsed Signal Injection (PSI) [3], [17]–[19]
- 2) High Frequency Signal Injection (HFSI) at constant high frequency [12], [13], [20]–[22];
- 3) Current regulator reaction [13];
- 4) Low Frequency Signal Injection (LFSI) [14], [23], [24];
- 5) Binary Sequence Signal Injection (BSSI) [15], [25], [26].

For the PSI methods studied in literature, the results presented in [18] are closed to the ones presented in the present work, but deeper focused on a pure inductive and a balanced three phase impedance. Authors of [17] proposed a solution able to estimate grid admittance considering also power con-

verters connected in parallel, however the activation of the pulse injection is not fully described and results were only tested under real-time emulation by an OPAL-RT simulator. Other approaches as [19] proposed a method with a larger computational burden and memory requirements than the one in the present work. Results in [3] are obtained under the absence of fundamental excitation. HFSI methods present some issues regarding the selection of the frequency range, since it is possible to produce a reaction in any other active power filter (APF) connected to the same PCC, compensating the high frequency and depreciating the estimation. Organizing LFSI methods depending into those adding an additional excitation signal at a given frequency and analyzing the response of the grid at that frequency to obtain the impedance, it is highlighted the results obtained in [11], [23], where it is used a 75Hz current signal. The continuous injection of the signal may produced distortion in the components and the impedance is only estimated for the frequency of the signal injected. It has also to be considered that this low-frequency signal is suitable to be compensated by the own dynamic response of the current regulators, reacting at that frequency and compensating the disturbance signal, which reduces the effectiveness of the method. On the other hand, considering the LFSI methods that modifies the commands delivered by the converter, a solution modifying the  $P$  and  $Q$  command to analyze the response of the system and to estimate the impedance is proposed in [24], however the results are not validated under real situation neither unbalanced conditions and present a drawback considering the coupling terms between the regular operational condition and the ones induced to perform the estimation. Other approaches for estimation based on frequency methods, such BSSI, which is based on injecting a pulse-train of signals and analyzing the response are also present in literature. This approach requires larger processing time and computational burden than PSI methods and they are not tested under unbalanced grid conditions.

This paper presents a strategy for grid estimation, based on the PSI technique, considering a distribution grid with parallel connected converters and operated under balanced and unbalanced conditions. The proposed PSI method injects a pulse at the zero crossing of each three phase voltages, which reduce the THD of the system when compared to other strategies, and the estimation is based on the performance of a Recursive Least Square (RLS) algorithm. The proposed strategy is supported with experimental results. The purpose of the study is to analyze the behavior of the grid impedance under these conditions and evaluate how is affected by the operation of additional converters connected to the same grid. The study also addresses the behavior of the estimator under those conditions. The contributions of this work can be summarized as: 1) online identification of the grid impedance, including unbalance conditions; 2) Definition of a model to evaluate the grid impedance under balanced and unbalanced condition; 3) identification and evaluation of the grid impedance estimation with multiple converters connected to the same grid.

This paper is organized as follows. In Section II is presented

the impedance modeling technique, which highlight a coupling between the impedance of the system and the sequences generated under an unbalance in the system. Simulation and also experimental results related to the impedance model are included in this part. In Section III the PSI strategy is presented. Section IV describes the algorithm of the RLS used for the estimation, as well as the simulation results. Section V presents the laboratory results obtained and finally Section VI summarizes the conclusions of the work.

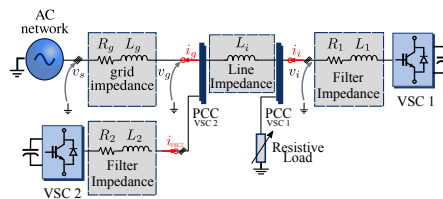


Fig. 1. Schematic of the considered system. Two power converters and a resistive load are considered for the present work. VSC1 represents the converter implementing the PSI method.

## II. SYSTEM MODELING AND IMPEDANCE DEFINITION

The equations for the system presented in Fig.1 are suitable to be defined both in stationary  $(\alpha, \beta, 0)$  or synchronous  $(d, q, 0)$  reference frame. For this work,  $\alpha, \beta, 0$  reference was selected, following same procedure as stated in [27], since it leads to a simpler formulation in the presence of unbalances. The objective of this work is to define a model suitable for the identification of the grid impedance. This impedance contribution may be split into two parts; a first one imposed by the cabling and the connection/disconnection of passive loads and a second active part that is determined by the operational mode of the power converters, including harmonic generation or compensation.

### A. Equivalent Impedance of Passive Loads

Voltage equation at the PCC, considering a RL filter for interconnection between the grid and the converter, is defined as

$$\mathbf{v}_{\alpha\beta} = \mathbf{R}_{\alpha\beta} \mathbf{i}_{\alpha\beta} + \mathbf{L}_{\alpha\beta} \frac{d\mathbf{i}_{\alpha\beta}}{dt} \quad (1)$$

By considering the angle of the impedance as the angle for the spatial orientation in the stationary reference frame, the equivalent expression for the static impedance as seen by the converter may be defined as (2).

$$\mathbf{Z}_{\alpha\beta i} = \mathbf{R}_{\alpha\beta i} + \mathbf{j}\omega L_{\alpha\beta i} = \begin{pmatrix} Z_{\alpha\alpha i} & Z_{\alpha\beta i} \\ Z_{\alpha\beta i} & Z_{\beta\beta i} \end{pmatrix} \quad (2)$$

Subscript  $i$  is related to each individual impedance seen from the PCC. In case the impedance is balanced, diagonal terms ( $Z_{\alpha\alpha i}$  and  $Z_{\beta\beta i}$ ) are equal and cross-coupling between phases, represented by non diagonal terms ( $Z_{\alpha\beta i}$ ), are not present. For the case of unbalance, expression (2) can be

rotated to a common  $\alpha\beta$  reference frame, with  $n$  impedance elements, leading to (3).

$$\mathbf{Z}_{\alpha\beta 0} = \sum_{i=1}^n \left[ \Sigma Z_i \begin{pmatrix} 1 & 0 \\ 0 & 1 \end{pmatrix} + \Delta Z_i \begin{pmatrix} \cos \theta_e^i & -\sin \theta_e^i \\ -\sin \theta_e^i & -\cos \theta_e^i \end{pmatrix} \right] + Z_{\alpha\beta i} \begin{pmatrix} -\sin \theta_e^i & \cos \theta_e^i \\ \cos \theta_e^i & \sin \theta_e^i \end{pmatrix} \quad (3)$$

where  $\Sigma Z_i = \frac{Z_{\alpha\alpha i} + Z_{\beta\beta i}}{2}$ ,  $\Delta Z_i = \frac{Z_{\alpha\alpha i} - Z_{\beta\beta i}}{2}$ , and  $\theta_e^i$  is the spatial angular phase of the unbalance impedance. For a balanced system, only the matrix terms depending on  $\Sigma Z_i$  will remain. Relationship with phase impedances are:  $\Sigma Z_i = \frac{z_{a_i} + z_{b_i} + z_{c_i}}{3}$ ,  $\Delta Z_i = \frac{z_{a_i} + a z_{b_i} + a^2 z_{c_i}}{3}$ , where  $a = e^{j2\pi/3}$ .

Figure 2 shows the results of the variation in the equivalent impedance of the system according to variation induced in the load. Initially, for a voltage level of 400V, the equivalent impedance of the system,  $\Sigma Z$ , is 18  $\Omega$ , for that case, the system is balanced and consequently, only positive sequence current is present on the system, with peak value of 22A, the rest of the components are zero. At instant  $t = 0.125s$ , there is a change in one of the impedance phases, increasing a 50% its nominal value. As consequence of this unbalance in the impedance, negative and homopolar current components are flowing through the system. The value for the components of the impedance are  $\Sigma Z = 21.48\Omega$  and  $\Delta Z = 2.791\Omega$ , the angle of the unbalance is reflected through  $\theta$  with a value of  $-8.5^\circ$ . In the next step of the simulation at  $t = 0.25s$ , the impedance of the three phases are increased in 50% its value. This change is produced at same time and magnitude in the three phases, so that there is not unbalance, either negative sequence components. For same reason,  $\Delta Z$  component is zero and the impedance variation is only affecting the  $\Sigma Z$  component. In the last part of the simulation a change in two phases is made simultaneously producing an equivalent impedance of  $\Delta Z = 5.2\Omega$  and a  $\Sigma Z = 27\Omega$  with an angle for the unbalance of  $150^\circ$ .

By considering the overall grid impedance dominated by the resistance and inductance terms, it can be expressed as

$$\Sigma Z_i = \Sigma R_i + j\omega_e \Sigma L_i \quad (4a)$$

$$\Delta Z_i = \Delta R_i + j\omega_e \Delta L_i \quad (4b)$$

$$\mathbf{Z}_{\alpha\beta i} = \mathbf{R}_{\alpha\beta i} + j\omega_e \mathbf{L}_{\alpha\beta i} \quad (4c)$$

where,  $\Sigma R_i = \frac{R_{\alpha\alpha i} + R_{\beta\beta i}}{2}$ , and  $\Sigma L_i = \frac{L_{\alpha\alpha i} + L_{\beta\beta i}}{2}$ ,  $\Delta R_i = \frac{R_{\alpha\alpha i} - R_{\beta\beta i}}{2}$ ,  $\Delta L_i = \frac{L_{\alpha\alpha i} - L_{\beta\beta i}}{2}$ . From here it can be obtained a voltage expression (5),

$$\mathbf{v}_{zeq}^{\alpha\beta} = \mathbf{v}_g^{\alpha\beta} - \mathbf{v}_s^{\alpha\beta} = \mathbf{R}_{\alpha\beta} \mathbf{i}_g^{\alpha\beta} + \mathbf{L}_{\alpha\beta} \frac{d\mathbf{i}_g^{\alpha\beta}}{dt} \quad (5)$$

where  $\mathbf{v}_{zeq}^{\alpha\beta}$  is the voltage drop vector across the overall equivalent impedance,  $\mathbf{v}_g^{\alpha\beta}$  and  $\mathbf{v}_s^{\alpha\beta}$  are the PCC voltage and the grid voltage vectors (see Fig. 1), and  $\mathbf{i}_g^{\alpha\beta}$  is the grid current vector.  $\mathbf{L}_{\alpha\beta}$  and  $\mathbf{R}_{\alpha\beta}$  are, respectively, the sum of

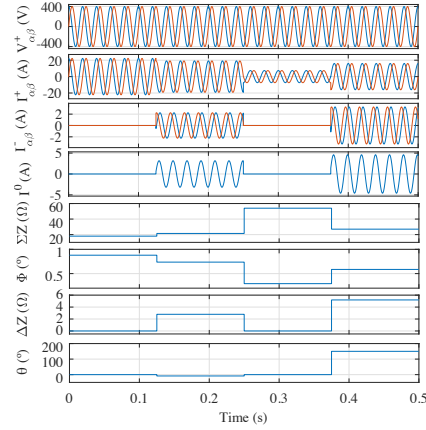


Fig. 2. From top to bottom, 1) Positive Sequence of AC-Grid Voltage in the  $\alpha\beta$  reference frame; 2) Positive Sequence of Current in the  $\alpha\beta$  reference frame; 3) Negative Sequence of Current in the  $\alpha\beta$  reference frame; 4) Homopolar Current; 5) Equivalent impedance of  $\Sigma Z$  according to expression (3); 6) Angle of  $\Sigma Z$ ; 7)  $\Delta Z$ , Equivalent impedance of the system under an unbalance situation; 8)  $\theta$ , Angle of the unbalance

the inductance and resistance matrices for the different grid impedances as expressed in (4c).

#### B. Equivalent Impedance of Active Loads

Impedance identification in those applications considering power converters, Fig.1, requires considering the effect of the converter operating point in the equivalent impedance. Power converters, working as STATCOMs, behave as an active filter, modifying their equivalent impedance to achieve the reactive power requirements of the system. Consequently, it is need to estimate an initial approach of the converter impedance working under such operation. In Fig.1, VSC2 was connected to the grid in STATCOM mode. The  $d$  component of the control loop is dedicated to control the dc-link of the converter and  $q$  component is devoted to inject different levels of reactive current into the grid. Measuring voltage and current at the converter PCC and implementing the modeling technique previously described, it is possible to estimate an initial value for the impedance of the converter. Figure 3 represents the real impedance of VSC2 for a range of frequencies and current injection from 6 to 11A. According to the results, the whole impedance value decreases proportionally to the current and the frequency rise. The results of the same experiment are presented in Fig. 4 in time domain and for the main frequency of the grid. In this case, the inductance part of the impedance is kept constant for same current level. Values of the impedance are 50mH for the highest current of 11A and 70mH for the lowest current at 6A. The resistive part varies much less

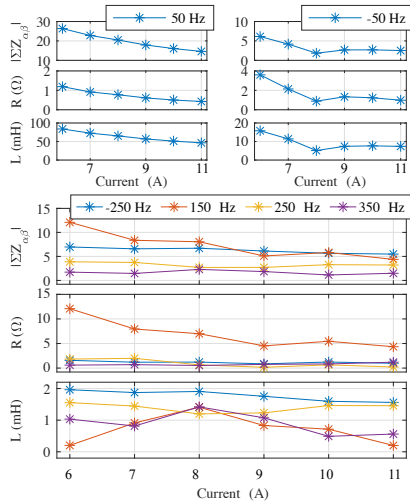


Fig. 3. From top to bottom: 1) In the left; a) Equivalent impedance of the system at different reactive current values for a frequency of 50 Hz; b) Equivalent resistance of the system for different values of reactive current at 50 Hz; c) Inductance value of the system at a frequency of 50 Hz for different reactive current injection. 2) In the right: Idem 1) at -50 Hz. 3) In the bottom: a) Equivalent impedance of the system at different frequencies and current injection; b) Equivalent resistance of the system at different frequencies and current injection; c) Inductance equivalent for different frequencies and current injection

according to the currents, keeping constant at value of 1  $\Omega$  for the whole set of currents.

Since those currents are balanced, there is no presence of negative or homopolar sequence components, so the results are feasible to identify the  $\Sigma Z$  component from expression (3). The rest of non-diagonal components are result of interaction between non-positive sequence components in the system. Theoretical relationship between sequences are illustrated in Fig.5. As said above, under balanced situation, only  $\Sigma Z$  is interacting at main frequency. Only under an unbalance situation,  $\Delta Z$  is contributing to the cross-term element.

According [27] and expanding (1) for every single impedance in the system, it is possible to obtain a relation between positive and negative sequence components and the system impedance, as it states in (6)

$$\begin{aligned} \mathbf{i}_{\alpha\beta} &= [\mathbf{Z}_{\alpha\beta}]^{-1} \cdot \mathbf{v}_{\alpha\beta} & (6) \\ &= \mathbf{v}_{\alpha\beta} \cdot \frac{1}{\Sigma Z_i^2 - \Delta Z_i^2} \\ &\cdot \left[ \left( \begin{matrix} \Sigma Z_i & 0 \\ 0 & \Sigma Z_i \end{matrix} \right) + \Delta Z_i \begin{pmatrix} -\cos \theta_e^i & \sin \theta_e^i \\ \sin \theta_e^i & \cos \theta_e^i \end{pmatrix} \right] \\ &= \frac{\Sigma Z_i}{\Sigma Z_i^2 - \Delta Z_i^2} \cdot V_{\alpha\beta} e^{j\omega t} - \frac{\Delta Z_i}{\Sigma Z_i^2 - \Delta Z_i^2} \cdot V_{\alpha\beta} e^{-(j\omega t + \theta)} \end{aligned}$$

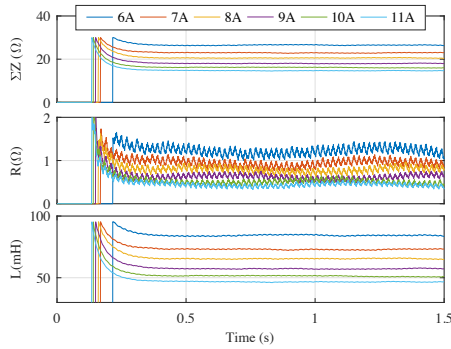


Fig. 4. From top to bottom: 1) Equivalent impedance for the converter under balanced situation at 50 Hz; 2) Resistive part of the impedance at 50 Hz; 3) Inductance part of the impedance at 50 Hz

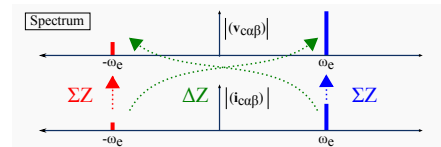


Fig. 5. Relationship between voltage and current, in frequency domain, according expression of the equivalent impedance  $\Sigma Z$  and  $\Delta Z$ .

Expanding the terms from (6), considering positive and negative sequence component, leads to equation (7)

$$\begin{aligned} \begin{bmatrix} i_{\alpha}^{(+)} \\ i_{\beta}^{(+)} \\ i_{\alpha}^{(-)} \\ i_{\beta}^{(-)} \end{bmatrix} &= & (7) \\ \frac{1}{\Sigma Z_i^2 - \Delta Z_i^2} \begin{bmatrix} \Sigma Z_i & 0 & -\Delta Z_i & 0 \\ 0 & \Sigma Z_i & 0 & -\Delta Z_i \\ -\Delta Z_i & 0 & \Sigma Z_i & 0 \\ 0 & -\Delta Z_i & 0 & \Sigma Z_i \end{bmatrix} \begin{bmatrix} v_{\alpha}^{(+)} \\ v_{\beta}^{(+)} \\ v_{\alpha}^{(-)} \\ v_{\beta}^{(-)} \end{bmatrix} \end{aligned}$$

Considering the power expression depicted in (8), where the constant value are terms associated to the positive sequence and the other terms the interacting between different sequences.

$$\begin{aligned} \begin{bmatrix} p \\ q \end{bmatrix} &= \begin{bmatrix} v_{\alpha}^{+} \cdot (i_{\alpha}^{+} + i_{\alpha}^{-}) + v_{\beta}^{+} \cdot (i_{\beta}^{+} + i_{\beta}^{-}) \\ v_{\beta}^{+} \cdot (i_{\alpha}^{+} + i_{\alpha}^{-}) - v_{\alpha}^{+} \cdot (i_{\beta}^{+} + i_{\beta}^{-}) \end{bmatrix} & (8) \\ &= \begin{bmatrix} \bar{P} + \tilde{P} \\ \bar{Q} + \tilde{Q} \end{bmatrix} \end{aligned}$$

Combination of (7) and (8) allows to establish a relationship between every term of the equivalent impedance and power. Multiple combinations are possible, however for this work it was only considered the case of negative sequence current, resulting in (9)

$$\begin{bmatrix} \bar{P} \\ \bar{P} \\ \bar{Q} \\ \bar{Q} \end{bmatrix} = \frac{1}{\Sigma Z_i^2 - \Delta Z_i^2} \cdot \begin{bmatrix} \Sigma Z_\alpha + \Sigma Z_\beta \\ -\Delta Z_\alpha - \Delta Z_\beta \\ -\Sigma Z_\alpha + \Sigma Z_\beta \\ \Delta Z_\alpha - \Delta Z_\beta \end{bmatrix} \cdot \begin{bmatrix} v_{\alpha^+}^2 \\ v_{\beta^+}^2 \end{bmatrix} \quad (9)$$

The term that relates every term in the graph To estimate those components inside the system of Fig.1, the current control of the converter was forced to inject harmonic components at  $-50Hz$ . In this way it is possible to see a negative sequence current flowing through the system. Figure 6 presents the results of the negative sequence current injection. Voltage at

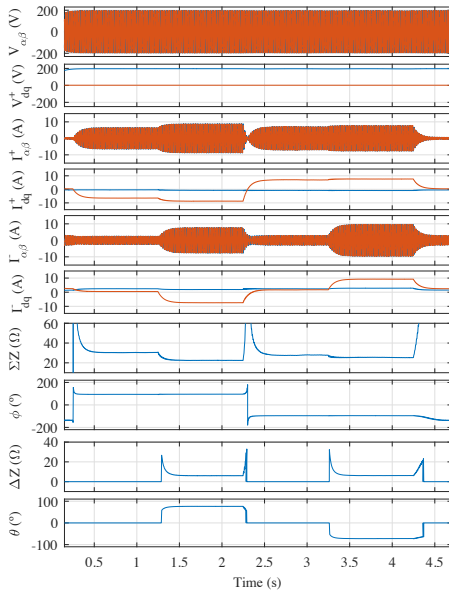


Fig. 6. From top to bottom: 1) Grid voltage in  $\alpha\beta$  reference frame; 2) Grid voltage in  $dq$  reference frame; 3) Positive sequence of converter current in  $\alpha\beta$  reference frame; 4) Positive sequence of converter current in  $dq$  reference frame; 5) Negative sequence of converter current in  $\alpha\beta$  reference frame; 6) Negative sequence of converter current in  $dq$  reference frame; 7)  $\Sigma Z$  component of the equivalent converter impedance; 8) Angle of the  $\Sigma Z$  component, expressed in degrees; 9)  $\Delta Z$  component of the equivalent converter impedance; 10)  $\theta$  angle of the unbalance, expressed in degrees.

the grid was set to 200V, at instant 0.125s the converter started to inject  $-7A$  of positive sequence current into the

system. That reaction is perceptible at the  $\Sigma Z$  component of the impedance that is already set at value 30.23 $\Omega$  with an angle of 90°, the rest of the components are kept to zero. At instant 1.25s, the negative component of the current is set to  $-9A$ . At that instant the  $\Sigma Z$  decreases to 22.45 $\Omega$  and  $\Delta Z$  increases to 25.46 $\Omega$  and the angle the unbalance,  $\theta$ , is 76°. In the next step of the experiment,  $t = 2.25s$ , the positive sequence current starts to inject 7A,  $\Sigma Z$  reaches the previous value of 30.23 $\Omega$  but its angle  $\phi$  changes to  $-90^\circ$ ; consequently, since there is not any negative sequence component,  $\Delta Z$  is zero. At instant  $t = 3.25s$ , the negative sequence current is set to 9A. The magnitude of  $\Delta Z$  increases to the same previous value of 25.46 $\Omega$  and same happened to angle that has changed the direction and now it is  $-76^\circ$ .

III. PULSED SIGNAL INJECTION

According the injection parameters, there are multitude of PSI strategies which can be implemented. The one selected in this paper is implemented in the  $dq$  reference frame. The signal is injected aligned with the zero crossing of the grid voltage, detected by the PLL, in order to minimize the voltage distortion. Fig. 7 shows a detailed view about the injection mechanism.

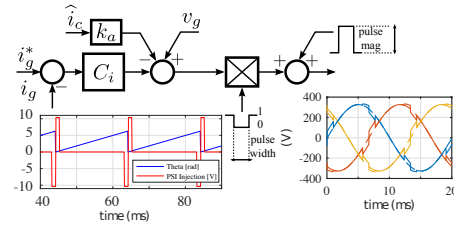


Fig. 7. PSI Loop implementation. The pulse injection is synchronized with respect to the grid voltage zero crossing and it is added in the  $q$  component.

The pulses are injected by modifying the duty cycle provided by the current controller. The pulse is added to the  $q$  component of the fundamental voltage. The magnitude and duration of the pulse may contribute to ease the detection of the impedance but also might increase the current THD, for this reason it is convenient to establish a trade-off between duration and also magnitude. The values presented in Table I have been used. Fig. 7 illustrates the strategy chosen for the experimental analysis. It is important to highlight the fact that since the pulse injection is symmetrical with respect to the zero crossing, thus resulting in a zero average voltage error. During the experimental analysis the injection was implemented in the  $q$  component of the voltage, since the  $d$  component is responsible to command the charge of the DC-Link.

IV. RLS ALGORITHM IMPLEMENTATION

In this paper, the estimation of the system parameters is carried out by using an RLS approach [18], [28]. Starting from

equation (5) and according [29], the discrete approximation of the grid current in  $\alpha\beta$  reference frame, employing Tustin method and a sample time  $T_s$  is

$$i_{g[k]}^\alpha = a_1^\alpha \cdot i_{g[k-1]}^\alpha + a_2^\alpha \cdot i_{g[k]}^\beta + a_3^\alpha \cdot i_{g[k-1]}^\beta + b_0^\alpha (v_{\alpha[k]} + v_{\alpha[k-1]}) \quad (10)$$

$$i_{g[k]}^\beta = a_1^\beta \cdot i_{g[k-1]}^\beta + a_2^\beta \cdot i_{g[k]}^\alpha + a_3^\beta \cdot i_{g[k-1]}^\alpha + b_0^\beta (v_{\beta[k]} + v_{\beta[k-1]}) \quad (11)$$

where

$$\begin{aligned} a_1^\alpha &= \frac{\frac{2}{T_s} L_{\alpha\alpha} - R_{\alpha\alpha}}{\frac{2}{T_s} L_{\alpha\alpha} + R_{\alpha\alpha}}, & a_2^\alpha &= -\frac{\frac{2}{T_s} L_{\alpha\beta} + R_{\alpha\beta}}{\frac{2}{T_s} L_{\alpha\alpha} + R_{\alpha\alpha}} \\ a_3^\alpha &= \frac{\frac{2}{T_s} L_{\alpha\beta} + R_{\alpha\beta}}{\frac{2}{T_s} L_{\alpha\alpha} + R_{\alpha\alpha}}, & b_0^\alpha &= \frac{1}{\frac{2}{T_s} L_{\alpha\alpha} + R_{\alpha\alpha}} \\ a_1^\beta &= \frac{\frac{2}{T_s} L_{\beta\beta} - R_{\beta\beta}}{\frac{2}{T_s} L_{\beta\beta} + R_{\beta\beta}}, & a_2^\beta &= -\frac{\frac{2}{T_s} L_{\alpha\beta} + R_{\alpha\beta}}{\frac{2}{T_s} L_{\beta\beta} + R_{\beta\beta}} \\ a_3^\beta &= \frac{\frac{2}{T_s} L_{\alpha\beta} - R_{\alpha\beta}}{\frac{2}{T_s} L_{\beta\beta} + R_{\beta\beta}}, & b_0^\beta &= \frac{1}{\frac{2}{T_s} L_{\beta\beta} + R_{\beta\beta}} \end{aligned}$$

and  $v_\alpha, v_\beta$  represent the components of the difference between the PCC and the grid voltages. From (10), (11) the values for the resistance and inductance terms can be obtained as (12).

$$\begin{aligned} R_{xx} &= \frac{1 - a_1^x}{2b_0^x}, & L_{xx} &= \frac{T_s}{4} \frac{1 + a_1^x}{b_0^x}, \\ R_{xy} &= -\frac{a_2^x + a_3^x}{2b_0^x}, & L_{xy} &= \frac{T_s}{4} \frac{a_2^x - a_3^x}{b_0^x} \end{aligned} \quad (12)$$

where  $x, y$  could be either  $\alpha$  or  $\beta$ .

The RLS algorithm will allow to estimate the resistances and inductances in (12) by determining the values of the coefficients  $a_i^x$  and  $b_j^x$ . The difference between the measured converter current,  $\hat{i}_i^x[k]$ , and the one calculated by the estimator,  $\hat{i}_i^x[k]$ , leads to the error driving the RLS update. Since it is assumed that the grid voltage is stiff enough, it is not necessary to consider any effect due to the pulse injection, so it is possible to decoupling the unknown grid voltage  $v_s^{\alpha\beta}$ , by only considering the current induced by the pulse injection.

The least squares problem is formulated as in [29], in recursive form using the equations (13)-(16). The system equations are represented by defining the variables and coefficients vectors,  $\mathbf{X}^x[k]$ ,  $\mathbf{W}^x[k]$ , as (17) and (18) respectively, where superscript  $x$  could be either  $\alpha$  or  $\beta$ . The estimated RLS current,  $\hat{i}_g^x[k]$ , is determined by the product  $\mathbf{W}_{[k-1]}^x \cdot \mathbf{X}_{[k]}^x$  in (13). All the variables names are referred to those shown in Fig. 1.

$$\alpha_{[k]}^x = i_{g[k]}^x - \mathbf{W}_{[k-1]}^x \cdot \mathbf{X}_{[k]}^x \quad (13)$$

$$\mathbf{g}_{[k]}^x = \mathbf{P}_{[k-1]}^x \cdot \mathbf{X}_{[k]}^x \cdot \left[ \lambda + \mathbf{X}_{[k]}^x T \cdot \mathbf{P}_{[k-1]}^x \cdot \mathbf{X}_{[k]}^x \right]^{-1} \quad (14)$$

$$\mathbf{P}_{[k]}^x = \lambda^{-1} \cdot \mathbf{P}_{[k-1]}^x - \mathbf{g}_{[k]}^x \cdot \mathbf{X}_{[k]}^x T \lambda^{-1} \cdot \mathbf{P}_{[k-1]}^x \quad (15)$$

$$\mathbf{W}_{[k]}^x = \mathbf{W}_{[k-1]}^x + \left( \alpha_{[k]}^x \cdot \mathbf{g}_{[k]}^x \right)^T \quad (16)$$

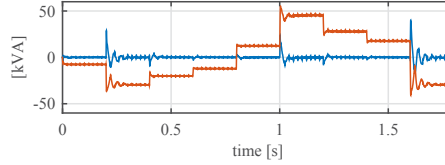


Fig. 8. Simulation results. Active (blue) and reactive (red) power in the VSC2 operated in STATCOM mode.

$$\mathbf{X}^x[k] = \left[ i_{g[k-1]}^x, i_{g[k]}^y, i_{g[k-1]}^y, v_{g[k]}^x, v_{g[k-1]}^x \right]^T \quad (17)$$

$$\mathbf{W}^x[k] = \left[ a_1^x[k], a_2^x[k], a_3^x[k], b_0^x[k], b_0^x[k] \right] \quad (18)$$

where  $\mathbf{P}_{(5 \times 5)}$  is the covariance matrix and it is initialized to  $\mathbf{P} = 0.01 \cdot \mathbf{I}_{(5 \times 5)}$ ;  $\mathbf{g}_{(5 \times 1)}$  is the adaptation gain, and  $\lambda = [0, 1]$  is the forgetting factor, which need to be selected as a tradeoff of the expected estimation bandwidth and the signal to noise ratio. Values between 0.95 and 1 are often selected. For this paper, the values shown in Table I have been used. After the injection of a new pulse, the estimation of the  $\mathbf{W}$  components for both the  $\alpha$  and the  $\beta$  components is updated and a new estimation for  $\mathbf{R}_{\alpha\beta}$  and  $\mathbf{L}_{\alpha\beta}$  is obtained using (12).

The algorithm has been considered to be fast enough to be implemented on medium performance digital signal controllers as has been demonstrated in [29].

The simulation results for the impedance estimation using the RLS algorithm under the setup in Fig. 1 are shown in Fig. 8 and 9. As shown, the individual components react to the STATCOM commands as expected.

## V. EXPERIMENTAL RESULTS

In order to prove the performance of the technique, three different experiments were carried out in the experimental setup of Fig. 10. The converter was operated with the system shown in Fig. 10 under different configurations: 1) Converter VSC 1 feeding a load, isolated from the grid. In this configuration, the DC-side was kept constant at its nominal value of 750V by an independent source. 2) Converter VSC 2 connected to grid in STATCOM mode. DC-link is controlled by the  $d$ -axis component whereas the pulses are injected at the  $q$ -axis. The estimation for different impedances was also performed. 3) Converter connected as the schematic presented in Fig. 1 with converter VSC 2 injecting reactive current steps in the grid, in order to evaluate the effect over the estimation technique. Fig. 11 shows the voltage and current waveforms of VSC1 with the pulsed injection signal when both converters are connected in parallel (configuration 3), and the current resulted from that injection. For all the three cases the same load connected to the PCC is used. Results are exposed in Fig. 12. All values used are presented in Table I.

Figure 12 presents the results of the estimator under real conditions. The left column shows the results for the first case, where the VSC 1 was connected only to a 18Ω load. The

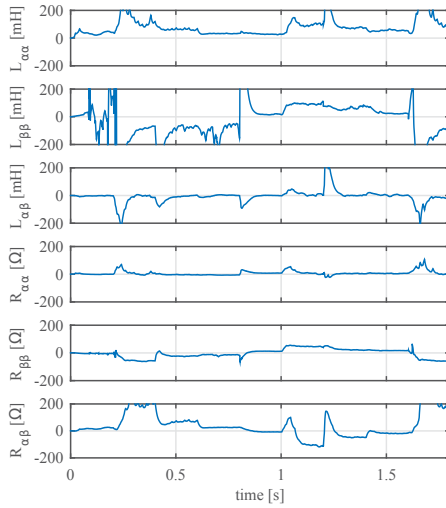


Fig. 9. Simulation results. RLS Identified impedance components.

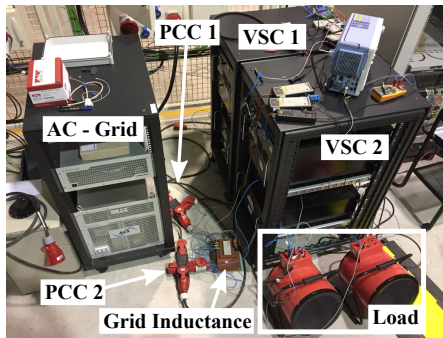


Fig. 10. Experimental setup according to the schematic shown in Fig. 1. At the left side the AC Grid emulator is shown. Converters VSC1 and VSC2 are shown at the right. Two resistive loads are used for varying the estimated impedance.

upper graph shows the  $\alpha, \beta$  resistance and the down graph the  $\alpha, \beta$  inductance. During this experiment the impedance of the system was kept constant. The second graph shows the performance of the estimation method when its operated as a grid-tied converter while keeping the same load. At  $t=1.1$  s, the load is changed inducing an unbalance condition in phase A ( $18\Omega \rightarrow 9\Omega$ ). The estimator is able to perceive the change and is reflected in the resistance part, changing the resistance value

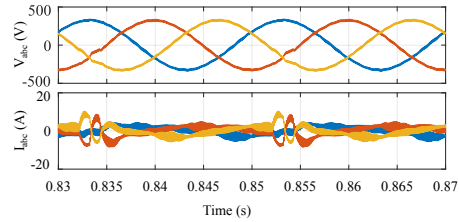


Fig. 11. Voltage and Current Waveforms of converter VSC1 with the pulse injection signal with both converters connected in parallel (configuration 3).

from  $18$  to  $9\Omega$ . In the third case, VSC 1 is connected in parallel with VSC 2, including an impedance between both in order to emulate the grid. VSC2 is injecting  $2A$  reactive current steps each two seconds. Current injection starts at  $0.2$  and at  $0.9$  seconds the same unbalance described for previous experiment is applied. For this case, it is clear that the inductive component of the impedance estimation is reacting to the changes.

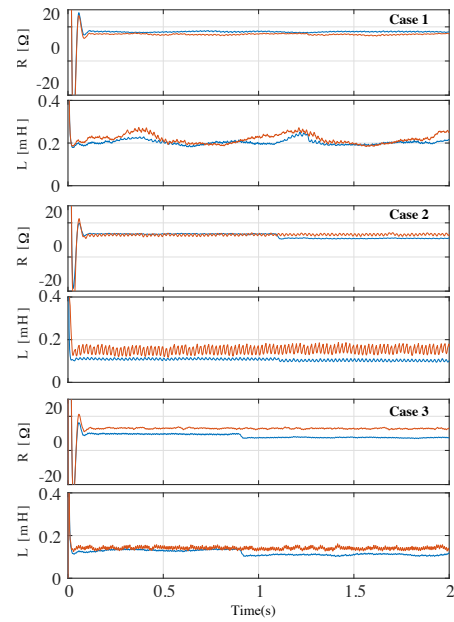


Fig. 12. Experimental Results obtained from the estimation of the  $\alpha, \beta$  components of the impedance. From top to bottom, 1) VSC 1 feeding an isolated load; 2) VSC1 connected to a AC Grid emulator; 3) VSC1 and VSC 2 connected in parallel

TABLE I  
PARAMETERS

Nominal parameters	Value
$R_1, R_2$ [ $\Omega$ ]	0.33
$R_{Load}$ [ $\Omega$ ]	18
$L_1, L_2$ [mH]	1.7
$L_{Grid}$ [mH]	0.879
pulse mag. [p.u]	0.1
pulse width. [ms]	2
$\lambda$	0.9/0.8

## VI. CONCLUSIONS

This paper has proposed an online grid impedance estimation technique based on a RLS estimator, able to perform an accurate estimation under unbalanced conditions and with other power converter operating in STATCOM mode connected to the same grid. An analytical model for determine the grid impedance both with passive and active loads has been built. The model was used within the RLS algorithm for the parameters estimation. The validity of the proposal has been demonstrated with both simulation and preliminary experimental results.

## REFERENCES

- [1] H. Xiao, X. Qu, S. Xie, and J. Xu, "Synthesis of active damping for grid-connected inverters with an LCL filter," in *2012 IEEE Energy Conversion Congress and Exposition (ECCE)*, Sep. 2012, pp. 550–556.
- [2] J. Xu, S. Xie, and T. Tang, "Active Damping-Based Control for Grid-Connected-Filtered Inverter With Injected Grid Current Feedback Only," *IEEE Transactions on Industrial Electronics*, vol. 61, no. 9, pp. 4746–4758, Sep. 2014.
- [3] Z. Staroszczyk, "A method for real-time, wide-band identification of the source impedance in power systems," *IEEE Transactions on Instrumentation and Measurement*, vol. 54, no. 1, pp. 377–385, Feb 2005.
- [4] M. Sumner, B. Palethorpe, D. W. P. Thomas, P. Zanchetta, and M. C. D. Piazza, "A technique for power supply harmonic impedance estimation using a controlled voltage disturbance," *IEEE Transactions on Power Electronics*, vol. 17, no. 2, pp. 207–215, Mar 2002.
- [5] M. Liserre, F. Blaabjerg, and R. Teodorescu, "Grid Impedance Estimation via Excitation of LCL -Filter Resonance," *IEEE Transactions on Industry Applications*, vol. 43, no. 5, pp. 1401–1407, 2007.
- [6] A. Vidal, A. G. Yepes, F. D. Freijedo, O. López, J. Malvar, F. Baneira, and J. Doval-Gandoy, "A method for identification of the equivalent inductance and resistance in the plant model of current-controlled grid-tied converters," *IEEE Transactions on Power Electronics*, vol. 30, no. 12, pp. 7245–7261, Dec 2015.
- [7] A. K. Broen, M. Amin, E. Skjong, and M. Molinas, "Instantaneous frequency tracking of harmonic distortions for grid impedance identification based on kalman filtering," in *2016 IEEE 17th Workshop on Control and Modeling for Power Electronics (COMPEL)*, June 2016, pp. 1–7.
- [8] A. Bechouche, D. O. Abdeslam, H. Seddiki, and A. Rahoui, "Estimation of equivalent inductance and resistance for adaptive control of three-phase pwm rectifiers," in *IECON 2016 - 42nd Annual Conference of the IEEE Industrial Electronics Society*, Oct 2016, pp. 1336–1341.
- [9] A. Ghanem, M. Rashed, M. Sumner, M. A. Elsayas, and I. I. I. Mansy, "Grid impedance estimation for islanding detection and adaptive control of converters," *IET Power Electronics*, vol. 10, no. 11, pp. 1279–1288, 2017.
- [10] D. Martin and E. Santi, "Auto tuning of digital deadbeat current controller for grid tied inverters using wide bandwidth impedance identification," in *2012 Twenty-Seventh Annual IEEE Applied Power Electronics Conference and Exposition (APEC)*, 2012, pp. 277–284.
- [11] L. Asiminoaei, R. Teodorescu, F. Blaabjerg, and U. Borup, "A digital controlled PV-inverter with grid impedance estimation for ENS detection," *IEEE Transactions on Power Electronics*, vol. 20, no. 6, pp. 1480–1490, 2005.
- [12] D. Reigosa, F. Briz, C. Charro, P. Garcia, and J. Guerrero, "Active Islanding Detection Using High-Frequency Signal Injection," *IEEE Transactions on Industry Applications*, vol. 48, no. 5, pp. 1588–1597, 2012.
- [13] D. Reigosa, F. Briz, C. Blanco, P. Garcia, and J. Manuel Guerrero, "Active Islanding Detection for Multiple Parallel-Connected Inverter-Based Distributed Generators Using High-Frequency Signal Injection," *IEEE Transactions on Power Electronics*, vol. 29, no. 3, pp. 1192–1199, 2014.
- [14] L. Asiminoaei, R. Teodorescu, F. Blaabjerg, and U. Borup, "A digital controlled pv-inverter with grid impedance estimation for ens detection," *IEEE Transactions on Power Electronics*, vol. 20, no. 6, pp. 1480–1490, Nov 2005.
- [15] T. Roinila, M. Vilko, and J. Sun, "Online grid impedance measurement using discrete-interval binary sequence injection," in *2013 IEEE 14th Workshop on Control and Modeling for Power Electronics (COMPEL)*, June 2013, pp. 1–8.
- [16] M. Cespedes and J. Sun, "Three-phase impedance measurement for system stability analysis," in *2013 IEEE 14th Workshop on Control and Modeling for Power Electronics (COMPEL)*, June 2013, pp. 1–6.
- [17] M. A. Azzouz and E. F. El-Saadany, "Multivariable grid admittance identification for impedance stabilization of active distribution networks," *IEEE Transactions on Smart Grid*, vol. 8, no. 3, pp. 1116–1128, May 2017.
- [18] M. Cespedes and J. Sun, "Adaptive control of grid-connected inverters based on online grid impedance measurements," *IEEE Transactions on Sustainable Energy*, vol. 5, no. 2, pp. 516–523, April 2014.
- [19] M. Céspedes and J. Sun, "Online grid impedance identification for adaptive control of grid-connected inverters," in *2012 IEEE Energy Conversion Congress and Exposition (ECCE)*, Sept 2012, pp. 914–921.
- [20] M. Sumner, B. Palethorpe, and D. Thomas, "Impedance measurement for improved power quality-Part I: the measurement technique," *IEEE Transactions on Power Delivery*, vol. 19, no. 3, pp. 1442–1448, 2004.
- [21] N. Hoffmann and F. Fuchs, "Minimal Invasive Equivalent Grid Impedance Estimation in Inductive  $\pi$ 2013;Resistive Power Networks Using Extended Kalman Filter," *IEEE Transactions on Power Electronics*, vol. 29, no. 2, pp. 631–641, 2014.
- [22] X. Guo, Z. Lu, X. Sun, H. Gu, and W. Wu, "New grid impedance estimation technique for grid-connected power converters," *Journal of Engineering Research*, vol. 2, no. 3, p. 19, 2014. [Online]. Available: <http://dx.doi.org/10.7603/s40632-014-0019-7>
- [23] L. Asiminoaei, R. Teodorescu, F. Blaabjerg, and U. Borup, "Implementation and Test of an Online Embedded Grid Impedance Estimation Technique for PV Inverters," *IEEE Transactions on Industrial Electronics*, vol. 52, no. 4, pp. 1136–1144, 2005.
- [24] A. Timbus, P. Rodriguez, R. Teodorescu, and M. Ciobotaru, "Line Impedance Estimation Using Active and Reactive Power Variations," in *IEEE Power Electronics Specialists Conference, 2007. PESC 2007*, 2007, pp. 1273–1279.
- [25] A. Riccobono, S. K. A. Naqvi, A. Monti, T. Caldognetto, J. Siegers, and E. Santi, "Online wideband identification of single-phase ac power grid impedances using an existing grid-tied power electronic inverter," in *2015 IEEE 6th International Symposium on Power Electronics for Distributed Generation Systems (PEDG)*, June 2015, pp. 1–8.
- [26] T. Roinila, T. Messo, and A. Aapro, "Impedance measurement of three phase systems in dq-domain: Applying mimo-identification techniques," in *2016 IEEE Energy Conversion Congress and Exposition (ECCE)*, Sept 2016, pp. 1–6.
- [27] A. Suárez-González, P. García, Á. Navarro-Rodríguez, G. Villa, and J. M. Cano, "Sensorless unbalance correction as an ancillary service for lv 4-wire/3-phase power converters," in *2017 IEEE Energy Conversion Congress and Exposition (ECCE)*, Oct 2017, pp. 4799–4805.
- [28] A. Arriagada, J. Espinoza, J. Rodríguez, and L. Moran, "On-line filtering reactance identification in voltage-source three-phase active-front-end rectifiers," in *The 29th Annual Conference of the IEEE Industrial Electronics Society, 2003. IECON '03*, vol. 1, Nov. 2003, pp. 192–197 vol.1.
- [29] P. García, J. M. Guerrero, J. García, A. Navarro-Rodríguez, and M. Sumner, "Low frequency signal injection for grid impedance estimation in three phase systems," in *2014 IEEE Energy Conversion Congress and Exposition (ECCE)*, Sept 2014, pp. 1542–1549.

## **G.2 Sensorless Unbalance Correction as an Ancillary Service for LV 4-Wire/3-Phase Power Converters**



## Sensorless Unbalance Correction as an Ancillary Service for LV 4-Wire/3-Phase Power Converters

Andrés Suárez-González, Pablo García, Ángel Navarro-Rodríguez, Geber Villa and Jose M. Cano  
University of Oviedo. Dept. of Elec., Computer & System Engineering  
Gijón, 33204, Spain

e-mail: suarezandres@uniovi.es, garciafpablo@uniovi.es, navarroangel@uniovi.es, villageber.uo@uniovi.es, jmcano@uniovi.es

**Abstract**—This paper describes a method to provide LV four-wire three-phase power converters with the capability of correcting unbalance as an ancillary service to the main role that they play in the distribution system (distributed generator, energy storage system, drive, etc). Typically, dedicated grid/load current sensors are needed to effectively comply with unbalance compensation tasks, increasing system cost and reducing reliability. This is due to the difficulties that arises in the extraction of the zero and negative voltage components from the voltages at the PCC, such as the inadequate resolution of full-scaled voltage sensors and limited spectral separation. In this paper, the proposed compensation method does not rely on any more sensors that those typically used in VSCs, and in any case, those sensors are limited to the point of connection of the power converter. High frequency signal injection is evaluated for the compensation. For the zero sequence, an especial arrangement of the converter voltage sensors together with a repetitive controller is used.

### I. INTRODUCTION

The adoption of distributed generation has increased in the last years due to both politics and economics regulations [1], [2], emerging power electronics converters topologies which allow to improve network quality and reliability [3] and decrease in the costs for distributed generation. Power converters have been employed at the transmission network to improve power transmission capability, such as Static Synchronous Compensator (STATCOM) [4], Static Synchronous Series Compensator (SSSC) [5] and Unified Power Flow Controller (UPFC) [4]. Similar topologies have been later integrated at distribution levels i.e. Active Power Filters (APF) [6]–[8], allowing the increase of the distributed generation penetration and overcoming some problems related to the decentralized generation approach.

Among the problems related to distributed generation paradigm [9], [10], current and/or voltage unbalance or sag has recently received much attention [11]–[13]. There are several international standards which recommend maximum limits of the voltage unbalance: ANSI Standard C81.1 requires to keep

The present work has been partially supported by the predoctoral grants program Severo Ochoa for the formation in research and university teaching of Principado de Asturias PCTI-FICYT under the grant ID BP14-135. This work is also supported in part by the Research, Technological Development and Innovation Program Oriented to the Society Challenges of the Spanish Ministry of Economy and Competitiveness under grants ENE2013-44245-R and ENE2016-77919-R and by the European Union through ERFED Structural Funds (FEDER).

it within 3% [14], International Electrotechnical Commission (IEC) and the Comité Européen de Normalisation Electrotechnique (CENELEC) recommends the limit of 2% [15], [16].

Unbalance compensation can be achieved by shunt, series, or series/shunt combination of the power converter [17]. Among the three structures, series/shunt allows for an optimal [18] sharing of the voltage/current compensation. However, it requires a dedicated converter for the compensation problem. Solely shunt converter compensation can lead to high compensation currents through the converters, reducing the active/reactive power supply capability, and thus some sharing mechanism among the APF is needed [12]. Sharing of unbalance can be done either by exchanging information among the microgrid converters or by an autonomous method which is implemented in the form of a droop control [12], [13].

Measurement of the unbalanced components, negative and zero sequence voltages and currents, is a challenging task. By one side, use of the negative and zero sequence voltages at the PCC is affected by the ration between the grid impedance and the load to be compensated. By the other, use of negative and zero sequence currents needs for additional current sensors to be placed either at the load or at the grid side. At this paper, it is proposed to overcome these limitations by a combination of novel techniques. Negative sequence will be measured from the converter current sensors and by adding an additional excitation high-frequency signal over the voltage command. This high-frequency signal will interact with the unbalance load, creating a high-frequency negative current that will be used for the compensation. Zero sequence voltage will be measured by using a dedicated voltage sensor, fully scaled to this signal. This will allow to increase the resolution while, in conjunction with another two phase-neutral sensors, will allow the synchronization of the power converter to operate normally. Zero sequence compensation will also explore the use of the high-frequency signal in order to boost the measurement process.

This paper is organized as follows. In section II, a novel modeling technique will be used to analytical highlight the coupling between the positive, negative and zero current sequences with non-balanced loads and voltage unbalances. The proposed analysis allows for obtaining the expressions of the complex current vectors at the  $\alpha\beta$  reference frame



the current vector and  $V_{\alpha\beta}^+$ ,  $V_{\alpha\beta}^-$  and  $V_{\alpha\beta}^0$  are the positive, negative and zero sequence magnitudes of the voltage vector.

The above expressions have been evaluated by numerical simulation. For that, different changes at the phase impedance values as well as the phase voltages were applied. The results given by the proposed expressions have been compared with the results of a simulation in the  $abc$  reference frame and validated once both approaches were in close agreement.

Figures 3, 4 and 5 show, respectively, the voltage vector at the  $\alpha\beta 0$  reference frame, the considered grid impedance and current vector at the  $\alpha\beta 0$  reference frame. The simulation is carried out for a three phase system in a wye-connection with neutral configuration. The different test conditions are following enumerated: Initially, the system is at balanced condition. As expected,  $\Delta Z = 0$  and the angle of the asymmetry is also hold at zero. At  $t = 0.1s$ , the impedance from the three phases is changed from 180deg to 60deg for phase  $a$ , from 180deg to  $-90deg$  for phase  $b$  and from 180deg to 90deg for phase  $c$ . Consequently both  $\Sigma Z$  and  $\Delta Z$  vary from 1p.u. to 0.33p.u and from 0p.u. to 0.7p.u. respectively. It is also important to note that the  $\theta$  value is equal to the unbalance orientation, resulting in a value of 21deg. In summary, the unbalance level is codified by the  $\Delta Z$  level and the  $\theta$  angle provides its direction. The effect of the unbalance is coupled to the current vector components, as shown in 5. When the impedance unbalance is applied, the negative sequence component of the current vector ( $I_{\alpha\beta}^-$ ) is modulated according to the developed expressions. Considering the neutral connection, an homopolar current ( $I_0$ ) flows into the system.

Effects of a direct unbalance of the voltage vector at the PCC is analyzed starting at  $t = 0.2s$ . Phase  $b$  is lagged 90 respect to previous situation. Simultaneously, the impedance of phase  $b$  and  $c$  is changed to zero and the module of phase  $c$  is decreased to 0.7p.u. As expected, this causes a negative sequence voltage to be applied into the system and a variation in the resulting zero sequence voltage. Finally, at  $t = 0.3s$ , the voltage disturbance is cleared but the impedance values are kept unbalanced with  $|Z_a| = 0.8p.u.$ ,  $|Z_b| = 1 p.u.$  and  $|Z_c| = 0.7 p.u.$  This results in a variation of the negative sequence current and in the homopolar voltage as well.

From (8), it is clear load unbalances will cause negative and zero sequence currents to appear, which potentially will create an unbalance in the grid supplied voltages. Compensation can be done by injecting a negative and zero sequence currents in opposition to the respective unbalanced currents [12]. There are several methods proposed in the literature to compensate for this, all of them requires to separate (filter) the negative and zero sequences from the positive one and to cancel it out by using negative and zero sequence current controllers [12], [13]. In the following section, a compensation method based on the injection of a high frequency signal is proposed. The method will enable the measurement of the grid impedance from the converter side currents, thus leading to a sensorless compensation.

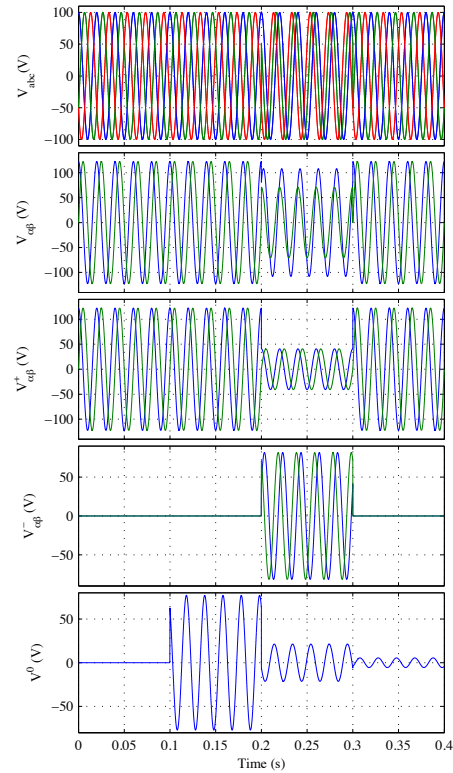


Fig. 3. Simulation results for the voltage at the PCC. From top to bottom: a) phase voltages, b)  $\alpha, \beta$  components, c), d) and e) are the positive, negative and zero components of the voltage vector.

### III. HFS-BASED UNBALANCE COMPENSATION

The current equation (8) is valid for any excitation voltage with fixed frequency. Adding a balanced high frequency ( $\omega_c$ ) carrier-signal voltage,  $v_{\alpha\beta}^{h.f.}$ , as denoted by (10), to the voltage at the PCC, results in a high frequency current (11) that shows a negative sequence component which is determined by the impedance unbalance. However, two fundamental differences exist compared to the fundamental excitation: 1) as the high frequency voltage is created by the converter and superimposed to the fundamental voltage, the resulting high frequency converter current,  $i_c^{h.f.}$ , contains the unbalance information, hence, is not needed to measure the current at the load,  $i_l$ , or at the grid side,  $i_g$ , to proceed with the compensation (see

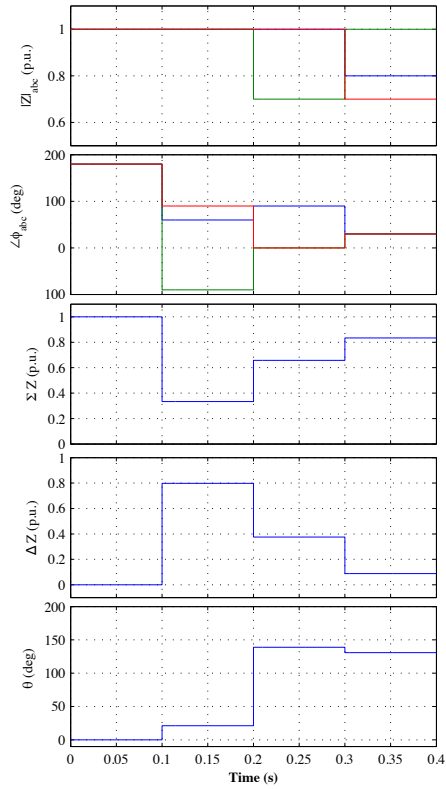


Fig. 4. Simulation results for the grid impedance as seen from the PCC. From top to bottom: a) module of the impedance, b) phase of the impedance, c) mean impedance, d) differential impedance and e) asymmetry angle.

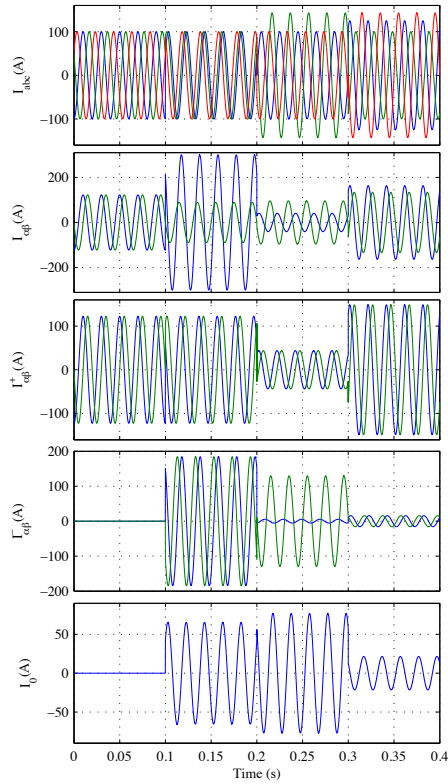


Fig. 5. Simulation results for the grid currents at the PCC. From top to bottom: a) phase currents, b)  $\alpha, \beta$  components, c), d) and e) are the positive, negative and zero components of the current vector.

Fig. 1); 2) filtering the negative sequence current from the positive one is easier at higher frequencies, since there is more spectral separation. This will allow to increase the resolution of the system to light unbalanced conditions.

$$\mathbf{v}_{\alpha\beta}^{hf} = V^{hf} e^{j\omega_c t} \quad (10)$$

$$\mathbf{i}_{\alpha\beta}^{hf} = V^{hf} \sum_{i=1}^n \left[ \Sigma Y_i^{hf} e^{j\omega_c t} + \Delta Y_i^{hf} e^{j(-\omega_c t + \theta_i^e)} \right] \quad (11)$$

Adding the appropriate value of negative sequence high frequency voltage allows to fully compensate the negative

sequence current arising from (11). Applying (8) to the carrier frequency and forcing  $\mathbf{i}_{C\alpha\beta}^{hf-}$  to be zero leads to

$$\mathbf{v}_{\alpha\beta}^{hf-} = \mathbf{v}_{\alpha\beta}^{hf+} \frac{-\Delta Y_i^{hf} e^{j\theta_i^e}}{\Sigma Y_i^{hf-}}. \quad (12)$$

As the information of the load unbalance is still included in  $\mathbf{v}_{\alpha\beta}^{hf-}$ , the proper correction action at grid frequency can be derived from this value.

In regard to the high frequency excitation signal, its magnitude and frequency values can be tuned separately. From a power quality perspective, increasing the frequency and reducing the magnitude is preferred. However, this reduces the signal to noise ratio of the method. Additionally, the injected

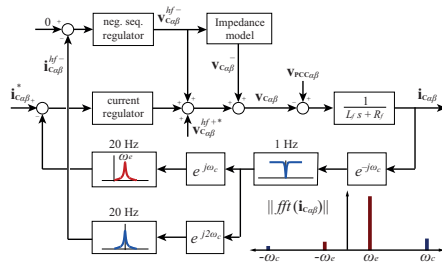


Fig. 6. High frequency signal injection and signal processing. Spectrum showing the main components of the converter current ( $i_c$ ) is shown on the lower right corner.

frequency should not be a harmonic of the fundamental frequency, in order to avoid the reaction of any existing harmonic compensator connected to the grid [20]. For this paper, the values shown at Table I have been chosen.

The control scheme shown in Fig. 6 is used to compensate for the negative sequence current at grid frequency. A positive sequence high frequency (333Hz) carrier voltage,  $v_{C\alpha\beta}^{hf+}$ , is added to the converter voltage, causing a negative sequence component to appear in the converter current at the same frequency,  $i_{C\alpha\beta}^{hf-}$ . Provided that the grid side is free from this frequency component and mostly balanced, this negative sequence component is the same that could be observed at the load, i.e.  $i_{C\alpha\beta}^{hf-} = -i_{\alpha\beta}^{hf-}$ . This negative sequence current is obtained from the converter current and controlled to be zero by using two PI regulators, one per each axis. The output of this regulator,  $v_{C\alpha\beta}^{hf-}$ , is used to estimate the negative sequence to be added at grid frequency to the converter voltage,  $v_{C\alpha\beta}^-$ , in order to achieve the compensating objective. An unbalance impedance model is used to relate injections at both frequencies, provided that a linear load is connected to the PCC.

#### IV. ZERO-SEQUENCE COMPENSATION

Zero-sequence currents arises in the LV distribution system as a consequence of both unbalanced and non-linear loads. The local compensation of zero-sequence currents in order to avoid their propagation upstream from the PCC is a desirable ancillary service for power converters, though only four-wire topologies are valid to comply with this function. This task can be easily done by measuring the zero-sequence current at the grid side and implementing a closed loop strategy for compensating it. Unfortunately, this requires not only an additional sensor but also the connection or communication between distant points. A theoretical alternative comes from the compensation of the zero-sequence voltage at the PCC, which could be calculated from the grid phase-voltage sensors of the VSC. However, the use of three voltage sensors ranged

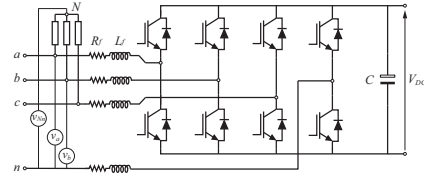


Fig. 7. Zero sequence voltage compensation. Proposed sensor arrangement for the measurement of the zero sequence component.

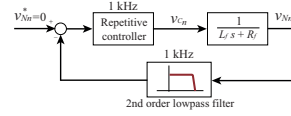


Fig. 8. Zero sequence voltage compensation. Control loop modeling based on the use of a repetitive controller.

at full scale to measure the voltages at the PCC makes it difficult to provide a suitable resolution in the calculation of this value, and can be even impossible in the interconnection to strong power systems. The arrangement proposed in Fig. 7 for a four-leg topology is used in this paper to solve this adversity. Two full-scale sensors are combined with a third one, ranged at a much lower scale. The latter sensor is devoted to measure the zero-sequence voltage component directly, by connecting it between the grounded neutral point of the installation and the artificial neutral point of a three-phase balanced high impedance load, intentionally located at the converter POC. The analytical expression for the zero sequence voltage is given by (13).

$$v_{Nn} = \frac{1}{3} (v_a + v_b + v_c) = v^0. \quad (13)$$

After applying a second-order low-pass filter to remove the high frequency components of  $v_{Nn}$ , a simple resonant controller could be used to cancel the fundamental frequency zero-sequence component seen from the grid side. Nevertheless, a repetitive controller (RC) was selected for this application in order to also remove other zero-sequence frequencies. This is of especial interest in this type of installations in which the massive use of single-phase non-linear loads can cause a significant flow of triplen current harmonics. Fig. 8 shows the control loop, which cancels the zero-sequence components by adding the proper signal to the modulation of the neutral leg of the converter. Notice that, although the total modulation of this leg contains other zero-sequence components to counteract the effect of the traditional zero sequence injection in the other legs, only the added output of the RC appears in  $v_{cn}$ .

#### V. SIMULATION RESULTS

For the simulation results, the network topology shown in Fig. 1 is used. The loads connected to the PCC are a

TABLE I  
SYSTEM PARAMETERS

Converter parameters	Value
Power [kW]	100
DC Link Voltage [V]	850
Max Current [A]	200
Switching frequency [Hz]	5000
AC Filter	$L_f = 5mH, R_f = 0.2\Omega$
Grid impedance	$L_g = 1mH, R_g = 0.02\Omega$
DC bus capacitor [ $\mu F$ ]	4400
Loads	
Three phase balance load	$R_l = 18\Omega$
Single phase loads	$R_{ls} = 18\Omega$
Control tuning	
$T_s$ [ $\mu s$ ]	100
DC voltage loop	$K_p = 0.2212, K_i = 80$
Current control loop	$K_p = 55.2920, K_i = 15$
High frequency parameters	
Carrier voltage [V]	10.0
Carrier frequency [Hz]	333

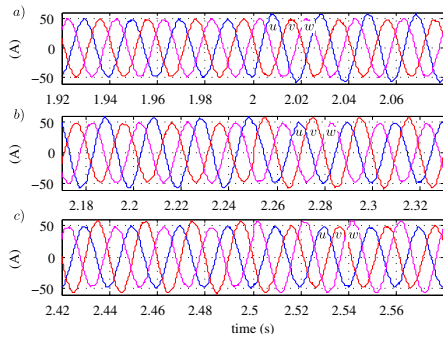


Fig. 9. Simulation results. Phase currents at grid for single phase loads connected at phases *a*), *u*,  $t = 2s$ ; *b*), *v* (*u* disconnected),  $t = 2.25s$ ; *c*), *w* (*v* disconnected),  $t = 2.5s$ . Load is resistive for the three cases  $R_l = 13.25\Omega$ .

three phase  $RL$  load and three single phase  $R$  loads between phases *u*, *v*, *w* and the neutral. These single phase loads are sequentially connected and disconnected in order to see the effects on the negative sequence currents. The parameters for the simulation are given at Table I. Phase grid currents when the single phase loads are connected are shown at Fig. 9. As clearly shown, the unbalance at the grid current is noticeable, being, as expected, the phase carrying more current the one at which the load is connected. The magnitudes of the negative sequence currents for the grid and converter current vectors are represented at Fig. 10 a), b) respectively. From Fig. 10 it is clear that both currents have information about the unbalance. However, using the converter current has important drawbacks due to the poor transient response. On the other side, using the grid current needs for additional current sensors in the grid side or at each feeder, which increases the system costs and decreases the reliability. For improving the unbalance measurement using only the converter side current sensors, a

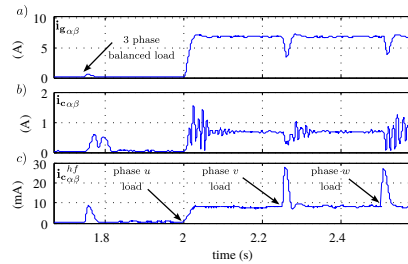


Fig. 10. Simulation Results. Negative sequence component magnitude resulting from single phase load connection at the PCC. *a*), negative sequence current ( $-50Hz$ ) for grid current vector; *b*), negative sequence current ( $-50Hz$ ) for converter current vector; *c*) negative sequence carrier current ( $-333Hz$ ) for converter current vector.

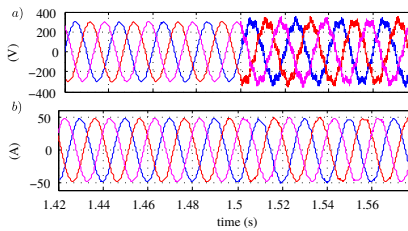


Fig. 11. Simulation results. *a*) phase voltages at PCC, *b*) phase currents at grid. High frequency signal injection is activated at  $t = 1.5s$ . THD is 6% and 3% for the voltages and the currents respectively.

high frequency signal is injected by the converter, as shown in Fig. 6. The high frequency signal added to the fundamental voltage command is shown at Fig. 11. Obviously, the injected high frequency current increases the resulting THD, both in the currents and in the voltages at the PCC. However, for the parameters shown at Table I, the THD is below the maximum allowed by international standards [14]–[16]. The resulting high frequency negative sequence current (being for the chosen high frequency frequency at  $-333Hz$ ) is shown at Fig. 10 c). From the figure, it is clear that the transient response is far better compared to the fundamental negative sequence current (Fig. 10 b). It is worth noting that the same bandwidth is used for isolating the negative sequence and the negative carrier currents (see Fig. 6). The transient shown when the three phase balance load is connected is because the filter used to isolate the negative carrier current can not reject the high frequency components from the transient. Alternatives based on the use of observers, already proposed for sensorless control of AC drives can be used if needed. However, it is considered that the compensation of the negative sequence current is an steady state phenomena and, even if fast transient response is desired, it is not an strong requirement.

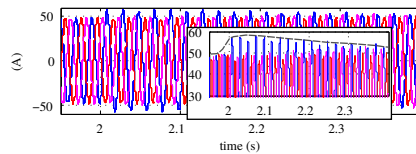


Fig. 12. Simulation results. Grid phase currents. Unbalance at phase  $u$  at  $t = 2s$ . Compensation using the high frequency negative sequence current is activated at  $t = 2.1s$ . Zoomed  $y$  axis is represented in the box.

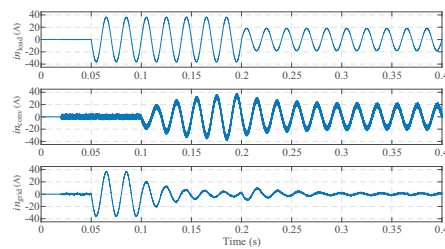


Fig. 13. Simulation results. Zero sequence compensation. (a) neutral current at the load, (b) current at the converter neutral leg, and (c) neutral current at the grid side.

The compensation results for the grid phase currents are shown at Fig 12. The unbalance, though not totally compensated, is noticeable reduced. In Fig. 13, the proper compensation of the zero sequence component is demonstrated. The neutral current at the load is presented in Fig. 13.a). As it can be seen, two single-phase loads are connected to phase  $u$  at time  $0.05s$  and one of them is disconnected at time  $0.2s$  to test transient performance. The application of the RC proposed in this paper together with the special arrangement of voltage sensors, leads to a fast compensation of grid neutral current by the converter.

VI. CONCLUSIONS

In this paper, a method for measuring and compensating unbalance currents for 4-wire 3-phase converters is presented. A high frequency signal injection is used for the negative sequence and a RC for zero sequence components. Both strategies allow a sensorless high-resolution alternative for unbalance compensation. A model considering unbalance loads and voltages has been developed. This model allows to estimate the negative sequence currents generated by the unbalance loads as well as by the cross coupling terms. From the general model, a high frequency model which show the resulting high frequency current in the presence of unbalance conditions has been obtained.

REFERENCES

[1] R. Lasseter, "Microgrids," in *Power Engineering Society Winter Meeting*, 2002. *IEEE*, vol. 1, 2002, pp. 305 – 308 vol.1.

[2] R. Lasseter and P. Paigi, "Microgrid: a conceptual solution," in *Power Electronics Specialists Conference, 2004. PESC 04. 2004 IEEE 35th Annual*, vol. 6, June 2004, pp. 4285 – 4290 Vol.6.

[3] J. M. Guerrero, "Editorial special issue on power electronics for microgrids, part ii," *Power Electronics, IEEE Transactions on*, vol. 26, no. 3, pp. 659 –663, March 2011.

[4] N. G. Hingorani and L. Gyugyi, *Understanding FACTS: Concepts and Technology of Flexible AC Transmission Systems*. New York: IEEE, 2000.

[5] L. Gyugyi, C. Schauder, and L. Sen, "Static synchronous series compensator: A solid-state approach to the series compensation of transmission lines," *IEEE Transactions on Power Delivery*, vol. 12, no. 1, pp. 406–417, 1997.

[6] B. Singh, K. Al-Haddad, and A. Chandra, "A review of active filters for power quality improvement," *Industrial Electronics, IEEE Transactions on*, vol. 46, no. 5, pp. 960 –971, Oct 1999.

[7] V. Corasaniti, M. Barbieri, P. Arnera, and M. Valla, "Comparison of active filters topologies in medium voltage distribution power systems," in *Power and Energy Society General Meeting - Conversion and Delivery of Electrical Energy in the 21st Century, 2008 IEEE*, July 2008, pp. 1 –8.

[8] H. Fujita and H. Akagi, "The unified power quality conditioner: The integration of series and shunt-active filters," *IEEE Transactions on Power Electronics*, vol. 13, no. 2, pp. 315–322, 1998.

[9] F. Bastiao, P. Cruz, and R. Fiteiro, "Impact of distributed generation on distribution networks," in *Electricity Market, 2008. EEM 2008. 5th International Conference on European*, May 2008, pp. 1 –6.

[10] R. Walling, R. Saint, R. Dugan, J. Burke, and L. Kojovic, "Summary of distributed resources impact on power delivery systems," *Power Delivery, IEEE Transactions on*, vol. 23, no. 3, pp. 1636 –1644, July 2008.

[11] V. Khadkikar, "Enhancing electric power quality using upqc: A comprehensive overview," *IEEE Transactions on Power Electronics*, vol. 27, no. 5, pp. 2284–2297, 2012.

[12] M. Savaghebi, A. Jalilian, J. Vasquez, and J. Guerrero, "Autonomous voltage unbalance compensation in an islanded droop-controlled microgrid," *IEEE Transactions on Industrial Electronics*, vol. PP, no. 99, p. 1, 2012.

[13] C. Po-Tai, C. Chien-An, L. Tzung-Lin, and K. Shen-Yuan, "A cooperative imbalance compensation method for distributed-generation interface converters," *IEEE Transactions on Industry Applications*, vol. 45, no. 2, pp. 805–815, 2009.

[14] *American National Standard for Electrical Power Systems and Equipment, Voltage Ratings (60 Hertz)*. ANSI c84.1-1995.

[15] *Voltage characteristics of electricity supplied by public distribution systems*. EN50160, 2011.

[16] *Electromagnetic compatibility (EMC) Part 4-30: Testing and measurement techniques and Power quality measurement methods*. IEC 6100-4-30, 2003.

[17] V. Khadkikar and A. Chandra, "Upqc-s: A novel concept of simultaneous voltage sag/swell and load reactive power compensations utilizing series inverter of upqc," *Power Electronics, IEEE Transactions on*, vol. 26, no. 9, pp. 2414 –2425, Sept. 2011.

[18] A. Al-Zamil and D. Torrey, "A passive series, active shunt filter for high power applications," *Power Electronics, IEEE Transactions on*, vol. 16, no. 1, pp. 101 –109, Jan 2001.

[19] J. Guerrero, M. Savaghebi, and R. Teodorescu, "Modeling, analysis, and design of stationary reference frame droop controlled parallel three-phase voltage source inverters," in *Power Electronics and ECCE Asia (ICPE ECCE), 2011 IEEE 8th International Conference on*, June 2011, pp. 272–279.

[20] F. Briz, D. Diaz-Reigosa, M. Degner, P. Garcia, and J. Guerrero, "Dynamic behavior of current controllers for selective harmonic compensation in three-phase active power filters," in *Energy Conversion Congress and Exposition (ECCE), 2011 IEEE*, June 2011, pp. 2892–2899.



### **G.3 Improved Efficiency of Local EPS through Variable Switching Frequency Control of Dis- tributed Resources**



## Improved Efficiency of Local EPS through Variable Switching Frequency Control of Distributed Resources

José M. Cano, Andrés Suárez, Ángel Navarro-Rodríguez and Pablo García

Department of Electrical Engineering

University of Oviedo

33204 Gijón, Spain

Email: jmcانو@uniovi.es, suarezandres@uniovi.es, navarroangel@uniovi.es, garciafpablo@uniovi.es

**Abstract**—This contribution explores the possibility of improving the global efficiency of three-phase inverter-based distributed resources (DR) embedded in low-voltage (LV) distribution feeders, by the adaptation of their switching frequency (SF) to the operation point of both the converter and local loads. The core of this proposal lies on the fact that in a good number of applications, in both services and residential sectors, the owner of the DR is also in charge of the losses caused in the local electric power system (EPS). This fact leaves room for a global optimization of the power losses, i.e., converter losses will be considered together with those losses caused by the current harmonics injected into the local grid. A dynamic adaptive SF frame of the DR is considered in this proposal to allow its operation beyond its rated frequency at light loads, subjected to the thermal constraints of the device. Simulation results obtained using PLECS software as well as an experimental validation of the method are included.

### I. INTRODUCTION

The soaring use of inverters in distributed generation and energy storage applications has increased the attention paid to the efficiency of these devices in recent years. The efficiency of power converters interconnected to the EPS is influenced by regulations such as [1], which states limits for the harmonic current injection of these devices at the PCC. In common applications, such as solar and wind, power converters operate rarely at rated values, being the efficiency at light loads a source of great concern [2]. According to [3], the tests to comply with [1] takes only into account the first 40 harmonics. This allows using relatively low switching frequencies (SF), typically higher than 3 kHz, as the high-frequency harmonics induced by PWM will be in this case over the stated limit.

The efficiency of the inverter as a separate unit is the only concern of the owner when he is not responsible for the losses upstream. In this case, once verified that the selected switching frequency complies with the harmonic emission limits, it can be maintained constant at any operating condition. In most cases, increasing the SF reduces the efficiency of the device due to the rise of the converter switching losses, while decreasing this parameter could make the device not conform with [3]. Notice that the tests must be conducted not just at 100% but also at 66% and 33% of the output rated current.

In a good number of common applications, e.g. PV and small wind turbines used in residential buildings and connected to the LV grid, the owners of the DR are also responsible for the local losses caused by the inverter current

harmonics both in the line and local loads, up to the metering location at the distribution transformer (either on the LV or MV side). In assessing the efficiency of the DR in this scenario, the inverter losses should be taken into account together with the distortion losses caused in the local grid. Furthermore, the high impedance of the transformer at high frequencies allow us to neglect those losses up from this point. Even if by design, a thermal constraint in the increment of the SF at rated power is likely to exist, the possibility of operating the device at higher frequencies when working at light loads is still there. Increasing the SF rises the converter switching losses but reduces the distortion losses in the local grid at the same time. This fact, together with the great advances carried out in recent years in the field of grid impedance estimation techniques [4]–[9], opens the door for a dynamic optimization of the SF capable of achieving an improved overall efficiency.

In Section II a study of the effect of the SF on the harmonic emission in three-phase VSCs is carried out. Three-phase two-level inverters with first-order inductive filters are considered, as one of the preferred technologies in LV applications. The evaluation of inverter losses, considering thermal constraints, is presented in Section III. Section IV deals with the estimation of the distortion losses caused by the inverter in the local grid. The proposed method for the on-line optimization of the SF is described in Section V. Section VI presents a case study to demonstrate the validity of the proposal and experimental results are given in Section VII. Finally, the conclusions of the study are drawn in Section VIII.

### II. SWITCHING FREQUENCY AND CURRENT HARMONICS

As a general rule, a higher SF leads to a displacement of the harmonic spectrum of the voltage at the converter's terminals to a higher frequency range. Consequently, the inductive behavior of the filter and grid upstream yields to a reduction in the induced current harmonics due to the higher impedance of these inductances at the new frequencies. However, it is important to note that the IGBTs' dead-time limits the validity of the said statement, leading to the emergence of low-frequency harmonics (mainly 5<sup>th</sup> and 7<sup>th</sup> order) [10], [11] with a growing impact at higher SFs. Nevertheless, this effect can be mitigated by current regulators, whose bandwidth use to fall within these values. Fig. 1 shows the current distortion of an inverter given by the parameters shown in Table I as a

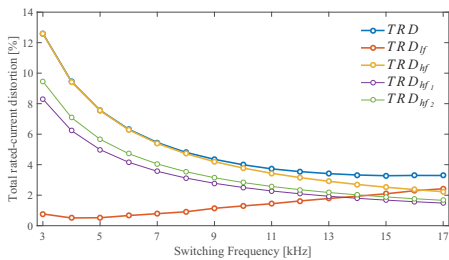


Fig. 1. Current  $TRD$  as a function of the SF for different frequency bands. Effect of the dead-time in low-frequency harmonics

function of the SF. This distortion has been reported as the total rated-current distortion ( $TRD$ ) according to [1], which can be defined as the total root-sum-square of the current harmonics created by the DR unit divided by the rated current capacity of that unit,  $I_n$ . In Fig. 1,  $TRD$  has been split in two terms,  $TRD_{lf}$  and  $TRD_{hf}$  using the 40<sup>th</sup> harmonic included in [3] as a limit between low and high frequencies. Thus, those parameters can be related as

$$TRD = \sqrt{TRD_{lf}^2 + TRD_{hf}^2}, \quad (1)$$

which allows to show the different behavior of the theoretical PWM harmonics and the non-idealities induced by the dead-time. As it is shown in Fig. 1, the effect of the dead-time reaches such an importance in  $TRD$  that increasing the SF over a certain limit becomes counterproductive. The use of dead-time compensation techniques [12], [13] could potentially raise this limit. It is also interesting to point out that the results shown in Fig. 1 are independent of the load of the converter, as only the fundamental component varies on a significant scale with this parameter. On the contrary, the values shown in this graph can be affected to some extent by the system impedance at the converter terminals, especially in weak systems. This suggests that an online measurement of harmonic distortion will provide better results than a theoretical estimation. Nonetheless, the simplicity of this estimation can be valuable in most cases.

### III. CONVERTER LOSSES AND THERMAL LIMITS

Converter losses,  $P_{VSC}$ , are mainly determined by switching losses,  $P_{sw}$ , and conduction losses,  $P_{cd}$  [14], [15]. Other issues should be considered when assessing the efficiency of these devices, such as cooling power; however, as they are not normally affected by the SF, they will not be considered in this work. Switching losses are strongly influenced by the SF,  $f_{sw}$ , as well as the load of the converter,  $c$ . Even if the power factor of the converter also affects this parameter due to variations in the commutation phenomenon, this effect is hardly noticeable and can be neglected with little error for the aim of this study. As increasing the SF results in a proportional rise of switching events, the relationship between SF and

TABLE I  
CONVERTER PARAMETERS

Hardware	
Grid voltage	$V_{rms} = 400$ V, $f = 50$ Hz
Rated power/current	$S = 30$ kVA, $I_n = 43.3$ A
System impedance	Ideal grid
Coupling inductor	$L_{filter} = 1.0$ mH, $R_{filter} = 0.16$ m $\Omega$
DC link	$v_{dc} = 800$ V, $C = 350$ $\mu$ F
IGBT modules	2MBI200HH-120-50
Dead-time	$t_d = 1$ $\mu$ s
Control	
PWM Type	Sym. regular sampled w/ 3 <sup>rd</sup> harm. injection
SF at rated power	$f_{sw} = 3$ kHz
PLL	Dual SOGI
Anti-aliasing filter	Butterworth 2 <sup>nd</sup> order, $f_c = f_{sw}/2$
Current reg. bandwidth	300 Hz
Power factor	1

switching losses is almost lineal. Conduction losses, for its part, are mainly affected by the load of the converter, and in a more subtle way, by the SF due to the increased current distortion that arises at lower frequencies. Taking these facts into consideration, an approach to the converter losses, taking  $c$  and  $f_{sw}$  as parameters, can be faced up by using

$$P_{VSC}(c, f_{sw}) = P_{sw}(c, f_{sw}) + P_{cd}(c, f_{sw}). \quad (2)$$

The assessment of the aforementioned power losses for the specific IGBT power modules mounted in the converter used for the experimental validation included in Section VII, is shown in Fig. 2. To obtain the said graph, a PLECS model of the converter was implemented. This model includes the thermal performance of the IGBT power modules, which allows to depict the operational constraints of the converter in terms of SF. Thus, the imperative derating of the device is shown in Fig. 3. This figure was calculated for each SF by assessing the load level of the converter at which the junction temperature of the solid state devices equals the temperature reached at rated values. The inclusion of these data in a two-dimensional look-up table together with the use of interpolation, is enough to obtain a good estimation of converter losses as a function of  $c$  and  $f_{sw}$  in the optimization scheme proposed in this work. The exploitation of this table for control purposes by operating the converter at variable SF is analyzed in Section V. In any case, it is clear from Fig. 3 that if the SF command  $f_{sw}^*$  lies on the forbidden area of the graph, it has to be reduced to the nearest feasible value,  $f_{sw}^{**}$ .

### IV. DISTORTION LOSSES IN THE LOCAL GRID

Even if limited by regulations, the injection of current harmonics into the distribution grid can cause significant power losses that are classified in two categories: (1) copper losses in the distribution line and distribution transformer and, (2) power losses in local loads. Notice that additional losses could exist upstream from the distribution transformer which are not on the Local EPS owner's responsibility. However, this term can be neglected not only because of the low value of the resistive contribution from the MV level when compared with the LV side, but also because of the low capability of high-order

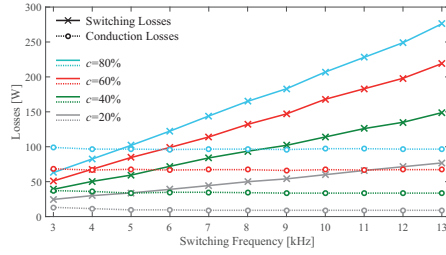


Fig. 2. Converter switching and conduction losses as a function of the SF

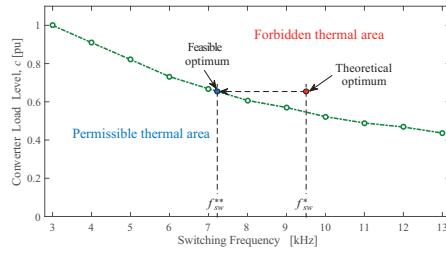


Fig. 3. Thermal constraints for variable SF operation

current harmonics to travel deep into the EPS. Fig. 4 shows a layout of the benchmark system considered in this paper. The Local EPS, with embedded DRs, is connected to the Area EPS through a distribution transformer, being the metering devices connected either in the MV or LV side according to the ownership of this piece of equipment. Both the DRs and the local loads are connected to the distribution line. Those local loads located close to the power converters are more prone to suffer from distortion losses. In Fig. 4, a local load is connected directly to DR point of coupling, PC, to highlight this phenomenon. The effect of the distortion power in local loads is different according to the type of device (motor, lighting, heating, etc.) and its nature (linear/non-linear). In any case, distortion power can be, as a general rule, considered undesirable [16]. Different types of penalization criteria could be considered in order to take into account the harmful effects of higher levels of injected current distortion in particular loads, e.g. cost associated to the loss of life. However, in this work only the cost associated with the power transmitted at non-fundamental frequency is taken into account. A pure resistive load is considered in this contribution as the easiest way to underline the benefits of the proposal.

A precise calculation of the power transmitted by the converter at harmonic frequencies can be done by assessing the expression

$$P_{losses} = Re\left\{\sum_{i=2}^N \mathbf{v}_{PCi} \cdot \mathbf{i}_{conv i}^*\right\}, \quad (3)$$

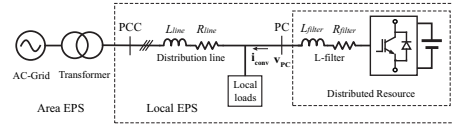


Fig. 4. Area EPS with embedded DRs

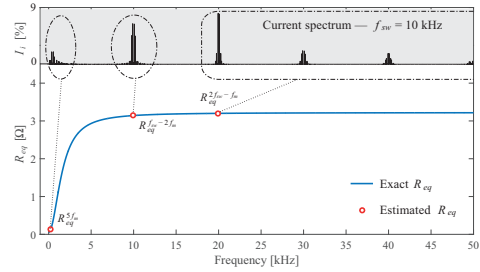


Fig. 5. Estimation of the resistive component of system impedance at the PC as a function of frequency

where  $\mathbf{i}_{conv i}$  and  $\mathbf{v}_{PCi}$  are the power invariant space vector harmonic components of the converter current and voltage at its point of coupling, obtained by applying the DFT algorithm. For the practical implementation of (3), natural sampling of voltages and currents at SF is not enough due to Nyquist limit, but oversampling can help in complying with these requirements. In any case, other simplified methods such as Goertzel algorithm [17] are better suited for on-line applications [18]. In this light method, just a selected number of harmonics are identified, which can be enough to calculate the resistive component of grid impedance,  $R_{eq}$ , at the most significative bands of the spectrum. This reduced set of values can be used together with the expected injection of current harmonics, as given in Fig. 1, to formulate a good estimation of the said power losses. Fig. 5 shows the value of  $R_{eq}$  for the installation depicted in Fig. 4, with the parameters shown in Table II. The identification of just 3 impedance values, one at the low-frequency band ( $5^{th}$  or  $7^{th}$ ) and two at the two lower PWM frequency bands (e.g.  $f_{sw} - 2f_m$  and  $2f_{sw} - f_m$ ,  $f_m$  being the modulation frequency), can be enough to estimate distortion losses by using

$$P_{losses} \approx 3I_n^2 \cdot (R_{eq}^{f_m} \cdot TRD_{if}^2 + R_{eq}^{f_{sw} - 2f_m} \cdot TRD_{hf1}^2 + R_{eq}^{2f_{sw} - f_m} \cdot TRD_{hf2}^2). \quad (4)$$

Notice that with this aim,  $TRD_{hf}$  has been segregated in two components,  $TRD_{hf1}$ , for the harmonic band around the SF and  $TRD_{hf2}$ , for the rest of higher frequency values. The specific contribution of these components can be observed in Fig. 1.

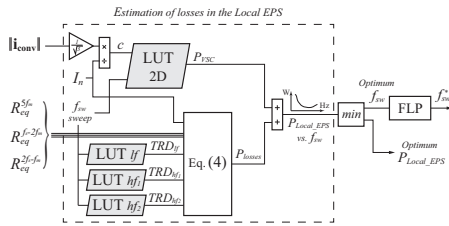


Fig. 6. On-line method for the optimization of the SF

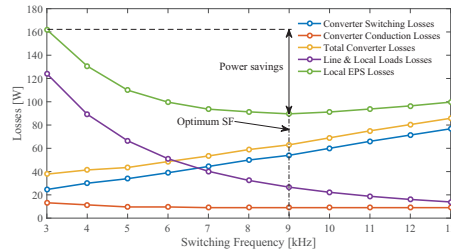
### V. ON-LINE OPTIMIZATION OF THE SWITCHING FREQUENCY

The fundamentals of the on-line optimization of the SF proposed in this work are schematically summarized in Fig. 6. The inputs for the algorithm are the space vector of the converter current, which is already available as calculated from current samples for the operation of its inner controller, and the resistive component of grid impedance for the different frequency bands considered in Section IV. The application of a look-up table system together with a SF sweep allows the on-line calculation of the  $P_{Local\_EPS}$  vs.  $f_{sw}$  curve for the present operating point. With this aim, the converter losses,  $P_{VSC}$ , are obtained from a 2D-look-up table built by adding the conduction and switching losses of the specific converter according to (2). A set of three 1D-look-up tables, built from the distortion data depicted in Fig. 2, provides the  $TRD$  of the converter at the different frequency bands for each SF used in the sweep. From these results, the losses at the line and local loads,  $P_{losses}$ , are obtained by using (4). The addition of both converter and line and local loads losses at each SF leads to the desired curve. Then, the minimum of this curve is identified, which gives the optimum losses at the local EPS and, even more important, the optimum SF for the current operating point. Notice that the bandwidth of the SF command,  $f_{sw}^*$ , must be much lower than the inner controllers of the inverter not to interfere with its dynamic performance. As a consequence, a low update rate of this command is acceptable and the required computational burden can be assumed by the controller without a significant effort either in a synchronous or asynchronous scheme. In order to avoid the effect of noise in the sampled parameters, as well as steep frequency variations due to sudden changes in the inverter load level or in the grid impedance – due to the connection/disconnection of local loads, a first-order low-pass (FLP) filter is used to smooth the frequency command.

Although not depicted in Fig. 6 for the sake of clarity, the frequency command,  $f_{sw}^*$ , should pass a final limitation stage in order to make the control compatible with the thermal constraints shown in Fig. 3. As already stated in Section III, if the pair  $(f_{sw}^*, c)$  lies in the forbidden area of this graph, the SF command is reduced to the maximum SF compatible with the present converter load level,  $f_{sw}^{**}$ .

TABLE II  
INSTALLATION PARAMETERS

<b>Transformer</b>	
Rated power	$S_n = 100$ kVA
Short-circuit impedance & resistance	$Z_{pu} = 0.06, R_{pu} = 0.01$
<b>Distribution Line</b>	
Length	$l = 200$ m
Resistance	$R_{line} = 0.2$ mΩ/m
X/R ratio	0.32
<b>Local Loads</b>	
Power factor	1
Active power	$P = 50$ kW

Fig. 7. Local EPS losses as a function of SF -  $c = 20\%$ 

### VI. CASE STUDY

In this section a case study is used to illustrate the advantages of using an overall efficiency optimization of the DR within its Local EPS. With this aim, the LV distribution feeder and the distributed generator (DG) depicted in Fig. 4 are considered. The parameters of the grid infrastructure are shown in Table II while those from the inverter-based DG are given in Table I (except for the system impedance, that for this case study is derived from Table II). Fig. 7 shows the total losses in the Local EPS, together with its different components, i.e. converter losses and grid & local loads losses for a DR working at 20% of its rated power with unity power factor. It is concluded from this drawing that increasing the SF from the design parameter, 3 kHz, to 9 kHz, reduces the Local EPS losses in a 44.6%, and improves the overall efficiency at this load level (i.e. the ratio between the Local EPS losses and the power delivered by the converter) in 1.20%.

Fig. 8 expands the analysis to different load levels of the DR. As it is depicted in this figure, connecting the values of the minimum Local EPS losses at each converter load level,  $c$ , leads to the optimum trajectory of the inverter SF. Furthermore, the thermal limit of the device is also given in Fig. 8. This limit is established by calculating the maximum acceptable SF at each load level, which is determined by the frequency that leads to the design temperature (i.e. the one obtained at 3 kHz and rated power). From the said graph it can be concluded that for the device under test, a variable SF mode with losses optimization is only feasible for loads lighter than 80% of rated power. Moreover, it is also observed that the

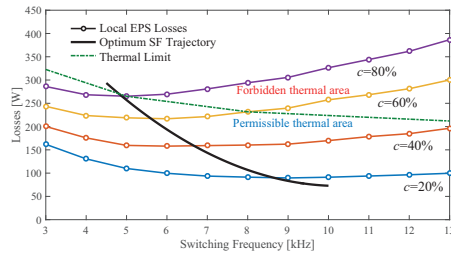


Fig. 8. Optimum trajectory of the SF as a function of converter load

benefit of the proposal is much more relevant at light loads: e.g. the saved power is higher at 20% than at 80% on both relative and absolute terms (72 W vs. 21 W and 1.20% vs. 0.09%).

Fig. 9 shows simulation results of the application of the on-line optimization method proposed in Section V to the present case study. An update rate of 10 ms was used for the SF command and a bandwidth of 0.6 Hz was selected for the FLP filter. The SF sweep included in the algorithm is conducted with a resolution of 100 Hz in order to limit the computational burden. As it is shown in Fig. 9 (a), the converter load level is started at  $c = 20\%$  and increased to  $c = 80\%$  after 2 s always with unity power factor. Moreover, the local loads stay at rated power according to Table II and are reduced to 50% of this value, i.e. 25 kW, at 4 s. Fig. 9 (b) shows the effect of the steep variation on the resistive component of grid impedance induced by the local load reduction, together with the slight changes caused by the modification of the SF along the process. The optimum SF value obtained by the algorithm along with the final SF command is depicted in Fig. 9 (c). The converter is started with a conservative SF value of 5 kHz and, from this instant, the algorithm competently tracks the optimum SF increasing the efficiency of the installation. In Fig. 9 (d) the optimum and real power savings, compared to a traditional operation of the DR at constant SF, are depicted. As expected, greater power savings are obtained with the converter working at light loads as well as with an increased value of the resistive component of grid impedance.

### VII. EXPERIMENTAL RESULTS

Two sets of experimental tests were carried out in this work: the first one is aimed to prove the power saving potential of the stated proposal, and the second, to demonstrate the validity of the on-line SF optimization method described in Section V.

#### A. Test 1

The test setup used in this case is shown in Fig. 10. A 4-quadrant grid simulator, TC.ACS by Regatron, is used to emulate the electric system, 400 V – 50 Hz, and a 0.32 mH inductor,  $L_1$ , is used to emulate the LV line and transformer according to Fig. 4. An almost purely resistive air-heating

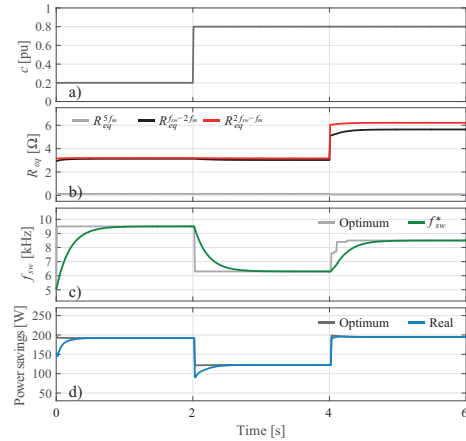


Fig. 9. Application of the optimization method to the proposed case study. (a) converter load profile, (b) grid impedance, (c) SF command, and (d) power savings

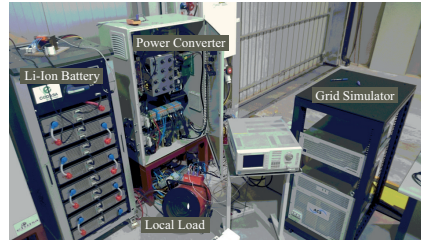


Fig. 10. Test setup.

system with a rated power of 9 kW is used to emulate the local loads according to the said figure. Finally, a custom-made three-phase two-level VSC, with a rated power of 30 kVA and a design SF of 6 kHz, is coupled to the grid through a 0.88 mH inductor,  $L_2$ , to play the role of the DR.

During this test the converter is operated in STATCOM mode at a light load, 10 kVA (i.e.  $c = 33\%$ ), delivering reactive power to the LV grid. Similar results are expected from other operation modes, due to the small influence of the power factor in converter losses, as it was stated in Section II. The three-phase voltages and currents at the coupling point of the DR (PC in Fig. 4) were registered in steady-state for different SFs within the range 6 kHz to 16 kHz. An off-line handling of these measurements were carried out to calculate their DFT, and subsequently, the losses at harmonic frequencies at the line and local loads (i.e. those caused by the air-heating system and stray resistance of  $L_1$ ) were calculated by the application of

TABLE III  
EXPERIMENTAL RESULTS -  $c = 33\%$

SF	Converter	Losses Line&Loads	Local EPS	Pwr. savings
6 kHz	781.2 W	253.8 W	1035.0 W	0.0 W
8 kHz	790.5 W	178.4 W	968.9 W	66.1 W
10 kHz	814.0 W	139.8 W	953.8 W	81.1 W
12 kHz	836.3 W	111.2 W	947.6 W	87.5 W
14 kHz	868.1 W	91.6 W	959.7 W	75.3 W
16 kHz	896.9 W	76.9 W	973.8 W	61.2 W

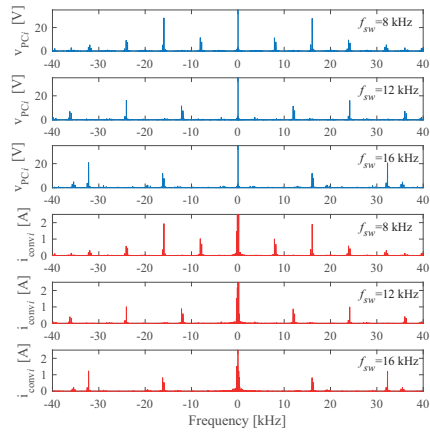


Fig. 11. Voltage and current spectra for different SFs during experimental tests

(3). For the particular case of the STATCOM operation mode, just adding the term at the fundamental frequency in (3) leads directly to the converter losses, so finally, the losses at the Local EPS can be computed in a simple way as

$$\begin{aligned}
 P_{Local\_EPS} &= \text{Re}\{\sum_{i=2}^N v_{PC1} i_{conv1}^*\} - \text{Re}\{\sum_{i=1}^N v_{PC1} i_{conv1}^*\} \\
 &= -\text{Re}\{v_{PC1} i_{conv1}^*\}.
 \end{aligned} \quad (5)$$

Notice that this is just a particular result, valid only for STATCOM operation mode. In a general scheme (inverter/rectifier mode), with the DR participating in the active power flow, a look-up table with and estimation of converter losses as a function of the SF and the load of the converter is to be used, as stated in Section III.

The test results are presented in Table III and Fig. 11. As expected, an optimum SF is obtained, capable of achieving the minimization of system losses. As it is highlighted in the said table, the operation at 12 kHz reduces system power losses in 87.5 W when compared with the operation at the design value. This means a reduction of around 8.4% of the losses at this operation point, and an improvement of the Local EPS efficiency of 0.87%.

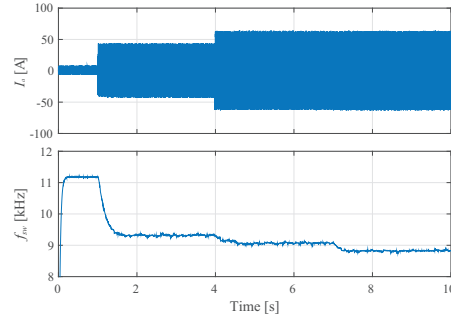


Fig. 12. On-line SF optimization test: (a) converter ac current - phase  $a$ , and (b) converter SF

### B. Test 2

Slight changes are introduced in the test setup for this case. The 30 kVA converter is now operated in inverter mode to effectively replicate the performance of a DR. With this aim the DC-bus of the converter is fed from the Li-Ion battery shown in Fig. 10 through a DC-DC stage. Furthermore, the converter is now coupled to the utility grid, 400 V - 50 Hz, through a dedicated distribution line and transformer according to the values shown in Table II. Four separate air-heating systems, each with a rated power of 9 kW, are used to emulate the local loads. The connection/disconnection of these systems allows to test the effect of a sudden change in system impedance.

The custom-made converter is operated through a controller using a TI C2000 Delfino™ TMS320F28335 MCU. The algorithm described in Section V was included in the firmware with the LUT system embedded in non-volatile RAM memory. Moreover, a variable SF inner current controller for the converter was specifically designed for this test, including an adaptive tuning of the associated regulators.

During the test the converter is started at a light load, 2.8 kVA (i.e.  $c = 9.3\%$ ), delivering active power to the grid with unity power factor. After 1 s the converter load level is increased to 17.1 kVA (i.e.  $c = 57.1\%$ ) and then to 26.9 kVA (i.e.  $c = 89.8\%$ ) at time 4 s. Fig. 12 shows the phase current of the converter during these variations together with the performance of the SF in reaction to those load step changes. Finally, at time 7 s one of the air-heating systems is added to the three devices already connected to the local grid, thus shifting the local demand from 27 kW to 36 kW. As predicted, the consequent change in system impedance at the converter point of coupling causes a variation of local losses moving the optimum value of the SF.

## VIII. CONCLUSIONS

This work presents an operation strategy for DRs based on an adaptive SF framework with the aim of achieving an overall

improvement of the efficiency within the Local EPS. The proposal demonstrates the interest in considering the converter losses together with the induced harmonic losses in the local line and loads when the ownership/operation of both assets are held by the same entity. The thermal limits of the power modules used in the inverter have been taken as a constraint in order to assure a safe operation of the device beyond its design SF when working at light loads. A LUT-based system, valid for an on-line implementation, was designed to provide the DR with a smart regulation of its SF. The results demonstrate that an improvement of the overall efficiency of the system at light converter loads by about 1% is readily achieved with the proposed method.

ACKNOWLEDGMENT

This work has been funded by the Spanish Government, Innovation Development and Research Office (MEC), under research grants ENE2014-52272-R and ENE2013-44245-R. It has also been partially supported by the predoctoral grant ID BP14-135 under the program Severo Ochoa for the formation in research and university teaching of Principado de Asturias PCTI-FICYT.

REFERENCES

[1] "IEEE standard for interconnecting distributed resources with electric power systems," *IEEE Std 1547-2003*, pp. 1–28, July 2003.

[2] Z. Chen, H. Wu, K. Sun, L. Ni, and Y. Xing, "Light-load efficiency optimization for module integrated converters in photovoltaic systems," in *Energy Conversion Congress and Exposition (ECCE), 2013 IEEE*, Sept 2013, pp. 5560–5565.

[3] "IEEE standard conformance test procedures for equipment interconnecting distributed resources with electric power systems," *IEEE Std 1547.1-2005*, pp. 1–62, July 2005.

[4] H. Gu, X. Guo, D. Wang, and W. Wu, "Real-time grid impedance estimation technique for grid-connected power converters," in *Industrial Electronics (ISIE), 2012 IEEE International Symposium on*, May 2012, pp. 1621–1626.

[5] N. Hoffmann and F. Fuchs, "Minimal invasive equivalent grid impedance estimation in inductive-resistive power networks using extended kalman filter," *Power Electronics, IEEE Transactions on*, vol. 29, no. 2, pp. 631–641, Feb 2014.

[6] L. Asiminoaei, R. Teodorescu, F. Blaabjerg, and U. Borup, "Implementation and test of an online embedded grid impedance estimation technique for pv inverters," *Industrial Electronics, IEEE Transactions on*, vol. 52, no. 4, pp. 1136–1144, Aug 2005.

[7] B. Arif, L. Tarisciotti, P. Zanchetta, J. Clare, and M. Degano, "Grid parameter estimation using model predictive direct power control," *Industry Applications, IEEE Transactions on*, vol. 51, no. 6, pp. 4614–4622, Nov 2015.

[8] J. G. Normiella, J. M. Cano, G. A. Orcajo, C. H. Rojas, J. F. Pedrayes, M. F. Cabanas, and M. G. Melero, "Analytic and iterative algorithms for online estimation of coupling inductance in direct power control of three-phase active rectifiers," *IEEE Trans. Power Electron.*, vol. 26, no. 11, pp. 3298–3307, Nov. 2011.

[9] P. Garcia, J. Guerrero, J. Garcia, A. Navarro-Rodriguez, and M. Sumner, "Low frequency signal injection for grid impedance estimation in three phase systems," in *Energy Conversion Congress and Exposition (ECCE), 2014 IEEE*, Sept 2014, pp. 1542–1549.

[10] C. Wu, W.-H. Lau, and H.-H. Chung, "Analytical technique for calculating the output harmonics of an h-bridge inverter with dead time," *Circuits and Systems I: Fundamental Theory and Applications, IEEE Transactions on*, vol. 46, no. 5, pp. 617–627, May 1999.

[11] S. Kaitwanidvilai, W. Khan-ngern, and M. Panarut, "The impact of deadtime effect on unwanted harmonics conducted emission of pwm inverters," in *Environmental Electromagnetics, 2000. CEEM 2000. Proceedings. Asia-Pacific Conference on*, May 2000, pp. 232–237.

[12] S.-G. Jeong and M.-H. Park, "The analysis and compensation of dead-time effects in pwm inverters," *Industrial Electronics, IEEE Transactions on*, vol. 38, no. 2, pp. 108–114, Apr 1991.

[13] D.-H. Lee and J.-W. Ahn, "A simple and direct dead-time effect compensation scheme in pwm-vsi," *Industry Applications, IEEE Transactions on*, vol. 50, no. 5, pp. 3017–3025, Sept 2014.

[14] L. K. Mestha and P. D. Evans, "Analysis of on-state losses in pwm inverters," *IEE Proceedings B - Electric Power Applications*, vol. 136, no. 4, pp. 189–195, July 1989.

[15] J. W. Kolar, H. Ertl, and F. C. Zach, "Influence of the modulation method on the conduction and switching losses of a pwm converter system," in *Industry Applications Society Annual Meeting, 1990., Conference Record of the 1990 IEEE*, vol. 1, Oct 1990, pp. 502–512.

[16] "IEEE recommended practices and requirements for harmonic control in electrical power systems," *IEEE Std 519-1992*, pp. 1–112, April 1993.

[17] G. Goertzel, "An algorithm for the evaluation of finite trigonometric series," *The American Mathematical Monthly*, vol. 65, no. 1, pp. 34–35, 1958.

[18] J.-H. Kim, J.-G. Kim, Y.-H. Ji, Y.-C. Jung, and C.-Y. Won, "An islanding detection method for a grid-connected system based on the goertzel algorithm," *Power Electronics, IEEE Transactions on*, vol. 26, no. 4, pp. 1049–1055, April 2011.



# Modelling of 4-wire low voltage systems for enhanced control strategies of grid-tied power converters

Dissertation submitted in fulfillment of the requirements for the degree of Doctor of Philosophy in the Energy and Process Control PhD program of the University of Oviedo

Thesis supervisors: Pablo García Fernández and José Manuel Cano Rodríguez.

Professors at the Department of Electrical, Electronics, Computers, and Systems Engineering.  
University of Oviedo



Ed. Torres Quevedo (Departamental Oeste), bloque 4.  
Campus Universitario, 33204 Gijón.

Department of Electrical, Electronics,  
Computers and Systems Engineering



Universidad de Oviedo  
*Universidá d'Uviéu*  
University of Oviedo